

Study and Experimental Characterization of a Novel Photo Injector for the CLIC Drive Beam

THÈSE N° 5020 (2011)

PRÉSENTÉE LE 5 MAI 2011
À LA FACULTÉ SCIENCES DE BASE
LABORATOIRE DE PHYSIQUE DES ACCÉLÉRATEURS DE PARTICULES
PROGRAMME DOCTORAL EN PHYSIQUE

ÉCOLE POLYTECHNIQUE FÉDÉRALE DE LAUSANNE

POUR L'OBTENTION DU GRADE DE DOCTEUR ÈS SCIENCES

PAR

Öznur METE

acceptée sur proposition du jury:

Prof. O. Schneider, président du jury
Prof. L. Rivkin, Dr S. Döbert, directeurs de thèse
Prof. A. Bay, rapporteur
Dr H.-H. Braun, rapporteur
Dr F. Stephan, rapporteur



Suisse
2011

Résumé

Dans cette thèse, les propriétés transversales et longitudinales de faisceaux du photoinjecteur PHIN sont caractérisées. L'objectif de la recherche est de démontrer la production sûre et ferme d'un train de bouquet longueur $1.3 \mu s$, avec $2.33 nC$ charge par bouquet et $4.5 nC$ de charge totale, par le photoinjecteur PHIN. Dorénavant, la thèse constitue l'étude de faisabilité pour l'implémentation d'un photoinjecteur comme la source de faisceau "drive" du Collider Linéaire Compact.

Le photoinjecteur PHIN a été conçu et installé sur un éventaire d'essai dévoué à CERN en 2008, par une collaboration entre LAL, CCLRC et CERN. Dans cette collaboration, LAL et RAL ont engagé au design et à la construction du canon RF et du laser, respectivement. La production de la photocathode aussi bien que la coordination générale et le fait de commander était sous la responsabilité du CERN. Le projet est dans le cadre de la deuxième Activité de Recherche Collective PHIN du programme de CARE Européen.

Pendant le fait de commander du photoinjecteur PHIN, les propriétés de faisceaux ont été étudiées par les mesures systématiques rigoureuses et les simulations. La charge maximum par bouquet produit par la cathode Cs_2Te a été trouvée comme $4.4 nC$, en accord avec la limite théorique de $4.7 nC$. L'émittance normalisée transversale, l'énergie du faisceau et la propagation d'énergie ont été mesurés dans un coup simple ainsi qu'en fonction du temps. Les mesures de coup simples ont révélé des informations utiles sur la stabilité de coup-à-coup propriétés du faisceau, alors que les mesures en fonction du temps ont reflété la stabilité le long du train de bouquet. Le système de mesures d'émittance avec multifente, les moniteurs de profil d'OTR avec gated CCD cameras et une calorimetre segmentée ont été conçus, implementés et utilisés pour les mesures principales.

La caractérisation expérimentale et les études numériques indiquent clairement la faisabilité d'un photoinjecteur dans les spécifications définies par la facilité d'épreuve de CLIC existante. Des études de design et simulations plus avancés ont été accomplis basés sur les modifications du courant PHIN RF canon. Dans ce modèle successif, un canon RF avec les spécifications du faisceau "drive" de CLIC a été enquêté et proposé comme le design préliminaire pour les futures études d'injecteur du faisceau "drive" CLIC.

Mots-Clés: Le photoinjecteur, le canon RF, la source du faisceau "drive" CLIC, le faisceau d'électron dominé par la charge spatiale, la mesure d'émittance avec la technique multifente.

Abstract

In this thesis, the transverse and longitudinal beam properties of the PHIN photoinjector are characterized. The objective of the research is to demonstrate the reliable and stable production of a $1.3\ \mu\text{s}$ long bunch train, with $2.33\ nC$ charge per bunch and $4.5\ \mu\text{C}$ of total charge, by the PHIN photoinjector. The results of this thesis are the important steps towards the feasibility demonstration of a photoinjector as the Compact Linear Collider's drive beam source.

The PHIN photoinjector has been conceptualized by a collaboration between “Laboratoire de l'Accélérateur Linéaire (LAL)”, “Rutherford Appleton Laboratory (RAL)” and “Organisation Européenne pour la Recherche Nucléaire (CERN)”. Within this collaboration, LAL and RAL have committed to the design and the construction of the RF gun and laser, respectively. The photocathode production as well as the overall coordination and commissioning were under the responsibility of CERN. The project is in the framework of the second Joint Research Activity PHIN of the European CARE program.

The photoinjector has been installed, in 2008, on a dedicated test-stand at CERN. During the commissioning of the PHIN photoinjector, the beam properties have been studied by rigorous systematic measurements and simulations. The maximum charge per bunch yield of the Cs_2Te cathode has been found to be $4.4\ nC$, in agreement with the theoretical limit of $4.7\ nC$. The transverse normalized emittance, beam energy and energy spread have been measured both in a single shot and the time-resolved manner. The single shot measurements revealed useful information about the shot-to-shot stability of the beam properties, whereas the time-resolved measurements have reflected the stability along the bunch train. The multi-slit emittance measurement set-up, OTR profile monitors with gated CCD cameras and a segmented beam dump have been designed, implemented and utilized for the main measurements.

The experimental characterization and the numerical studies clearly indicate the feasibility of a photoinjector within the specifications defined by the existing CLIC test facility. Further simulation and design studies have been conducted based on several modifications of the current PHIN RF gun design. In this successive model an RF gun with the specifications of the CLIC drive beam has been investigated and proposed as the preliminary design for the future CLIC drive beam injector studies.

Keywords: Photoinjector, RF gun, CLIC drive beam source, space charge dominated electron beam, multi-slit emittance measurement.

Contents

Preface	1
1 Introduction to the Compact Linear Collider Project	3
1.1 Accelerator Aspects of Multi-TeV Physics Studies	3
1.2 Scenarios for a Lepton Collider in the Post-LHC Era	4
1.3 Compact Linear Collider (CLIC), A Multi-TeV e^-e^+ Linear Collider	5
1.3.1 Description of the CLIC General Layout	6
1.3.2 Power Generation for CLIC: Drive Beam and Its Injector Specifications	9
1.3.3 History of the CLIC Study	11
1.4 Photo-injector Option for the Drive Beam	13
2 A Review of Beam Dynamics Aspects of the Photoinjectors	15
2.1 Longitudinal Dynamics in an RF Gun	16
2.2 Emittance Growth Mechanisms	20
2.2.1 RF Field Dependence	20
2.2.2 The Space Charge Effect	20
2.2.3 Thermal Effects during the Photoemission Process	21
2.2.4 Conclusion	22
2.3 Emittance Compensation Schemes	23
2.3.1 Compensation of Space-Charge-Induced Emittance with a Lens	23
2.3.2 Compensation of Space-Charge-Induced Emittance with Focusing RF Force	24
2.4 A Model for Optimization of the Parameters	25
2.5 Applications of RF Photoinjectors	28
2.6 PHIN Photoinjector Test Facility at CERN	31
3 Beam Dynamics Simulations for the PHIN Photoinjector	33
3.1 PARMELA, A Particle Tracking Code	34
3.1.1 Highlights from the PARMELA Program	34
3.1.2 Representation of PHIN in PARMELA Input	35
3.2 Model for the PHIN Photoinjector	39
3.2.1 RF Phase Dependence	40
3.2.2 Laser Spot Size Dependence	41
3.2.3 Gradient Dependence	43
3.2.4 Charge per Bunch Dependence	44
3.2.5 Summary for the PHIN Baseline Configuration	47
3.3 Stability Aspects of PHIN: e^- Beam Sensitivity to the Jitter on the Parameters	53
3.3.1 Phase Jitter	53
3.3.2 Gradient Jitter	55
3.3.3 Charge Jitter	56
3.3.4 Laser Spot Size Jitter	57
3.3.5 Laser Pulse Length Jitter	58

4 Instrumentation and Experimental Set-Up for PHIN	61
4.1 Photocathode	62
4.1.1 Electron Emission: Thermionic, Field-Emission, Photo-Emission	62
4.1.2 <i>Cs₂Te</i> Cathode Preparation for PHIN at CERN Photo-Emission Laboratory	63
4.2 Laser System	64
4.3 Design and Simulations for the PHIN RF Gun	65
4.4 OTR Profile Monitoring for Beam Size, Emittance and Energy Measurements	70
4.4.1 Emittance Measurement for Space Charge Dominated Beams: The Multi-Slit Method	72
4.4.2 Optimization of a Multi-Slit Measurement System and the Design of the PHIN Emittance-Meter	74
4.4.3 Magnetic Spectrometer	77
4.5 Instruments for the Time Resolved Measurements	79
4.5.1 Specifications of the Intensified-Gated CCD Camera	79
4.5.2 Segmented Dump for the Energy Measurements	80
4.6 Automated Software for the Measurements	82
5 Experimental Results of the PHIN Commissioning	85
5.1 Charge Production	86
5.2 Beam-Loading Compensation	91
5.3 Transverse Phase Space	91
5.3.1 Beam-Size Measurement Results	92
5.3.2 Data Analysis Techniques for the Transverse Emittance Measurements	96
5.3.3 Systematic Error Calculation for the Emittance Measurement	102
5.3.4 Emittance Measurement Results	105
5.4 Time-Resolved Transverse Characterization of the Beam	108
5.4.1 Beam size along the Pulse Train of 1.2 μs	108
5.4.2 Emittance along the Pulse Train of 1.2 μs	109
5.5 Longitudinal Phase Space	115
5.6 Time-Resolved Longitudinal Characterization of the Beam	116
5.7 Correlation Between the PHIN Laser Beam and the Electron Beam	119
5.8 Conclusions and The Post-Commissioning Activities for PHIN	121
6 The Conceptual Study of a New RF Gun for the CLIC Drive Beam Photoinjector	123
6.1 The Requirements and the Stability Challenges of the CLIC Drive Beam Photoinjector	123
6.2 The design of an 1 GHz RF Gun for the CLIC Drive Beam Photoinjector	125
6.3 The Beam Dynamics Aspects	128
Conclusions	137
Acknowledgments	139
Appendix 1 - Thermal Injector of CTF3	141

Appendix 2 - The Beam Dynamics for Different Bunch Charge Values	142
Appendix 3 - Correlation Between the Fluctuations along the Pulse Train and on the RF Field	144
References	145

List of Figures

1	Livingstone plot.	4
2	An accelerating structure for CLIC that has been tested to 100 MV/m. Designed at CERN, the components were manufactured by KEK and the assembly and bonding as well as testing with high-power RF was done by SLAC (Courtesy SLAC).	7
3	CLIC general layout.	8
4	The schematic of the beam recombination and the time structure of the drive beam before and the beam recombination process.	10
5	Schematic of the CLIC two-beam acceleration module.	10
6	The illustration of two-beam acceleration.	11
7	Layout of the CLIC Test Facility. A downscaled version of the CLIC Drive Beam Generation System.	12
8	Axial electric field for a $2 + \frac{1}{2}$ cell cavity (a) and half geometry the cavity cross-section which is symmetric with respect to the horizontal axis.	17
9	Solution of Eq.8 for $\phi_\infty = \frac{\pi}{2}$	18
10	PARMELA simulation result shows a) the energy gain in the RF field as a function of the relative phase of the cell with respect to the master clock, b) the ramping of the beam energy in the cavity at the nominal phase of 35°	19
11	Analytic estimations for the thermal emittance with respect to laser spot size and the cathode temperature.	22
12	Transverse phase space (a) after the gun and (b) at a downstream position of 115.6 cm where the emittance compensation occurs.	25
13	Maximum achievable accelerating gradient values for different RF guns including the CLIC designs in comparison with the Killpatrick criteria.	27
14	The illustration of the PHIN RF gun from different view angles.	31
15	PHIN Layout.	36
16	The example of a PARMELA input file for PHIN.	38
17	The background magnetic field for PHIN as it is represented in the PARMELA program.	39
18	The simulation result of the scan in the search of (a) the on-crest phase for the PHIN simulations and (b) the evolution of the bunch length along the beamline at these emission phases (b).	41
19	(a) The variation of the transverse beam size and (b) the transverse emittance with respect to the focusing solenoid current for different laser spot sizes. The magnet settings that are providing the minimum emittance for each laser spot size are marked with the red dots on the beam size curves. The simulations have been performed for a charge per bunch value of 2.33 nC.	42
20	The transverse beam size (a) and the emittance (b) evolution along the beamline up to a downstream point at 150 cm. The simulations have been performed under the optimum focusing for the nominal PHIN specifications which corresponds to 237.65 A.	43

21	The transverse beam size (a) and the emittance (b) evolution along the beamline up to a downstream point at 150 cm. The curves show the case under the focusing conditions that are optimized for minimum emittance for each different laser spot size.	44
22	The behavior of (a) the beam size and (b) the transverse normalized emittance with respect to the focusing solenoid current for different gradient values. The red dots on (a) are used to emphasize the settings for the minimum emittance. The evolution of the parameters along the beamline up to a downstream position of 150 cm, with respect to the cathode, is given in (c) and (d).	45
23	The longitudinal beam parameters for different gradient values. The bunch length (a) and the energy spread (b) along the beamline increases when the gradient is lower. As a result the longitudinal normalized emittance grows after a longitudinal position of ~ 70 cm.	46
24	The behavior of the beam size (a) and the transverse normalized emittance (b) with respect to the focusing solenoid current for different charge values. The red dots on (a) are used to emphasize the settings for the minimum emittance. The evolution of the parameters along the beamline up to a downstream position of 150 cm, with respect to the cathode, is given in (c) and (d).	47
25	The transverse normalized emittance scales with the square root of the charge per bunch value.	48
26	The longitudinal beam parameters for different charge per bunch values. The energy spread (a) and the bunch length (b) along the beamline increases inversely proportional to the charge per bunch. As a result the longitudinal normalized emittance grows after a longitudinal position of ~ 80 cm.	49
27	The beam dynamics parameters at the gradient of 85 MV/m for the nominal beam charge of 2.33 nC.	51
28	The effect of the phase jitter on energy (a), energy spread (b), bunch length (c) and longitudinal emittance (d).	54
29	The effect of the gradient jitter on energy (a), energy spread (b), the bunch length (c) and the longitudinal emittance (d).	55
30	The effect of the charge jitter on transverse (a) and longitudinal emittance (b), energy spread (c) and bunch length (d).	57
31	The effect of the jitter of laser spot size on the beam size (a) and the transverse normalized emittance (b).	58
32	The effect of the changes in laser pulse length on longitudinal beam parameters.	59
33	Layout of the laser system.	64
34	A photograph from the laser-driven PHIN RF gun that consists of a 2+1/2 cell normal conducting S-band standing wave cavity.	66
35	Illustration of the electric field in the cavity that is excited in the π -mode. The figure obtained as the result of the SUPERFISH simulation for the 2 + 1/2 cell normal conducting S-band standing wave PHIN cavity.	66
36	The on-axis electric field that is excited in the PHIN RF gun for the π mode.	67

37	The result of the SUPERFISH frequency scan. The resonance frequencies for different modes are, 2897.15 MHz , 2944.15 MHz , 2998.55 MHz . The resonance frequency of 2998.55 MHz has been used for the PHIN RF gun, which corresponds to the π -mode.	67
38	An example SUPERFISH input file for the PHIN RF gun for the π resonance mode.	68
39	A view from the beamline including the PHIN RF gun and the solenoids that are installed at both ends of the cavity.	69
40	The intensity distribution of the OTR for different beam energies, according to the Eq. (42). For a beam with the 5.5 MeV energy, the detector can be placed with the optimum observation angle of 2.7° , with respect to the incident surface normal, in order to receive the maximum OTR intensity.	70
41	The schematic representation of the angular distribution of the backward OTR.	71
42	The illustration of the PHIN OTR profile monitoring system for emittance and beamsize measurements.	71
43	The illustration of the PHIN OTR profile monitoring system for energy and energy spread measurements.	72
44	The concept of the emittance measurement with the multi-slit set-up at the PHIN photoinjector.	73
45	The implementation of the magnetic spectrometer on the PHIN beamline.	78
46	a) The magnetic field intensity distribution of the spectrometer dipole. b) The same distribution can be represented with a contour plot. The path that the beam follow is denoted with the “yellow” line.	78
47	The Proxitronic CCD camera and its digital control box unit that are used in the PHIN measurements.	79
48	The spectral response characteristics of the intensified CCD camera for different photocathode types.	80
49	A drawing of the 20 channel segmented dump that has been used for the time resolved energy and energy spread measurements of the PHIN photoinjector.	81
50	The signals from the segmented dump.	81
51	The collection of software in order to perform the data acquisition, online and offline analysis for the PHIN measurements.	82
52	A snapshot from the scope during the operation with an electron pulse train of 1300 ns . The yellow signal in Channel 1 belongs to the FCT which is located at the exit of the RF gun. The green signal in Channel 2 has been acquired from the FC which is located after the spectrometer magnet at the end of the beamline.	88
53	a) Saturation of the photoemission of the electrons with the increasing laser energy per pulse. b) The linear behavior of the photoemission in terms of the integrated charge and the laser energy over the pulse train.	88
54	The field emission. a) The emission increases proportional to the square of the field. b) The Fowler-Nordheim analysis for the field emission. The field enhancement factor β , for 3 GHz PHIN gun has been deduced as 77 from the slope of the curve.	89

55	The field emission. a) PARMELA simulation presents the beam intensity change with respect to the RF phase, by taking into account the photoemission only. b) The measured charge production as a combination of the photoemission and a “Schottky-like” field emission effect.	89
56	Beam loading compensation. a) RF power in the gun (1a) and reflected power (2a) when no beam is present. b) RF power in the gun (1b) and reflected power (2b) when the beam is present.	91
57	An example beam size measurement with single-shot OTR profiling from 02 March 2010. The 1σ beam size has been measured as 1.5 mm	92
58	Beam size measurement as a function of the focusing magnet current for a 200 ns - long bunch train with 2.07 nC bunch charge and at the energy of 5.46 MeV	93
59	The comparison of the saturated intensity distribution with the Gaussian curve reconstructed by using a simulated beam size. a) The 3D intensity distribution of the beam under the saturation effect of the CCD camera. b) The example cross-section of the intensity distribution and the Gaussian fit to the feet of the profile.	94
60	The measured and reconstructed beam size scan in comparison with the PARMELA simulation (left).	95
61	Beam size measurements for different laser spot sizes within a range of the focusing solenoid current.	95
62	Energy deposition of 5.5 MeV pencil e^- beam in a 2 mm thick tungsten slab.	96
63	a) The typical beam profile after the multi-slit mask and the region of interest for the background fit. b) Gaussian background on the original profile. c) The beam profile after the Gaussian background subtraction. d) Individual beamlets with the Gaussian fit curves.	97
64	The searches for the correct background model for the beam profile. a) The profile with the Gaussian envelope. b) Resulting emittance with respect to different background subtraction levels.	99
65	The steps of the emittance analysis. a) The image which is observed after the multi-slit mask. b) Beam profile with Gaussian fit curves for individual beamlets. c) The summary of the mean position and the divergence of each beamlet determined from Gaussian fit curves. d) Reconstructed phase space. The transverse rms normalized emittance has been measured as 7.4 mm mrad with a single shot measurement.	100
66	The phase space, simulated (left) and reconstructed from the measurement (right). The emittance was measured as 10.7 mm mrad for 1.28 nC beam at the energy of 5.5 MeV . The measurement was performed with the laser spot size of 4 mm	101
67	The comparison of the statistical and the systematic errors on the multi-slit method for the emittance measurement.	104
68	Emittance measurement with respect to the laser spot size. (Blue) $\sigma_{Knife Edge} = 4\text{ mm}$, $Q=1.28$, $E=5.512\text{ MeV}$, Train Length = 200ns . (Green) $\sigma_{Knife Edge} = 2\text{ mm}$, $Q=1.1$, $E=5.67\text{ MeV}$, Train Length = 200ns	106

69	a) Emittance scan with respect to the focusing magnet current at different RF phase values for a bunch train of 500 ns with the 1.6 nC/bunch. b) The emittance measurement with respect to the RF phase for a bunch train of 1300 ns with the 0.4 nC/bunch. The emittance values in (b) are given with respect to the value at $\Delta\Phi = 0^0$	106
70	Emittance measurement for different train lengths. 200 ns, 1.7 nC, 5.616 MeV. 1300 ns, 1.7 nC, 5.616 MeV.	107
71	The illustration of the time-resolved OTR profiling of the electron beam. The scheme as shown in the figure would allow a measurement over a region from 400 ns to 600 ns along the bunch train.	108
72	Beam size measurement along the pulse train in comparison with the measurement with the full train. 1.4 nC, 4.8 MeV	109
73	Beam size scan along the pulse train for a beam of 1.4 nC, 4.9 MeV. a) Horizontal beam size. b) Vertical beam size. c) Representation of the measurement under a focusing current of 202 A at different gate positions.	110
74	Emittance scan, with a beam of 1.6 nC, 4.8 MeV, along the pulse train with the steps of 400 ns.	111
75	Emittance measurement along the pulse train with the steps of a) 400 ns (1.6 nC, 4.8 MeV), b) 200 ns (1.4 nC, 4.9 MeV), c) 100 ns (1 nC, 5 MeV).	113
76	The emittance fluctuations along the pulse train in comparison with the RF pulse shape.	114
77	An example from the energy measurement in the spectrometer by OTR monitoring. a) The image that is captured by the CCD camera. b) The horizontal profile of the image.	116
78	Energy and energy spread measurement with respect to the RF phase.	116
79	An example from the laser pulse train length measurement with the streak camera. The average of several subsequent measurements resulted with a 1σ of $2.8 (\pm 0.2)$ ps. This indicates a 7% shot to shot stability for the laser micropulse length.	117
80	The time-resolved energy and energy spread measurement by the segmented dump. a) The contour plot of the energy change during the 1300 ns electron beam hitting the segmented dump. b) Deviation of the mean energy in correlation with the RF pulse shape.	117
81	The time-resolved energy spread measurement.	118
82	The comparison of the energy spread measurement with the segmented dump and the OTR profiling. The measurement has been performed as a function of the longitudinal position along the bunch train.	118
83	Horizontal position stability for a) laser beam and b) electron beam.	119
84	The correlation of the position stability between the laser and the electron beam for a) horizontal and b) vertical beam positions.	120
85	Intensity stability for a) laser beam and b) electron beam.	120
86	a) An example to demonstrate the intensity of the electron beam follows the laser intensity profile. b) An example of the flat laser intensity profile.	120
87	The SUPERFISH solution for the 1 GHz RF gun that is excited in π -mode.	125
88	An example SUPERFISH input file for the 1 GHz RF gun which is designed for the CLIC drive beam photo injector.	126

89	The result of the SUPERFISH frequency scan which shows the resonance frequencies for different modes. The resonance frequency of 1 GHz has been used for the conceptual study of RF gun for the CLIC Drive Beam photoinjector.	127
90	An example PARMELA input file for the 1 GHz RF gun which is designed for the CLIC drive beam photo injector.	128
91	The on-axis electric field of 40 MV/m is excited in the cavity.	129
92	The variation of the beam energy and the transverse normalized emittance as a function of the emission phase.	130
93	a) The bunch length along the beamline. In PARMELA simulations, a constant the bunch of 19.5 ps has been achieved at the particular emission phase of 155° . b) The variation of the energy spread with respect to the emission phase. The minimum energy spread of 168.6 KeV can be obtained at the emission phase of 160° . c) The variation of the longitudinal emittance as a function of the emission phase. The minimum longitudinal emittance of $75\text{ }\mu\text{m}$ occurs at the phase of 150°	131
94	a) The energy ramp up through the cells of the $2 + 1/2$ cell cavity and throughout the beamline for different emission phases. b) The evolution of the transverse normalized emittance for various emission phases.	132
95	The evolution of a) the transverse beam size and b) the normalized emittance along the beamline. The emittance compensation occurs at a distance of 250 cm away from the cathode.	133
96	The evolution of the transverse normalized beam emittance with respect to the focusing magnet field at a downstream point, 250 cm away from the cathode. The emittance compensation occurs under the focusing of a magnetic field of 965.5 Gauss	133
97	The evolution of the beam size with respect to the focusing magnet field at a downstream point, 250 cm away from the cathode.	134
98	The background magnetic field that is created by PARMELA program as a result of the defined coil positions and currents.	134
99	The transverse phase space for the 1 GHz RF gun, at the magnet settings for the emittance compensation a) for the RF gun at a downstream location where the emittance compensation occurs (27.1 mm mrad @ 8.8 MeV), b) for the thermionic gun at the end of the injector (32.9 mm mrad @ 50 MeV).	136
100	The longitudinal phase space for a) the 1 GHz RF gun and b) the thermionic gun at the end of the injector.	136
101	The streak camera image of the bunches in the delay loop and the unwanted satellite bunches.	141
102	The beam dynamics parameters at the gradient of 85 MV/m for the beam charge of 1 nC	142
103	The beam dynamics parameters at the gradient of 85 MV/m for the beam charge of 1.5 nC	142
104	The beam dynamics parameters at the gradient of 85 MV/m for the beam charge of 2 nC	143
105	The beam dynamics parameters at the gradient of 85 MV/m for the beam charge of 2.5 nC	143
106	Correlations between the fluctuations along the train.	144

List of Tables

1	Overall CLIC parameters from 2010 conceptual design study.	7
2	The parameters for the CLIC main beams before and after the pre-damping rings.	8
3	The baseline parameters of the CLIC drive beam from the conceptual design studies (2010).	9
4	The longitudinal beam parameters of PHIN according to model.	19
5	According to model, the contributions of different sources to the total transverse normalized emittance for beam parameters of PHIN.	23
6	The design specification for recent photoinjectors.	29
7	Highlights in photoinjector development*. (Modified from S. J. Russell) . . .	30
8	The cards that are used in the PARMELA input file for PHIN.	36
9	Some of the attributes used in the PARMELA cards.	37
10	The baseline parameters used for simulations of PHIN.	40
11	The reference calibration for the baseline settings of the solenoids.	40
12	The longitudinal positions where a PARMELA simulation output is retrieved for the corresponding parameter.	40
13	Transverse beam parameters as a function of the laser spot size. The magnet settings are optimized for the minimum transverse normalized emittance.	43
14	Transverse and longitudinal parameters of the beam as a function of the gradient for the settings that are optimized for the minimum transverse normalized emittance.	45
15	Transverse and longitudinal parameters of the beam as a function of the charge per bunch for the settings that are optimized for the minimum emittance.	48
16	Summary of the optimum working points for PHIN for the given beam energy and the charge per bunch values.	52
17	The measure PHIN laser stability and the stability of the conventional RF power generator.	53
18	The deviation from the nominal longitudinal parameters under $\pm 1\%$ phase variation.	55
19	The deviation from the nominal longitudinal parameters under $\pm 1\%$ gradient variation.	56
20	The effect of the $\pm 1\%$ charge variation on the beam parameters.	56
21	The effect of the $\pm 1\%$ laser spot size variation on the transverse beam parameters.	58
22	The effect of the $\pm 1\%$ laser pulse length variation on the longitudinal beam parameters at 150 cm downstream of the beamline.	58
23	The design specifications for the PHIN laser-driven RF gun.	65
24	The PHIN RF gun properties that are retrieved from the SUPERFISH calculations.	69
25	The design specifications of the PHIN multi-slit emittance measurement set-up.	76
26	PHIN Commissioning timetable.	86
27	The specifications for the PHIN photoinjector.	86

28	The errors on the position and the divergence of the beamlets have been calculated in terms of the slit width and the mask-screen distance. The error on the beamlet intensities have been calculated as the product of measured individual beamlet intensities and the 4% electron beam intensity stability.	105
29	The summary of the results from the time-resolved transverse normalized emittance measurements with different resolutions.	112
30	The specifications in comparison with the achieved values for the PHIN photoinjector.	121
31	The measured PHIN stability in comparison with the simulated CLIC Drive Beam (DB) tolerances at the end of the injector.	124
32	Some the design parameters for the CLIC Drive Beam Linac at the end of the injector with the energy of 50 MeV.	125
33	The RF parameters that are given by the SUPERFISH simulations for the π -mode.	127
34	The reference calibration for the nominal settings of the solenoids.	133
35	The design specifications and the resulting beam dynamics parameters for the 1 GHz RF gun in comparison with the thermionic gun.	135

Preface

The Compact Linear Collider (CLIC) study proposes a multi-TeV, high luminosity, electron-positron linear collider in order to fulfill the current need for a lepton collider. The study has been started in the late 80s at CERN and currently is a joint effort with a collaboration of 40 institutes.

An innovative scheme of high peak RF power production for the high accelerating gradient has been proposed for CLIC. The so called "two-beam scheme" consists of two beams that are running parallel to each other. One of the beams is to be accelerated for the collision experiments and called "the main beam". The second beam of the CLIC scheme is "the drive beam" and will be employed for the power production. The two-beam acceleration scheme of CLIC Study proposes a unique power production technique. The scheme uses efficient low frequency klystrons to energize a very long drive beam train which is folded into short trains. The process provides high peak power that is adopted to the 12 GHz accelerating structures. The two-beam scheme should deliver a power of 275 MW per active accelerating metre, which is necessary to produce the electric fields of 100 MV/m.

The quality of the main beam acceleration depends on the stability of the power that is generated by the drive beam. Therefore, the optimization of the drive beam production with the proper time structure and within the required beam dynamics tolerances is one of the most important accelerator physics aspects of the project. The drive beam consists of a high current (101 A), low energy (2.37 GeV) beam with a repetition rate of 12 GHz. The high current is needed for the high peak power production in the so called "Power Extraction and Transfer Structures (PETS)". Consequently, a design for the CLIC drive beam source should provide high charge and adequate intensity stability as the paramount criteria.

Currently in the conceptual level, the baseline design of the drive beam injector consists of a thermionic gun. This electron source has to be combined with a sub-harmonic bunching system in order to provide the required time structure of the drive beam. However, a big disadvantage of this scheme is the parasitic satellite bunches due to the sub-harmonic bunching system.

A photoinjector has been raised as another option in this thesis in order to replace the existing thermionic gun of CLIC test facility (CTF3) and to form the bases of a source for the CLIC drive beam. A photoinjector is an electron source that uses laser pulses in order to extract electrons from the surface of a metallic or a semiconductor cathode. It has been proposed as a candidate for the CLIC drive beam for being a compact, high charge, low emittance electron source. The system is compact since it does not require an additional bunching system. The time structure is provided by manipulating the time structure of the laser pulses. Therefore the production of the parasitic charge is not an issue for the photoinjectors.

The goals of this thesis are:

- to perform comprehensive simulations of the PHIN photoinjector test beam line by using the PARMELA program,
- to optimize a working point for the PHIN photoinjector based on these simulations for the operation specifications,
- full experimental characterization of the PHIN beam with the short and the long

bunch trains,

- to compare the simulation and the measurements,
- to develop a single shot emittance measurement for space charge dominated beams (multi-slit method),
- to perform time-resolved measurements and to determine the evolution of the beam properties along the bunch train,
- to study the consequences of the findings in order to constitute a preliminary RF gun design for the CLIC drive beam injector specifications.

The following manuscript consists of six chapters.

The first chapter presents the Compact Linear Collider Project with an introduction of the several scenarios for the construction of a lepton collider. This chapter has a deductive structure which later focuses on the CLIC drive beam and its injector specifications. In this context, the photoinjector concept is given in this chapter.

The second chapter reviews the beam dynamics aspects of the photoinjectors in conjunction with the design of the PHIN photoinjector. Regarding the analytic and the numerical considerations, a general design strategy is summarised.

The third chapter has been devoted to the comprehensive characterization of a photoinjector by numerical studies. For this purpose, the PARMELA program has been used and introduced. A model for the PHIN photoinjector has been studied as a function of the key parameters and the stability aspects.

The experimental set-up with an emphasize on the beam diagnostics is discussed in details in Chapter 4.

The Chapter 5 includes the experimental results of the PHIN photoinjector. The beam measurements concerning the charge production, the transverse and the longitudinal phase space has been reported in this chapter. The data analysis techniques which developed for the multi-slit emittance measurement set-up are given in detail.

The findings of the research program and the general simulation studies have been compiled in order to lead to a conceptual design for a new RF gun. This new design has been intended to initiate a photoinjector technical design for the CLIC drive beam photoinjector. In Chapter 6, this design study is presented following a short introduction to the requirements and the stability challenges of the drive beam injector in comparison with PHIN commissioning results.

1 Introduction to the Compact Linear Collider Project

Contents

1.1 Accelerator Aspects of Multi-TeV Physics Studies	3
1.2 Scenarios for a Lepton Collider in the Post-LHC Era	4
1.3 Compact Linear Collider (CLIC), A Multi-TeV e–e+ Linear Collider	5
1.3.1 Description of the CLIC General Layout	6
1.3.2 Power Generation for CLIC: Drive Beam and Its Injector Specifica-	
tions	9
1.3.3 History of the CLIC Study	11
1.4 Photo-injector Option for the Drive Beam	13

1.1 Accelerator Aspects of Multi-TeV Physics Studies

Throughout the 20th century, the history of particle physics has recorded many explorations in different laboratories. The hadron-hadron colliders have been built to achieve discoveries in the energy frontiers. Essentially, the lepton-lepton colliders accomplished the precision measurements in the energy ranges charted by the hadron machines. Whereas the inner structure of a hadron was better probed by a lepton-hadron collider.

The realization of this tripodal scheme has been established by several colliders until the beginning of the 21st century. Some examples are TEVATRON (Fermilab, 1983-2011) for proton-antiproton collisions, LEP (CERN, 1989-2000) and SLC (SLAC, 1962-1998) for electron-positron collisions and HERA (DESY, 1992-207) for electron-proton collisions. It should be noted that the linear collider concept has been first demonstrated by SLAC Linear Collider (SLC). The centre of mass energies that are provided over the years by several accelerators have been summarized in the “Livingstone Chart”. The chart can be seen in Fig. 1.

Today, high energy physics experiments are focused on the tera electron volt (TeV) energy regions to explore the physics beyond the Standard Model such as supersymmetry, extra dimensions and new gauge bosons. In conjunction with these, the energy frontier will be extended by LHC up to 14 TeV. LHC physics program will confirm the standard model and will address the current open questions such as the existence of Higgs boson. In pursuit of new particles and their interactions, the searches “Beyond the Standard

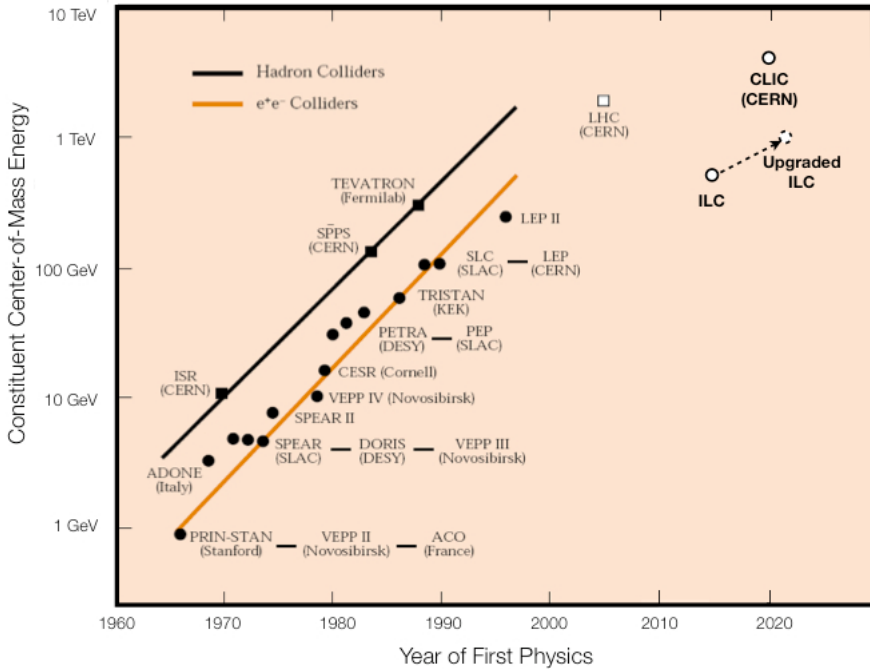


Figure 1: Livingstone plot.

Model" will be possible with the machine's high discovery potential in the "terascale" era. Consequently, LHC will determine the prospects of any future collider project to complement its results.

1.2 Scenarios for a Lepton Collider in the Post-LHC Era

There are several collider concepts in the context of providing complementary data to the LHC results. The International Linear Collider (ILC), Muon Collider (MC) and the Compact Linear Collider (CLIC) will be given as examples of lepton colliders. Those different schemes have been proposed for their certain particle physics prospects. However, their feasibility should be investigated from the accelerator physics point of view.

The ILC study is one of the international efforts in progress. It is an electron-positron linear collider with centre-of-mass energy of 0.5 TeV with a possible future upgrade to 1 TeV. This study proposes an RF system using superconducting accelerator cavities with the nominal accelerating gradient of 31.5 MV/m resulting with a total length of 31 km for the case of 0.5 TeV. The ILC machine would probably be sufficient to search a light Higgs boson or light supersymmetric particles. However, in order to explore a possible supersymmetric spectrum and the new strong interactions, a lepton-antilepton collider with multi-TeV centre-of-mass energy is required. In this case, the implementation of the ILC technology raises a feasibility issue in terms of the length of the linear accelerator.

A muon collider raises as another option. In theory the Higgs boson couples to the particles proportional to their masses. Therefore a muon collider would produce a higher Higgs production rate compared to a e^+e^- collider since the muon is heavier than the electron. Its potential to serve as a neutrino factory can be also added among a muon collider's physics prospects. The technological challenges of building a muon collider would

be beam cooling, difficulties in final-focus parameters, synchrotron and neutrino radiation concerns [1, 2, 3, 4]. Although the continuing effort to explore innovative solutions to these challenges, regarding the ongoing effort for e^+e^- colliders, the muon collisions would possibly come after the realization of a e^+e^- collider.

To summarise, one can conclude that, a multi-TeV electron-positron collider is necessary in order to make precision measurements in the LHC era. Due to the nature of this thesis, the accelerator physics aspects of such a collider will be the main focus for the following discussion.

Energy loss due to the synchrotron radiation can be considered as an argument while building a lepton collider. The charged particles emit “synchrotron radiation” when they are accelerated to relativistic velocities along the circular orbits. The circular orbit of particles in an accelerator is provided by magnetic fields. The particles are subject to a transverse deflection force due to the magnetic field. This is the so called “Lorentz force” given in Eq. (1), where \mathbf{p}_\perp , \mathbf{v}_\perp are the momentum and the velocity vectors perpendicular to the magnetic field vector, \mathbf{B} , m is the mass of the particle under the effect of the magnetic field. The radiation power, P_γ , emitted by a charged particle with the energy of, E , in a magnetic field is given in Eq. (2-3). In this equation, the r_c and μ_0 denote the classical electron radius and the magnetic permeability of free space, respectively. According to this expression, the energy loss as the synchrotron radiation is inversely proportional to the fourth power of the mass of the circulating particle. This loss has to be compensated by supplying additional RF power to the accelerator.

$$\frac{d\mathbf{p}_\perp}{dt} = \gamma m \mathbf{v}_\perp = e \frac{[c]}{c} [\mathbf{v} \times \mathbf{B}] \quad (1)$$

$$P_\gamma = \left[\frac{4\pi}{\mu_0} \right] \frac{2r_c^2 c}{3(mc^2)^2} B^2 E^2 = C_B B^2 E^2 \quad (2)$$

$$C_B = \left[\frac{4\pi}{\mu_0} \right] \frac{2r_c^2 c}{3(mc^2)^2} \quad (3)$$

The energy loss by radiation means an inefficient consumption of the RF power for a lepton accelerator. Therefore, the linear accelerators are advantageous for a future tera scale e^+e^- collider. Within this context, the CLIC project introduces the “two-beam acceleration” technology in order to build a compact linear e^+e^- collider with the reach of multi TeV energies.

1.3 Compact Linear Collider (CLIC), A Multi-TeV e^-e^+ Linear Collider

Compact Linear Collider (CLIC) study proposes a multi-TeV, high luminosity, electron-positron linear collider in order to fulfill the current need for a lepton collider [5, 6]. The study has been started in the late 80s at CERN and currently is a joint effort with a collaboration of 40 institutes.

For a high energy linear accelerator, such as CLIC, the length of the machine is a paramount item to be optimized in terms of cost-effectiveness. Therefore, the development of the accelerating structures capable of producing the required high gradient is one of

the technological challenges of the CLIC scheme. Within the CLIC study, an RF system has been proposed by using normal accelerator cavities operating at 12 GHz, in pulses 239 ns long, with the nominal accelerating gradient of 100 MV/m. The implementation of such cavities would result a total machine length of 48 km for a 3 TeV centre of mass energy of colliding beams.

The choice of an optimum acceleration frequency is an essential item of optimization for the linear collider studies. This optimization is done concerning the RF power consumption and the achievable accelerating gradient. In the last fifty years, a significant number of research activities have been carried out under the assumption that the achievable accelerating gradient extends with the increasing RF frequency [7, 8]. The limitation comes from the phenomenon called RF breakdown and the early investigations has been done by Kilpatrick [9] in 1957. The RF breakdown is a localized dissipation of energy on the accelerating structure surface due to high electric or magnetic fields. The process causes surface damages such as crater forming and melting on the structure surface. The experimental results confirm that the gradient limit increases with the square root of the frequency in a range of 300 MHz to 3 GHz in agreement with the Kilpatrick type criteria in Eq. (4),

$$E \sim \sqrt{f}, \quad (4)$$

where f is the RF frequency and E is the maximum electric field. However the criteria does not work for the absolute value of the achievable gradient.

The accelerating structure development is a crucial research activity within the CLIC study. The aspects of this research are studying the RF breakdown phenomenology and determining the limitations on the achievable accelerating gradient. The experiments focus on the RF frequency and pulse length dependence of the phenomenon as well as the impact of the material type and the surface treatment of the structures. The target structure should operate at low RF breakdown rates and remain undamaged by the inevitable RF breakdowns and RF heating. Among several designs, the candidate structure for CLIC has demonstrated an extremely low RF breakdown probability of less than one in 10^7 pulses. The tests have been done for 100 MV/m at the nominal pulse length. The mentioned accelerating structure can be seen in Fig. 2.

1.3.1 Description of the CLIC General Layout

The general CLIC layout is shown in Fig. 3. An innovative scheme of high peak RF power production for the high accelerating gradient has been proposed for CLIC. The so called "two-beam scheme" consists of two beams that are running parallel to each other. The overall CLIC parameters as denoted in the conceptual design studies in 2010, is given in Table 1.

One of the beams is to be accelerated for the collision experiments and called "the main beam". For a linear collider providing the colliding beams of high charge and ultra-low emittance is essential to obtain high collision luminosity. This implies the requirement for an injection system that has been designed, efficiently. The lower part of the layout illustrates the injector system for the CLIC main beams. The pre-damping and the damping rings are shown as a part of the system. These rings have been designed to reduce the beam emittance of the high charged electron and positron beams. The circumference,

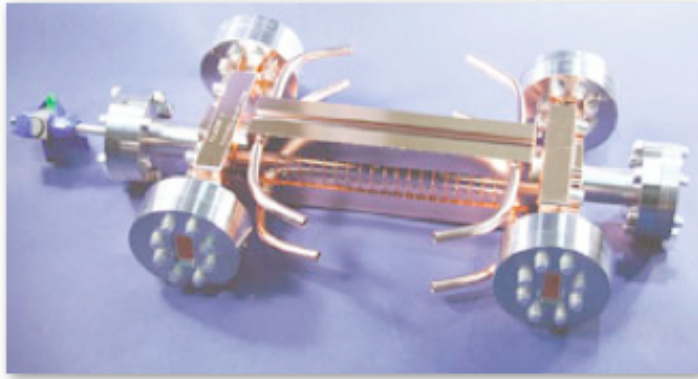


Figure 2: An accelerating structure for CLIC that has been tested to 100 MV/m. Designed at CERN, the components were manufactured by KEK and the assembly and bonding as well as testing with high-power RF was done by SLAC (Courtesy SLAC).

Table 1: Overall CLIC parameters from 2010 conceptual design study.

Centre of Mass Energy (GeV)	3000
Main Linac RF Frequency (GHz)	11.994
Luminosity ($10^{34} cm^{-2}s^{-1}$)	5.9
Linac Repetition Rate (Hz)	50
Number of Particles / Bunch	3.72×10^9
Number of Bunches / Train	312
Bunch Separation (ns)	0.5
Bunch Train Length (ns)	156
Beam Power / Beam (MW)	14
Unloaded / Loaded Gradient (MW/m)	120 / 100
Overall Two Linac Length (km)	42.16
Total Beam Delivery System Length (km)	2×2.75
Proposed Site Length (km)	48.4
Wall Plug to Main Beam Power Efficiency (%)	7

therefore the design of the optical lattice of the damping rings can be accomplished by considering the beam parameters such as injection emittance, number of bunches in the bunch trains, bunch spacing and bunch charge. The necessary extraction emittance is obtained depending on the damping time, which determines the energy of the ring. More details on the damping ring design and issues can be found in reference [10]. The pre-damping rings of CLIC has been designed to receive a 2.86 GeV beam with a large emittance. They reduces emittance of electron and positron beams before the injection to the damping rings. Damping rings produce the ultra-low emittance needed for the luminosity performance of CLIC [11, 12]. Some of the beam parameters before and after the pre-damping rings, and damping rings are given in the Table 2.

Additionally, further emittance reduction is possible by minimizing the emittance growth due to wake fields that are generated by the beam itself. The accelerating cavities of the

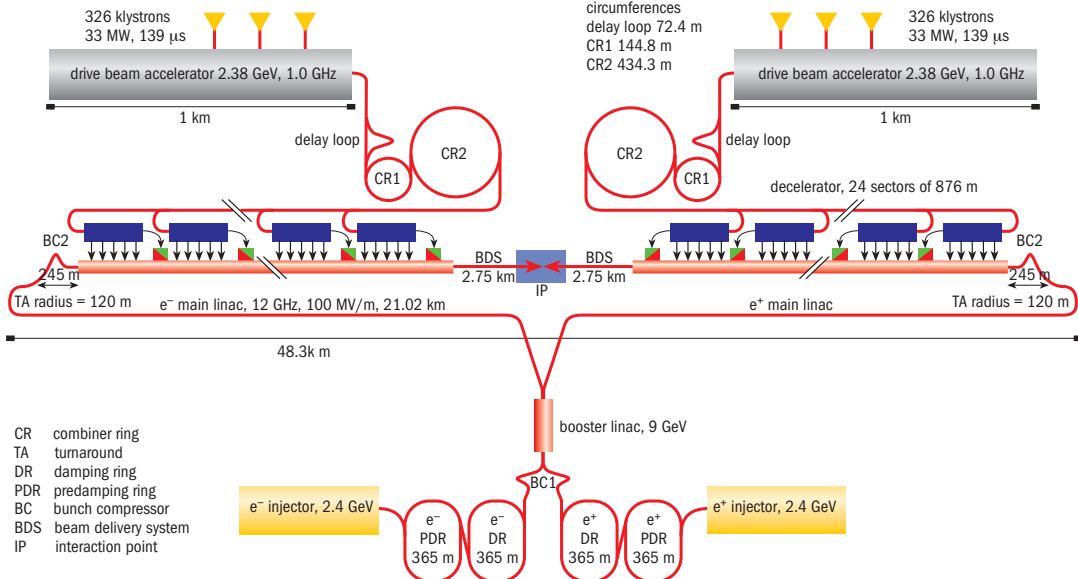


Figure 3: CLIC general layout.

Table 2: The parameters for the CLIC main beams before and after the pre-damping rings.

	Pre-Damping Rings		Damping Rings	
	e^-	e^+	Injected	Extracted
Bunch Population (10^9)	4.7	6.4	4.5	4.1
Bunch Length (mm)	1	9	10	1.4
Bunch Spacing (ns)				0.5
Number of Bunches / Train				312
Energy Spread (%)	0.07	1	0.5	0.13
Longitudinal Emittance (keV.m)	2	257	121	6
Horizontal Normalized Emittance (μ m)	100	7.10^3	63	0.5
Vertical Normalized Emittance (μ m)	100	7.10^3	1.5	5.10^{-3}

main linac have been optimized in order to minimize this effect. Eventually, after the beam delivery system, the beam has the emittances of 1 nm rms and 40 nm rms, in the vertical and horizontal planes, respectively.

The second beam of the CLIC scheme is "the drive beam" and will be employed for the power production. The two-beam scheme should deliver a power of 275 MW per active accelerating metre, which is necessary to produce the electric fields of 100 MV/m. The drive beam generation system can be seen in the upper part of the layout. The quality of the main beam acceleration depends on the stability of the power that is generated by the drive beam. Therefore, the optimization of the drive beam production with the proper time structure and within the required beam dynamics tolerances is one of the most important accelerator physics aspects of the project.

1.3.2 Power Generation for CLIC: Drive Beam and Its Injector Specifications

The two-beam acceleration scheme of CLIC Study proposes a unique power production technique. The scheme eliminates the utilization of the conventional klystrons and it is less expensive and more efficient in providing the high peak power required by the CLIC accelerating structures (275 MW/m). This also prevents the additional underground building of a scheme with klystrons.

The drive beam consists of a high current (101 A), low energy (2.37 GeV) beam with a bunch repetition rate of 12 GHz. The design specifications of drive beam is shown in Table 3. The high current is needed for the high peak power production in the so called “Power Extraction and Transfer Structures (PETS)” [13].

According to the CLIC scheme, the drive beam is generated as a long train ($139 \mu s$) of electron bunches. The separation between the individual bunches is 60 cm. This beam with a large bunch separation is accelerated up to 2.37 GeV in a linac with high efficiency, using the fully-beam-loaded acceleration mode [14]. In this mode, the most of the RF power is transferred to the beam so that the accelerating gradient in the end of the structure reduces nearly down to zero.

Table 3: The baseline parameters of the CLIC drive beam from the conceptual design studies (2010).

Energy (decelerator injection)(GeV)	2.37
Energy (final, minimum) (MeV)	237
Average Current in the Pulse (A)	101
Train Duration (ns)	243.7
Number of Bunches / Train	2922
Bunch Charge (nC)	8.4
Bunch Separation (ns)	0.083
Bunch Length (rms) (mm)	1
Normalized Emittance (rms) (mm mrad)	150

The drive beam linac is built by using normal conducting accelerating structures that operate at 1 GHz. Those structures are powered by the conventional klystrons. A series of rings are located in the drive beam generation system. These rings can be seen in Fig. 3 as “delay loop” and two successive “combiner rings (CR1 and CR2)”. This system of three rings is designed to achieve the frequency multiplication of the drive beam in order to increase its current up to 101 A. This innovative technique is called “the beam combination”. In the delay loop, the $139 \mu s$ long bunch train is divided into 24 sub-trains with the length of 243.7 ns. The 500 MHz RF deflectors are used to separate the “even” and “odd” buckets to be transferred to the delay loop or toward CR1 and CR2 that are equipped with RF deflectors of 1 GHz and 3 GHz, respectively. The “even” buckets are delayed while they are circulating the delay loop. Then, they are interleaved between the “odd” buckets by means of the combiner rings. After the whole procedure, the 24 sub-trains form a burst with the average beam current of 101 A. The time structure of the drive beam before and after the “beam combination process” is shown in Fig. 4.

The drive beam system generates 24 of such bursts with the separation of $5.8 \mu s$ and sends them to the decelerators for the power production. A decelerator module houses

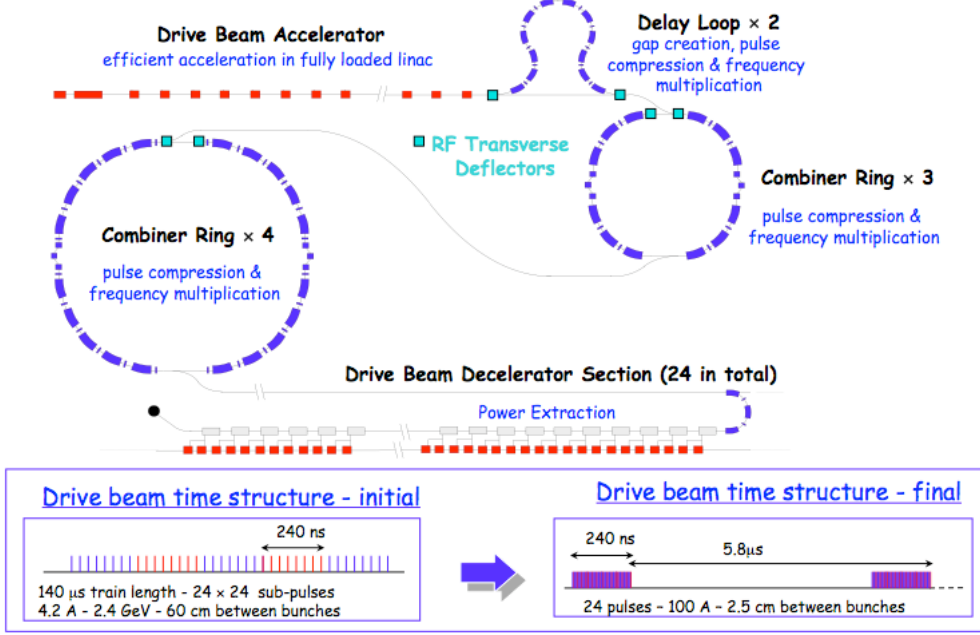


Figure 4: The schematic of the beam recombination and the time structure of the drive beam before and the beam recombination process.

PETS, quadrupoles and high power RF networks. The layout of the CLIC two-beam module can be seen in Fig. 5. When the bursts of drive beam enters one of the PETS, it excites preferentially the synchronous mode by interacting with the impedance of the periodically loaded waveguide. In this way, a single PETS generates 12 GHz RF power and drives two accelerating structures of the main beam, as shown in Fig. 6.

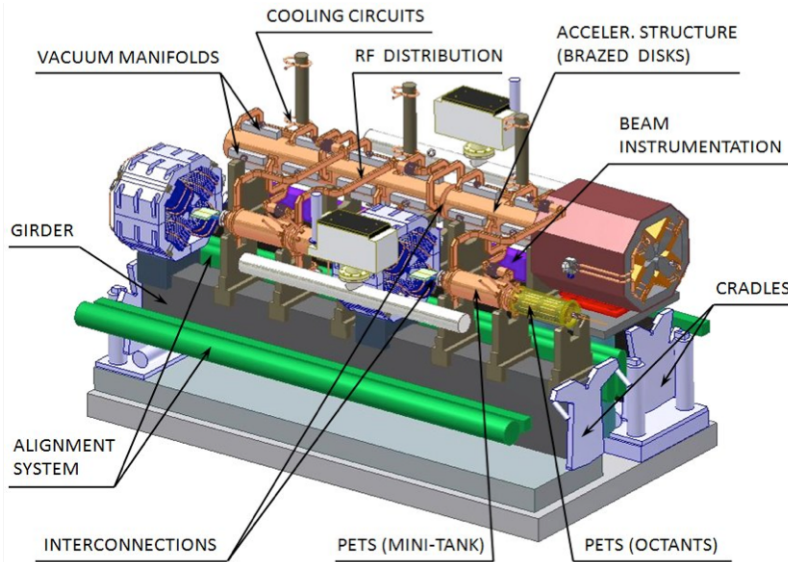


Figure 5: Schematic of the CLIC two-beam acceleration module.

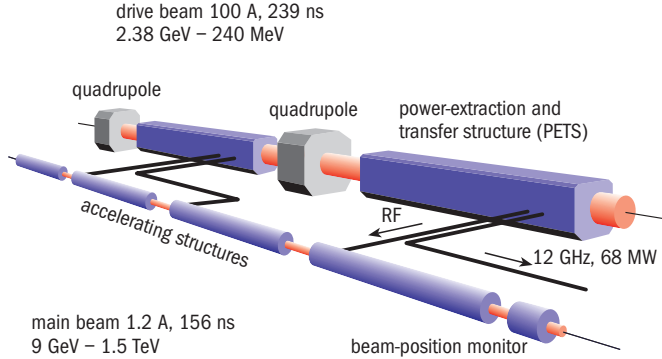


Figure 6: The illustration of two-beam acceleration.

1.3.3 History of the CLIC Study

A series of CLIC Test Facilities (CTF) have been built at CERN in order to experimentally approve the technologies necessary to build a linear collider. The CTF1 came into being to test the first CLIC prototype [15]. The prototype has been constructed from a 3 GHz, $1 + \frac{1}{2}$ RF gun and an accelerating section. The gun has been equipped with a laser-driven photocathode and operated at 100 MV/m resulting in a beam of 4.5 MeV. The generation of high frequency power (30 GHz) has been demonstrated with a structure excited by the bunch train of 24 bunches. The first phase of the CTF has been completed at the end of 1995 and the construction of a new phase has been initiated.

The new phase, CTF2, started soon after the first phase [16]. The facility had to demonstrate the feasibility of a number of technological challenges. The goals of CTF2 were:

1. to demonstrate the feasibility of CLIC two-beam accelerating scheme with 30 GHz technology;
2. to produce and test the prototypes of the CLIC modules;¹
3. to study the beam dynamics of a high-charge, multi-bunch drive beam;
4. to test the dynamic alignment system;
5. to test the CLIC instrumentation for beam monitoring.

During this second phase, the goals that are mentioned above have been successfully fulfilled [17]. Nevertheless CTF2 continued its operation for the investigations of a phenomena observed during the 30 GHz structure tests [18]. The structures under test, showed the signs of damage due to RF breakdown for the gradients higher than 60 MV/m. Hence the facility was transformed into a test stand for the investigations of the RF breakdown phenomena and meanwhile the construction of the third phase has been started.

¹A CLIC module is the building block for the CLIC accelerator. It consists of the accelerating structures operating at 30 GHz and the power extraction structures (PETS) to produce the 30 GHz RF power from the drive beam. It also houses the support girders and the active alignment system. Today the CLIC modules are based on the 12 GHz technology.

The third and the current phase (CTF3) is a downscaled version of the CLIC scheme. It is an international collaboration that is continuing the efforts towards the feasibility studies for CLIC [19]. It has to demonstrate the main feasibility issues such as two-beam acceleration towards the preparation of Conceptual and Technical Design Reports of CLIC Study.

The layout of the facility is given in the Fig. 7. The beam initiates from a thermionic gun which is located at the left-hand-side of the layout. After the gun and the following bunching system, the electron beam is accelerated in the CTF3 linac in the fully-beam-loaded mode. In CTF3, this operation mode has been tested with a $1.5 \mu\text{s}$ long pulse train that is accelerated by six fully-loaded structures, with a transfer efficiency of 98%.

In the end of the linac, the beam has a current of 3.5 A, a train length of $1.4 \mu\text{s}$ and the energy of 150 MeV. A novel CLIC technique to produce high current, the beam recombination, has been experimentally shown in CTF3. Regarding the technique, the pulse compression and the frequency multiplication occur in the CTF3 delay loop and the combiner ring. Eventually the train length is compressed down to 140 ns and the average beam current is increased up to 28 A.

After the beam recombination in the combiner ring, the beam is sent it the CLIC Experimental Area (CLEX), towards the left of the layout. There are several installations in the CLEX hall such as the Test Beam Line (TBL), Two-Beam Test-Stand (TBTS), probe beam injector CALIFES and the linac. The stability of the drive beam in PETS is tested in TBL. The beam can also be transferred to the TBTS by using a magnetic chicane in order to test the 12 GHz power production and the e^- beam acceleration [20]. This test is done with two beams that are running parallel to each other. The first one is the drive beam, as already mentioned, and the second one is the probe beam that is generated by the CALIFES photo-injector in the CLEX hall. The latest results from CTF3 towards the demonstration of the feasibility of CLIC can be found in the reference [21]

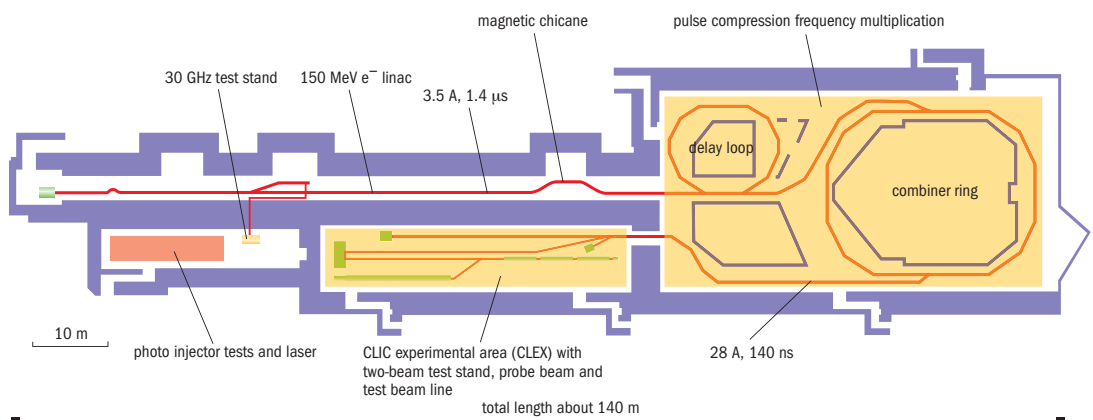


Figure 7: Layout of the CLIC Test Facility. A downscaled version of the CLIC Drive Beam Generation System.

1.4 Photo-injector Option for the Drive Beam

A photoinjector is an electron source that uses laser pulses in order to extract electrons from the surface of a metallic or a semiconductor cathode. The electrons can escape the cathode surface provided that the laser pulses satisfies the energy to decrease the potential barrier of the surface. The cathode plug is placed in one end of an RF cavity. This RF cavity is used for the rapid acceleration of the electrons after the production. The photoinjectors are high brightness, low emittance electron beam sources. The theory and implementation of them date back to 80s. A review of technical details and the beam dynamics aspects of the photoinjectors are introduced in Chapter 2.

A photo-injector option for CLIC drive beam has been also discussed during the early stages of the test facility studies [22]. The previous studies for the CLIC photo-injector can be found in the reference [23]. Indeed, there would be certain advantages of implementing an RF gun as the CLIC drive beam injector.

First of all, as a laser-driven system, a photo-injector can provide flexibility in manipulating the time structure of the beam. This manipulation is provided by a phase coding technique of a laser system. Additionally, a laser system does not require the switching time needed for a buncher system that should be utilized for a thermionic gun.

Moreover, in the drive beam linac every second bucket is populated and the interleaving buckets are supposed to be empty. However, the parasitic charge in the supposedly-empty buckets is inevitable due to the sub-harmonic bunching system. Those bunches are called as "the satellite bunches" above. The charge in the satellite bunches can cause radiation problems and compromises the power production efficiency. The necessary time structure can be provided by a photo-injector without producing this parasitic charge.

A photo-injector can provide a beam with small transverse and longitudinal emittances compared to a thermionic gun. Therefore, the beam transportation and bunch length manipulation become easier throughout the machine. A photo-injector is capable of producing long electron pulse trains by ensuring the stability of the beam parameters within the defined tolerances.

The feasibility research on the implementation of a photoinjector as the current CTF3 and future drive beam source is the main objective of this thesis. Within this research program the commissioning of the PHIN photoinjector has been completed [24]. The produced electron beam has been characterized in terms of the longitudinal and transverse properties.

The PHIN photoinjector has been designed and installed on a dedicated test-stand at CERN in 2008, by a collaboration between LAL, CCLRC and CERN. The project is in the framework of the second Joint Research Activity PHIN of the CARE (Coordinated Accelerator Research Europa) program.

Throughout this manuscript the photoinjector concept is introduced. The PHIN experimental set-up and a variety of accompanying beam diagnostics instrumentation are described. The PHIN commissioning has been continued with the intermittent runs between 2008 and 2010. The results of the beam characterization measurements are presented in comparison with the design specifications and the simulations. The current PHIN specifications aims an injector as a replacement of the existing CTF3 thermal injector. Therefore, as a part of the research program, several modifications have been performed on the current design of the PHIN RF gun according to the conceptual design parameters of the CLIC drive beam. In the end of the thesis, this design is explained

and the beam dynamics response is presented in comparison with the drive beam specifications. This final chapter is expected to constitute a preliminary effort and a reference towards the further studies of the CLIC drive beam electron source.

2 A Review of Beam Dynamics Aspects of the Photoinjectors

Contents

2.1 Longitudinal Dynamics in an RF Gun	16
2.2 Emittance Growth Mechanisms	20
2.2.1 RF Field Dependence	20
2.2.2 The Space Charge Effect	20
2.2.3 Thermal Effects during the Photoemission Process	21
2.2.4 Conclusion	22
2.3 Emittance Compensation Schemes	23
2.3.1 Compensation of Space-Charge-Induced Emittance with a Lens	23
2.3.2 Compensation of Space-Charge-Induced Emittance with Focusing RF Force	24
2.4 A Model for Optimization of the Parameters	25
2.5 Applications of RF Photoinjectors	28
2.6 PHIN Photoinjector Test Facility at CERN	31

The photoinjector concept has been first proposed by J. S. Fraser in 1985 and R. L. Sheffield in 1988 [25, 26]. It consists of an RF gun and the laser system. A semiconductor or metallic cathode is used to extract the electrons under the illumination of the laser pulses. The cathode is placed inside the half cell of the RF gun.

The modern accelerator applications, such as high energy physics experiments and light sources need high brightness electron beams. Over a few decades, the RF photoinjectors are favorably chosen for their stability and compactness to produce high brightness electron beams for free electron lasers (FEL), energy recovery linacs (ERL), and particle colliders. The brightness of the beam is defined as the ratio of the square of total beam emittance to the peak beam current, as shown in Eq. (5). Hence a low emittance, ϵ_{tot} , and a high peak current, I , are required for a high brightness, B . This can be obtained by maintaining a high longitudinal charge density which might be a result of either high bunch charge or a short bunch length or both. The photoinjectors became popular for their performance in providing these specifications.

$$B = \frac{2I}{\epsilon_{tot}^2} \quad (5)$$

They are compact since they do not require an additional bunching system. The time structure of the electron beam resembles the laser time structure therefore it is easily manipulated by coding the laser temporal structure. The transverse properties of the beam also depends on the transverse properties of the laser so that the laser spot size and shape can be used to obtain small emittances.

There are several beam dynamics aspects of designing and optimizing an RF photoinjector. These aspects define certain physical limitations on frequency, gradient and geometry. A model for estimation of the basic set of parameters can be determined by using those limitations. Despite the fact that a simplified model is useful for the first estimation of the critical parameters, rigorous simulations are mandatory for a full-fledged design study.

This thesis will refer to a combination of two models for the initial estimation of the design parameters. The first one is the so called Kim's model [27]. In the model the dynamics of an electron beam in a laser-driven RF gun was explained. Kim develops his model under the assumptions that the beam does not expand longitudinally or transversely during the acceleration and the bunch length is small when compared to the RF period. The second model has been proposed by C. Travier [28]. The latter is based on Kim's model and it introduces some corrections to the formulas which are derived from the numerical studies. This improved model will be considered as a guideline in the scope of this thesis.

2.1 Longitudinal Dynamics in an RF Gun

In order to investigate the longitudinal dynamics, one can start with an RF gun that consists of a cavity with $(n + 1/2)$ cells, where n is the number of cells in the cavity. The on-axis electric field envelope in the cavity is considered as a perfect sinusoidal. The example geometry of a $2 + \frac{1}{2}$ cell cavity and its on-axis electric field envelope can be seen in the Fig. 8. The equation for the field envelope is given in the Eq. (6), where $k = 2\pi/\lambda$ is the RF wave number, λ is the RF wave lenght, E_0 is the amplitude, z is the longitudinal position and it extends across $[0, (n + 0.5)\lambda/2]$.

$$E_z(z) = E_0 \cos(kz) \quad (6)$$

The particles that are travelling through the cavity cells gain energy from the field according to their phases with respect to the field. This can be written as the Eq. (7) under the sine convention,

$$\Delta W = q \int_{-L/2}^{+L/2} E_z(z, t) dz = q \int_{-L/2}^{+L/2} E_0 \cos(kz) \sin(\omega t + \phi_\infty) dz, \quad (7)$$

where q is the charge of the particle, L is the lenght of the cavity and ω is the angular frequency of the RF field. The asymptotic phase of the reference particle in the exit of the gun is given as ϕ_∞ . The reference particle has the phase ϕ_0 as it emerges from the cathode. Physically, the phase ϕ_0 is the phase difference between the reference particle and the RF field, as it emerging from the cathode. Whereas, in PARMELA program, the

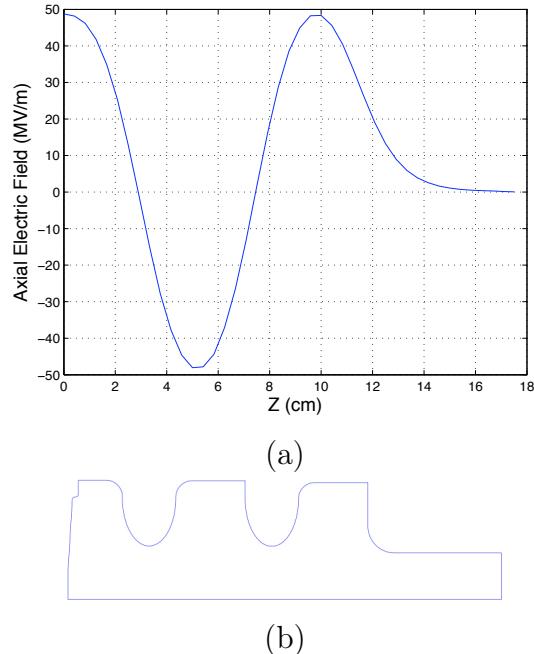


Figure 8: Axial electric field for a $2 + \frac{1}{2}$ cell cavity (a) and half geometry the cavity cross-section which is symmetric with respect to the horizontal axis.

phase ϕ_0 determines the phase difference between the angle of the master clock and the phases of the time-varying elements such as cells. The phase ϕ_∞ is defined as a function of the initial phase ϕ_0 and it is expressed in Eq. (8) in the practical units. The RF field strength is represented by the dimensionless parameter α as shown in the Eq. (9).

$$\phi_\infty = \phi_0 [^\circ] + \frac{f [MHz]}{E_0 [MV/m]} \left(\frac{0.61}{(\sin(\phi_0 [^\circ]) + 4.4\sqrt{\frac{f [MHz]}{E_0 [MV/m]}})} + 0.26 \right) \quad (8)$$

$$\alpha = 46.7 \frac{E_0 [MV/m]}{f [MHz]} \quad (9)$$

This model under the sine convention requires an optimum phase of $\pi/2$ for the reference particle in the exit of the cavity, in order to obtain the maximum energy gain from the RF field. In this respect, the α and ϕ_0 parameters are subject to optimization in order to provide an effective acceleration.

In Fig. 9, the behavior of the dimensionless field parameter, α , is shown with respect to the initial phase of the reference particle. The figure shows that, in the case of $\phi_\infty = \frac{\pi}{2}$ there exist no solution for $\alpha \leq 0.9$. Moreover, in the plot, one can obtain two ϕ_0 values which are fulfilling the condition $\alpha \geq 0.9$, one smaller and one larger than $\pi/4$. The value which constitutes the physical solution can be identified in the light of the following discussion.

The model assumes that the phase slippage of the electrons on the RF wave is limited to the cathode region. Therefore energy increases rapidly near the cathode. The relativistic Lorentz factor is given as Eq. 10. The rapid acceleration can be indicated by a high γ factor. Consequently, in the below expression, the term $\alpha \sin(\phi_0)$ holds the information

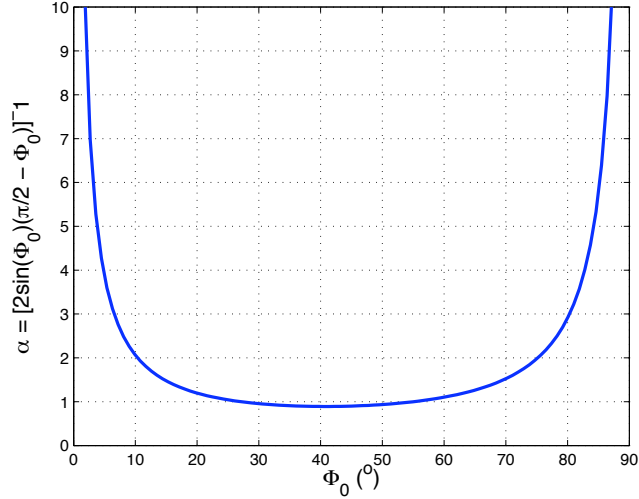


Figure 9: Solution of Eq.8 for $\phi_\infty = \frac{\pi}{2}$.

of gradient in connection with the parameters α and, the emission phase of the reference particle, ϕ_0 . As a conclusion, the values in the $\phi_0 \geq \pi/4$ region can be considered as the preferable solutions.

$$\gamma = \pi n \alpha \sin(\phi_0) + 1 \quad (10)$$

The Eq. (11) summarises the above discussion. In fact, one can deduce from these limits that $\alpha \sin(\phi_0) \geq 0.64$. Substitution of this value in the formula results a relativistic Lorentz factor of $\beta \approx 0.9$ for $n = 0.5$. The physical meaning of the result is the acceleration of the electrons up to the relativistic energies until the middle of the first cavity.

$$\alpha \geq 0.9, \quad \phi_0 \geq \pi/4 \quad (11)$$

Furthermore, the energy spread of the beam can be expressed in terms of the model parameters as in Eq (12) and Eq. (13). These equations result with the values at the exit of the gun for the short bunches with Gaussian distribution in both transverse and longitudinal planes. The given parameters are the *rms* energy spread $\sigma_{\Delta\gamma}$, the *rms* relative energy spread $\Delta U/U$,

$$\sigma_{\Delta\gamma} = 2\pi\alpha f \sigma_b \quad (12)$$

$$\frac{\Delta U}{U} = \frac{\sigma_{\Delta\gamma}}{\gamma - 1} = \frac{2f\sigma_b}{n + 0.5}, \quad (13)$$

where σ_b is the *rms* bunch length in time. The longitudinal beam parameters for PHIN have been calculated according to the model and can be found in Table 4.

Analogously, in PARMELA, the phase of the time-varying elements, such as a cell as in this example, has to be determined with respect to the master clock. The phase of the cell element, that provides the maximum energy gain, is determined after a phase scan in PARMELA. The simulations revealed that the nominal emission phase for the electrons

Table 4: The longitudinal beam parameters of PHIN according to model.

Parameter	Model
The field strength parameter, α	1.32
The particle phase during the photoemission, $\phi_0[^\circ]$	~ 65
The particle phase at the end of the gun, $\phi_\infty[^\circ]$	90
Relativistic Lorentz Factor, γ	11.4
The rms Energy Spread (keV), $\sigma_{\Delta\gamma}$	197
The Relative Energy Spread (%), $\frac{\Delta U}{U}$	0.7

is 35° for a gradient of 85 MV/m at a resonance of 3 GHz .

The ramping of the beam energy throughout the cavity at the optimum emission phase is simulated by using PARMELA. The parameters of the PHIN RF gun has been used for modelling. The acceleration occurs in the RF field that is generated by a $2 + \frac{1}{2}$ cell cavity with the gradient of $E_0 = 85 \text{ MV/m}$ and the frequency of 3 GHz . The example is given in Fig. 10. In the figure, a) presents a phase scan that reveals the nominal phase for the maximum energy gain from the field, and b) shows the ramping of the beam energy at this nominal phase as a function of the distance from the cathode. The particles gain 5.5 MeV at the exit of the RF gun with the length of 17.5 cm , at the emission phase of 35° . This phase introduces a phase difference between the particles and the RF field in order to compensate the phase slippage of the electrons that are at unrelativistic velocities during the photoemission.

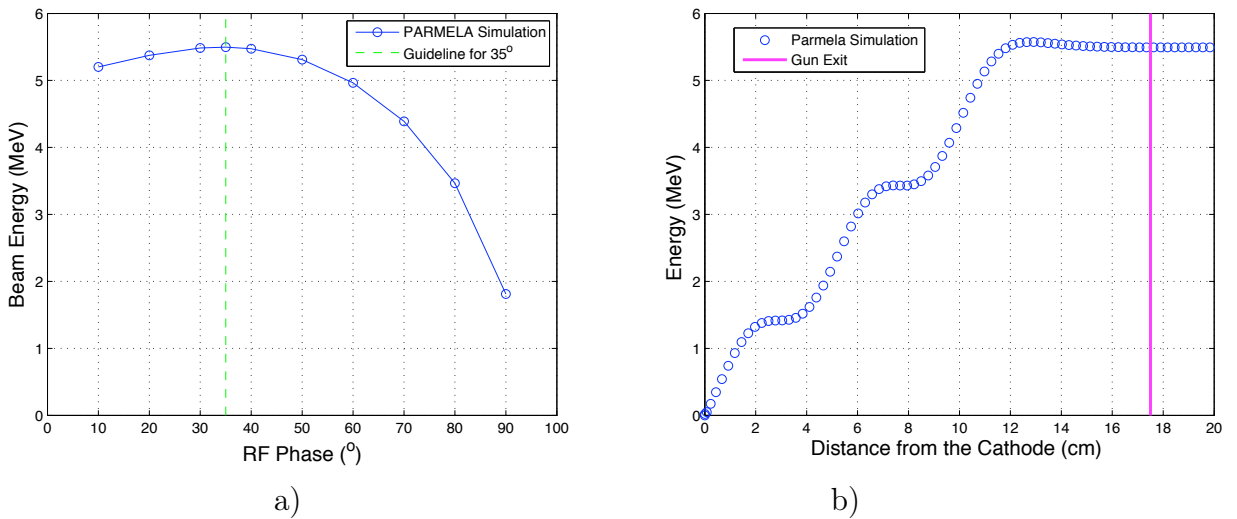


Figure 10: PARMELA simulation result shows a) the energy gain in the RF field as a function of the relative phase of the cell with respect to the master clock, b) the ramping of the beam energy in the cavity at the nominal phase of 35° .

2.2 Emittance Growth Mechanisms

The total emittance of the electron beam in an RF gun arises from the combination of several effects. In this section, the time dependence of the RF focusing in the gun, space charge forces in the vicinity of the cathode and thermal effects will be described as the typical sources of emittance growth in photoinjectors. The dominant source of emittance will be investigated among those effects under consideration.

2.2.1 RF Field Dependence

During the acceleration in the RF cavity, the electrons at different longitudinal positions experience different focusing of the RF field due to its time dependence. This time dependence of the RF field gives rise to a radial force and an increase in the total emittance. According to the Maxwell's equations, radial electric field component can be written as Eq. (14) due to a longitudinal electric field E_z which is a function of longitudinal position, z and time, t , in addition it is independent of radial coordinates θ and r .

$$E_r = -\frac{r}{2} \frac{\partial}{\partial z} E_z \quad (14)$$

The radial force, F_r , acting on an electron is given as,

$$F_r = e(E_r - \beta c B_\theta), \quad (15)$$

where e is the charge of the electron, B_θ is the magnetic field and β is the velocity of the particle.

In the photoinjector models, the variation of RF field during the acceleration and over the electron pulse duration is taken into account. The emittance contribution of RF field, ϵ_{rf} , is given as Eq. (16) in practical units [28],

$$\epsilon_{rf} [\text{mm mrad}] = 2.73 \times 10^{-11} E_0 [\text{MV/m}] f^2 [\text{MHz}] \sigma_x^2 [\text{mm}] \sigma_b^2 [\text{ps}] \quad (16)$$

where E_0 is the peak gradient, f is the resonance frequency of the RF cavity, σ_x is the *rms* beam size and σ_b is the *rms* bunch length. Under these considerations, the RF contribution to the emittance has been calculated for the PHIN photoinjector. As the result, the emittance has been found to increase as 1.33 mm mrad due to the RF field. A beam with the bunch length of 8 ps and a typical beam size of 1 mm which is accelerated by a gradient of 85 MV/m at the frequency of 3 GHz has been used for the calculations.

2.2.2 The Space Charge Effect

The space charge has significant degrading effects on the emittance of a high brightness beam. The Coulomb force between the particles causes the emittance growth.

As the electrons are extracted from the cathode they experience the electric field produced by the surface charge distribution, ρ . When this space charge induced electric field is high due to the high charge density, it can balance the accelerating field and limits the amount of charge production. This decelerating field, E_{dec} , is given in Eq. (17) according to the Gauss' law,

$$E_{dec} = \frac{\rho}{\epsilon_0} \quad (17)$$

where ϵ_0 is the permittivity of the vacuum. The decelerating field can be expressed in terms of the peak charge density of a Gaussian distribution given in Eq. (18) and becomes as in Eq. (19). In the equations, Q is the extracted charge and σ_x is the size of the spot that is illuminated on the cathode. The balance between the space charge field and the accelerating field has been experimentally studied in several references [29, 30, 31, 32]. It has been shown that the extracted charge yield linearly increases with the increasing accelerating field. Nevertheless, the charge yield has a limitation due to the maximum achievable gradient as indicated in the Killpatrick criterion, which is mentioned in Section 2.4.

$$\rho = \frac{Q}{2\pi\sigma_x^2} \quad (18)$$

$$E_{dec} = \frac{Q}{2\pi\epsilon_0\sigma_x^2} \quad (19)$$

According to the model, the expression for the space charge contribution to the transverse normalized emittance is given in Eq. (20) in practical units [28].

$$\epsilon_{sc}[mm\ mrad] = 3.76 \times 10^3 \frac{Q[nC]}{E_0[MV/m](2\sigma_x[mm] + \sigma_b[ps])} \quad (20)$$

The agreement between the model and PARMELA simulations has been investigated. This investigation shows that the dynamics under space charge effect gives rise to an space charge induced transverse normalized emittance of $10.3\ mm\ mrad$ for the PHIN specifications, as a model prediction. Similarly the simulations results a value of $10.7\ mm\ mrad$ at the nominal emission phase.

2.2.3 Thermal Effects during the Photoemission Process

In addition to the emittance growth due to the properties of RF field and the space charge effect, thermal emittance of the electrons has to be also considered [33]. The thermal emittance depends on the area of the emission surface, momentum distribution and angular distribution of the emitted electrons. It originates during the photoemission process and it arises from the temperature of the cathode surface. In order to understand the nature of the thermal emittance one should look into the photoemission process. The details of the photoemission are presented in Chapter 4. In this section only the thermal emittance is given as a consequence of this process.

Thermal Emittance

The electrons are emitted isotropically inside a half-sphere in front of the cathode surface. The thermal emittance of those electrons is given by Eq. (21) [33],

$$\epsilon_{th} = \frac{\gamma r_c}{2} \sqrt{\frac{k_b T_e(eV)}{m_0 c^2}} \sqrt{\frac{2 + \cos^3 \phi_{max} - 3\cos \phi_{max}}{2(1 - \cos \phi_{max})}}, \quad (21)$$

where ϕ_{max} is the emission angle of the particles with respect to the cathode surface nor-

mal. The r_c is the laser spot size illuminating the cathode surfaces for the photocathodes. For the thermionic cathodes this variable refers to the cathode radius. For simplicity, the expression in Eq. (21) can be reduced to Eq. (22) when $\phi_{max} = \pi/2$. In Fig. 11, the thermal emittance is estimated as a function of the laser spot size according to this model. The behavior at the typical temperature for the PHIN has been plotted. The temperature for a photocathode is considered as the corresponding laser energy illuminating the cathode surface.

$$\epsilon_{n,th} = \gamma \frac{r_c}{2} \sqrt{\frac{k_b T_e}{m_e c^2}} \quad (22)$$

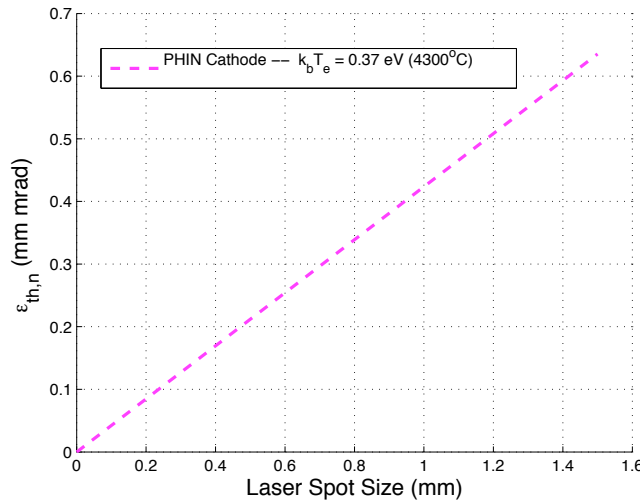


Figure 11: Analytic estimations for the thermal emittance with respect to laser spot size and the cathode temperature.

As a result, it can be concluded that the thermal emittance contribution is in the range of 0.2 - 0.6 mm mrad in the laser spot size range tested for PHIN. The thermal emittance can be measured by using a beam with a very low charge and short pulse duration [34]. This condition ensures to minimize the contribution from the other sources of emittance.

2.2.4 Conclusion

The emittance contributions from different sources have been investigated for PHIN photoinjector. These individual contributions from the above mentioned effects are added to the total beam dynamics emittance quadratically. The general formula can be seen in Eq. (23).

$$\epsilon_{n,x,y,tot} = \sqrt{\epsilon_{rf}^2 + \epsilon_{sc}^2 + \epsilon_{th}^2} \quad (23)$$

The results of the model are given in Table 5. According to the model, the dominant cause of emittance growth is the space charge effect near the cathode for a typical RF gun. The contributions of thermal effects and RF to the total emittance are almost negligible.

Table 5: According to model, the contributions of different sources to the total transverse normalized emittance for beam parameters of PHIN.

Parameter	Model
Space Charge Induced Emittance (mm mrad)	10.3
RF Induced Emittance (mm mrad)	1.33
Thermal Emittance (mm mrad)	0.42
Total Beam Dynamics Emittance (mm mrad)	10.4

As a consequence the emittance growth due to the space charge effect has to be the main item for the emittance compensation. Two of the compensation techniques are given in the next section.

2.3 Emittance Compensation Schemes

There are different compensation techniques for the different sources of beam emittance that are described previously. In PHIN photoinjector, the compensation has been achieved by placing a solenoid magnet after the RF gun. Therefore the scheme by using the constant magnetic field of a focusing magnet will be explained more detailed throughout the section.

2.3.1 Compensation of Space-Charge-Induced Emittance with a Lens

In a high brightness photoinjector, the bunch density varies as a function of the longitudinal position across the bunch. Therefore, analytically it is convenient to consider that the bunch consists of longitudinal slices. In each slice the space charge force can be different due to the longitudinal dependence of the bunch density. In this case, despite the transverse emittance of the individual slices are conserved, the projection of all slices in the phase space results with the emittance growth. A theory for compensation of this emittance growth due to linear space charge effect has been developed by B. E. Carlsten in 1988 [35].

To begin with, a laminar beam of radius r_0 is considered with zero initial beam divergence, that has the beam edge at $z=0$. Additionally, for simplicity, the space charge force is assumed to have no time dependence. This condition is called the weak focusing limit. The unrelativistic transverse motion of the particles within the bunch can be investigated, in this limit. Here the cylindrical coordinates ρ and ξ should be introduced, where $\rho = 1$ is defining the radial edge and $\xi = \pm 1$ is defining the longitudinal ends. The equations governing the motion under space charge force $\lambda(\rho, \xi)$, at the distance z , within the beam at location (ρ, ξ) are,

$$r(\rho, \xi, z) = r_0 + \lambda(\rho, \xi)z^2/2 \quad (24)$$

$$r'(\rho, \xi, z) = \lambda(\rho, \xi)z$$

In this case the ratio of the beam radius and the divergence is a function of ρ and ξ .

The spread in this ratio is the origin of the emittance growth. When a lens with the focal length of $1/\alpha_L$ (ex: a solenoid magnet) is placed at $z = z_l$, the equations have the following form,

$$r(\rho, \xi, z) = r_0 + \lambda(\xi)(z_l + z)^2/2 - \alpha_L[r_0z + \lambda(\xi)z_l^2z/2], \quad (25)$$

$$r'(\rho, \xi, z) = \lambda(z_l + z) - \alpha_L(r_0 + \lambda(\xi)z_l^2/2).$$

If the focal length is chosen as,

$$f = \frac{z^2}{2(z_l + z)} \quad (26)$$

the ratio of the beam divergence and beam radius at a downstream position of z_d from the lens reads,

$$\frac{r'(\rho, \xi, z)}{r(\rho, \xi, z)} = \frac{2(z_l + z_d)}{z_d(z_d + 2z_l)}. \quad (27)$$

Eq. (27) is independent of λ and ξ , namely, position of the particle within the bunch. The linear focusing force of the lens causes a rotation of the slices in the phase space so that they all lie in the same line. Therefore at a position z the emittance is zero since all the points have the same orientation in phase space.

In this model, transverse normalized emittance has the following form, as a function of the longitudinal position and the focal length of the lens.

$$\epsilon_{x,n} = \frac{1}{2}\beta\gamma\sqrt{\langle\Lambda^2\rangle\langle\rho^2\rangle - \langle\Lambda\rho\rangle^2}(2r_0(z_l + z_d) - \frac{z_d^2r_0}{f}) \quad (28)$$

According to Eq. (28), the transverse emittance growth due to space charge can be minimized by choosing an appropriate focal length for the lens. The theory and implementation of the emittance compensation has been discussed in several publications [36, 37].

Fig. 12 illustrates the phase space evolution during the emittance growth and compensation. In the figure, the phase space has been shown after the $2 + \frac{1}{2}$ cell cavity (a), and at a downstream point where the compensation occurs (b). The data has been retrieved from the PARMELA simulation by using the PHIN photoinjector design specifications.

2.3.2 Compensation of Space-Charge-Induced Emittance with Focusing RF Force

After the compensation by using a constant magnetic focusing field, a residual emittance of the beam might still exist. According to the theory, the line up of the slices in the beam can be improved with an additional RF focusing which leads to a decrease in the emittance. As a matter of fact, at the low gradients the emittance compensation can be accomplished by the constant magnetic field of a focusing solenoid. However, as the gradient increases the compensation starts degrading, and gives rise to a need for additional focusing. In this case, further compensation is possible by using a radial RF focusing force.[38]

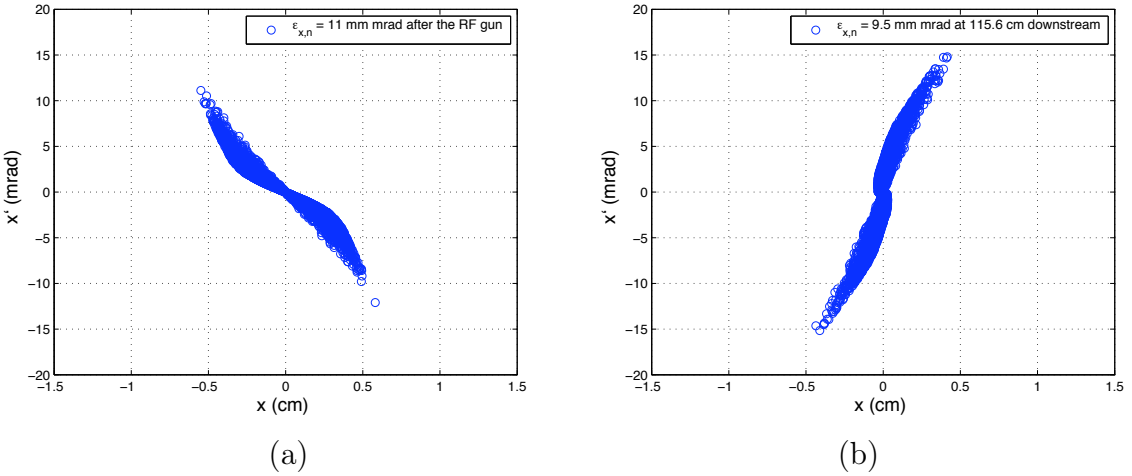


Figure 12: Transverse phase space (a) after the gun and (b) at a downstream position of 115.6 cm where the emittance compensation occurs.

The recent projects such as SwissFEL [39], LCLS [40], SCSS [41] and PITZ [42] focused their research on the low emittance injector studies. Concerning these recent facilities, one of the conclusions of ICFA Future Light Sources (FLS 2010) Conference [43] was the validity of relation in Eq. (29) for a well optimized injector, regardless of its type, when the compensation schemes are applied and the proper laser pulse shaping is provided.

$$\epsilon_{x,y,n} [\text{mm mrad}] \approx 1 \mu\text{m} \sqrt{Q [\text{nC}]} \quad (29)$$

For PHIN photoinjector, the transverse normalized emittance specified as $< 25 \text{ mm mrad}$. It is a relatively larger emittance budget compared to the needs of X-FEL facilities. Nevertheless, the above condition indicates that an emittance of 1.5 mm mrad would be possible to obtain for PHIN with a charge per bunch of 2.33 nC. In order to achieve this emittance, it would be interesting to study the transverse and longitudinal laser profile shaping. And therefore, a systematic measurements could be conducted on the effects of the laser properties to the transverse phase space.

2.4 A Model for Optimization of the Parameters

The different design and optimization criteria can be specified for the RF photoinjectors. These different approaches originate from the trade offs between several parameters according to the implementation purposes of the photoinjector. Furthermore, possible technological challenges have to be taken into account for the realization of any design. In this section those aspects of designing an RF photoinjector will be summarized according to the Travier's model and the design parameters for the PHIN photoinjector will be examined.

RF Frequency

As a first parameter of the photoinjector, one could determine the frequency of the RF gun. The frequency of the RF gun plays a key role for many of the other properties of the injector such as the charge production, size of the cavity therefore the vacuum needs.

The maximum achievable gradient is a function of the frequency. Consequently, frequency choice has an impact on the charge production which is related to the gradient. The volume of the cavity is inversely proportional to the cube of the resonance frequency of the cavity ($V \sim 1/f^3$). At the higher frequencies, the volume of the cavity is relatively small than a lower frequency cavity. In small cavities, it is easier to achieve the good vacuum conditions. For the charge production of a photocathode, the high vacuum conditions are necessary. Therefore a lower limitation to the design frequency can be defined as 144 MHz regarding the existing CEA facility. On the contrary, shorter RF wave lengths will require short laser pulses hence bringing another limitation for the charge production. Under these circumstances, the frequency range has been considered as $144 \text{ MHz} \leq f \leq 17 \text{ GHz}$ in Travier's studies.

Maximum Gradient

In the high brightness sources such as RF guns the dynamics is space charge dominated. In order to obtain a low emittance, the space charge induced emittance growth has to be suppressed as much as possible. As shown in Eq. (20), this can be achieved provided that the accelerating gradient is as high as possible. The normal conducting accelerating cavities are capable of producing such high gradients. The Killpatrick criterion can be used as an indication for the highest achievable gradient as described in Chapter 1. Travier introduced a practical formula for the gradient as given in Eq. (30). The more information can be found in reference [44].

$$E_{0,max}[\text{MV}/\text{m}] = 8.47 + 1.57\sqrt{f[\text{MHz}]} \quad (30)$$

The achievable gradient has been calculated as a function of the resonance frequency, according to the above formula. The resulting curve can be seen in the Fig. 13 as a Killpatrick-like criteria. The achievable gradient values of several photoinjector studies have been presented in the figure. The PHIN RF gun has been designed and commissioned with the achievable gradient value of 85 MV/m at 3 GHz. Furthermore, a successive design study for CLIC DB injector uses an RF gun with the gradient of 40 MV/m at 1 GHz. These two values indicate agreement with the Killpatrick criteria therefore confirm the consistency of design choices. In addition, the figure indicates the design gradient values of other recent photoinjector studies. These studies have been summarized in Section (2.2).

Maximum Beam Size

In an RF gun, the field is strongly non-linear near the cavity walls. This non-linear effect cause emittance growth at the large beam spot sizes. Travier suggests to have a beam spot size smaller than the one-third of the cavity aperture in order to avoid this effect.

Maximum Bunch Length

A maximum bunch length can be defined in connection with a reasonable energy spread. The relation in Eq. (31) gives a practical limitation on the bunch length, σ_b . Together with the condition in Eq. (31), the relative energy spread given in Eq. (13) can be limited to $< 1\%$ with a $2 + \frac{1}{2}$ cell cavity. According to this formula, for a 3 GHz RF cavity with $2 + \frac{1}{2}$ cell, as in PHIN, a maximum bunch length up to 16 ps is allowed in order to limit energy spread to 4%. Regarding the PHIN specifications and this model, a bunch length of 8 ps results with the 2% relative energy spread which is also consistent with the measurements.

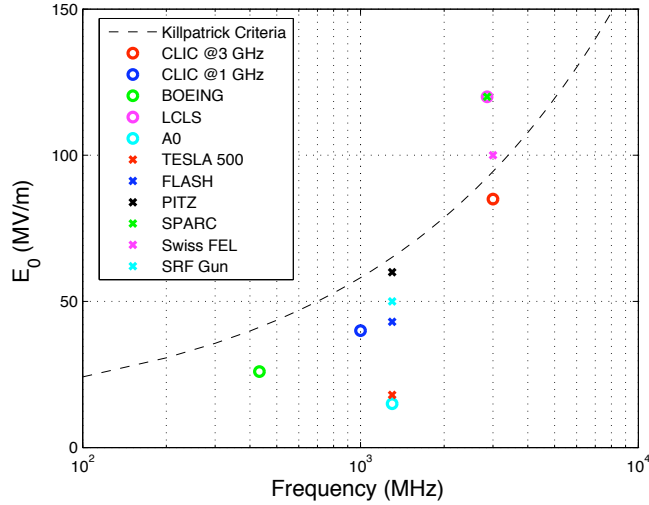


Figure 13: Maximum achievable accelerating gradient values for different RF guns including the CLIC designs in comparison with the Killpatrick criteria.

$$\sigma_b[ps] \leq \frac{5 \times 10^4}{f[MHz]} \quad (31)$$

Achievable Charge

The maximum charge is given in Eq. (33) provided that the electrons are extracted when the accelerating field, E_{acc} , is equal to the decelerating space charge field that is given in Eq. (19),

$$E_{dec}[MV/m] = 18 \frac{Q[nC]}{\sigma_x^2[mm^2]}, \quad (32)$$

$$Q_{max}[nC] = \frac{E_{acc}[MV/m]\sigma_x^2[mm^2]}{18}. \quad (33)$$

According to this model, with a typical laser spot size of 1 mm (sigma) and an accelerating gradient of 85MV/m, as in the PHIN specifications, would yield a maximum charge of 4.7 nC. This result has been confirmed by recording the maximum charge of 4.5 nC during the commissioning of PHIN photoinjector that will be presented in detail later in the Chapter 5. The charge measurements have been done under the optimized emission phase of the electrons with respect to the RF field which results the maximum transmission of the emitted electrons through the RF gun.

Vacuum

High vacuum conditions should be maintained in order to improve the cathode lifetime. The vacuum pressure has been observed to increase as a function of the total extracted charge in the past studies for CTF2. Referring to these studies, the simulations showed that the vacuum condition should be lower than $2 \times 10^{-10} mbar$ inside the first half-cell where the Cs_2Te cathode is placed.

2.5 Applications of RF Photoinjectors

Photoinjectors have been used for several applications such as Free Electron Lasers (FELs), colliders and Energy Recovery Linacs (ERLs). The beam dynamics in a photoinjector has been well understood with an exception of some details in photoemission process. The sources for different applications can be designed by using photoinjector principle within the frame of various design and optimization strategies as described above. The emittance tolerances, charge per bunch, beam current, time structure of the beam, stability requirements are some of the application specific parameters.

Photoinjector development is a dynamic field with lots of innovations as of it has first proposed. Several review studies of photoinjectors in terms of their technology and application areas have been done in the past years. The advanced photoinjector laboratories and pioneering design studies have been reviewed by C. Travier in 1994 [45]. The publications on recent photoinjectors have been updated and the status of the advanced facilities have been given in Table 6. The highlights in photoinjector development has been given by S. J. Russell until 2002, as shown in Table 7. This table has been updated in this section in order to cover the highlights since 2002.

In general, the properties of the outcome are attained from the initial conditions of the electron beam that is produced by the photoinjector. For example, the properties of the light that is produced by an FEL are based on the quality of the electron beam. Therefore a short wavelength, high brightness laser pulse can be obtained by means of an electron beam with a high transverse brightness and low energy spread. The transverse brightness refers to the transverse emittances in both directions as shown in Eq. (34),

$$B_{\perp} = \frac{2I}{\epsilon_{n,x}\epsilon_{n,y}} \quad (34)$$

where, I is the peak current, $\epsilon_{n,x}$ and $\epsilon_{n,y}$ are the transverse normalized beam emittances. High optical gain of an FEL, therefore an efficient amplification can be achieved with a high brightness electron beam. The typical values for a high brightness beam are, the peak current of several kA and the normalized transverse emittance of $\sim 1\mu m$. A detailed overview of FEL injectors has been prepared by S. J. Russell in 2003 [64] and later by M. Ferrario in 2006 [65]. The modern examples of photoinjectors that are used to drive X-FELs are LCLS (SLAC), PITZ (DESY), FLASH (DESY), SPARC (INFN) and SwissFEL (PSI).

Despite the fact that the ultra-low emittance is essential for the colliders, it is achieved by several damping rings after the injector. Therefore, for the collider beams, the emittance requirement is more relaxed compared to the FELs in the early stages of the particle production. A photoinjector design effort for e^-e^+ linear colliders, that is based on the **T**eV **E**nergy **S**uperconducting **L**inear **A**ccelerator (TESLA) technology, has been initiated at FNAL with the collaboration of Univ. of Rochester, UCLA, INFN-Milano and DESY. A0 photoinjector test-stand at FNAL, has aimed to prototype a source for TESLA of DESY and to investigate the possible issues for the designers. The injector study for TESLA 500 (TESLA at 0.5 TeV) took place at DESY in parallel with A0. The parameters for both designs can be found in Table 6. The high intensity bunches with the charge of $\sim 8nC$ and the relaxed emittance requirements of $\sim 11\text{ mm mrad}$ for the post-injector stage are the common specifications for the collider sources as in the examples of A0, TESLA500. This also strengthens the proposal of using a photoinjector for the CLIC

Table 6: The design specification for recent photoinjectors.

Parameter	BNL (BOE- ING)	SLAC (LCLS)	FNAL (A0)	DESY (TESLA 500)	DESY (PITZ)	DESY (FLASH)	INFN (SPARC)	PSI (Swiss FEL)	ELBE (SRF Gun)	CERN (PHIN)
Purpose	ERL	FEL	Linear Collider	Linear Collider	X-FEL	X-FEL	X-FEL	X-FEL	FEL	DB*
First Operation	1992	-	1999	-	2002	2004	2006	2010	2009	2008
Number of Cells	4	1.5	1.5	1.5	1.5	1.5	1.6	2.5	3.5	2.5
Frequency (MHz)	433	2856	1300	1300	1300	1300	2856	2997.9	1300	2998.55
Macropulse (μs)	10000	-	-	800	800	800	-	1.2	CW	1.27
Repetition Rate (Hz)	30	120	-	10	10	5	1-10	10	1000	5-50
RF Gradient (MV/m)	26	120	35	35	60	43	120	25	50	85
Cathode Type	K_2CsSb	Cu/Mg	Cs_2Te	Cs_2Te	Cs_2Te	Cs_2Te	Cu/Mg	Cu	Cs_2Te	Cs_2Te
Quantum Efficiency (%)	5-12	$\sim 10^{-5}$	1	1	2-10	2-10	10^{-4}	10^{-5}	1	3
Laser	-	$Nd : YLF$	$Nd : YLF$	$Ce : YAG$	$Nd : YLF$	$Ti : Sa$	$Ti : Sa$	$Nd : YLF$	$Nd : YLF$	$Nd : YLF$
Wavelength (nm)	527	255	263	262	257	262	266	250-300	262	266
Laser Energy / Pulse (μJ)	0.47	200	30	5	1	1	500	200	-	0.37
Laser Spot Size FWHM (mm)	3.5	2.5	-	6.3	0.2-3	3.5	-	0.1-0.27	2.7	2.4
Pulse Length FWHM (ps)	53	10-20	10	7.4	20	20	10	3-10	20	8
Beam Energy (MeV)	5	5	3.8	3.8	6.6	5	5.6	6.6	9.5	5.5
Charge/Bunch (nC)	1-7	1	8	8	1	1	1.1	0.2	1	2.33
Energy Spread (%)	2-3	0.1	1.15	1.15	1-2	0.2	-	-	1	1
Norm. Trans.	20-40	1	19.3	20	0.9	1.5	2	<0.4	2.5	14
Emitance (mm mrad)										

* Drive Beam

Table 7: Highlights in photoinjector development*. (Modified from S. J. Russell)

Year	Highlight	Ref.
1985	First photoinjector experiment at LANL.	[25]
1988	Stanford FEL has been driven by a photoinjector.	[46]
	Theory of emittance compensation has been proposed.	[36]
1989	First high gradient S-band photoinjector at BNL.	[47]
1991	First RF integrated photoinjector with emittance compensation at LANL.	[48]
1992	High duty factor, RF photoinjector experiment at Boeing.	[49]
	First photocathode in a superconducting cavity.	[50]
1993	LANL photoinjector driven FEL lasers in the UV.	[51]
1995	Experimental demonstration of the emittance compensation.	[52]
1996	First operation of DC photoinjector at TJNAF.	[53]
	Experimental demonstration of microbunching in a photoinjector.	[54]
1997	Envelope analysis of emittance compensation.	[55]
1999	TJNAF FEL demonstrates 1.72 kW average power.	[56]
2000	First systematic measurement of multipacting in a photocathode RF gun.	[57]
2001	First operation of an X-band (8.547 GHz) photoinjector.	[58]
2002	First operation of a superconducting RF photoinjector.	[59]
2003	The initial studies on the use of needle cathodes in photoinjectors to enhance the beam brightness.	[60]
2007	SPARC has done the first direct observation of the double emittance minimum.	[61]
2008	First Operation of PHIN photoinjector.	[62]
2009	The first simultaneous demonstration of emittance compensation and velocity bunching.	[63]

*The modifications to the original table have been denoted with bold blue fonts.

DB production. A future CLIC DB photoinjector is required to produce an electron beam with the charge per bunch of 8.4 nC and with a normalized transverse emittance of $\leq 100\text{ mm mrad}$.

The photoinjectors can also provide beams for ERLs. An example of operating facility is BOEING high duty cycle photoinjector installed at Photoinjected Energy Recovery Linac (PERL) at Brookhaven National Laboratory (BNL). The injector has provided a

high duty cycle by delivering a macropulse repetition rate of 30 Hz with the micropulses of 8.3 ms. The remarks from the first operation of PERL's BOEING injector can be found in [66].

PHIN (CERN) and SRF Gun (ELBE/FZR) injectors were among the tasks of the CARE project. SRFgun is an example of the superconducting RF gun to maintain the electron beam for an IR-FEL facility [67]. PHIN photoinjector is a research program in order to investigate the feasibility of using a photoinjector as the source of the CLIC DB. It is designed to provide long electron pulse trains with high charge density. The stability of the long pulse trains have a paramount importance for the power production from the drive beam. The demonstration of this stability is another aspect of this research program.

2.6 PHIN Photoinjector Test Facility at CERN

The PHIN photoinjector has been designed and installed on a dedicated test-stand at CERN in 2008, by a collaboration between LAL, RAL and CERN. Within this collaboration, LAL and RAL have committed to the design and the construction of the RF gun and laser, respectively. The photocathode production as well as the overall coordination and commissioning were under the responsibility of CERN. The project is in the framework of the second Joint Research Activity PHIN of the European CARE program. The purpose of PHIN photoinjector is, to investigate the feasibility as a possible source for the CLIC DB [68, 69, 70]. An illustration of the PHIN RF gun can be found in Fig. 14.

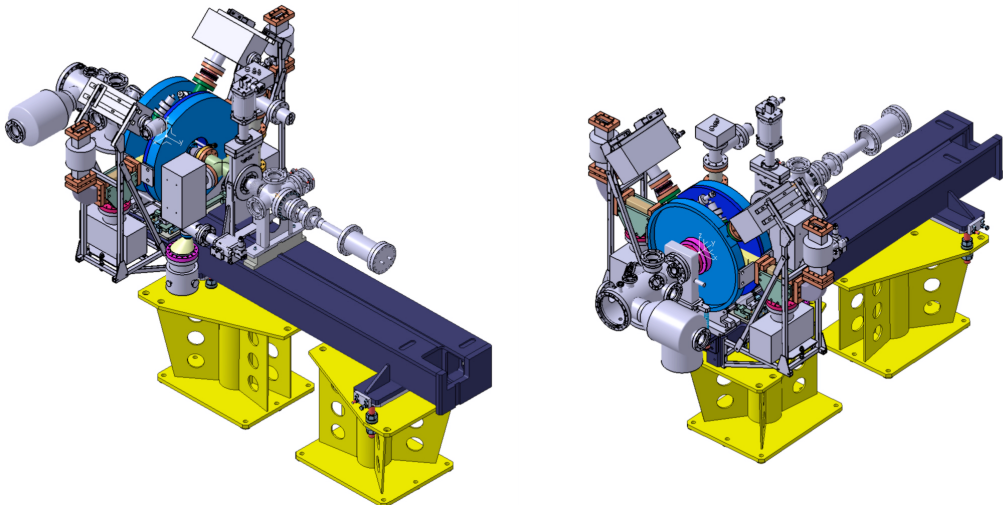


Figure 14: The illustration of the PHIN RF gun from different view angles.

The PHIN photoinjector is capable of delivering a $1.3 \mu s$ long train containing 1908 bunches with 2.33 nC charge per bunch with stability of 1-2%. It is equipped with a $2 + \frac{1}{2}$ cell RF gun that supplies 85 MV/m gradient at 3 GHz . The production of this very long bunch train with a high charge per bunch is the prominent characteristic of the PHIN photoinjector among the other photoinjector implementations. In addition to the RF gun, a beam diagnostics section has been installed on the beamline. This section is equipped with the beam position and current monitors, OTR screens and CCD cameras

for beam profiling, multi-slit mask for emittance measurements and a spectrometer with an additional segmented-dump. A phase-coding scheme is under development for the PHIN laser system which will provide the required beam temporal structure without generating satellite bunches as in the case of the current thermionic CTF3 gun. More details on the instrumentation of the PHIN photoinjector will be given in Chapter 4.

The main challenges for PHIN commissioning are the demonstration of the high charge production and the stability of the beam parameters along the pulse train. Because these are also main feasibility items for the CLIC DB. All the beam measurements have been simulated with the measured parameters of both the e^- and the laser beam in order to ensure the reliability of the results. The beam dynamics of PHIN photoinjector has been modelled with the PARMELA simulation code [71]. Additionally, RF field calculations within the study has been done with SUPERFISH simulation code [72]. The rigorous numerical studies have been done over a wide range of parameters in order to optimize the system and investigate the beam dynamics.

The PHIN layout with the instrumentation on the beamline and the commissioning results obtained between the years 2008-2010 will be given in the following chapters. In this thesis, the studies have been extended towards the optimization of a generic photoinjector for the CLIC DB. This optimization has been based on the learned lessons from the commissioning of the PHIN photoinjector. The details of this conceptual study of a photoinjector for CLIC DB is also presented in Chapter 6.

3 Beam Dynamics Simulations for the PHIN Photoinjector

Contents

3.1 PARMELA, A Particle Tracking Code	34
3.1.1 Highlights from the PARMELA Program	34
3.1.2 Representation of PHIN in PARMELA Input	35
3.2 Model for the PHIN Photoinjector	39
3.2.1 RF Phase Dependence	40
3.2.2 Laser Spot Size Dependence	41
3.2.3 Gradient Dependence	43
3.2.4 Charge per Bunch Dependence	44
3.2.5 Summary for the PHIN Baseline Configuration	47
3.3 Stability Aspects of PHIN: e- Beam Sensitivity to the Jitter on the Parameters	53
3.3.1 Phase Jitter	53
3.3.2 Gradient Jitter	55
3.3.3 Charge Jitter	56
3.3.4 Laser Spot Size Jitter	57
3.3.5 Laser Pulse Length Jitter	58

The simulation studies for the beam dynamics of the PHIN photoinjector have been done with the PARMELA simulation program. The main features of PARMELA are described by focusing on the photoinjector example in the beginning of this chapter. Some descriptions of the laser and electron beam parameters of PHIN as well as the beamline elements will be given as they are used in PARMELA.

The modeling of a photoinjector was one of the main intentions for the development of this program. Therefore, it provides the flexibility to investigate the operational dynamics within the large number of parameters.

PHIN has been developed and studied in order to prototype a photoinjector to replace the existing CLIC Test Facility 3 (CTF3) injector and later to constitute the base for the future CLIC Drive Beam (DB) injector. The design of the RF gun and the initial simulation studies can be found in reference [73].

The DB has been designed to provide RF power to accelerate the main beams of CLIC by means of the Power Extraction and Transfer Structures (PETS), as described in Chapter 1. Therefore the quality of the power production in terms of the stability and the power uniformity depends on the DB injector, significantly. The small variations in the beam properties are called “the jitter”. In this context, the jitter on the key parameters has been simulated for the PHIN photoinjector. A comparison of these results with the DB stability tolerances is another aspect of the feasibility for a photoinjector as the source of the DB. The stability of the PHIN photoinjector is discussed in this chapter.

3.1 PARMELA, A Particle Tracking Code

PARMELA is a particle beam dynamics simulation program particularly for the electron linacs. The name, PARMELA, stands for the “Phase and Radial Motion in Electron Linear Accelerators”. It is written in FORTRAN 95 for the Windows operating system. The version under consideration for PHIN has been developed by Lloyd Young and distributed by the Los Alamos Accelerator Code Group. James H. Billen has prepared a detailed documentation of the code [71].

The program can be used for the design and simulation studies of the linear accelerators for medical, sterilization and ion implanter applications as well as the photoinjectors, transport systems, high intensity electron and ion linacs.

3.1.1 Highlights from the PARMELA Program

PARMELA simulates the beam dynamics by integrating the particle trajectories in the presence of the user-defined fields. The independent variable is the phase (time) for the integration. Additionally, the program can import RF fields or static magnetic fields generated by the other simulation programs.

PARMELA provides many input cards that enable the user to define the elements of the beamline under study. It includes accelerating and focusing elements. It is possible to run PARMELA in real-time or in batch mode. The output options and the flow logic also can be specified in the input file. The cards can be considered as the commands with particular attributes. These attributes give the parameters for each element that is represented in the input card. Some of the key input cards and their attributes that concern PHIN are mentioned later in the text.

The space charge effect can be included in the simulations. The 2D or 3D space charge effects can be activated for the beam dynamics. The 2-D space charge calculations included for the PHIN simulations. PARMELA calculates the space charge effect by using a particle in cell (PIC) method. According to the 2-D case of the method, the program transforms the beam to the rest frame. The beam volume is divided into a grid of discrete rings with the radial and longitudinal coordinates of (r_i, z_j) , respectively. The PIC method uses the “Green’s function” method to approximately calculate the radial and longitudinal components of the electric fields for each ring by taking into account the effects of every other ring. For the numerical calculation, the integration step and the number of steps are specified in PARMELA by the user. The space charge impulse is calculated for each space charge step. Each particle receives a space charge impulse according to this computation. In general, at each integration step, the program examines the necessary

impulses to be applied to the particles and applies them in the beginning of each step. These impulses can come either from the space charge or from a defined background field.

It is useful to denote the PARMELA conventions on the charge, coordinates and phase of the particles. Since PARMELA has been originally written for the electron linacs, the charge of the electron is given as the default value. The conventional charge is -1 for the positively charged particles.

The particles are tracked in six coordinates. The three of them are the horizontal, vertical and longitudinal position coordinates of (x, y, z) , respectively. The rest is the dimensionless momentum coordinates of $(\beta\gamma)_x$, $(\beta\gamma)_y$ and $(\beta\gamma)_z$. A reference particle is defined in the program. The initial values of the z coordinate and the kinetic energy of the reference particle is given by the user. Initially the particles are generated with the total number of N_T . This number is only limited by the availability of the computer memory. The particles can be lost during the calculations for different reasons. For the case of the PHIN beamline, particles can be lost if they exceed the radial aperture of 20 mm in any of the elements or if they are behind the reference particle by a given z_{limit} value. The surviving particles are called “the good particles”. The number of good particles is tracked by a variable N_G .

In general, there are two common conventions for the definition of the time variation of the RF field. The *cosine* convention is common between the designers and the textbooks. According to the *cosine* convention the energy gained from the axial electric field, E_z , in an standing wave cavity by the particle with charge q , is given by,

$$\Delta W = q \int_{+\frac{L}{2}}^{-\frac{L}{2}} E_z(z) \cos(\omega t + \phi), \quad (35)$$

where, L is the length of the cavity, ω is the resonance frequency and ϕ is the phase at $t = 0$. In the case of the *cosine* convention, $\phi = 0$ represents the crest of the RF wave where the maximum energy gain occurs.

On the other hand, PARMELA follows the *sine* convention where the time variation of the axial electric field is given by,

$$\Delta W = q \int_{+\frac{L}{2}}^{-\frac{L}{2}} E_z(z) \sin(\omega t + \phi). \quad (36)$$

Therefore, in PARMELA calculations, at $\phi = 0$ the rising field crosses zero. The wave crest is at $\phi = 90^\circ$.

Additionally, there is an independent variable called the master clock, Φ , in the program. The master clock is a reference for the possible elements in the beamline using the time-varying fields. Therefore all “the inner clock’s” of these elements are set with respect to the master clock that can be set in the PARMELA input.

PARMELA creates output files with the various content that are defined by the user.

3.1.2 Representation of PHIN in PARMELA Input

A PARMELA input file has been prepared in order to simulate the beam dynamics of the PHIN beamline. Fig. 15 illustrates the beamline elements that are included in the PARMELA input. The positions of these elements are given in cm with respect to the

cathode which is located at “0” position.

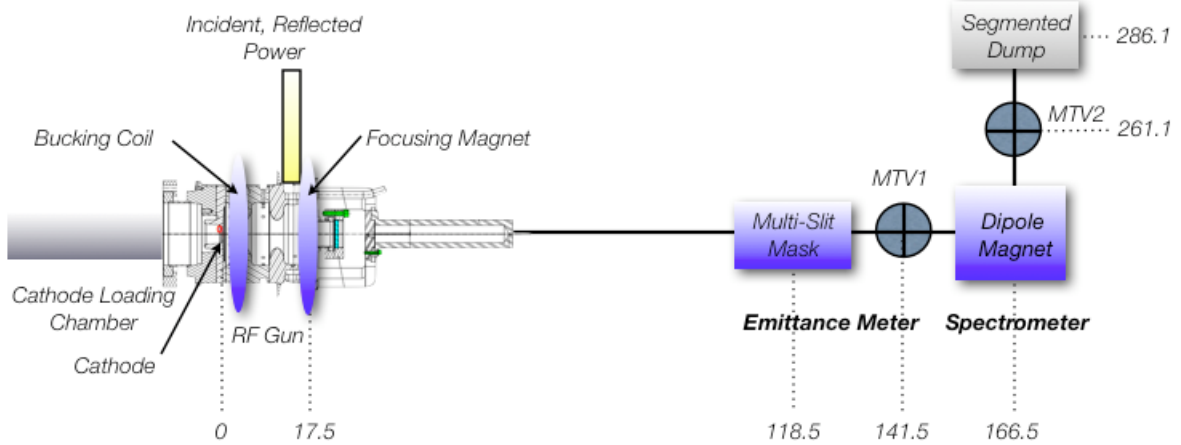


Figure 15: PHIN Layout.

The various cards which are relevant to this study are described and summarized in Table 8 and the corresponding attributes are described in Table 9. The program manual is referred [71] for more details.

Table 8: The cards that are used in the PARMELA input file for PHIN.

Card	Attributes
<i>RUN</i>	<i>RunNumber, PrintFlag, f₀, Z₀, W₀, LinacType</i>
<i>INPUT</i>	<i>Type, N_A, σ_r, r_{max}, σ_ϕ, ϕ_{max}</i>
<i>CELL</i>	<i>L, R_a, OutputFlag, ϕ₀, E₀, CellType, ΔΦ_{max}, Config</i>
<i>COIL</i>	<i>Z, R_C, I_C, Z_{min}, Z_{max}</i>
<i>SCHEFF</i>	<i>I_T, ΔR_{SC}, ΔZ_{SC}, N_R, N_Z, N_{Bunch}, L_{Bunch}</i>

An example input file for the PHIN beamline is given Fig. 16. The line numbers are introduced in order to help the explanations. Normally they are not included in the input file.

In the third line of the example input file, the *RUN* card introduces some global parameters. The RF frequency, f_0 , is given in this card. The initial beam parameters are assigned also in this stage. The reference particle is placed in the middle of the phase spread of the beam. Z_0 denotes a negative longitudinal position of the reference particle behind the cathode large enough for the entire beam. Therefore, the beam is created behind the cathode. Z_0 is calculated as the distance travelled by the reference particle with its given initial energy, W_0 , during the time corresponding to the half of the phase spread. The initial energy is equal to the kinetic energy of the particles during the photoemission from the cathode surface as explained in Chapter 2.

Table 9: Some of the attributes used in the PARMELA cards.

Attribute	Description
f_0 (MHz)	Resonance frequency of the RF gun.
Z_0 (cm)	Negative distance where the particles created behind the cathode.
W_0 (MeV)	Initial kinetic energy of the particles as they are emitted from the cathode surface.
N_A	Number of macroparticles in the calculation.
σ_r (cm)	1 <i>sigma</i> radius of the laser spot on the cathode in units of cm.
r_{max} (cm)	Maximum value for the radius of the laser spot on the cathode.
σ_ϕ (ps)	1 <i>sigma</i> length of the laser pulse.
ϕ_m (ps)	Maximum value for the length of the laser pulse.
ϕ_0 ($^\circ$)	The phase difference between the cell and the master clock.
E_0 (MV/m)	The axial electric field strength.
I_T (A)	The total current on the solenoid magnet.
$\Delta R_{SC}, \Delta Z_{SC}, N_R, N_Z$	The intervals and number of steps for the radial and longitudinal meshes.
N_{Bunch}, L_{Bunch}	Number of the bunches and the bunch length.

The initial distribution of the laser beam is specified in the *INPUT* card that is shown in line 5 of Fig. 16. Among many different input types, the *INPUT* 9 is used for the photocathodes. This defines an initial beam with the Gaussian and uniform radial and longitudinal distribution with zero initial energy spread. The initial distribution of the beam is defined according to the laser transverse and the temporal properties. The attributes, σ_r and r_{max} represent the transverse size of the laser spot on the cathode and its maximum value, respectively. These are given in the units of *cm*. Naturally, the maximum size of the laser spot is limited by the cathode size. The longitudinal properties of the laser pulse are introduced to the program via the attributes, σ_ϕ and ϕ_{max} in units of *ps*.

The RF cavity of PHIN has been represented by the *CELL* card as in the line 7. The attribute ϕ_0 is the phase of the RF field in degrees with respect to the master clock. The axial electric field strength is given as E_0 in the units of *MV/m*.

The RF field data is imported from the output of another program, SUPERFISH, for the PARMELA simulations of PHIN. SUPERFISH is a program consisting of various subroutines to calculate the static magnetic and electric fields or RF fields in the 2D Cartesian coordinates or axially symmetric cylindrical coordinates [72]. The geometry of PHIN's $2 + \frac{1}{2}$ cell cavity has been provided for SUPERFISH and the RF field has been retrieved in a text file with the extension of "T7". The *CField* card, in line 8, is used in order to inform PARMELA that the RF field will be provided externally, for the cell line

```

1 TITLE
2 PHIN RFGUN
3 RUN /n0=1 /ip=999 /freq=2998.55 /z0=-0.001 /W0=1.0e-6
/itype=1
4 OUTPUT 5 (or OUTPUT 1)
5 INPUT 9 /np=5999 /sigr=0.1274 /rmax=1.0 /sigt=3.0 /tmax=10
6 DRIFT 0 2 1
7 CELL /l=17.5 /aper=2.0 /iout=1 /phi0=35 /E0=85 /nc=1
/dwtmax=5.0 /sym=-1
8 CFIELD 1
9 RF_PHIN.T7
10 COIL 0 20 -1.2758e5 0 250
11 COIL 8 20 1.6745e5 0 250
12 COIL 25 20 -2.7110e4 0 250
13 DRIFT /l=12.5 /aper=2.0 /iout=1
14 DRIFT /l=88.5 /aper=2.0 /iout=1
15 DRIFT /l=23 /aper=2.0 /iout=1
16 DRIFT /l=15 /aper=2.0 /iout=1
17 BEND 19.6 20 1 5.486 90
18 DRIFT /l=0 /aper=2.0 /iout=1
19 DRIFT /l=86 /aper=2.0 /iout=1
20 DRIFT /l=24 /aper=2.0 /iout=1
21 DRIFT /l=50 /aper=2.0 /iout=1
22 ZOUT 600 0 0 250 0 0
23 SCHEFF /beamI=6.9866215 0.5 5 10 20 1908 0
24 START /wt=0 /dwt=1 /nsteps=30000 /nsc=1 /nout=10
25 end

```

Figure 16: The example of a PARMELA input file for PHIN.

that is denoted by *CellType*. After the *CField* card the program expects to receive the name of the text file which has the RF data.

The elements that provide the static magnetic fields can be also defined in the input file. PARMELA can generate the fields of the focusing solenoids and the dipole on the PHIN beamline. It utilizes the information passed by the attributes of *COIL* and *BEND* cards. *COIL* card is not considered as a beamline element by the program. It only provides the background field within the longitudinal range determined by the Z_{min} and Z_{max} attributes. Two solenoid magnets were used in the PHIN set-up. The measured magnetic field provided by these two solenoids can be best represented by means of three *COIL* lines in the PARMELA input file. The background magnetic field for the PHIN is given in the Fig. 17. As seen in the figure, the combination of the solenoids should provide zero magnetic field at the longitudinal position of zero, where the cathode is placed. The details of this arrangement will be given in Chapter 4.

In PARMELA, calculation of the space charge impulses is performed according to the information given by the *SCHEFF* card. The beam current I_T is the first attribute and it is defined as the product of the RF frequency and the charge per bunch. The

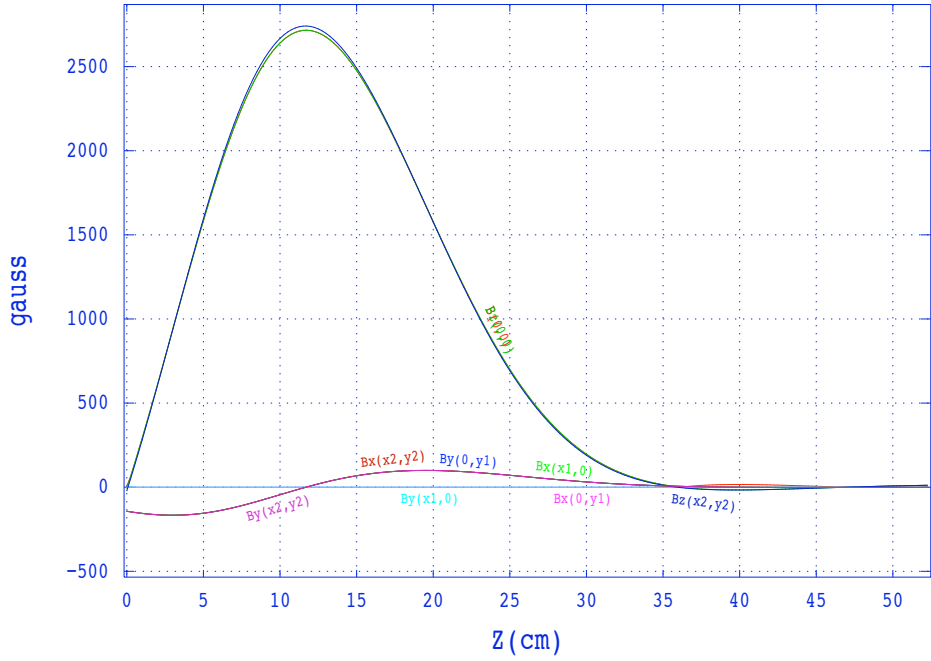


Figure 17: The background magnetic field for PHIN as it is represented in the PARMELA program.

number of bunches and the length of the bunches can also be specified by the attributes N_{Bunch} , L_{Bunch} . The program generates radial and longitudinal mesh regions for the space charge calculations. The number of these regions are given as N_R and N_Z , respectively. ΔR_{SC} and ΔZ_{SC} are the mesh region lengths in cm .

After the proper definition of the beamline and the beam parameters, the *START* card invokes the beam dynamics calculation.

3.2 Model for the PHIN Photoinjector

In the frame of the modelling studies the general beam dynamics of a photoinjector have been investigated under the variation of the certain parameters. The laser spot size on the cathode, charge per bunch, RF phase, on-axis electric field of the cavity and magnetic focusing of the solenoid magnet have been determined as the variables of the modelling study. A set of values for these parameters will be considered as a reference point for the simulations. This set of values are assigned in connection with the PHIN specifications and will be called “the baseline configuration”. The baseline values for the aforementioned parameters are given in the Table 10. The calibration from the three-coil system of PARMELA to the two-coil system of the actual set-up is given in Table 11. The effects on the overall beam dynamics have been investigated under the variation of the model parameters, individually. The beam dynamics parameters have been calculated on the locations where measurement of the corresponding observable is possible on the set-up as given in Table 12. The results of these investigations are given in this section.

Table 10: The baseline parameters used for simulations of PHIN.

Parameter	Value
Laser Spot Size (1σ) (mm)	1.2
Charge / Bunch	2.33
RF Phase ($^{\circ}$)	35
Gradient (MV/m)	85
Focusing Solenoid Current (A)	238
Laser Pulse Length (1σ) (ps)	3

Table 11: The reference calibration for the baseline settings of the solenoids.

PARMELA Settings ($\times 10^5$)			Laboratory Settings		
COIL 1	COIL 2	COIL 3	Bucking Coil (A)	Focusing Solenoid (A)	Peak Magnetic Field (Gauss)
-1.7935	2.3539	-3.8111	223.1	237.7	2716

Table 12: The longitudinal positions where a PARMELA simulation output is retrieved for the corresponding parameter.

Parameter	Measurement Position
Beam Size (mm)	Screen 1
Transverse Emittance (mm mrad)	Multi-Slit Mask
Bunch Length (ps)	Screen 2
Energy Spread (keV)	Screen 2
Longitudinal Emittance (μ m)	Screen 2
Energy (MeV)	After RF Gun

3.2.1 RF Phase Dependence

A phase scan has been simulated in order to search the on-crest phase, where the maximum energy gain from the RF field occurs. The evolution of the bunch length is another criteria for the phase choice. The RF phase has to be chosen so that the bunch length should stay constant with respect to the longitudinal position on the beamline.

The simulations have been performed in the baseline configuration by only changing the RF phase with the steps of 5° . The result can be seen in Figure 18-a. The phase difference between the particles (master clock of PARMELA) and RF field can be determined so that the particles catch the RF field at the on-crest phase while they are emitted from the

cathode. This phase difference has been found to be 35° for the rest of PHIN simulations. As explained before, this phase is an arbitrary parameter which introduces a given phase difference between the RF field and the master clock in the program in order to compensate the phase slippage of the unrelativistic electrons. In Fig. 18-b, the bunch length evolution is shown for different RF phases. It is seen that the bunch length is fairly constant for the nominal phase of 35° .

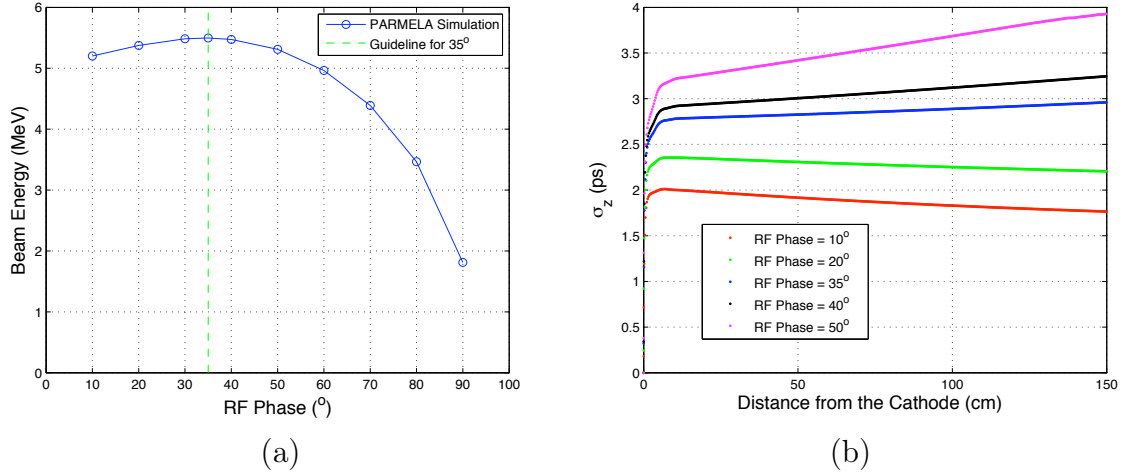


Figure 18: The simulation result of the scan in the search of (a) the on-crest phase for the PHIN simulations and (b) the evolution of the bunch length along the beamline at these emission phases (b).

3.2.2 Laser Spot Size Dependence

The laser spot size is one of the most determining factors for the photoinjector beam dynamics. It has an impact on the initiation of the characteristics from the charge production to the transverse beam size and emittance. It has been already given in the Chapter 2 that the maximum achievable charge increases proportional to the laser spot size on the cathode. Here, the effects of the laser spot size on the beam dynamics will be investigated.

In the Fig. 19-a the parabolic behavior of the beam size with respect to the focusing solenoid current is shown. The beam size values have been extracted for the longitudinal position of the OTR screen which is installed 141.5 cm downstream in the beam line. Each different curve in the plot represents the simulation result with respect to different laser spot size. In the figure the blue curve is the typical laser spot size for PHIN. For this typical case, the minimum beam size occurs under a focusing that is provided by solenoid current of 230 A. These simulation results show that when laser spot size changes, it is not possible to obtain the same beam size with the same focusing force. The minimum beam size occurs for different focusing solenoid settings.

The behavior of the transverse normalized emittance is plotted in the Fig. 19-b. The emittance compensation is accomplished at a certain focusing solenoid current for each curve in the figure. The nominal magnet settings are denoted by the red dots where the emittance compensation occurs. As a result, the emittance is minimized, in each case,

just after the focus region where the beam starts to become divergent. However, it has been observed that the emittance increases significantly with the increasing laser spot size. Additionally, the focusing condition which is providing the minimum emittance changes for each different laser spot size. In reality the determination of the nominal laser spot size should be a compromise between the maximum achievable charge per bunch and the minimum achievable transverse normalized emittance. For the PHIN commissioning, the typical laser spot size has been determined as $\sim 1\text{ mm}$ (1σ). This yields 4.7 nC maximum charge per bunch and an transverse normalized emittance of 14 mm mrad .

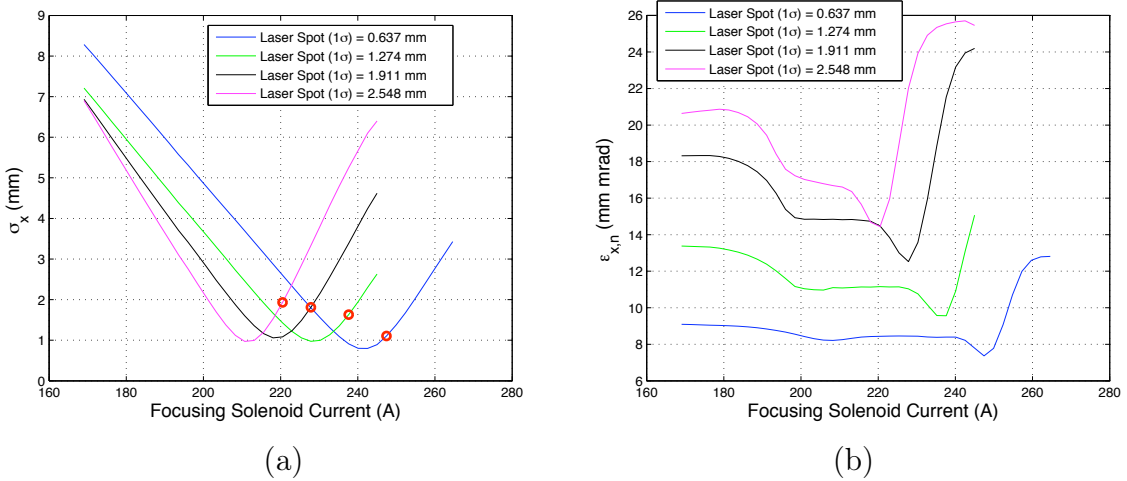


Figure 19: (a) The variation of the transverse beam size and (b) the transverse emittance with respect to the focusing solenoid current for different laser spot sizes. The magnet settings that are providing the minimum emittance for each laser spot size are marked with the red dots on the beam size curves. The simulations have been performed for a charge per bunch value of 2.33 nC .

The same simulation results can be investigated from a different point of view. In Fig. 20 the evolution of the transverse beam size (a) and the normalized emittance (b) are presented along the beamline up to a downstream point of 150 cm. According to these simulation results, in Fig. 20-a, the larger the laser spot size, the closer the beam waist occurs with respect to the cathode position. A drastic change in the beam envelope occurs by varying the laser spot size under the same focusing conditions. This shows that a proper focusing has to be provided for a smoother beam envelope in order to avoid the emittance growth, due to laser spot size changes, that is shown in the Fig. 20-b.

Regarding the emittance scan with respect to the focusing solenoid current in Fig. 19-b, a nominal focusing current can be specified that provides the minimum emittance for different laser spot size. The value of the parameters under the optimized focusing are given in the Table 13. In this case, a variation of the emittance can be observed along the beamline after the beam becomes divergent around 87.5 cm as seen in the Fig. 21-a. In this optimized case, the emittance growth is not as drastic as the case with the lack of an optimized focusing. Nevertheless, as an overall behavior, the beam emittance increases with the increasing laser spot size as seen in the Fig. 21-b.

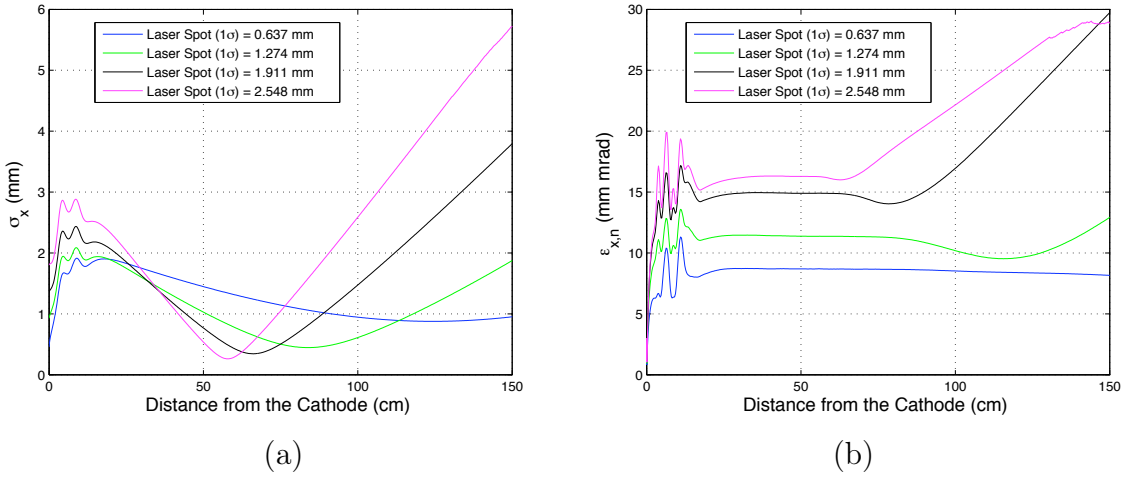


Figure 20: The transverse beam size (a) and the emittance (b) evolution along the beam-line up to a downstream point at 150 cm. The simulations have been performed under the optimum focusing for the nominal PHIN specifications which corresponds to 237.65 A.

Table 13: Transverse beam parameters as a function of the laser spot size. The magnet settings are optimized for the minimum transverse normalized emittance.

Laser Spot Size (mm)	Solenoid Current (A)	Beam Size (mm)	Transverse Emittance (mm mrad)
0.64	247.4	1.1	7.4
1.23	237.7	1.6	9.6
1.91	227.8	1.8	12.5
2.55	220.5	1.9	14.4

3.2.3 Gradient Dependence

The energy of the particles has an effect on both the transverse and the longitudinal dynamics. These effects have been studied by using PARMELA simulations including the PHIN energy specification of 5.5 MeV. The results are shown in Fig. 22 and Fig. 23.

The transverse properties of the beam under the energy variation is shown in Fig. 22. The behavior of the beam size with respect to the focusing magnet current can be seen in the Fig. 22-a, for different energies. One has to apply a stronger focusing for the higher energies in order to obtain the beam waist of these parabolic curves at the same longitudinal position. The data points where the transverse normalized emittance reaches a minimum in Fig. 22-b for each energy value, have been marked on the beam size curves in Fig. 22-a. This has revealed that each time the minimum emittance occurs just after the beam becomes divergent under the effect of magnetic focusing. As a matter of fact, the transverse normalized emittance decreases by increasing energy. Fig. 22-b reveals this

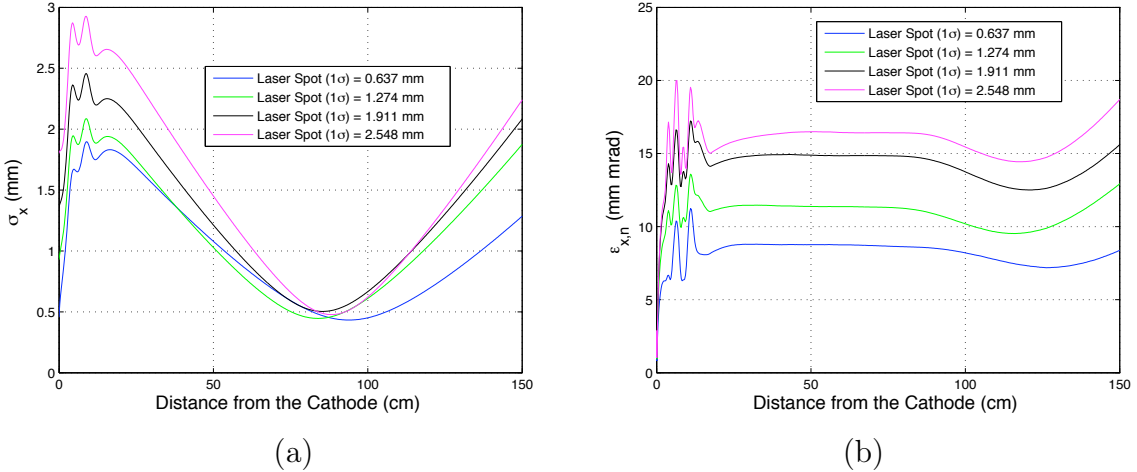


Figure 21: The transverse beam size (a) and the emittance (b) evolution along the beamline up to a downstream point at 150 cm. The curves show the case under the focusing conditions that are optimized for minimum emittance for each different laser spot size.

behavior provided that the magnetic focusing is optimized for the minimum emittance. The beam size and transverse normalized emittance are given in Fig. 22-c and d, along the beamline. Each curve is generated for the optimum focusing. The beam waist appears approximately at the same longitudinal position and the minimum possible emittance is shown for each energy. However, the emittance growth is a characteristic behavior for the decreasing energy.

The longitudinal beam properties can be seen as a function of the beam energy and the focusing in Fig. 23. The phase of the RF with respect to the particles has been optimized for the PHIN nominal case of 5.5 MeV. This optimized phase has been kept constant as the energy changes to observe the effect of deviations around the nominal emittance. Besides the overall bunch length changes for different energies, an additional bunch lengthening is observed along the beamline as shown in Fig. 23-a for the lower energies. The bunch lengthening leads to an increase in the energy spread of the beam as shown in Fig. 23-b. As a consequence the longitudinal emittance blows up along the beamline after a longitudinal position of ~ 70 cm, in an inversely proportional manner to the beam energy, as shown in Fig. 23-c.

The summary of the transverse and longitudinal beam characteristics under the energy variation is given in Table 14, for the optimum focusing.

3.2.4 Charge per Bunch Dependence

Production of the high charge per bunch is one of the main goals of the PHIN photoinjector. This brings the issue of the space charge induced decelerating force. The transverse normalized emittance grows significantly due to the space charge effect. In this section, the transverse and longitudinal beam characteristics are studied for different charge values, including the nominal PHIN charge of 2.33 nC. All the parameters except from the charge have been kept at their values specified as the “baseline configuration” for the simulations.

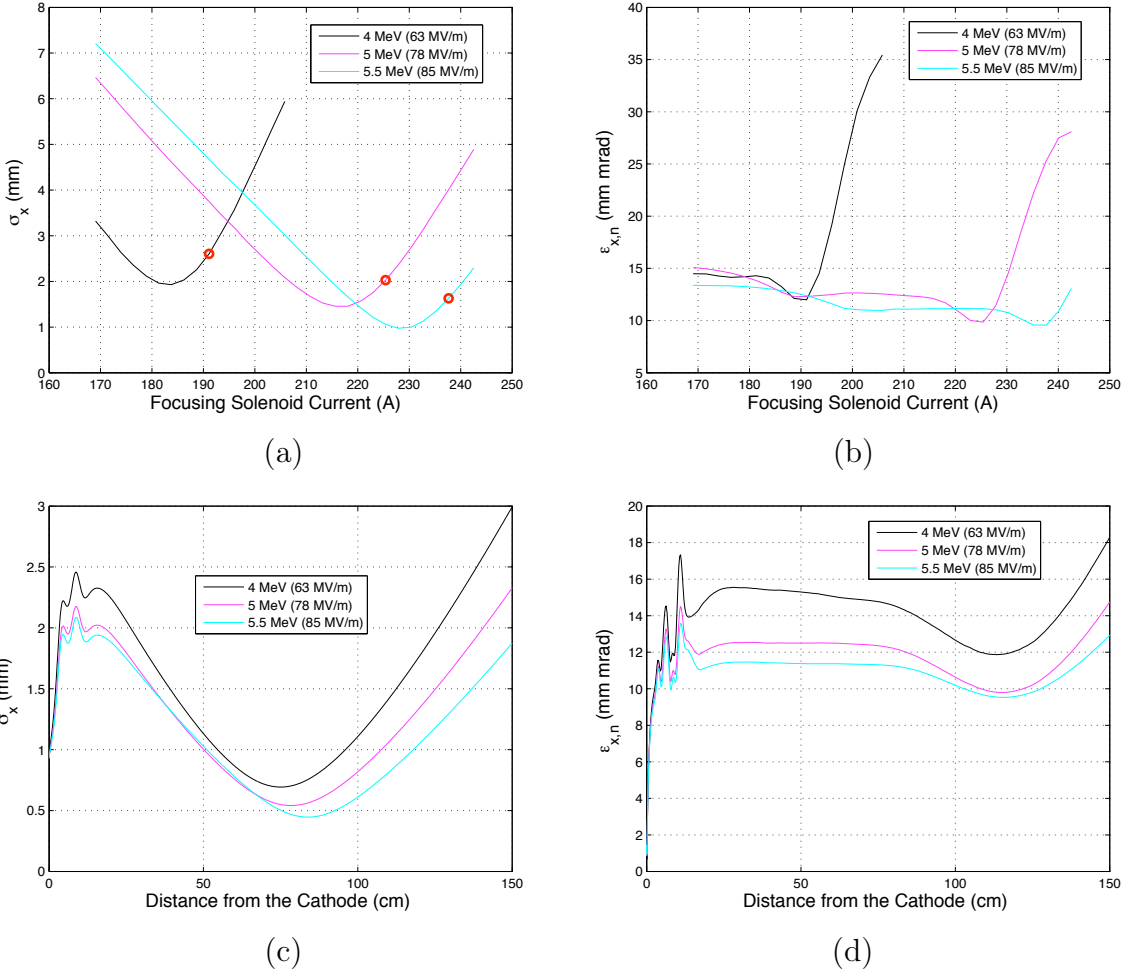


Figure 22: The behavior of (a) the beam size and (b) the transverse normalized emittance with respect to the focusing solenoid current for different gradient values. The red dots on (a) are used to emphasize the settings for the minimum emittance. The evolution of the parameters along the beamline up to a downstream position of 150 cm , with respect to the cathode, is given in (c) and (d).

Table 14: Transverse and longitudinal parameters of the beam as a function of the gradient for the settings that are optimized for the minimum transverse normalized emittance.

Gradient (MV/m)	Energy (MeV)	Solenoid Current (A)	Beam Size (mm)	Transverse Emittance (mm mrad)	Bunch Length (ps)	$\Delta E/E$ (%)	Longitudinal Emittance (μm)
63	4.0	191.10	2.60	12.00	5.10	2.66	12.7
78	5.0	225.40	2.03	9.80	3.20	1.55	11.0
85	5.5	237.70	1.63	9.60	2.60	1.03	8.6

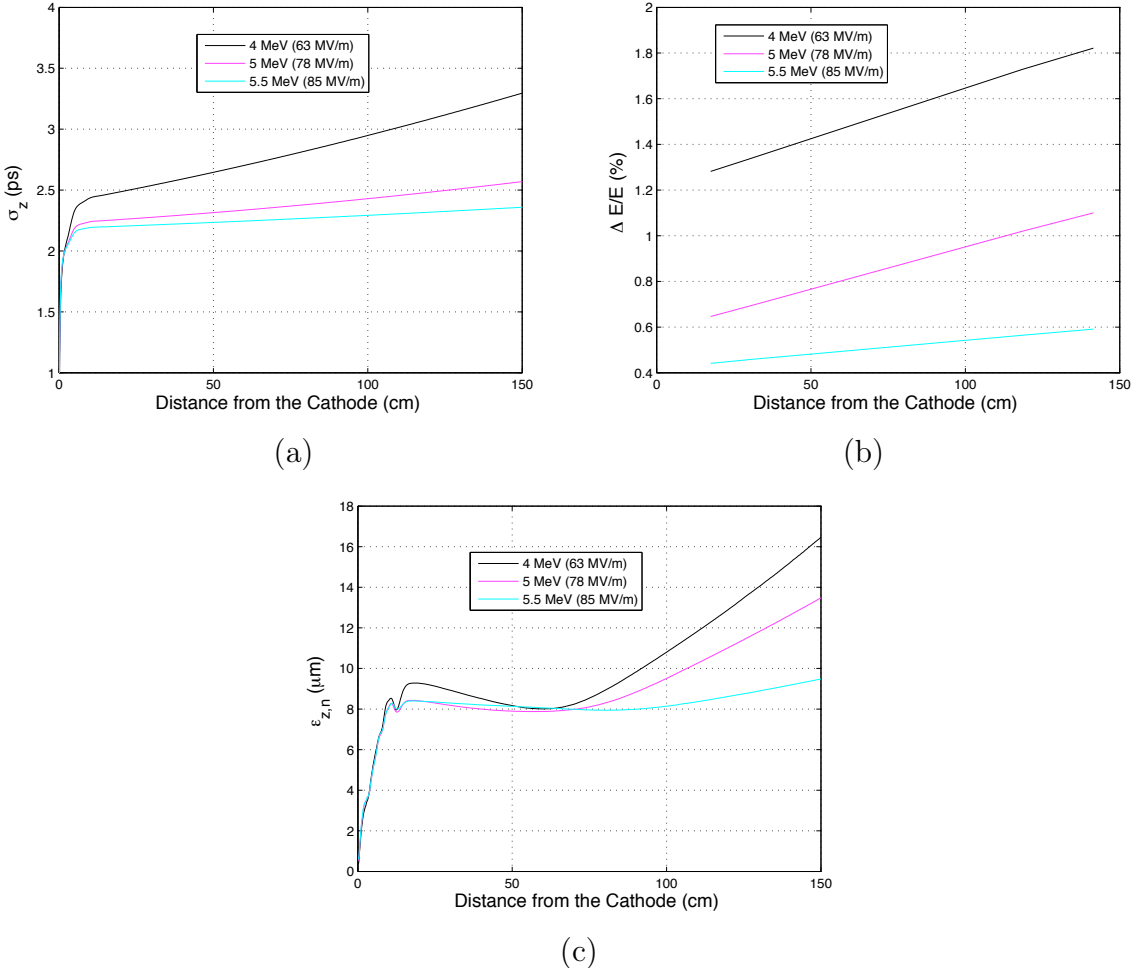


Figure 23: The longitudinal beam parameters for different gradient values. The bunch length (a) and the energy spread (b) along the beamline increases when the gradient is lower. As a result the longitudinal normalized emittance grows after a longitudinal position of $\sim 70\text{ cm}$.

The space charge effect on the transverse normalized emittance is clearly visible, from the increasing emittance with the charge, in the Fig. 24-b. This phenomena has been explained in Chapter 2 in more details. The space charge induced transverse emittance growth is compensated by the magnetic focusing force that is provided by a solenoid magnet in PHIN set-up. The emittance minimum occurs under a stronger focusing condition proportional to the charge per bunch. The evolution of the beam size and the emittance can be seen in Fig. 24-c and d under the proper focusing conditions for each charge value. The emittance compensation occurs after a certain distance from the cathode. The compensated transverse normalized emittance values has been investigated with respect to the charge per bunch. The result is presented in Fig. 25, where there is a linear proportionality between the emittance and the square root of the charge.

The overall longitudinal beam parameters changes proportional to the value of charge per bunch as it appears in Fig. 26. The energy spread increases along the beamline. But the bunch length is fairly constant due to the emission phase that is optimized for

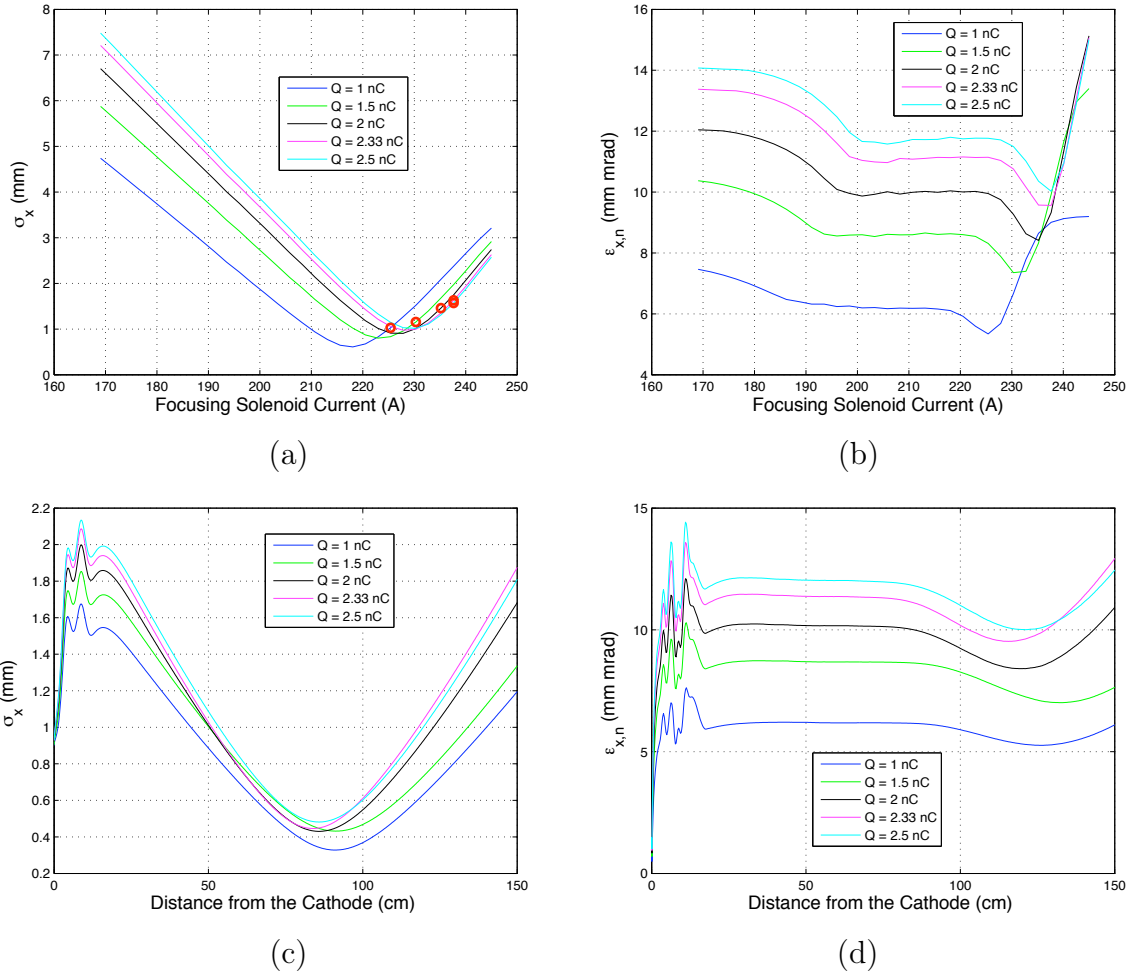


Figure 24: The behavior of the beam size (a) and the transverse normalized emittance (b) with respect to the focusing solenoid current for different charge values. The red dots on (a) are used to emphasize the settings for the minimum emittance. The evolution of the parameters along the beamline up to a downstream position of 150 cm, with respect to the cathode, is given in (c) and (d).

the baseline energy that is used in these simulations. Despite the increase in energy spread, there is no significant blow up in the longitudinal normalized emittance along the beamline.

The summary of the transverse and longitudinal beam characteristics under the energy variation is given in Table 15, for the optimum focusing.

3.2.5 Summary for the PHIN Baseline Configuration

The optimum operation settings can be determined for the PHIN photoinjector after the previous general investigation. A range of the charge per bunch values spanned from 1 nC to 2.5 nC . As a consequence, a quick reference for working points at different charge values has been provided. This has been used as a look-up table during the operations where the cathode quantum efficiency is degrading and resulting different charge yields over time with the same cathode. The results of these simulations are presented in this

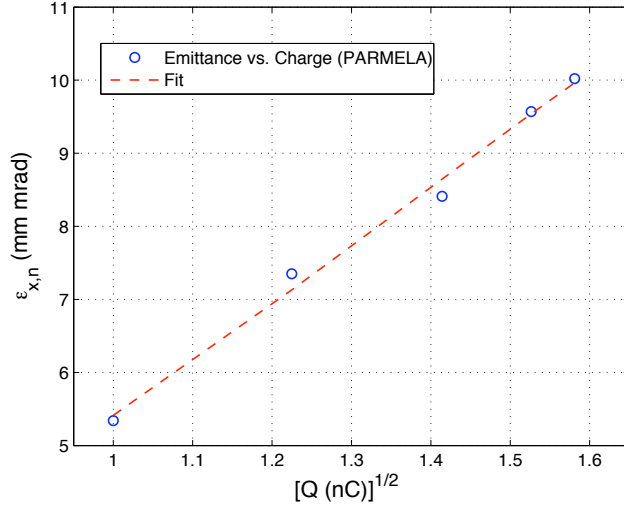


Figure 25: The transverse normalized emittance scales with the square root of the charge per bunch value.

Table 15: Transverse and longitudinal parameters of the beam as a function of the charge per bunch for the settings that are optimized for the minimum emittance.

Charge (nC)	Solenoid Current (A)	Beam Size (mm)	Transverse Emittance (mm mrad)	Bunch Length (ps)	$\Delta E/E$ (%)	Longitudinal Emittance (μm)
1.00	225.4	1.03	5.3	2.01	0.30	5.3
1.50	230.3	1.15	7.3	2.13	0.40	6.4
2.00	235.2	1.46	8.4	2.26	0.50	7.6
2.33	237.7	1.63	9.6	2.36	0.56	8.6
2.50	237.7	1.57	10.0	2.40	0.60	8.9

section.

A procedure can be summarized for the optimization of the photoinjector parameters in the light of the simulations and the Travier's model. The aim is the search of a working point that provides a trade-off between the key parameters. The following optimization steps have been determined for this study:

1. The emission phase of the particles with respect to the RF (master clock in PARMELA) is determined according to the result of the simulated phase scan at a given gradient. This emission phase should be chosen which provides the maximum energy gain from the RF field. Additionally, a constant bunch length along the beamlne implies a proper bunching. The changes in the bunch length cause a change in the energy spread. Therefore, the evolution of the bunch length along the beamlne is another important criteria for the phase choice.
2. The nominal laser spot size is determined both empirically and numerically. The

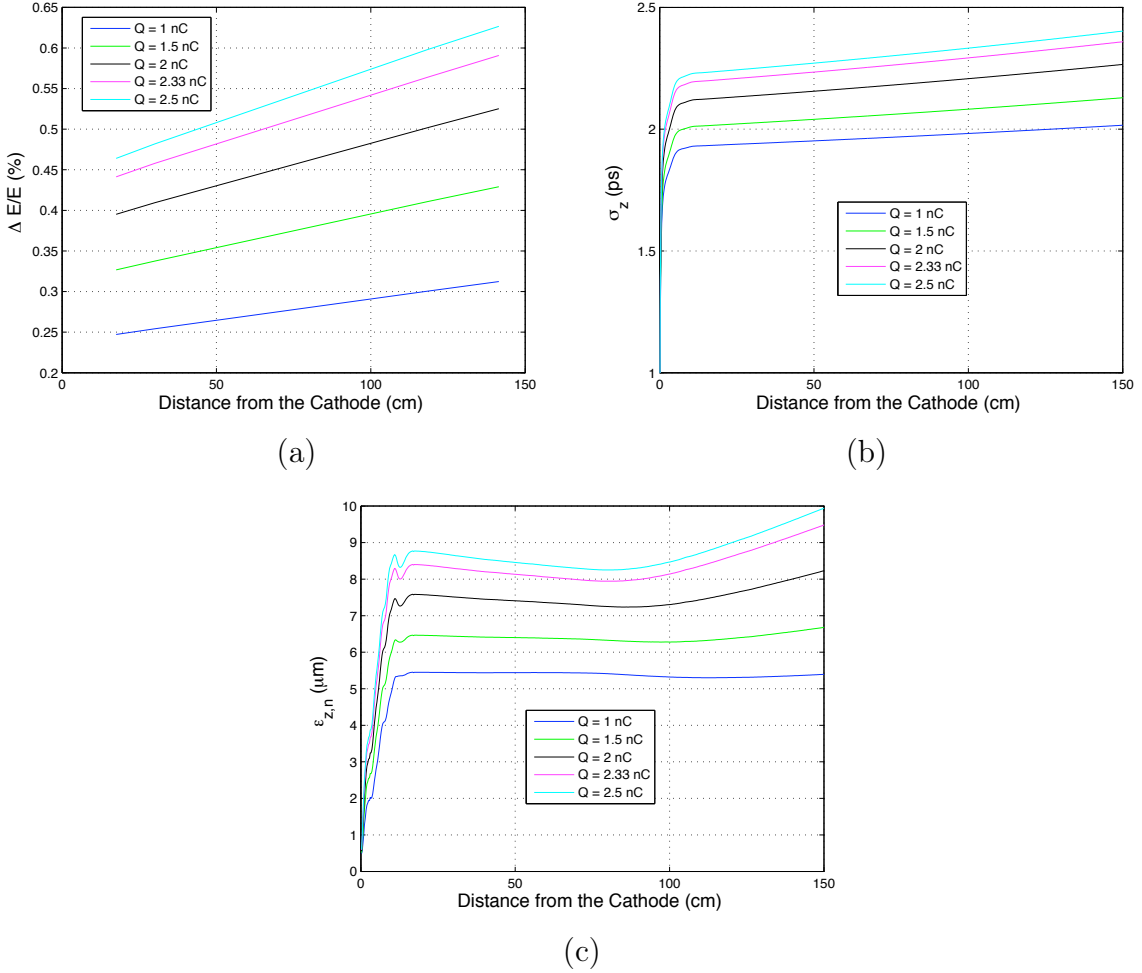


Figure 26: The longitudinal beam parameters for different charge per bunch values. The energy spread (a) and the bunch length (b) along the beamline increases inversely proportional to the charge per bunch. As a result the longitudinal normalized emittance grows after a longitudinal position of $\sim 80 \text{ cm}$.

charge production yield per bunch is a function of the laser spot size. Therefore the larger spot size is supposed to lead a higher charge production. On the contrary, an initially larger beam spot, inherited from the larger laser spot leads to an increase in the transverse normalized emittance. In reality the larger beam size would cause difficulties in focusing due to the current limits of the solenoids.

3. The focusing solenoid current after the RF gun is the next item to be optimized. In the simulations the solenoid settings that are controlling the background magnetic field can be scanned in a suitable range. The current range is chosen provided that no particles are lost during the transport through the beamline. The emittance compensation should occur within the determined focusing range for the given charge and energy values.
4. In most cases, to maintain the minimum emittance and the energy spread in the same time is not possible. Therefore, the settings can be chosen so that the set-up

is optimized for a working point between the minimum emittance and minimum energy spread.

5. For each step of the optimization, the particle transport along the beamline has to be checked to make sure that the particle loss is within the acceptable percentage.

For the rest of the optimization studies, the RF phase and the laser spot size values have been chosen as 35° and 1.2 mm , respectively, according to the previous discussions. The energy of the beam is given as 5.5 MeV , according to the photoinjector specifications. The PHIN laser pulse train has the 1.5 GHz inner structure, providing a micro pulse length of $\sim 6.62 (\pm 0.41)\text{ ps}$ (FWHM). Therefore, a bunch length of 3 ps (1σ) is used as an input for PARMELA simulations.

The fig. 27 illustrates the beam dynamics for the baseline configuration of PHIN photoinjector. The figure contains four plots to present the evolution of four different parameters as a function of the focusing solenoid current. These parameters are the transverse and longitudinal normalized emittances, the energy spread and the bunch lenght. The various simulation results for different charge values are summarized in Appendix 2. In each case, the transverse and longitudinal emittance, energy spread and the bunch length are shown. The values of these parameters are retrieved at various longitudinal positions of the beamline, usually, where a measurement of that particular parameter could be possible. For example, the transverse emittance is shown after the gun, at a point of 118.5 cm where the multi slit mask is located and at a downstream point of 150 cm . In the PHIN set-up, one can only measure the emittance at the location of the multi-slit mask. Therefore it is important to provide simulations at this location for the comparison with the measurements. The instrumentation and the measurement methods are presented in detail in the Chapter 4.

Once the focusing solenoid current is chosen for the minimum transverse emittance, the other parameters are determined at the same settings. The energy spread, the bunch length and therefore the longitudinal emittance are given at several locations. The values are tracked also after the dipole magnet, in the dispersive section of the beamline, for the longitudinal beam parameters. These are the locations that are denoted as the “Screen 2” and the “Segmented Dump”. The energy spread can be measured at these locations.

The downstream point of 150 cm is assumed to be the exit of the injector. Therefore the values of the parameters at a 150 cm downstream location, can be considered as the deliverable specifications by the PHIN photoinjector.

On the other hand, in order to present a more complete picture, the same research has been done also for different energies. For each case, the optimum focusing has been determined. The determination is done according to the emittance behavior at the longitudinal position of the multi-slit mask. The particular solenoid setting is chosen which provides the emittance compensation, namely, where the minimum emittance occurs during the focusing solenoid scan. The longitudinal parameters are also presented corresponding to these nominal solenoid magnet setting. The summary of the working points for different energies and charge values can be seen in Table 16. According to the table, the area occupied by the beam both in the transverse and the longitudinal phase space increases with the increasing charge per bunch values due to the space charge effects. Furthermore, the increase in energy results with a decrease in both transverse and the longitudinal normalized emittances as a consequence of the Liouville’s theorem on the conservation of

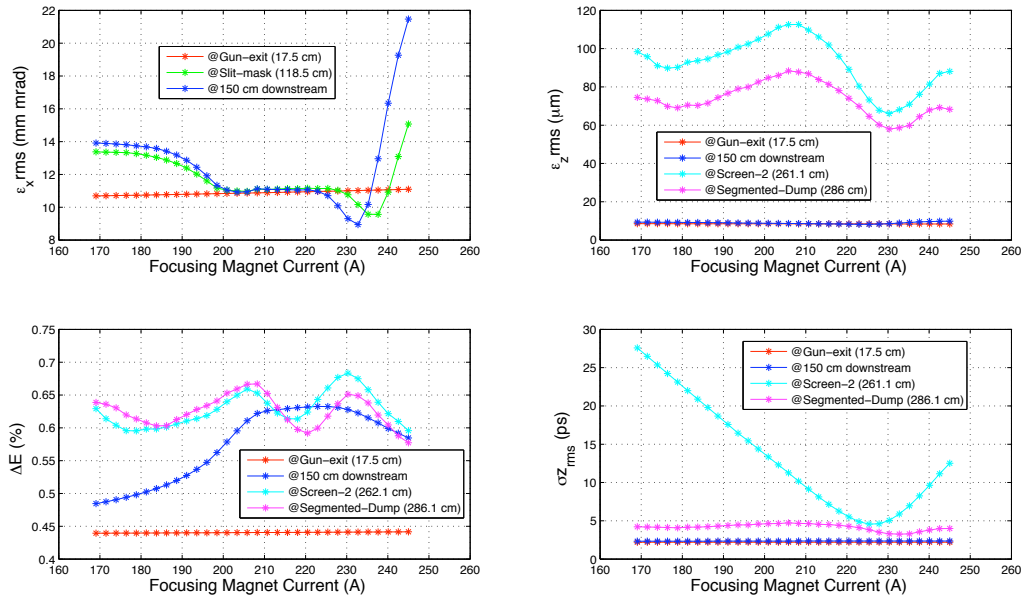


Figure 27: The beam dynamics parameters at the gradient of 85 MV/m for the nominal beam charge of 2.33 nC.

the phase space.

Table 16: Summary of the optimum working points for PHIN for the given beam energy and the charge per bunch values.

75 MV/m (4.8 MeV at 35°)					
Charge (nC)	1.0	1.5	2.0	2.33	2.5
$I_{focusing}(A)$	208.2	213.2	215.6	218.1	218.1
$\epsilon_x(mmmrad)(@Gun-Exit/@Slit Mask)$	6.8 / 5.7	9.5 / 7.8	11.0 / 9.0	12.3 / 10.1	13.1 / 10.8
$\epsilon_z(\mu m)(@Gun-exit/@Screen2)$	6.3 / 79.1	6.3 / 116.6	7.5 / 147.5	8.4 / 166.2	8.8 / 172.7
$\Delta E(KeV)(@Gun-exit/@Screen2)$	0.48 / 0.72	0.59 / 0.88	0.68 / 1.0	0.74 / 1.1	0.78 / 1.12
$\sigma_z(ps)(@Gun-exit/@Screen2)$	2.2 / 7.2	2.1 / 8.3	2.2 / 8.9	2.3 / 10.1	2.3 / 10.0
80 MV/m (5.2 MeV at 35°)					
Charge (nC)	1.0	1.5	2.0	2.33	2.5
$I_{focusing}(A)$	218.1	225.4	227.8	227.8	230.3
$\epsilon_x(mmmrad)(@Gun-Exit/Slit Mask)$	6.4 / 5.5	8.9 / 7.5	10.5 / 8.6	11.7 / 9.7	12.4 / 10.3
$\epsilon_z(\mu m)(@Gun-exit/Screen2)$	5.3 / 66.5	6.4 / 104.2	7.6 / 134.6	8.5 / 152.3	8.9 / 162
$\Delta E(KeV)(@Gun-exit/Screen2)$	0.36 / 0.62	0.45 / 0.78	0.53 / 0.9	0.6 / 1	0.6 / 1
$\sigma_z(ps)(@Gun-exit/Screen2)$	2.1 / 6.5	2.2 / 8.5	2.2 / 9.1	2.5 / 8.8	2.3 / 9.9
85 MV/m (5.5 MeV at 35°)					
Charge (nC)	1.0	1.5	2.0	2.33	2.5
$I_{focusing}(A)$	225.4	230.3	235.2	237.7	237.7
$\epsilon_x(mmmrad)(@Gun-Exit/Slit Mask)$	5.9 / 5.3	8.4 / 7.3	9.8 / 8.4	11.0 / 9.5	11.7 / 10.2
$\epsilon_z(\mu m)(@Gun-exit/Screen2)$	5.4 / 33.7	6.7 / 47	8.2 / 63.3	9.5 / 76.1	9.9 / 76.9
$\Delta E(\%)(@Gun-exit/Screen2)$	0.25 / 0.35	0.33 / 0.48	0.2 / 0.6	0.44 / 0.64	0.5 / 0.7
$\sigma_z(ps)(@Gun-exit/Screen2)$	2.0 / 5.5	2.2 / 6.0	2.1 / 7.4	2.3 / 8.2	2.2 / 7.9

3.3 Stability Aspects of PHIN: e^- Beam Sensitivity to the Jitter on the Parameters

The performance of a photo-injector determines the initial conditions for many beam parameters such as the transverse and longitudinal emittances, energy spread and the bunch length. The errors or jitters in terms of the laser parameters, the phase, gradient and the charge can cause improper initiation of the beam. As a source for the CLIC drive beam, the stability and sensitivity of the PHIN photoinjector have been studied and presented in this section.

The phase error of the RF field relative to the laser and, the variations in the amplitude of the average accelerating gradient are important issues for the stability of photoinjectors. The phase and gradient errors are transferred to the beam energy, therefore to the normalized beam emittance and the bunch length. The impact of the laser and the charge jitter both on the transverse and longitudinal phase should be clarified.

The possible scenarios have been investigated in order to consider the errors on several parameters within the $\pm 1\%$. The tolerances of the PHIN photoinjector have been studied by performing jitter simulations with PARMELA program. The results are presented in this section. The measured stability of various laser parameters and the stability of RF according to the klystron specifications for the PHIN photoinjector are summarized in Table 17.

Table 17: The measure PHIN laser stability and the stability of the conventional RF power generator.

Parameter	Value
Laser Stability	
Intensity (%)	1.66
Spot Size (mm) (x / y)	0.064 / 0.053
Pulse Length (ps)	0.41
RF Stability	
Phase ($^\circ$)	0.24
RF Amplitude (%)	1

In the plots which are given within the jitter studies, the "0" value in the y-axis corresponds to the nominal case where no jitter has been introduced. The variation of a parameter under investigation has been given relative to the nominal value of this parameter.

3.3.1 Phase Jitter

The phase jitter has been simulated up to $\pm 1\%$ variation around the on-crest phase of 35° . The effect of the phase variation on energy, energy spread, bunch length and as a result the longitudinal emittance have been investigated. The results after the gun and at 150 cm downstream of the beamline are presented in Fig. 28. The variation on these

parameters have been calculated corresponding to the maximum phase variation of $\pm 1\%$. The results are given in Table 18 for the longitudinal location at 150 cm. As seen in this summary table all parameters vary less than $\pm 1\%$ under a phase jitter of $\pm 1\%$, except the energy spread. The largest impact of a phase jitter is shown to be on the energy spread of the beam. The bunch length deviates from the nominal value significantly due to the degradation in the bunching under the phase jitter. This leads to the similar change in the longitudinal emittance.

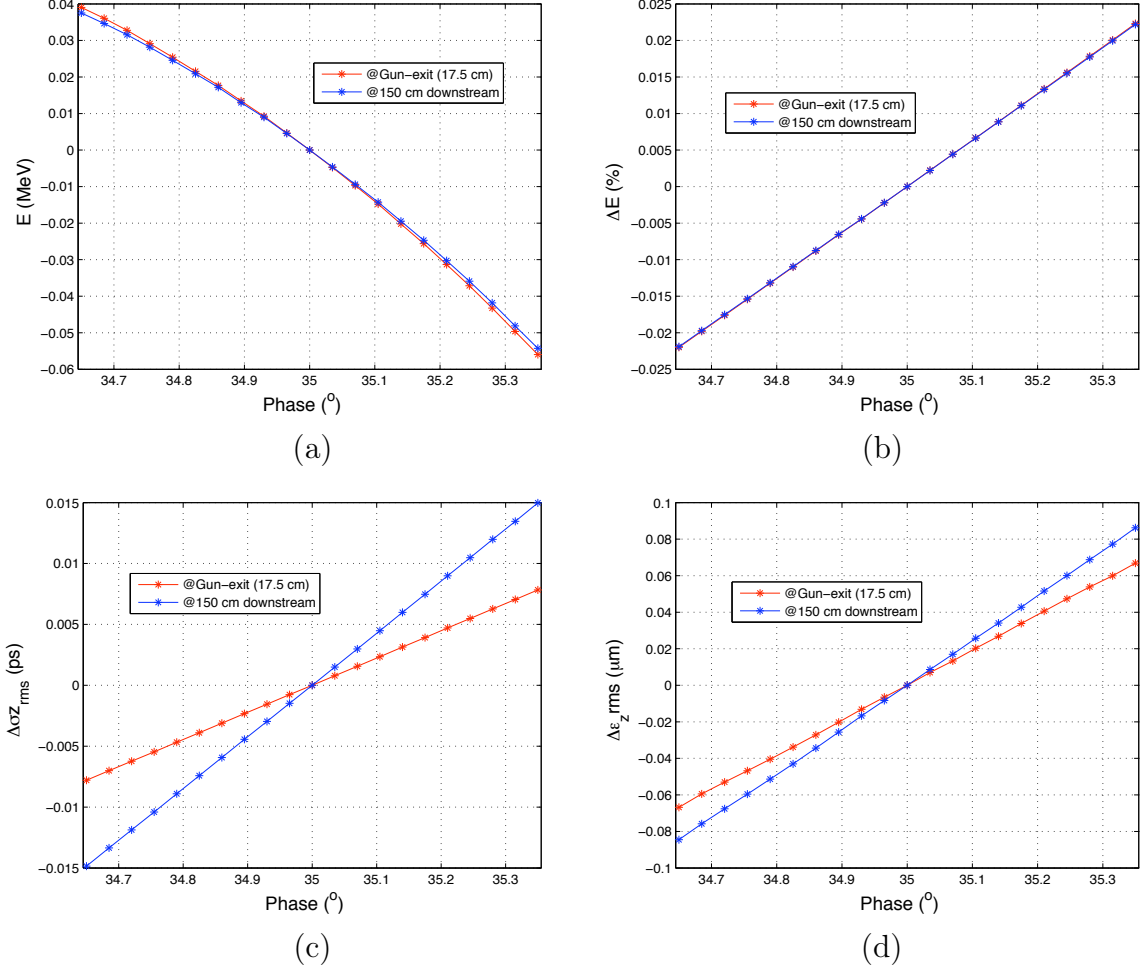


Figure 28: The effect of the phase jitter on energy (a), energy spread (b), bunch length (c) and longitudinal emittance (d).

Table 18: The deviation from the nominal longitudinal parameters under $\pm 1\%$ phase variation.

Parameter	Variation (%)
Energy	+0.67 / -0.98
Energy Spread	± 3.6
Bunch Length	± 0.63
Longitudinal Normalized Emittance	± 0.9

3.3.2 Gradient Jitter

A $\pm 1\%$ variation of has been introduced in PARMELA simulations to the average accelerating gradient of the RF gun. The irregularity in the gradient caused variations in the longitudinal beam parameters as seen in Fig. 29. The variation on the parameters

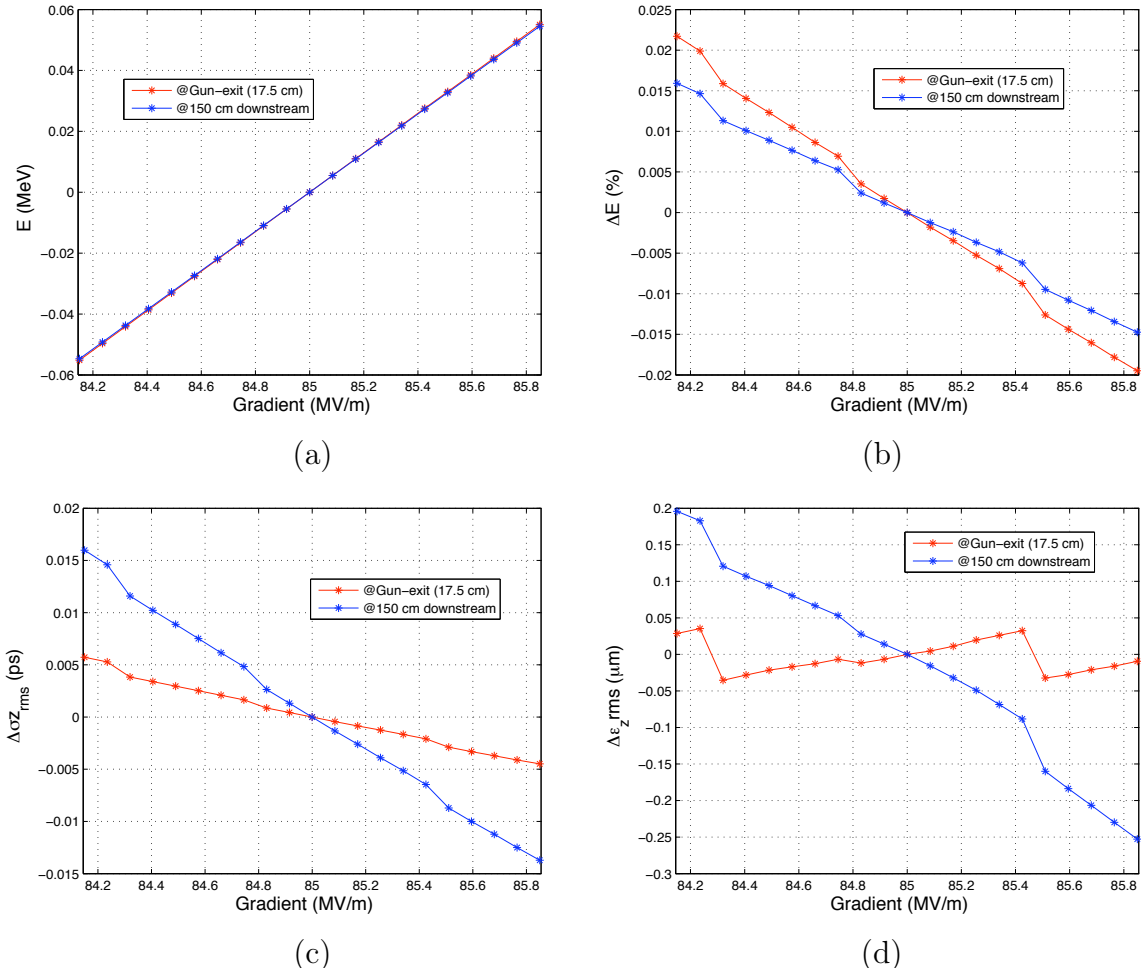


Figure 29: The effect of the gradient jitter on energy (a), energy spread (b), the bunch length (c) and the longitudinal emittance (d).

are given in Table 19 with their values at a 150 cm distance from the cathode.

Table 19: The deviation from the nominal longitudinal parameters under $\pm 1\%$ gradient variation.

Parameter	Variation (%)
Energy	± 1
Energy Spread	± 2.5
Bunch Length	± 0.6
Longitudinal Normalized Emittance	± 2.4

3.3.3 Charge Jitter

The variation of the charge within a range of $\pm 1\%$ has been investigated. The design specifications of the PHIN photo-injector includes a charge stability of $< 0.25\%$. Therefore the values given in Table 20 is more pessimistic than the design specifications. The nominal transverse normalized emittance is found 12 mm mrad. Within a $\pm 1\%$ variation of the charge value the impact on the beam emittance is significantly low. However the energy spread should be $< 1\%$ according to the PHIN specifications and the $\pm 0.9\%$ of variation due to the charge jitter would be an issue in this case.

During the commissioning studies a charge stability of 0.8% and a laser intensity stability of 1.66% have been recorded. Nevertheless, the improvement of the charge stability by implementing a feedback stabilization system for the laser is within the short-term plans of PHIN.

Table 20: The effect of the $\pm 1\%$ charge variation on the beam parameters.

Parameter	Variation (%)
Transverse Normalized Emittance	± 0.6
Longitudinal Normalized Emittance	± 0.8
Energy Spread	± 0.9
Bunch Length	± 0.3

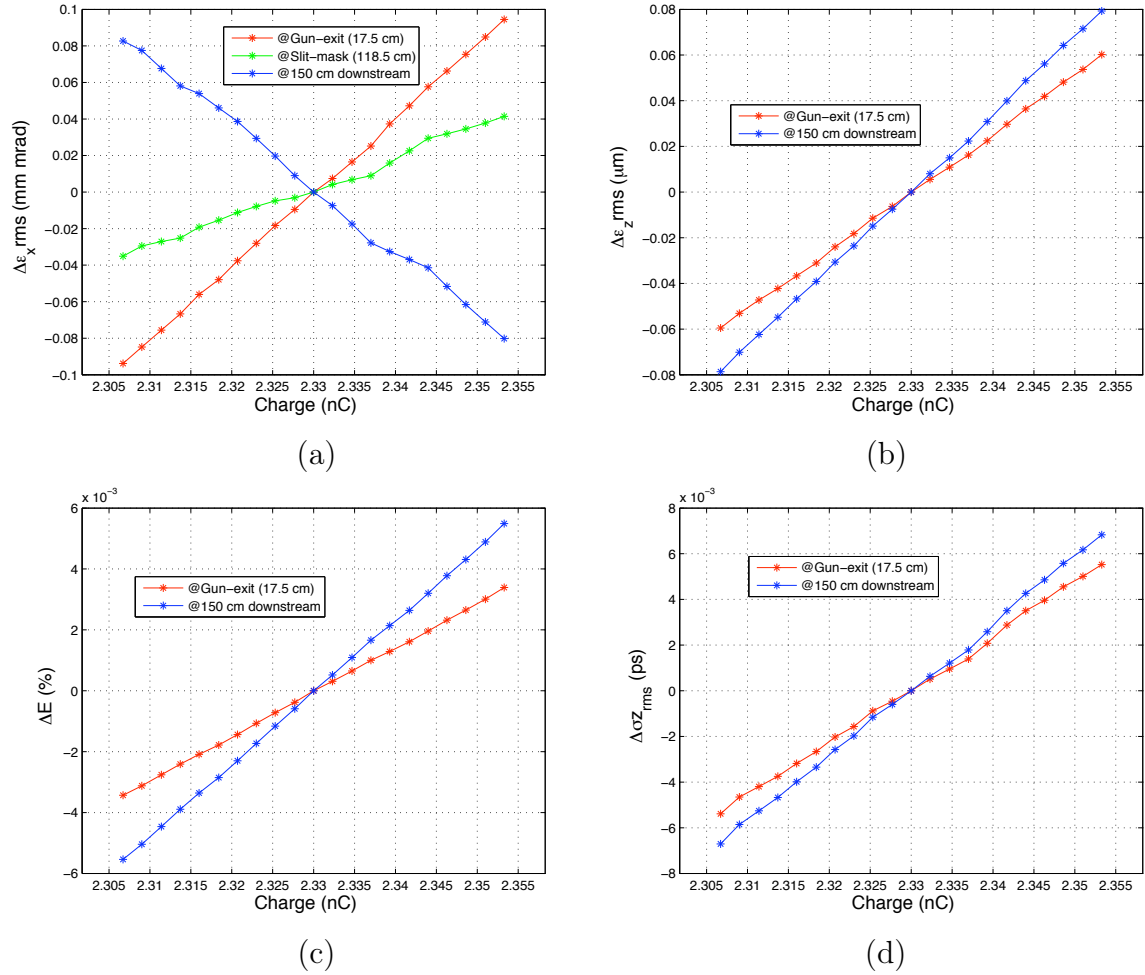


Figure 30: The effect of the charge jitter on transverse (a) and longitudinal emittance (b), energy spread (c) and bunch length (d).

3.3.4 Laser Spot Size Jitter

The effects of a $\pm 1\%$ jitter of laser spot size on the transverse beam parameters have been investigated. The results are introduced in Fig. 31. The PARMELA simulations showed that such a fluctuation during the operation can cause a transverse size deviation of $\sim \pm 2\%$ at 150 cm downstream of the beamline. The variation in the beamsize is reflected to the transverse normalized emittance as a variation of $\pm 0.3\%$ at the same position as given in Table 21. The standard deviation on the laser spot size has been measured as $\sim 0.064\text{ mm}$ in the horizontal axis which is a $\sim 5\%$ variation in the horizontal laser spot size. The corresponding transverse normalized emittance variation of $\pm 1.5\%$ has been extrapolated from the simulations.

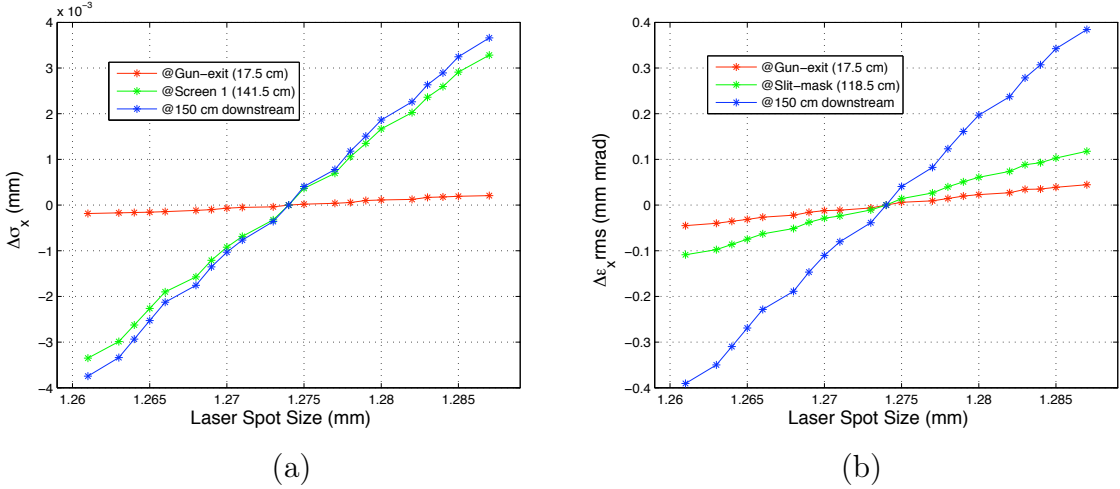


Figure 31: The effect of the jitter of laser spot size on the beam size (a) and the transverse normalized emittance (b).

Table 21: The effect of the $\pm 1\%$ laser spot size variation on the transverse beam parameters.

Parameter	Variation (%)
Beam Size	± 2
Transverse Normalized Emittance	± 0.3

3.3.5 Laser Pulse Length Jitter

The deviations around the nominal laser pulse length can effect the longitudinal beam dynamics, significantly. The results of the PARMELA simulations are presented in the Fig. 32. The variation of the longitudinal parameters under the $\pm 1\%$ jitter of the laser pulse length is presented in Table 22. The impact on the bunch length and the energy spread has been found less than $\pm 1\%$ while the longitudinal emittance varied within $\pm 1.67\%$ as a combination of both.

Table 22: The effect of the $\pm 1\%$ laser pulse length variation on the longitudinal beam parameters at 150 cm downstream of the beamline.

Parameter	Variation
e^- Bunch Length	$\pm 0.96\%$
Energy Spread	$\pm 0.67\%$
Longitudinal Normalized Emittance	$\pm 1.67\%$

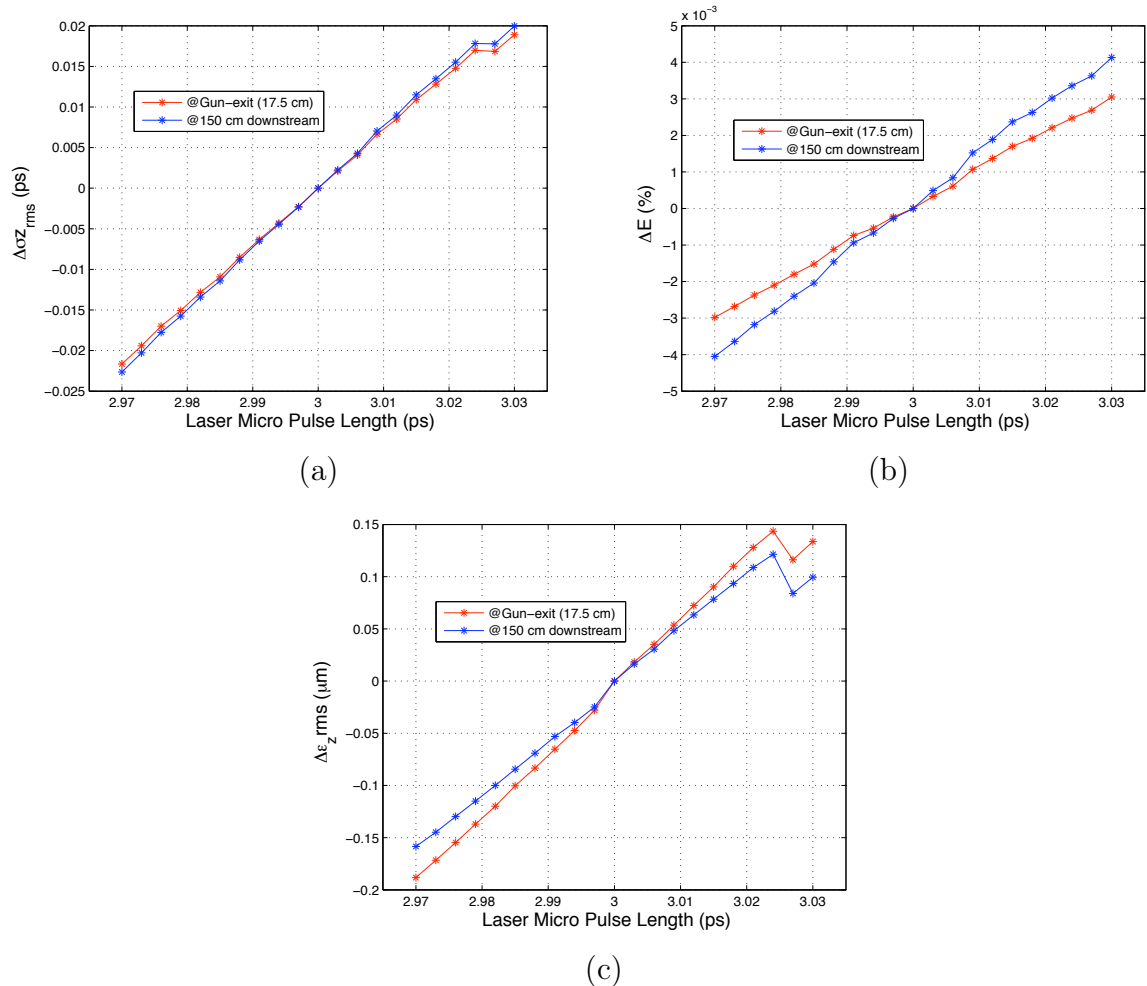


Figure 32: The effect of the changes in laser pulse length on longitudinal beam parameters.

4 Instrumentation and Experimental Set-Up for PHIN

4.1 Photocathode	62
4.1.1 Electron Emission: Thermionic, Field-Emission, Photo-Emission	62
4.1.2 C s2 T e Cathode Preparation for PHIN at CERN Photo-Emission Laboratory	63
4.2 Laser System	64
4.3 Design and Simulations for the PHIN RF Gun	65
4.4 OTR Profile Monitoring for Beam Size, Emittance and Energy Measurements	70
4.4.1 Emittance Measurement for Space Charge Dominated Beams: The Multi-Slit Method	72
4.4.2 Optimization of a Multi-Slit Measurement System and the Design of the PHIN Emittance-Meter	74
4.4.3 Magnetic Spectrometer	77
4.5 Instruments for the Time Resolved Measurements	79
4.5.1 Specifications of the Intensified-Gated CCD Camera	79
4.5.2 Segmented Dump for the Energy Measurements	80
4.6 Automated Software for the Measurements	82

The PHIN photoinjector consists of a semiconductor photocathode, a laser system and the RF gun and a set of solenoids for focusing. The test-stand at CERN also houses a section with various instruments to measure the transverse and the longitudinal beam parameters with different techniques.

The measurement section has been equipped with the beam current monitoring instruments such as a fast current transformer, a beam position monitor, a wall current monitor and a Faraday cup. The OTR profiling has been widely used in the system in order to measure the size, the transverse emittance and the energy of the beam. A magnetic spectrometer has been installed in the beam line. In addition, the spectrometer set-up includes a segmented beam dump.

The demonstration of the stability along the $1.3\ \mu s$ bunch train is one of the main focuses of the project. Therefore, the time-resolved measurements give the substantial results of the PHIN commissioning. In the beamline, the time resolved measurements

were done by using gated-intensified CCD (Charge Coupled Device) cameras in order to be used for the OTR monitoring. The segmented dump monitors the energy and the energy spread as a function of time.

This chapter introduces the specifications of the building blocks for the PHIN photoinjector. The details of the instruments are presented. The tolerances and the resolutions are discussed.

During the PHIN commissioning studies, sizeable amounts of data had to be acquired for various systematic measurements. A set of MatLab data acquisition scripts has been developed for the automation of the measurements. The package also has offline analysis components and is called “PHINEMA”. This data acquisition and analysis software is presented in this chapter.

4.1 Photocathode

For the PHIN photoinjector, the electron production is based on the photoemission of the electrons from a semiconductor surface, illuminated by laser pulses with the repetition rate of 1.5 GHz . In this section, the electron production process by using a photocathode is described in addition with the other electron emission mechanisms. The preparation of the Cs_2Te photocathodes for the PHIN photoinjector is summarized.

4.1.1 Electron Emission: Thermionic, Field-Emission, Photo-Emission

Electrons can be extracted from a metallic or semiconductor surface by heating the emitter surface, or applying high electric fields in the vicinity of the emitter surface which cause a decrease of the potential barrier for the electron emission. Another method is the illumination of a cathode by the laser pulses to employ the photoemission process. These electron emission methods are briefly summarized in this section. For further details on the theory of the electron emission the references [74, 75] are given.

Thermionic Electron Emission

The extraction of the electrons from a metallic cathode by heating the emission surface is called the “thermionic emission”. The Richardson law, given in Eq. 37, describes the thermionic emission of the electrons as a function of the temperature of the emitter surface,

$$j_{TE} = c_3 T^2 \exp\left(-\frac{\phi}{k_B T}\right) \quad (37)$$

where j_{TE} , is the current density of the emitted electrons, c_3 is a constant, T is the temperature of the emitter surface, ϕ is the work function and k_B is the Boltzmann constant.

Field Emission

The phenomenon is explained by the Fowler-Nordheim (FN) theory [76]. The field emission is described within the quantum theory. Basically, the electron emission is assisted by the strong fields that are lowering the potential barrier of the surface. The current density of the extracted charge is given by Eq. (38),

$$J = CF^2 e^{-\beta/F} \quad (38)$$

where F is the electric field, C and β are the coefficients as a function of the surface properties. β is called the “field enhancement factor” and it is a measure of the local field, $E_{loc} = \beta F$, on the emission surface.

The β can be experimentally estimated by using the FW plot of $\ln(J/F^2)$ versus $(1/F)$.

Photoemission

The photoemission from the semiconductor surfaces has been described by a process of three stages [77]. In the first stage the electrons are excited to the conduction band by the laser photons. The second stage is the migration of the electrons to the first density state of the conduction band. This band is located at the final state energy of $E_f = 4.05 \text{ eV}$ for the Cs_2Te cathodes. Detailed studies on the photoemission properties of Cs_2Te cathodes can be found in reference [78]. In the third stage, the electrons that are overcoming the surface barrier escape to the vacuum with the kinetic energy, E_{kin} . In order to escape, electrons should gain the energy from the laser photons that is high enough to pass over the energy gap, E_G , and the electron affinity, E_A . The energy gap and the electron affinity for Cs_2Te are 3.3 eV and 0.2 eV , respectively. The sum $E_T = E_G + E_A$ is called the threshold energy. The kinetic energy of the electrons that are emerging from the semiconductor surface can be expressed by,

$$E_{kin} = E_f - E_T. \quad (39)$$

In the view of the above discussion, one can calculate the kinetic energy of the photo-emitted electrons from the Cs_2Te cathode of PHIN as $E_{kin} = 0.55 \text{ eV}$.

Moreover, the “effective” temperature of the electrons can be deduced in term of the kinetic energy E_{kin} as given in Eq. (40).

$$E_{kin} = \frac{3}{2} k_b T_e \quad (40)$$

Considering the kinetic energy of 0.55 MeV , the effective temperature is calculated as $\sim 4300 \text{ K}$ for the PHIN electrons that are emerging from the Cs_2Te cathode surface.

4.1.2 Cs_2Te Cathode Preparation for PHIN at CERN Photo-Emission Laboratory

The electrons of the PHIN photoinjector are extracted from a semiconductor Cs_2Te cathode, which is mounted on one end of a $2 + 1/2$ cell RF gun. The cathode has been developed by the CERN photoemission laboratory and they have demonstrated a lifetime to allow $> 100h$ run at a 3% quantum efficiency for a 262 nm laser wavelength [79]. Excellent vacuum conditions, $P \leq 10^{-11} \text{ mbar}$ can be obtained by applying a bake-out at 300°C to achieve this lifetime.

The cathodes are prepared by co-evaporation of Cs and Te on a copper plug. After the preparation, they have to be transferred from the photoemission laboratory to the experimental area. The cathode transfer chamber, the so-called “Transport Carrier” (or T.C.), is a mechanical device designed to receive and deliver up to four photocathodes,

under Ultra High Vacuum conditions (*U.H.V.*), from the photo-emission laboratory to the PHIN photo-injector.

Before the measurements at the PHIN set-up, a bake-out at 130°C has been done. The vacuum value of $\sim 3 \times 10^{-10}$ has been measured on the RF cavity without the RF and the beam. During the measurements a vacuum value of $\sim 10^{-9}$ mbar have been maintained in the existence of the RF and the beam.

4.2 Laser System

In order to provide the laser pulses for PHIN, initially a Nd:YLF oscillator produces laser pulses at a repetition rate of 1.5 GHz with an average power of $P = 10\text{ W}$ in a continues wave (CW) train.

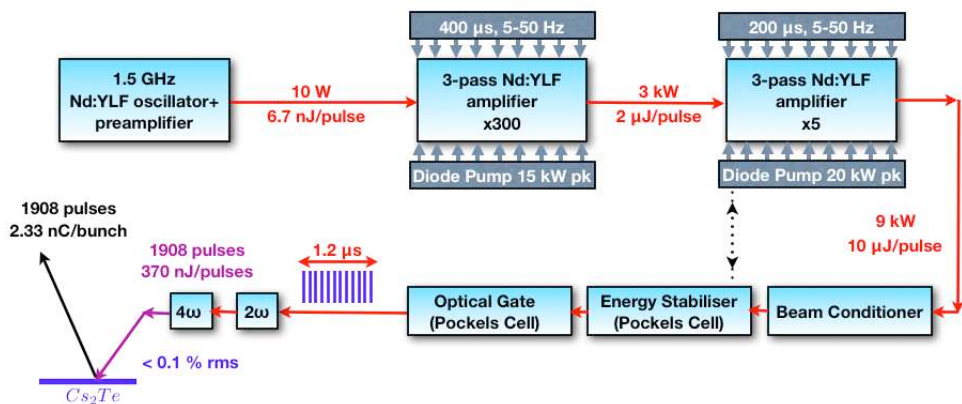


Figure 33: Layout of the laser system.

The layout of the laser is shown in Figure 33. In the layout, after the pre-amplification, two additional amplification stages follow in order to increase the laser power from 10 W CW power to 9 kW of quasi continues wave (QCW) mean power.

The length of the pulse train can be adjusted between 50 ns and $170\text{ }\mu\text{s}$ by using the Pockels cells [80, 81, 82]. The nominal pulse train length for the PHIN photoinjector is $1.27\text{ }\mu\text{s}$. The PHIN laser has been designed to produce pulse trains at a repetition rate of up to 50 Hz . A temporal structure that consists of a macropulse repetition rate of $1 - 5\text{ Hz}$ has been used during the measurements.

After the UV conversion the cathode is illuminated by the laser train of 1908 pulses ($1.27\text{ }\mu\text{s}$) at the wavelength of 262 nm and with the energy of 370 nJ/Pulse . This is the nominal energy in order to extract the bunch charge of 2.33 nC assuming the quantum efficiency of 3%. The laser spot size on the photocathode can be changed within a range of $0.1 - 5\text{ mm}$ (4σ). The micropulse width of $\sim 6.5 (\pm 0.41)$ ps (FWHM) has been measured for the UV laser.

During the commissioning runs a laser with the pulse train length of $200 - 1300\text{ ns}$ was used, alternatively, obtaining $300 - 1950$ bunches. The laser spot sizes of $2, 3, 4\text{ mm}$ have been used for different measurements as denoted in Chapter 5.

4.3 Design and Simulations for the PHIN RF Gun

The laser-driven PHIN RF gun consists of a $2 + 1/2$ cell normal conducting S-band standing wave cavity [73]. The gun has been designed by LAL and it has been installed on the PHIN beamline at CERN. The design has been based on a previous proto-type CERN RF gun. The previous design has been modified for the PHIN gun in order to provide the specifications that are needed by a possible CTF3 photoinjector. It has been optimised for the high charge by choosing an angle of 3.4° to the half-cell wall, around the photo-cathode, to provide additional transverse focusing with an RF gradient of 85 MV/m . Additionally, the shape of the iris was changed from circular to elliptical to decrease the surface electric field and therefore minimize the electrical breakdown and dark current levels. The specifications for the PHIN RF gun are summarized in the Table.23. The design of the RF gun aims to maximize the vacuum pumping speed which increases the dynamic vacuum. Therefore, a Non Evaporable Getter (NEG) thin film has been implemented on the wall of the anti-chamber that is placed around the cavity. A photograph of the PHIN RF gun is shown in Fig. 34.

Table 23: The design specifications for the PHIN laser-driven RF gun.

Parameter	Value
RF Frequency (GHz)	2.99855
RF Power (MW)	30
Gradient (MV/m)	85
Beam Energy (MeV)	5.5
Beam Current (A)	3.5
Charge / Bunch (nC)	2.33
Bunch Length (ps)	10
Energy Spread (%)	<1
Normalized Transverse Emittance (mm mrad)	<25
Pulse Length Duration (μs)	1.27
Vacuum Pressure (mbar)	2×10^{-10}

The π resonance mode is used for the acceleration in the PHIN RF gun which corresponds to a frequency of 2.99855 GHz . This mode has been presented in Fig. 35 from the result of SUPERFISH simulation program. The on-axis electric field that is excited on the cavity is presented in Fig. 36.

The first step of the SUPERFISH simulation studies is to define the geometry of the structure in the input file. The geometry of the RF gun has been defined in the SUPERFISH input file, as it is shown in Fig. 35, in order to simulate the field in the cavity. Once the geometry is defined, a “frequency scan” can be run in the SUPERFISH to calculate the modes that can be excited in the cavity. The simulation gives a $D(k^2) - f$ curve as the output, where D is the Dirichlet function, k is the wave number and f is the

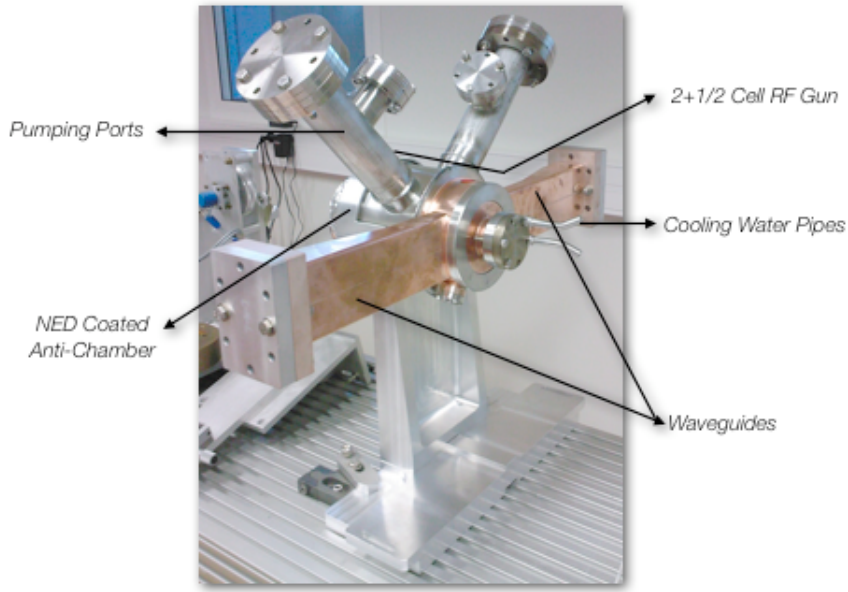


Figure 34: A photograph from the laser-driven PHIN RF gun that consists of a $2 + 1/2$ cell normal conducting S-band standing wave cavity.

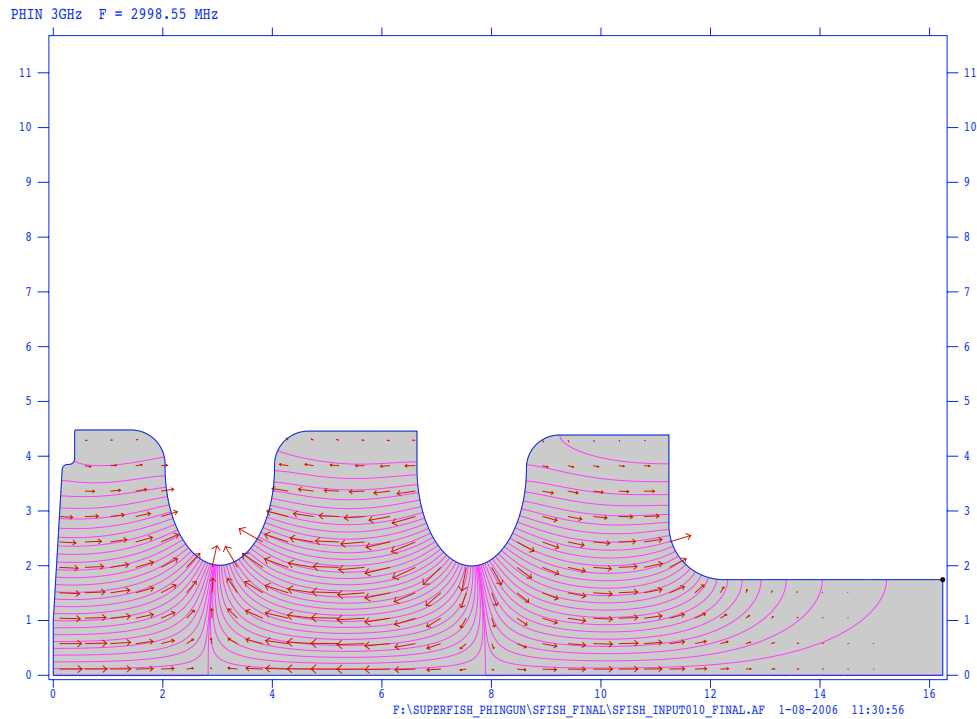


Figure 35: Illustration of the electric field in the cavity that is excited in the π -mode. The figure obtained as the result of the SUPERFISH simulation for the $2 + 1/2$ cell normal conducting S-band standing wave PHIN cavity.

frequency of the excited electromagnetic wave in the cavity. The frequencies, corresponding to $D(k^2) = 0$ where this curve has a slope of -1 , are the mode frequencies of the

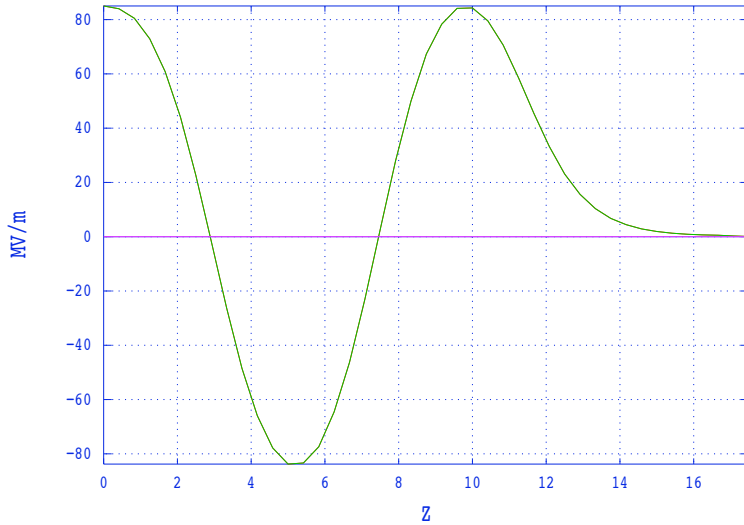


Figure 36: The on-axis electric field that is excited in the PHIN RF gun for the π mode.

structure. An example PHIN frequency scan result is shown in Fig. 37. The three of the resonance frequency modes can be recognized from the plot in the figure. The requested resonance frequency is chosen and the program is run once more by assigning the “starting frequency” as the required resonance frequency. As a result of the run a field map can be obtained in the text format. This map can be used as an input for the beam dynamics simulation programs such as PARMELA. An example SUPERFISH input file is shown in Fig. 38, that has been used for the PHIN RF gun simulations.

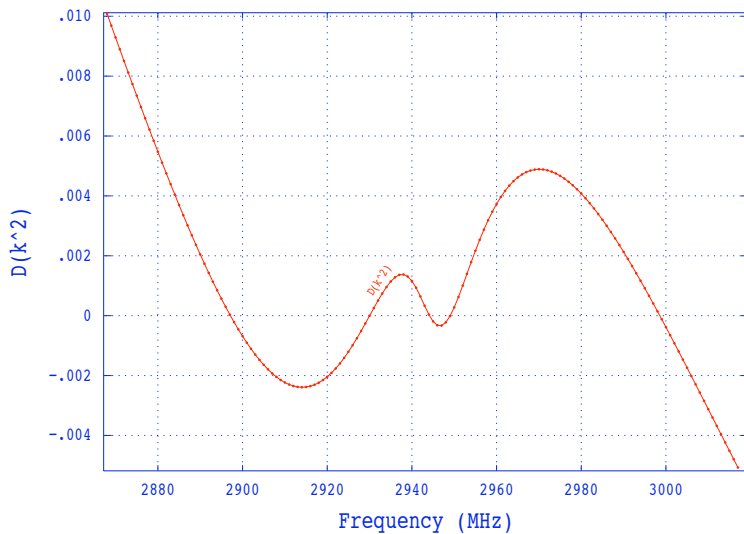


Figure 37: The result of the SUPERFISH frequency scan. The resonance frequencies for different modes are, 2897.15 MHz , 2944.15 MHz , 2998.55 MHz . The resonance frequency of 2998.55 MHz has been used for the PHIN RF gun, which corresponds to the π -mode.

```

PHIN 3GHz
&reg kprob=1, ; Superfish problem
dx=0.03,
freq=2998.55 , ; Starting frequency in MHz
dslope=-1, ; Allow convergence on first iteration
xdri=5.5,ydri=4.462 ; Drive point location&
&po x=0.0,y=0.0 &
&po x=0.0,y=1.0 &
&po x=0.163,y=3.75&
&po nt=2,x0=0.263,y0=3.75,x=0.0,y=0.1&
&po x=0.29,y=3.85&
&po nt=2,x0=0.29,y0=3.95,x=0.1,y=0.0&
&po x=0.39,y=4.4585 & ; tune for the first cell E field
&po nt=2,x0=0.41,y0=4.4585,x=0.0,y=0.02&
&po x=1.42,y=4.4785 &
&po nt=2,x0=1.42,y0=3.8585,x=0.62,y=0.0 &
&po x=2.04,y=3.7985&
&po nt=2,x0=3.04,y0=3.7985,A=1.0,B=1.79,x=1.0,y=0.0 &
&po x=4.04,y=3.8379161&
&po nt=2,x0=4.66,y0=3.8379161,x=0.0,y=0.62&
&po x=6.54,y=4.4579161 &
&po x=6.64,y=4.4579161&
&po x=6.64,y=3.7859161 &
&po nt=2,x0=7.64,y0=3.7859161,A=1.0,B=1.79,x=1.0,y=0.0 &
&po nt=2,x0=9.24,y0=3.7859161,x=0.0,y=0.6 &
&po x=11.24,y=4.3859161 & &po x=11.24,y=2.7459161 &
&po nt=2,x0=12.24,y0=2.7459161,x=0.0,y=-1.0 &
&po x=16.24,y=1.7459161 &
&po x=16.24,y=0.0 &
&po x=0.0,y=0.0 &

```

Figure 38: An example SUPERFISH input file for the PHIN RF gun for the π resonance mode.

The RF cavity can be considered as its equivalent *LCR* circuit and the Ohmic resistor parallel to this circuit is called the “shunt impedance” of the cavity. The shunt impedance is calculated in terms of the acceleration gradient, E_{acc} , the length of the cavity, L_c , and the dissipated power in the cavity, $P_{dissipated}$, as given in the Eq. (41).

$$R_{Shunt} = \frac{(E_{acc}L_c)^2}{P_{dissipated}} \quad (41)$$

Another figure of merit for an RF cavity is the “quality factor” of the cavity. It is defined as the ratio of the power delivered to the cavity and the dissipated power on the walls of the cavity in one cycle. Some of the parameters that are retrieved from the SUPERFISH calculations are shown in Table 24.

The RF gun is surrounded by two solenoids as shown in Fig. 39. The first solenoid is

Table 24: The PHIN RF gun properties that are retrieved from the SUPERFISH calculations.

Parameter	Value
Frequency (GHz)	2.99855
Operating Temperature ($^{\circ}\text{C}$)	20
Quality Factor, Q	14343.1
Shunt Impedance ($M\Omega$)	33.25
Peak Power Dissipation (kW)	4.9

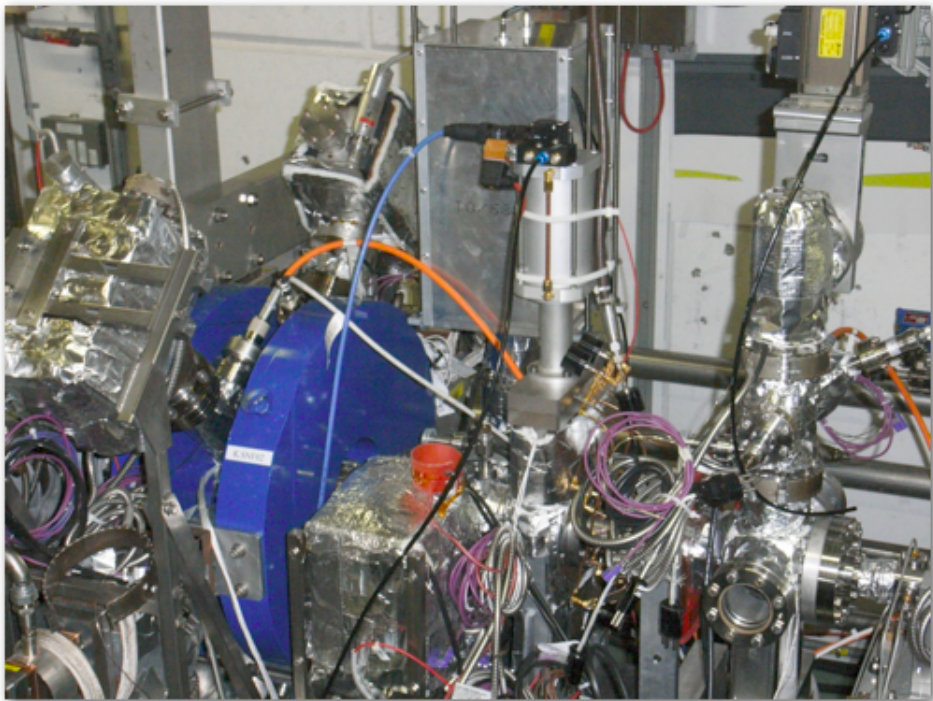


Figure 39: A view from the beamline including the PHIN RF gun and the solenoids that are installed at both ends of the cavity.

placed in the beginning of the cavity where the cathode is located. This solenoid is called the “bucking coil”. The function of the bucking coil is to compensate the magnetic field generated by the second solenoid and to ensure that the magnetic field on the cathode surface is zero. The magnetic field on the cathode surface should be zero in order to prevent the emerging particles from gaining transverse momentum. The initial transverse momentum of the particles cause an transverse emittance growth for the beam, therefore, it has to be avoided. The second solenoid in the system is called the “focusing solenoid” and it is used for the emittance compensation.

4.4 OTR Profile Monitoring for Beam Size, Emittance and Energy Measurements

The optical transition radiation (OTR) is emitted when a charged particle crosses a boundary with different dielectric properties. The radiation is emitted into the forward and the backward directions of the boundary surface. The corresponding electric field has two polarizations. These are the components that are parallel and the perpendicular to the observation plane. The total intensity of the emission is calculated as the sum of these two components. The intensity of the radiation per unit solid angle $d\Omega$ and per unit frequency $d\omega$ is given in Eq.(42), where q is the charge of the particle, γ is the relativistic Lorentz factor and θ is the angle between the normal of the surface and the direction of the emitted photons. The equation is an approximation under the condition that the boundary is a perfectly reflective metallic surface. More details on the OTR theory can be found in the reference [83].

$$I(\theta, \omega) = \frac{d^2W}{d\Omega d\omega} = \frac{d^2W_{||}}{d\Omega d\omega} + \frac{d^2W_{\perp}}{d\Omega d\omega} \approx \frac{q^2}{\pi^2 c} \frac{\theta^2}{(\gamma^{-2} + \theta^2)^2} \quad (42)$$

The angular distribution of the OTR intensity is presented in Fig. 40 for different electron beam energies. The maximum emission angle has been calculated as 2.7° for the 5.5 MeV electrons, according to the PHIN specifications. This result has been taken into account for the OTR profile monitoring systems on the PHIN beamline.

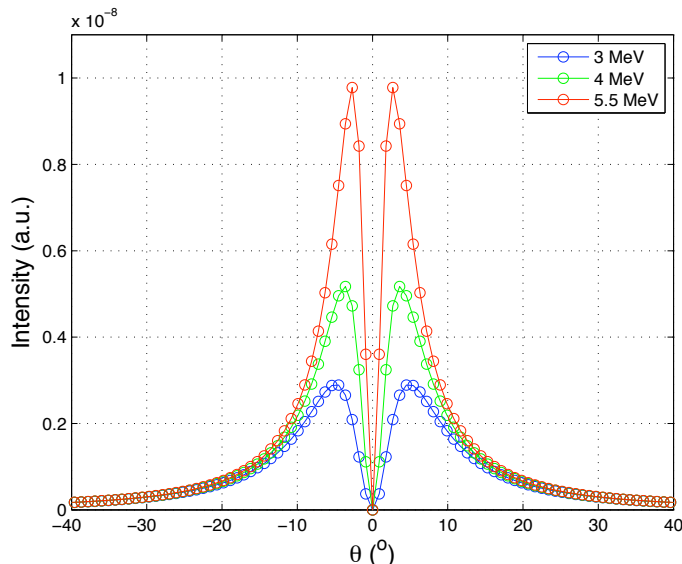


Figure 40: The intensity distribution of the OTR for different beam energies, according to the Eq. (42). For a beam with the 5.5 MeV energy, the detector can be placed with the optimum observation angle of 2.7° , with respect to the incident surface normal, in order to receive the maximum OTR intensity.

The schematic representation of the angular distribution of the backward OTR lobes is shown in Fig. 41. The OTR emission occurs in the backward and the forward directions of the screen, when the electrons, that are travelling in the vacuum, interact with the observation screen with different optical properties. In the PHIN OTR profile monitoring

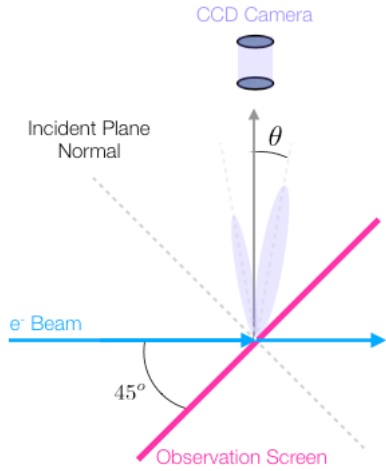


Figure 41: The schematic representation of the angular distribution of the backward OTR.

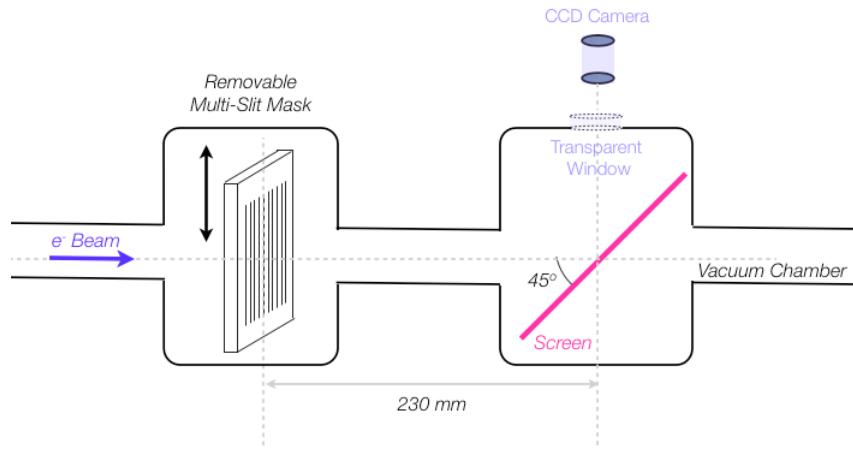


Figure 42: The illustration of the PHIN OTR profile monitoring system for emittance and beamsize measurements.

system the backward OTR emission is used. The backward emission is easier to image from the instrumentation point of view. To detect the backward OTR, the observation screen is placed inside the vacuum chamber with a 45° angle with respect to the direction of motion of the beam. Then, the detector is placed with an angle of 90° with respect to the beam axis as shown in the figure in order to image the backward OTR photons. The OTR is within visible range of the electromagnetic spectrum ($\sim 350\text{ nm} - 750\text{ nm}$). Therefore, an optical imaging device can be utilized as the detector, such as a CCD (charge coupled device) camera. The transmission of the radiation from the beam pipe to the camera is done via a transparent window. The layout of the PHIN OTR profile monitoring system is presented in Fig. 42. The system can be used both for the transverse emittance and the beamsize measurements. The so called multi-slit mask is used for the emittance measurement and will be described later. The system is configured to measure the transverse emittance when the mask is within the beam pipe. The mask is removed

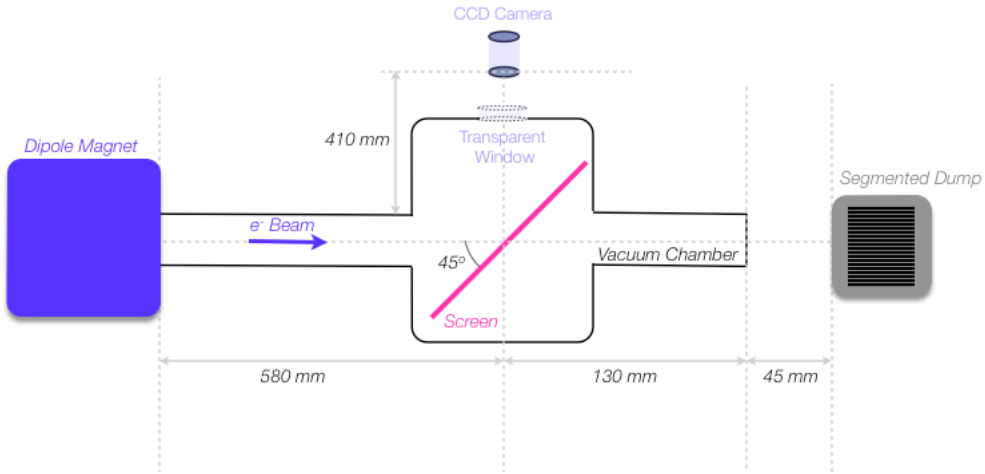


Figure 43: The illustration of the PHIN OTR profile monitoring system for energy and energy spread measurements.

in order to measure the beam size. The OTR profile monitor for the spectrometer line is shown in Fig. 43. A fixed aluminium observation screen with the thickness of $25\ \mu\text{m}$ is placed with the incident angle of 45° as shown in the figure. The beam travels through the aluminium screen and a vacuum window then reaches the segmented beam dump, which is another observation device for the time-resolved monitoring.

Several observation screens have been used for the PHIN OTR monitoring diagnostics. The aluminium, silicon and ceramic (alumina) thin radiator screens have been preferred, alternatively, according to the available OTR light intensity. Qualitatively, the ceramic screen is more sensitive than both the aluminium and the silicon screen while the latter two are similar in terms of the sensitivity. The system can host two different screens inside the vacuum chamber and the movements of the screens, as well as the multi-slit mask, are controlled by the control system software.

It is useful to shield the monitoring system in order to prevent the external-light perturbation. The background noise can be a problem for the OTR monitoring, especially when the OTR intensity is low. The photon yield can be as low as ~ 0.01 photons/electron. Additionally, a portion of the photons can be lost during the transmission. In this case, the quality of the image (signal/noise ratio) depends on the sensitivity of the CCD camera. A standard CCD camera can need thousands of photons per pixel in order to produce a significant signal. During the PHIN measurements an intensified-gated CCD camera has been used. The intensified camera has a high resolution image intensifier and it is up to 10^6 times more sensitive than the standard CCDs in order to image the low intensity light. The spectral sensitivity of the intensified CCD is from $180\ \text{nm}$ to $900\ \text{nm}$ covering the visible spectrum.

4.4.1 Emittance Measurement for Space Charge Dominated Beams: The Multi-Slit Method

The emittance of the PHIN beam has been measured using the multi-slit method. This method is applicable for low energy and space charge dominated beams [84, 85]. The

principle of the multi-slit method is to slice the beam transversely into beamlets, therefore the space charge effect becomes negligible during the measurements. The emittance in the slits position can be reconstructed from the beam profile measured after the multi-slits. After a drift section, the momentum distribution can be observed by imaging the beamlets from an OTR screen with a CCD camera. The first and second moments of the beamlets can be obtained from the measured profile, and used for the emittance calculation. The concept of the measurement is given in Fig. 44.

For the emittance measurements at the PHIN beamline, a 2 mm thick tungsten multi-slit mask was utilized. The mask has 25 slits with a width of 100 μm , spaced by 900 μm from centre to centre. A 25 μm thick aluminum OTR screen, at 45° incidence to the beam, was used in the system to image the beamlets after the slits. An intensified-gated CCD camera has been used to acquire the images.

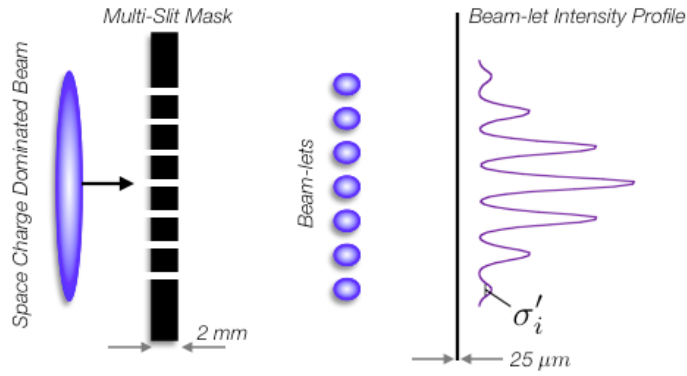


Figure 44: The concept of the emittance measurement with the multi-slit set-up at the PHIN photoinjector.

The following formulation shows the calculation of the transverse emittance by using the measured first and second moments of the beamlets. The distance between the slits on the slit mask is given as w and the distance between the mask and the observation screen is denoted as L . The intensities of the beamlets are taken into account and the intensity of the i th beamlet is represented as ρ_i . The correlated beam divergences are calculated by using the mean position of the beamlets, x_i , and the slit positions, $x_{i,c}$ as shown in Eq. (43). The spread in the divergence is given as Eq. (44) for the i th beamlet.

$$x'_{i,c} = \langle x_i - x_{i,c} \rangle / L = \langle x_i - iw \rangle / L \quad (43)$$

$$\sigma'_i = \sqrt{\langle x_i^2 \rangle / L^2 - (x'_{i,c})^2} \quad (44)$$

The phase space coordinates can be centered in both x and x' axis, by subtracting the overall value of the centroids as shown in Eq. (45) and Eq. (46). These coordinates will refer to their centered values for the rest of the calculations.

$$x_{i,c} = iw - \frac{\sum_{i=1}^N \rho_i iw}{\sum_{i=1}^N \rho_i} \quad (45)$$

$$x'_{i,c} = x'_{i,c}|_{old} - \frac{\sum_{i=1}^N \rho_i i w}{\sum_{i=1}^N \rho_i} \quad (46)$$

The transverse emittance is given as the Eq. (47). This equation can be rephrased in terms of the coordinates of the beamlets that created by a multi-slit mask. The substitution of the terms given in Eq. (48-50) leads to an expression Eq. (51) for the transverse emittance. The transverse normalized emittance, $\epsilon_{x,n} = \beta\gamma\epsilon_x$, is obtained by multiplying the geometric emittance with the relativistic Lorentz factor and the velocity of the electrons.

$$\epsilon_x \equiv \sqrt{< x^2 > < x'^2 > - < xx' >^2} \quad (47)$$

$$< x^2 > = \frac{\sum_{i=1}^N \rho_i x_{i,c}^2}{\sum_{i=1}^N \rho_i} \quad (48)$$

$$< x'^2 > = \frac{\sum_{i=1}^N \rho_i (x'_{i,c}^2 - \sigma_i'^2)}{\sum_{i=1}^N \rho_i} \quad (49)$$

$$< xx' > = \frac{\sum_{i=1}^N \rho_i x_{i,c} x'_{i,c}}{\sum_{i=1}^N \rho_i} \quad (50)$$

$$\epsilon_x \equiv \sqrt{\frac{(\sum_{i=1}^N \rho_i x_{i,c}^2)(\sum_{j=1}^N \rho_j x_j'^2) - (\sum_{i=1}^N \rho_i x_{i,c} x'_{i,c})^2}{(\sum_{i=1}^N \rho_i)^2}} \quad (51)$$

4.4.2 Optimization of a Multi-Slit Measurement System and the Design of the PHIN Emittance-Meter

The design of the multi-slit measurement set-up can be optimized in the guidance of some analytical, numerical and the mechanical considerations. In this section, some of the analytical criteria will be mentioned regarding the design of the PHIN multi-slit measurement set-up.

The discussions will be done in the frame of the four arguments on the multi-slit mask geometry: the beamlets after the multi-slit mask must be emittance dominated, the thickness of the multi-slit mask should be sufficient to stop the electrons [85], the overlap of the beamlets on the observation screen should be minimized and, the position and the divergence resolution of the system must be comparable [86].

For the first argument, one can consider the forces governing the beam envelope behavior. The evolution of the *rms* beam envelope is given by the invariant envelope equation as shown in Eq. (52) [87], specifically for the RF photoinjectors as in this example

and in general for any space charge dominated relativistic beam that is accelerated in high gradients. In the equation, the 3rd, 4th and 5th terms represents the focusing force due to the external focusing channel and the defocusing forces due to the space charge and the transverse normalized emittance, respectively.

$$\sigma'' + \sigma' \left(\frac{\gamma'}{\beta^2 \gamma} \right) + K_r \sigma - \frac{\kappa_s}{\sigma \beta^3 \gamma^3} - \frac{\epsilon_n^2}{\sigma^3 \beta^2 \gamma^2} = 0 \quad (52)$$

In the above equation, σ is the *rms* transverse beam size, β is the normalized beam velocity and γ is the relativistic Lorentz factor. The strength of the linear focusing is represented by K_r while κ_s is the beam perveance and ϵ_n is the transverse normalized beam emittance. The perveance is the proportionality constant between the space charge dominated beam current and the gun anode voltage, e.i., it is a measure of the space charge force.

In general, the dominant defocusing force is the space charge force, for the high brightness beams. Therefore, emittance measurement should be done by using a technique which takes into account this effect. The multi-slit or pepper-pot methods are widely and successfully used for the low energy, space charge dominated beams. The multi-slit method has been implemented on the PHIN beamline. According to the multi-slit emittance measurement method, the individual beamlets must be emittance dominant after the multi-slit mask. Therefore, in order to benefit from the method, the design of the set-up must ensure emittance dominant beamlets after the mask. According to Anderson's study, the ratio between the space charge force and the transverse normalized emittance after the multi-slit mask is given as Eq. (53),

$$R' = \frac{2I}{\gamma^2 I_0} \frac{wL}{d\epsilon_n} \quad (53)$$

where d is the distance between the neighbouring slits, w is the width of the slits and L is the distance between the multi-slit mask and the observation screen, I is the peak beam current, I_0 is a constant called the Alfen current with the value of 17 kA . The ratio, R' , should be less than unity in order to confirm the emittance dominant beamlets after the multi-slit mask.

Consequently, the ratio between the defocusing of the space charge and the emittance is calculated as $R' = 0.53$, indicating that the space charge contribution to the transverse momentum is insignificant for the individual beamlets. Therefore the beam is totally emittance dominated after the multi-slit mask, fulfilling the measurement principle.

The second argument is related with the choice of the multi-slit mask thickness. In order to determine the thickness of the mask one should consider the passage of the electrons in tungsten. The electrons should be stopped or scattered sufficiently within the mask which causes a flat background that can be removed during the data analysis. The stopping distance of the electrons in a tungsten slab is calculated with respect to the Eq. (54) where the $\rho = 19.25\text{ g cm}^{-3}$ is the density of tungsten and E is the energy of the electrons. The stopping power for the electrons in a tungsten has been retrieved from the well-described "Bethe-Bloch" plot as $1.5(\text{MeV cm}^2\text{ g}^{-1})$.

$$L_s = \frac{E}{\frac{dE}{dx}} \approx \frac{E(\text{MeV})}{1.5(\text{MeV cm}^2\text{ g}^{-1})\rho(\text{g cm}^{-3})} \quad (54)$$

The stopping distance of the tungsten slab for the 5.5 MeV electrons is calculated as 1.9 mm . Therefore, a tungsten mask with the thickness of 2 mm is fairly sufficient to stop the 5.5 MeV electrons of PHIN.

The third argument states a criterion in order to prevent the beamlets from overlapping on the observation screen. According to this criterion, the divergence resolution of the multi-slit mask should be, at least, a factor of four larger than the typical beam divergence. That is given in Eq. (55).

$$4\sigma' < \frac{d}{L} \quad (55)$$

The distance between the slits has been chosen as 0.9 mm and the screen has been placed at a distance of 230 mm from the multi-slit mask, within the availabilities of the PHIN beamline. Therefore the set-up is able to monitor the beam-lets without any overlap for the beam divergences up to $\sim 0.9\text{ mrad}$. Although, there will be certain overlaps on the profile of the beamlets above this value, the fitting of the profiles have not been disturbed for the PHIN operation conditions.

According to the fourth argument, the position and divergence resolution should be comparable for the set-up. This is phrased in Eq. (56),

$$\frac{\sigma}{d} = \frac{\sigma'}{(r_d/L)} \quad (56)$$

where r_d is the resolution of the detector and its value is $100\text{ }\mu\text{m}$ (**to be confirmed by proxitronic (pixel resolution X magnification)**) for the camera used for the set-up. These specifications give a position resolution of $\sigma/d = 1.7$ and a divergence resolution of $\sigma'/(r_d/L) = 6.9$, for the typical beam size of $\sim 1.5\text{ mm}$ and the typical divergence of $\sim 3\text{ mrad}$. Therefore, the measurement system provides for both the beam position and the divergence resolutions in the same order of magnitude.

As a summary, the design specifications of the PHIN multi-slit emittance measurement set-up is given Table (25).

Table 25: The design specifications of the PHIN multi-slit emittance measurement set-up.

Parameter	Value
Multi-Slit Mask Material	Tungsten
Thickness of the Mask (mm)	2
Mask-Screen Distance (mm)	230
Slit Width (μm)	100
Inter-Slit Distance (μm)	900
Screens	Aluminium/Silicon/Alumina
Detector	Intensified-Gated CCD Camera

The resolution of the emittance measurement system can be estimated with respect to $\epsilon_n = \gamma\sigma'\sigma_0$, where σ' is the beam angle associated to the finite beam emittance. One can

introduce the formula in Eq. (57) by using the criterion in Eq. (55).

$$\epsilon_n = \frac{\gamma\sigma_0 w}{5L} \quad (57)$$

By considering the above equation, PHIN multi-slit mask set-up can resolve the normalized transverse emittance values down to 1.5 mm mrad .

4.4.3 Magnetic Spectrometer

A magnetic spectrometer has been installed on the beamline in order to measure the energy and the energy spread [88]. The working principle of the magnetic spectrometer consists of the measurement of the beam momentum distribution after a dipole with a known magnetic field. The momentum of a particle which is deflected by an angle α_{tot} under the effect of the uniform magnetic field B_z can be calculated from Eq. (58) where s is the direction of movement of the beam. The integral in the equation is over the effective magnet length. The energy of the particle with a momentum, p , is given by Eq. (59). In addition, for the particles at relativistic energies, since $\gamma \gg 1$, the equation can be simplified as in Eq. (60).

The set-up for the PHIN spectrometer is presented in Fig. 45. It consists of a dipole magnet with a bending angle of 90° . An OTR profile monitor and a segmented-dump have been installed after the dipole, in order to image the beam. The OTR profile monitor is equipped with an aluminium radiative screen and an intensified-gated CCD camera. The single shot measurements of the beam is possible with the OTR profile monitor. In addition, the time-resolved characterization of the beam can be done by using the adjustable gate duration property of the CCD camera. Furthermore, the segmented dump is a device which is designed and implemented for the time-resolved energy measurements of PHIN. More details of the segmented-dump will be given later in this chapter.

$$p = \frac{e}{\alpha_{tot}} \int_{path} B_z ds \quad (58)$$

$$E = \sqrt{p^2 c^2 + (m_0 c^2)^2} \quad (59)$$

$$E = pc = \frac{ec}{\alpha_{tot}} \int_{path} B_z ds \quad (60)$$

The integral in the above equation is calculated by using the magnetic map of the spectrometer magnet [89]. The measured field distribution is presented in Fig. 46. The figure (a) presents the 3D intensity distribution of the magnetic field generated by the spectrometer magnet. Whereas a contour plot is given in the figure (b) including the beam path. This distribution is used to integrate the field along the beam path. The result has been found as $\int_{path} B_z dl \approx 545 \times 10^{-4} \text{ T.m}$ for a magnet current of 19.92 A .

A practical relation between the beam energy and the current of the spectrometer dipole is given in Eq. (61). In the equation, I_{Dipole} is the total spectrometer dipole current that is needed in order to focus the beam in the longitudinal axis, e.i., in the middle of the OTR screen. The OTR profile of the beam is analyzed and the energy corresponding to the peak of the profile is determined as shown in Eq. (62). In the equation, μ_x denotes the

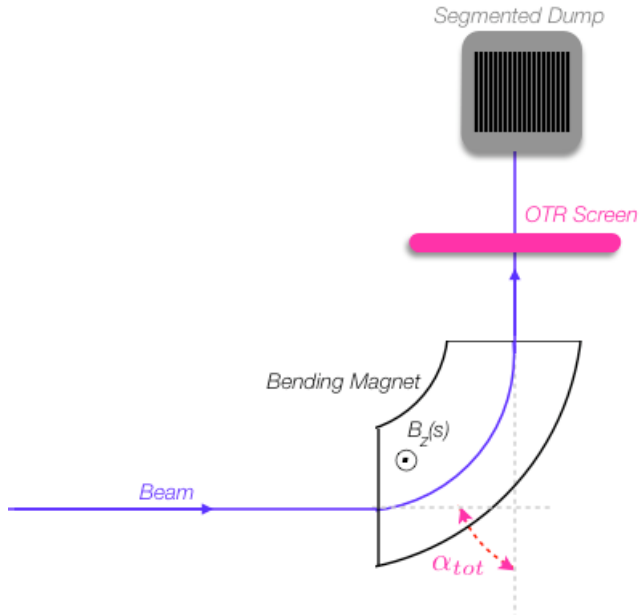


Figure 45: The implementation of the magnetic spectrometer on the PHIN beamline.

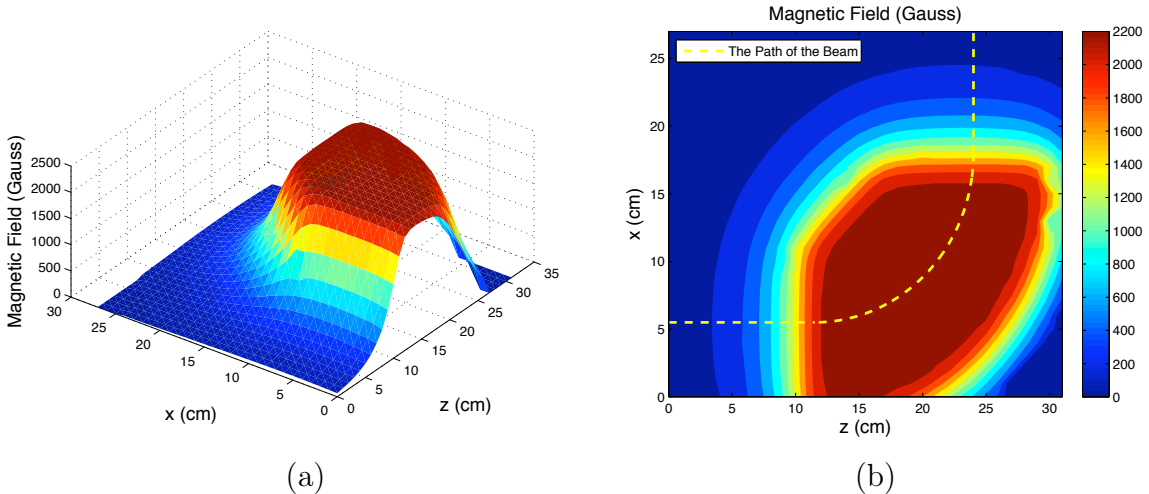


Figure 46: a) The magnetic field intensity distribution of the spectrometer dipole. b) The same distribution can be represented with a contour plot. The path that the beam follow is denoted with the “yellow” line.

distance between the position of the peak of the profile and the centre of the screen. The energy spread is retrieved by using the 1σ width of the distribution, σ_x , in the units of millimeter. The calibration relations are given in the Eq. (62) for the energy at the peak of the profile and in the Eq. (63) for the energy spread. The dispersion at the position of the observation screen has been calculated as 840 mm and used in the formulas.

$$E_0[\text{MeV}] = 0.52 \times I_{\text{Dipole}}[\text{A}] \quad (61)$$

$$E_{\text{peak}}[\text{MeV}] = E_0[\text{MeV}] + \frac{\mu_x[\text{mm}]}{840[\text{mm}]} E_0[\text{MeV}] \quad (62)$$

$$\Delta E[\text{keV}] = 10^3 \times E_{\text{peak}}[\text{MeV}] \times \frac{\sigma_x[\text{mm}]}{840[\text{mm}]} \quad (63)$$

4.5 Instruments for the Time Resolved Measurements

4.5.1 Specifications of the Intensified-Gated CCD Camera

The Proxitronic CCD camera has been used for the time-resolved OTR profile monitoring systems in the beamline. The camera and its digital control box unit are shown in Fig. 47. It includes a fiber optically coupled image intensifier unit which provides a light sensitivity order of magnitudes higher than conventional CCD cameras. Therefore, the camera is capable of operating with very low light conditions. Because if its high sensitivity, the camera has to be operated in a dark room. Before turning on the camera, the gain and the exposure (gate) duration always set to their minimum values in order to protect the instrument.

The spectral sensitivity of the CCD cameras are classified according to the type of their photocathodes. Fig. 48 shows the spectral response characteristics of the intensified CCD camera for different photocathode types. In the figure the curve which is labelled as “T” belongs to the camera that has been used in the PHIN measurements. This corresponds to a “UV enhanced S 20/quartz” type photocathode.



Figure 47: The Proxitronic CCD camera and its digital control box unit that are used in the PHIN measurements.

The timing properties of the camera provides the necessary flexibility for the unique PHIN time-resolved measurements in the nanosecond range. The camera has an exposure duration which can be reduced down to 100 ns that enables to measure the beam properties along the bunch train in the steps of 100 ns . The camera timing can be externally triggered and it has been synchronized with the laser timing for the measurements.

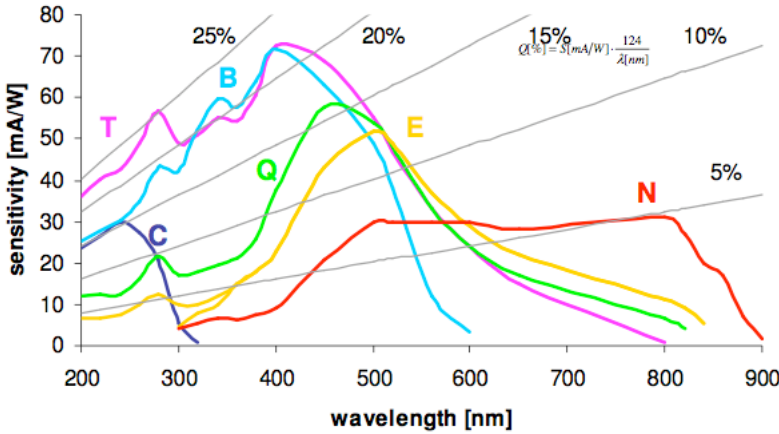


Figure 48: The spectral response characteristics of the intensified CCD camera for different photocathode types.

Therefore the intensified camera shutter has been synchronized to the beam itself. All the camera controls and the adjustments are done via a digital control box unit (DCU). The DCU gives remote access to all camera settings such as the gain, exposure duration, gate delay, power on/off of the camera. Therefore, the camera can be operated remotely from the location that it has been installed. More details on the technical specifications of the camera can be found in the operation manual [90].

Regarding the implementation on the beamline, the camera has been placed with an angle of 2.7° in order to receive the maximum OTR intensity from the screen. In addition, during a typical PHIN run, the gain of the camera has been adjusted according to the available light intensity. The light intensity can be higher or lower according to the type of the OTR screen in the system, the exposure duration, the bunch train length of the beam and the charge per bunch value of the beam. Higher gain values have been needed due to the light reduction by the introduction of the multi-slit mask. A camera gain of 35% has been used with a combination of aluminium OTR screen for the emittance measurements of the $1.2\mu\text{s}$ long bunch train. Whereas a gain of 10% is sufficient for the beam size measurements where the whole beam is available for the beam size measurement. Similar to the transverse phase space monitoring, the typical gain values of 10 – 30% have been used for the spectrometer OTR monitoring system.

4.5.2 Segmented Dump for the Energy Measurements

A segmented beam dump has been installed in the end of the PHIN beamline. This device enables to measure the energy and the energy spread in a time-resolved manner. It consists of 20 parallel stainless steel segments which are insulated from each other by epoxy resin insulators. The design of the segmented dump has been done in the guidance of several simulations regarding the electron beam interactions with the dump material. The beam dynamics simulations also have been used in order to investigate the cases with different beam properties. The GEANT4 and PARMELA programs have been used for those studies, respectively. The detailed information on the design and development of the segmented dump can be found in [88, 91].

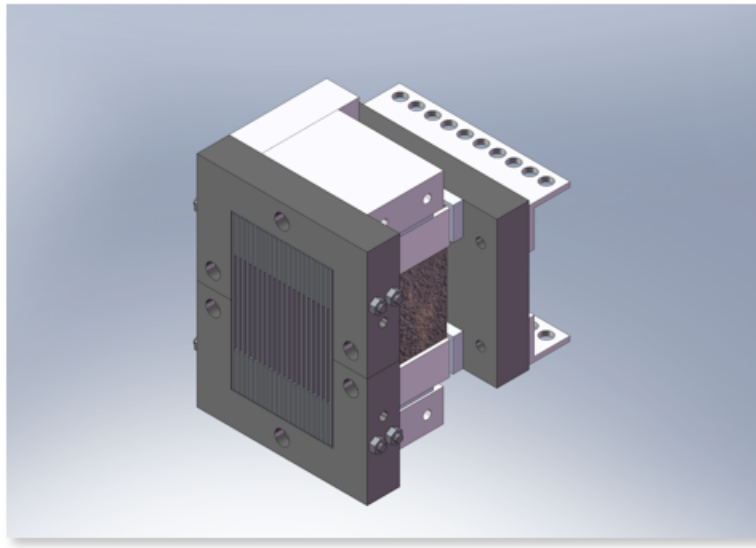


Figure 49: A drawing of the 20 channel segmented dump that has been used for the time resolved energy and energy spread measurements of the PHIN photoinjector.

A drawing of the segmented-dump that has been used during the measurements at the PHIN beamline is presented in Fig. 49. Before the beam arrives to the segmented dump, it travels through the fixed OTR screen and a aluminium vacuum window in the dispersive section of the beamline. A $25\mu m$ thick aluminized Mylar foil has been used as the OTR screen in order to decrease the broadening due to multiple scattering inside the screen. The screen has been found to broaden the beam size around 17.9%. The measurements with the segmented dump have been possible after taking into account this effect. The multi scattering inside the segmented dump is negligible within the PHIN energy regime. The measurements are done by monitoring the signal from the each segment. This signal originates from the energy deposition on the segments by the electron beam.

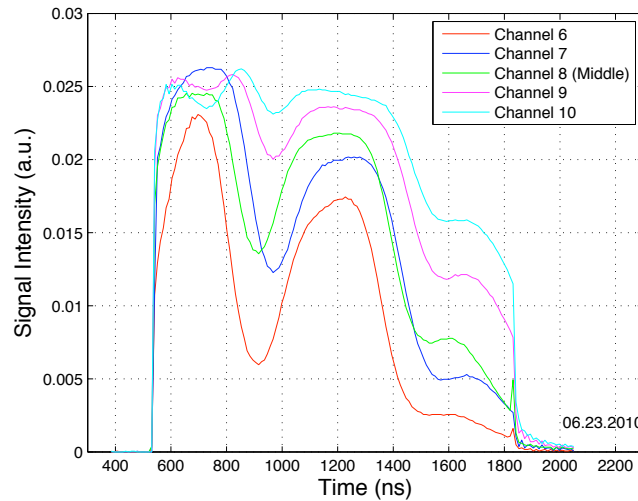


Figure 50: The signals from the segmented dump.

4.6 Automated Software for the Measurements

A collection of MatLab [92] scripts has been developed in order to perform the data acquisition and the analysis for the beam measurements of the PHIN photoinjector. The collection can be divided into three parts. These parts are the data acquisition, offline analysis and the library. The different parts and their ingredients are shown in Fig. 51.

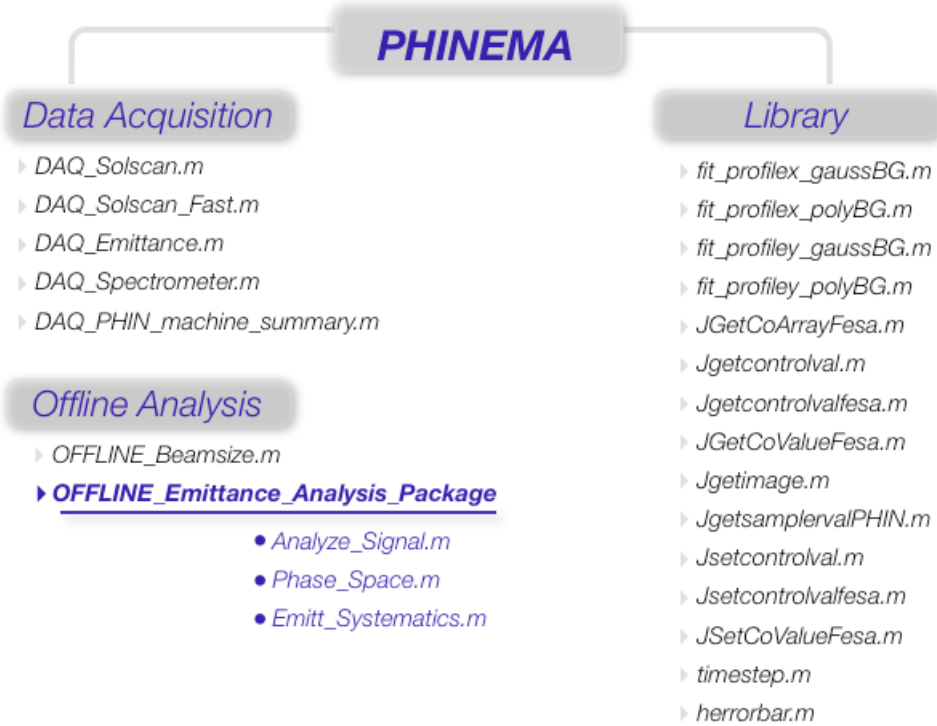


Figure 51: The collection of software in order to perform the data acquisition, online and offline analysis for the PHIN measurements.

The data acquisition part includes the programs that are interacting with the instrumentation, collecting the required data and if necessary setting new values for the system variables. For example, the acquisition software is responsible to read the data from the CCD cameras, set and get the values of the dipole, focusing and the corrector magnets on the system in order to perform the measurements. Consequently, the acquisition software is automated and is able to perform the set of systematic measurements within a user-defined range and initial parameters. The programs that are performing the beam size measurements are “DAQ_Solscan.m” and “DAQ_Solscan_Fast.m” as a function of the focusing. The latter is used to only collect the sizable amount of data without any online analysis. The “DAQ_Emittance.m” is the program that is used to scan the emittance values over a range of the focusing in order to study the emittance compensation for a space charge dominated beam. The “DAQ_Spectrometer.m” is used for the energy and energy spread measurements in the spectrometer as well as performing the time-resolved OTR profile monitoring. Eventually, a separate program has been developed in order to read all the system variables in a single shot, such as the magnets, CCD cameras, klystron voltage and phase, segmented dump signals, RF power inside the cavity and the laser profile. This program is called the “DAQ_PHIN_machine_summary.m” and has

been used effectively to acquire all the information regarding the beamline at a particular time. For each measurement, these recorded values are used as the input parameters for the PARMELA simulations.

The offline analysis tools are needed in order to study the stored data after a particular measurement is performed. Some parts of the energy measurements and all of the emittance measurements are analyzed offline. Because, the analysis of these measurements require special data treatment, such as the background subtraction, user interaction during certain stages of the analysis etc. There is an additional program called “OFFLINE_Beamsize.m” in the package. This enables a beam size scan data to be analyzed offline.

The essential component of the offline analysis part is the data analysis program for the emittance measurements. “OFFLINE_Emittance_Analysis_Package” hosts three programs. The main program of the package is “Analyze_Signal.m”. This program is responsible to process the OTR images of the beam after the multi-slit mask. This process includes the selection of a region of interest in the OTR image, producing the projection of the image on the requested axis and the noise subtraction from the resulting profile. The first and the second moments and the weighted intensities of the individual beamlets are needed for the emittance calculation as previously described in the section 4.51. These values are determined by this program by several fitting procedures. There are additional algorithms for several treatments up to the retrieval of the final values. These will be explained in Chapter 5. After the determination of the fit values, the “Analyze_Signal.m” calls the “Phase_Space.m” subroutine. This subroutine runs the emittance calculation algorithm that is given above and finalizes the emittance calculation. The phase space is also reconstructed by this subroutine. The transverse normalized emittance and related information for each beamlet are returned to the main program, “Analyze_Signal.m”. Finally, “Emitt_Systematic.m” is called in order to calculate the systematic error on the single shot emittance measurement. The details of the systematic error calculation and several results are presented in Chapter 5.

The library for the PHIN software includes several auxiliary programs. There are two groups of fitting routines for processing Gaussian and polynomial backgrounds of the beam profiles, separately. The proper profile fitting routine is defined by the user according to the behavior of the data. The programs that are starting with “Jget” or “Jset” are specific for particular device classes in the CERN control system. They are used to read and set the values of the corresponding devices.

5 Experimental Results of the PHIN Commissioning

Contents

5.1 Charge Production	86
5.2 Beam-Loading Compensation	91
5.3 Transverse Phase Space	91
5.3.1 Beam-Size Measurement Results	92
5.3.2 Data Analysis Techniques for the Transverse Emittance Measurements	96
5.3.3 Systematic Error Calculation for the Emittance Measurement	102
5.3.4 Emittance Measurement Results	105
5.4 Time-Resolved Transverse Characterization of the Beam	108
5.4.1 Beam size along the Pulse Train of 1.2 μ s	108
5.4.2 Emittance along the Pulse Train of 1.2 μ s	109
5.5 Longitudinal Phase Space	115
5.6 Time-Resolved Longitudinal Characterization of the Beam	116
5.7 Correlation Between the PHIN Laser Beam and the Electron Beam	119
5.8 Conclusions and The Post-Commissioning Activities for PHIN	121

The PHIN photoinjector has been designed to deliver a $1.3 \mu\text{s}$ long bunch train containing 1908 bunches with 2.33 nC charge per bunch. It is equipped with a $2 + \frac{1}{2}$ cell RF gun that supplies 85 MV/m gradient at 3 GHz . In addition to the RF gun, a beam diagnostics section has been installed on the beamline. This section consists of the beam position and current monitors, OTR screens and CCD cameras for OTR profile monitoring, multi-slit mask for emittance measurements and a spectrometer with an additional segmented-dump. These diagnostics have been used for systematic measurements of the beam parameters within a wide range.

The PHIN photoinjector has been commissioned with the intermittent runs between 2008 and 2010 with a total beam time of 60 workdays. The operation timetable is given in Table 26. The studies led to an eventual success by fulfilling the design specification which are given in Table 27. The table will be updated with the achieved parameters in the end of the chapter. In this chapter, several commissioning items are presented from charge production to the transverse and the longitudinal characterization of the PHIN photoinjector.

Table 26: PHIN Commissioning timetable.

Year	Period	Beam Time
2008	06 November - 14 November	7
2009	11 March - 24 March	10
2009	23 September - 16 October	18
2010	15 February - 03 March	13
2010	14 June - 29 June	12

Table 27: The specifications for the PHIN photoinjector.

Parameter	Specification
<i>Laser</i>	
UV Laser Pulse Energy (nJ)	370
Micropulse Repetition Rate (GHz)	1.5
Macropulse Repetition Rate	1-5
Train Length (ns)	1273
<i>Electron Beam</i>	
Charge per Bunch (nC)	2.33
Charge per Train (nC)	4446
Current (A)	3.5
Transverse Normalized Emittance (mm mrad)	< 25
Energy Spread (%)	< 1
Energy (MeV)	5.5
Charge Stability (% rms)	< 0.25
<i>RF Gun</i>	
RF Gradient (MV/m)	85
RF Frequency (GHz)	2.99855
Cathode	<i>Cs₂Te</i>
Quantum Efficiency (%)	3

5.1 Charge Production

The charge measurements have been done by using either the fast current transformer (FCT) or the Faraday cup (FC) that are installed in the set-up. The signals have been displayed by a scope. The total charge production is measured as the integral of the signals. The charge per bunch value is obtained by dividing the total charge value by the number of bunches in the bunch train. The integration of the signals are measured as the mean value of several shots in the units of nVs or μVs . The practical formulas for the

conversion, from the readouts of the FCT and the FC to nC , are shown in Eq. (64) and in Eq. (65), respectively,

$$Q_{FCT}(nC) = \frac{I(nVs) \times \text{Attenuation}(dB)}{\sigma_{FWHM}^L(ns) \times 1.5GHz} \quad (64)$$

$$Q_{FC}(nC) = \frac{I(nVs) \times \text{Attenuation}(dB)}{50\Omega \times \sigma_{FWHM}^L(ns) \times 1.5GHz} \quad (65)$$

where, I denotes the scope readings, σ_{FWHM}^L is the length of the laser pulse train and $1.5GHz$ is the constant micropulse repetition rate that is used during the commissioning. An external attenuation of 10dB or 20dB has been used according to the signal intensity in the input of the scope. A purely resistive, 50Ω , characteristic scope impedance has been used while probing the FC signals from the analog to digital converters (ADCs) to prevent the signal reflections.

The examples of the charge measurement is shown in Fig.52 where the measurement instrument is a FCT and a FC, respectively. The signals from these current monitors are integrated as shown as the “current” variable in the “Measurements” tab. The scope reading is $344.4 (\pm 27.1) nVs$ for FCT and $14.4 (\pm 0.51) \mu Vs$ for the FC. According to the equations that are given above, the charge values of $1.7 (\pm 0.14) nC$ and $1.5 (\pm 0.05) nC$ are calculated for the FCT and the FC, respectively, for this particular case. The difference between two readings corresponds to the amount of charge which is lost during the transmission up to the FC. In addition, this beam loss is one of the reasons for the distortion in the shape of the signal from the Faraday cup.

In the most of the charge measurements, the FCT has been preferred due to its location just after the RF gun. Nevertheless, the FC is the most useful in order to study the charge transmission along the downstream of the beamline.

The charge production characteristics have been studied, systematically. In principle, the amount of the charge produced by the photoemission increases with the laser energy per pulse. In Fig. 53-a a charge measurement is presented in order to demonstrate this behavior. The measurement reveals a region where the charge yield increases linearly with the laser energy per pulse. This linear region continues up to the energies of $200 nJ$. In a certain point the slope of the curve decreases and finally the increment converges to a maximum extractable charge value. This region is called the “saturation region”. The saturation of the photoemission has been showed to be an effect related to the micro pulse energy. This can be better seen in accordance with the measurement shown in Fig. 53-b, where the laser micro pulse energy has been kept constant at $420 (\pm 17) nJ$. During the measurement, no saturation has been observed in the integrated charge over the pulse train with respect to the increasing integrated laser pulse train energy with the increasing laser pulse train length.

In this case, the maximum charge yield of $4.4 nC$ per bunch has been achieved, even exceeding the PHIN specification of $2.33 nC$. The experimental value agrees the theoretical limit for the maximum achievable charge per bunch. In Chapter 3, the theoretical value has been calculated as $4.7 nC$, for the gradient of $85 MV/m$ and the laser spot size of $1 mm$, regarding the PHIN specifications.

Besides the photoemission, the field emission is an inevitable phenomenon in an RF gun due to the existence of high RF fields in the vicinity of the cathode. A measurable



Figure 52: A snapshot from the scope during the operation with an electron pulse train of 1300 ns . The yellow signal in Channel 1 belongs to the FCT which is located at the exit of the RF gun. The green signal in Channel 2 has been acquired from the FC which is located after the spectrometer magnet at the end of the beamline.

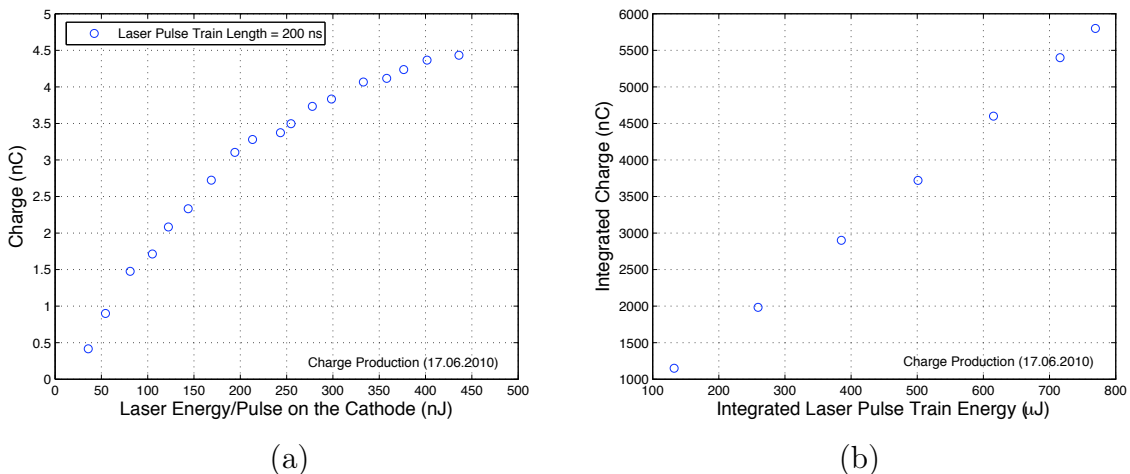


Figure 53: a) Saturation of the photoemission of the electrons with the increasing laser energy per pulse. b) The linear behavior of the photoemission in terms of the integrated charge and the laser energy over the pulse train.

charge is emitted from the cathode under the effect of the RF field. In Fig. 54, this quantity has been presented with respect to the increasing surface electric field and when no laser is present. This charge can be as high as 0.6 nC in the nominal PHIN RF power value of 30 MW . In Fig. 54-a, the measurement of the field emission is presented as a

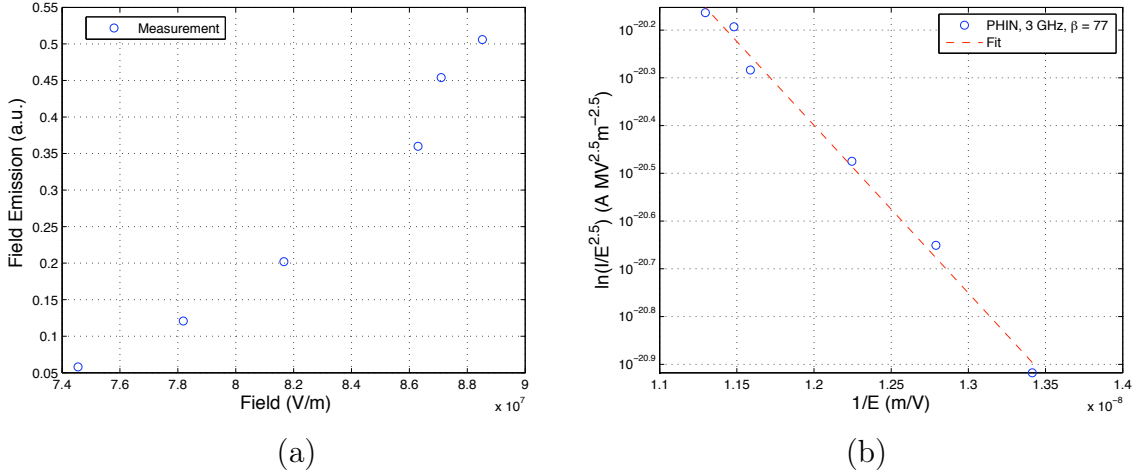


Figure 54: The field emission. a) The emission increases proportional to the square of the field. b) The Fowler-Nordheim analysis for the field emission. The field enhancement factor β , for 3 GHz PHIN gun has been deduced as 77 from the slope of the curve.

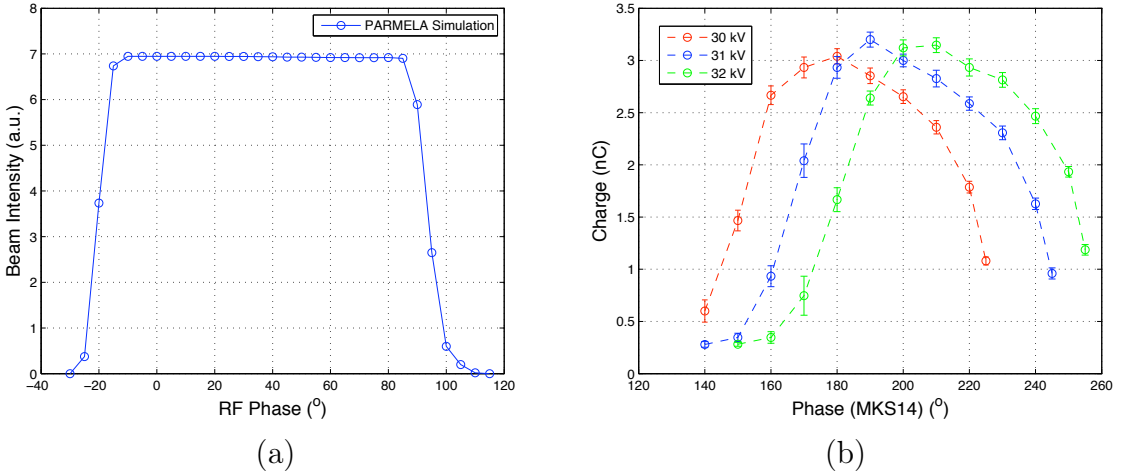


Figure 55: The field emission. a) PARMELA simulation presents the beam intensity change with respect to the RF phase, by taking into account the photoemission only. b) The measured charge production as a combination of the photoemission and a ‘Schottky-like’ field emission effect.

function of the field. This emission increases with the increasing RF field, as expected. Moreover, the data can be plotted in a Fowler-Nordheim representation. The Fowler-Nordheim (FW) analysis of the field emission [93] for 3 GHz PHIN RF gun is shown in Fig. 54-b. According to the FW theory the slope of the curve, that is plotted in the figure, can be used to calculate the field enhancement factor, β , for the emission surface. The field on the emission surface is perceived as increased by a factor of the enhancement value and, is given as $E_{loc} = \beta E$, where, E is the RF field and E_{loc} is the local field on the Cs_2Te cathode. The β value of 77 has been found for this case which is a typical value for the S-band cavities.

The electron emission characteristics can be also investigated with respect to the RF phase. A typical behaviour of the emission as a function of the RF phase is shown by the simulations and given in the Fig. 55-a. In the simulation, the electron intensity have been probed after the RF the gun. Therefore, a non-zero transmission of the electrons occurs with a constant amount of photoemission, in a particular range of the phase. In reality, the total number of emitted electrons are a combination of the photoemission and the field emission. The strong electric fields cause the decrease in the surface potential barrier. Therefore the charge production is enhanced by the additional field emission. This phenomenon is known as the “Schottky effect”.

Within the field emission context, the charge-phase scans have been performed for the PHIN photoinjector. This has been presented in Fig. 55-b. These particular measurements have been performed by using the Faraday cup on the beamline. A 200 ns long bunch train have been measured under the 20 dB external attenuation in addition with 50Ω characteristic scope impedance. Each curve has been measured for a different klystron voltage. A “Schottky-like” field emission is visible on the charge-phase scan curves. The slope of the emission curves follow the phase of the RF field and reaches a maximum at the on-crest phase. Whereas the maximum achievable charge increases with the increasing RF gradient corresponding to the given klystron voltages of 30, 31 and 32 kV . Furthermore, gradient variation under the phase scan and the solenoid focusing certainly effect the amount of charge which arrives to the current monitor. Consequently, it is suitable to perform the charge-phase scans with a current monitor which is as close as possible to the RF gun.

5.2 Beam-Loading Compensation

The electron beam is accelerated in the RF field provided by the PHIN RF gun. During the acceleration the beam absorbs energy from the RF field. However, it can also deliver energy to the accelerating mode of the cavity. This effect is called the “beam loading”. According to the *fundamental theorem of beam loading*, a charged particle q_1 sees a voltage induced by the particle q_2 that leaves the cavity, as given in Eq. (66). More information on the theory of beam loading can be found in reference [94].

$$V_{q_1} = \frac{V_{q_2}}{2} \quad (66)$$

The field that is seen by the electrons is a superposition of both the RF field and the beam induced field. The beam-induced field is 180° out of phase with respect to the RF field. In this case, the timing of the beam is chosen correctly in order to achieve a flat acceleration field.

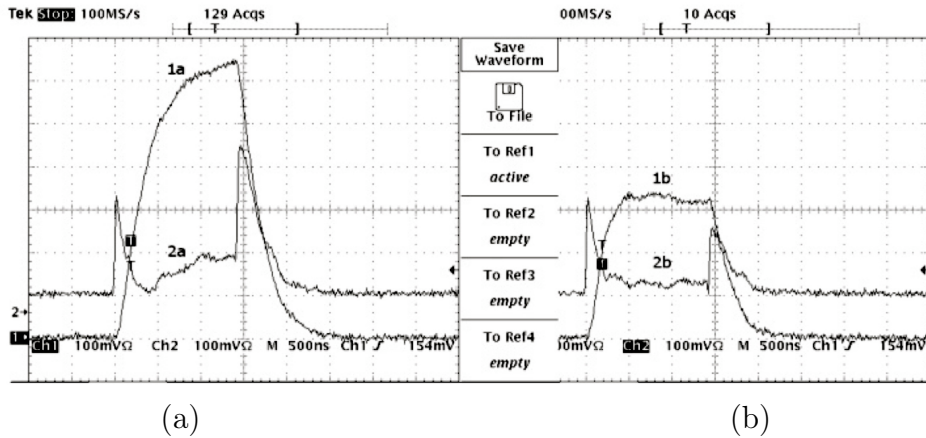


Figure 56: Beam loading compensation. a) RF power in the gun (1a) and reflected power (2a) when no beam is present. b) RF power in the gun (1b) and reflected power (2b) when the beam is present.

The beam loading compensation is studied and optimized for the PHIN photoinjector by adjusting the timing of the beam versus the RF pulse. The measured RF power and its reflection are shown for both of the cases in Fig. 56-a when there is no beam and in 56-b the beam is present. In the presence of the beam, a flat top RF pulse has been obtained resulting a mono-energetic beam. The timing has to be adjusted for different bunch charges. The measurements that are presented for the $1.2\ \mu\text{s}$ have been performed after the optimization of the beam loading for the rest of the commissioning.

5.3 Transverse Phase Space

The beam size and the transverse normalized emittance measurements have been performed, in the context of the transverse phase space studies for PHIN. The OTR profiling technique has been used for the measurements.

The emittance has been measured by introducing a multi-slit mask within the vacuum chamber. The details of the emittance analysis method is explained in this section. The

results of the systematic studies on the transverse normalized phase space are presented in comparison with the simulations.

5.3.1 Beam-Size Measurement Results

The electron beam size was measured and compared with the PARMELA simulations. In PARMELA simulations, the initial parameters of an electron beam emerging from a photocathode are given by the laser properties. These initial properties of the beam develop during the simulation according to the beamline elements. Therefore, the electron beam is defined as a round beam with a Gaussian distribution, having a $\sim 7\text{ ps}$ (FWHM) bunch length, in the simulations.

The transverse phase space measurements have been done by OTR profiling of the electron beam. A typical beam spot measured by a CCD camera and its horizontal profile is shown in Fig. 57.

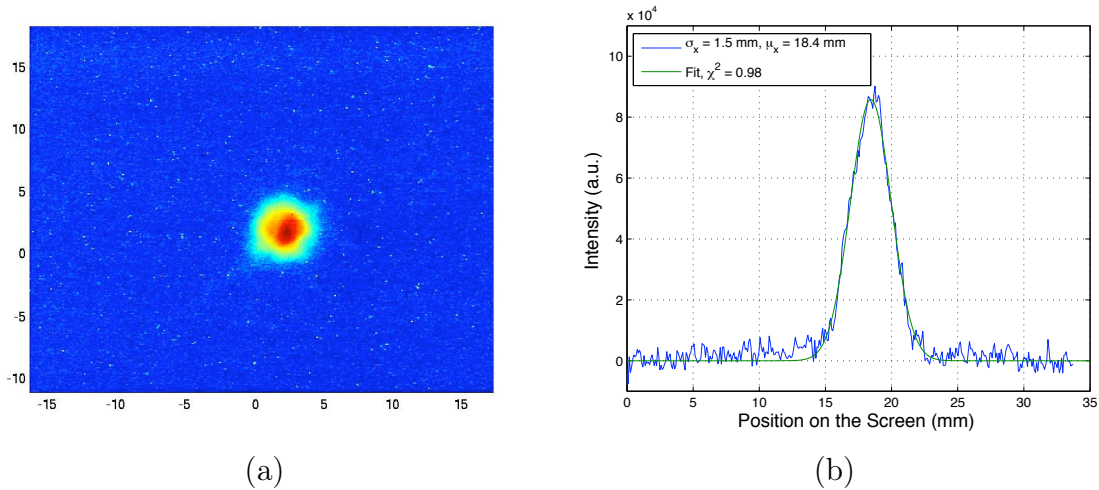


Figure 57: An example beam size measurement with single-shot OTR profiling from 02 March 2010. The 1σ beam size has been measured as 1.5 mm .

The beam size can be measured as a function of the solenoid magnet current. This measurement is called a “solenoid scan”. A solenoid scan is a benchmark measurement to understand the behaviour of the beam and the response of the instrumentation. An automated acquisition software has been developed in order to perform the measurements. An example for the solenoid scan is shown in Fig 58. The beam size has been measured several times at one particular focusing solenoid current setting. These subsequent measurements in the same setting have been used to calculate the statistical error on the corresponding measurement point. The scan reveals the variation of the beam size under the variation of the focusing conditions, e.i., the current of the focusing solenoid magnet. The three regions can be distinguished: the first as the particles converge, the second when they form the beam waist and the third they finally become diverging.

Furthermore, solenoid scans are effectively used to calibrate the simulation input parameters with respect to the actual system settings. One can take the setting of the solenoid magnet as an example. The calibration factor between the laboratory setting of the magnet and the settings in the simulation input file can be easily determined by using

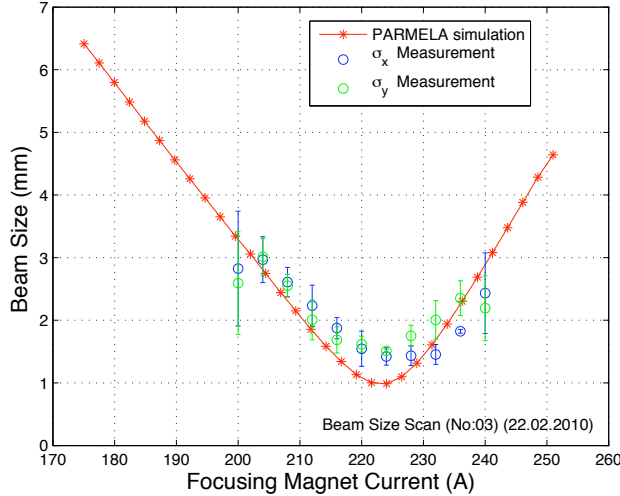
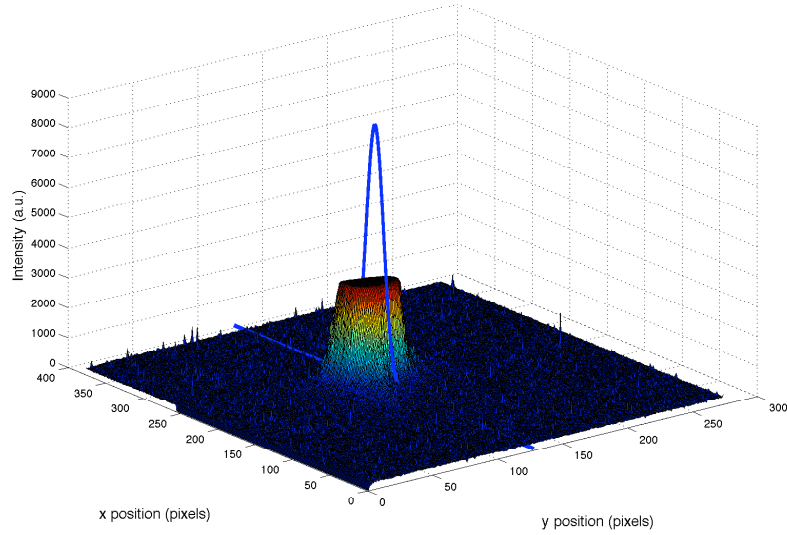


Figure 58: Beam size measurement as a function of the focusing magnet current for a 200 ns - long bunch train with 2.07 nC bunch charge and at the energy of 5.46 MeV .

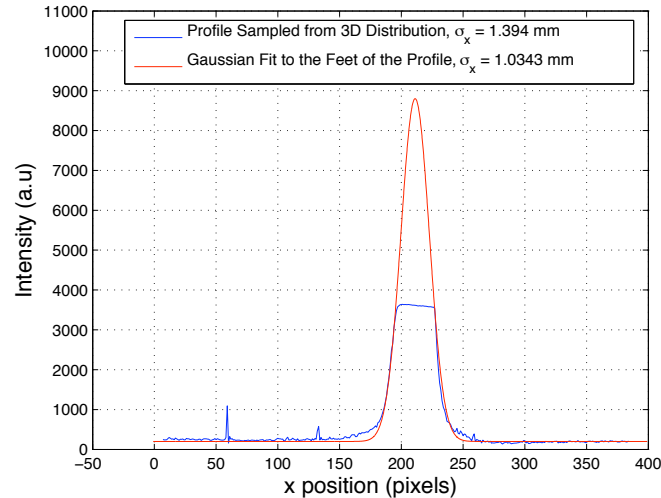
a beam size scan. And this factor is taken into account during the rest of the simulations for the same measurement conditions, systematically.

In addition, a quick investigation of the OTR profile of the beam often helps to the further adjustments of the instrumentation. This will prevent the repetition of relatively complex and time-consuming measurements. One of the cases is the early diagnosis of the CCD saturation. As an example, the 3D and 2D beam intensity distribution under the saturation of the CCD camera, as a result of the high camera gain, is shown in Fig. 59. In the figure, the 2D intensity distribution is extracted as a cross section of the 3D intensity distribution. One should note that, the projection of the 3D distribution is still a Gaussian curve and therefore it is not possible to observe the cutoff on the top of the profile unless one examines the 3D profile itself or the cross-section of the 3D profile as in Fig. 59-b. The measurements under the saturation effect overestimate the beam size, especially in the focus region of a beam size scan where the beam waist appears. An example is shown in Fig. 60. In this example, the beam size values have been reconstructed by fitting the feet of the cross-sections in order to prevent the cutoff regions on the top of the profiles. The simulated 1σ beam sizes, over the range of the focusing magnet current, have been used as the initial fit parameters. The result of the reconstruction shows the agreement of data and simulation at the focus region.

Another example of the beam based adjustment of the instrumentation have been noted for the aspect ratio of the laser spot size on the cathode. As the result of the first run in 2008, an asymmetric behavior has been observed between the vertical and horizontal beam sizes. The optics for the laser alignment and the positioning on the cathode, and the background field by the magnetic components in the set-up have been considered as the possible sources to be investigated for the asymmetry. Upon these investigations, it turned out that the laser was not aligned along the axis of the RF gun, correctly. This has been rectified by re-alignment of the laser in the region. During the second commissioning run in March 2009, the asymmetry in the beam envelope for the vertical



(a)



(b)

Figure 59: The comparison of the saturated intensity distribution with the Gaussian curve reconstructed by using a simulated beam size. a) The 3D intensity distribution of the beam under the saturation effect of the CCD camera. b) The example cross-section of the intensity distribution and the Gaussian fit to the feet of the profile.

and the horizontal beam sizes was no longer present, confirming a laser alignment problem before the re-alignment.

During the commissioning, beam size scans have been performed with respect to different laser spot sizes of 2, 3, and 4 mm at 5.7, 5.2 and 5.5 MeV, respectively. The laser spot size is typically given as knife edge value, defined as the spot size regarding 85% of the profile. The corresponding 1σ (64%) values of the laser spot sizes are 0.8 mm, 1.2 mm and 1.6 mm and these values have been used in the PARMELA simulations. The results

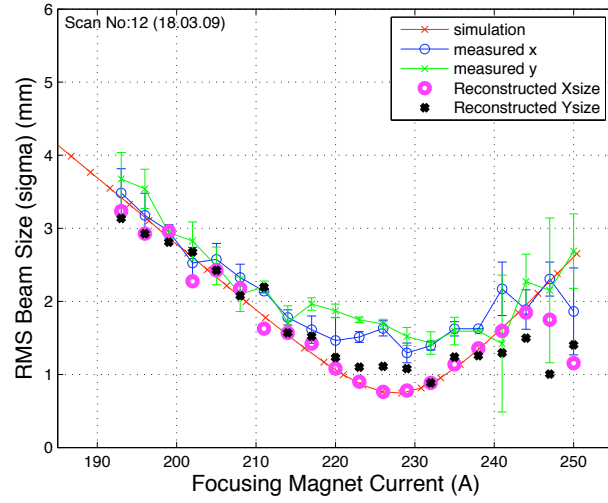


Figure 60: The measured and reconstructed beam size scan in comparison with the PARMELA simulation (left).

of the beam size scans for different laser spot sizes are shown in Figure 61. Measurements showed that the spot size scales and the position of the beam waist moves with the laser spot size, as expected.

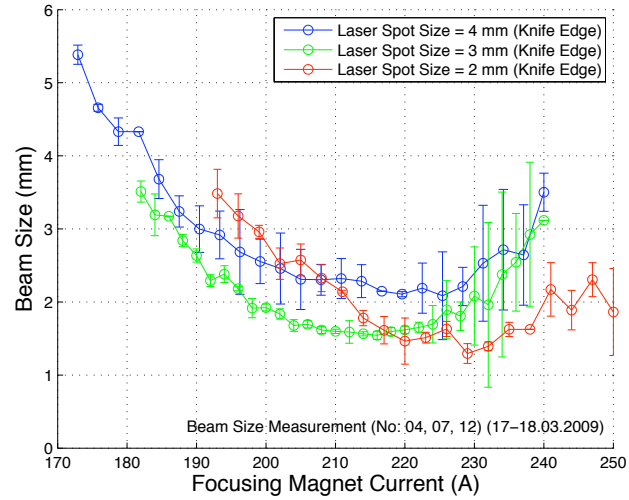


Figure 61: Beam size measurements for different laser spot sizes within a range of the focusing solenoid current.

5.3.2 Data Analysis Techniques for the Transverse Emittance Measurements

There are two important issues for the analysis of the multi-slit method. The first is the determination of the type and the level of the background for the beam profile after the multi-slit mask. The second one is the proper exclusion of the outermost regions in the tails of the profile, to prevent the misinterpretation of the noise fluctuations as the low-intensity beamlets.

After the slit-mask the beam profile has a background that might be a combination of several sources such as: the un-stopped electrons by the slit-mask, the overlapping between the individual beamlets, x-rays or external light pollution and radiation due to the heating of the screen. This background has to be determined and subtracted from the profile to be analyzed. FLUKA [95] simulations showed that the mask is able to totally stop a 5.5 MeV electron beam as shown in Fig. 62, while 20% of the incoming electrons are back-scattered [96].

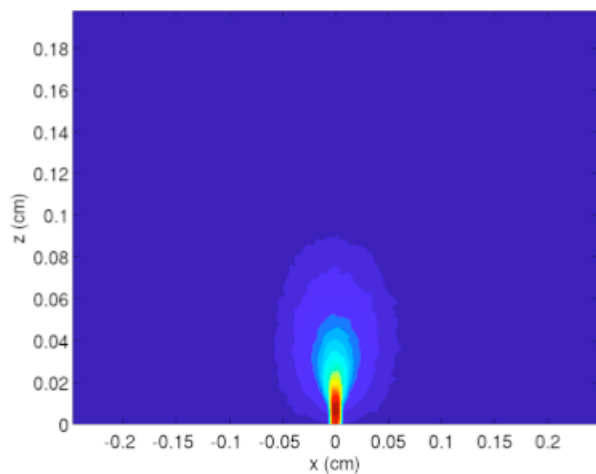


Figure 62: Energy deposition of 5.5 MeV pencil e^- beam in a 2 mm thick tungsten slab.

Therefore, under the conditions of current PHIN beam energies and intensities, one can assume that there are no electrons traversing the mask and interacting with the OTR screen except from the ones passing through the slits windows. However, the production of the x-rays should also be considered as a result of the interaction between the electrons and the mask. The x-ray shower on the OTR screen is another significant source of background for the OTR profiling. The background due to those x-rays can be prevented by shielding the surrounding environment of the multi-slit mask chamber. Additionally, a CCD camera with a low x-ray sensitivity should be chosen for the OTR profile monitor.

In this study, two different models have been assumed to describe the background of the profiles. The first one is a background with a Gaussian shape. The second model assumes the background as a zeroth order polynomial. Different experimental conditions revealed different types of backgrounds for the emittance measurements. These should be analyzed with the appropriate type of background subtraction algorithms.

An analysis software has been developed for the emittance measurements and the background subtraction algorithms have been implemented in the software. The program allows the user to select a background type to be fitted to the data.

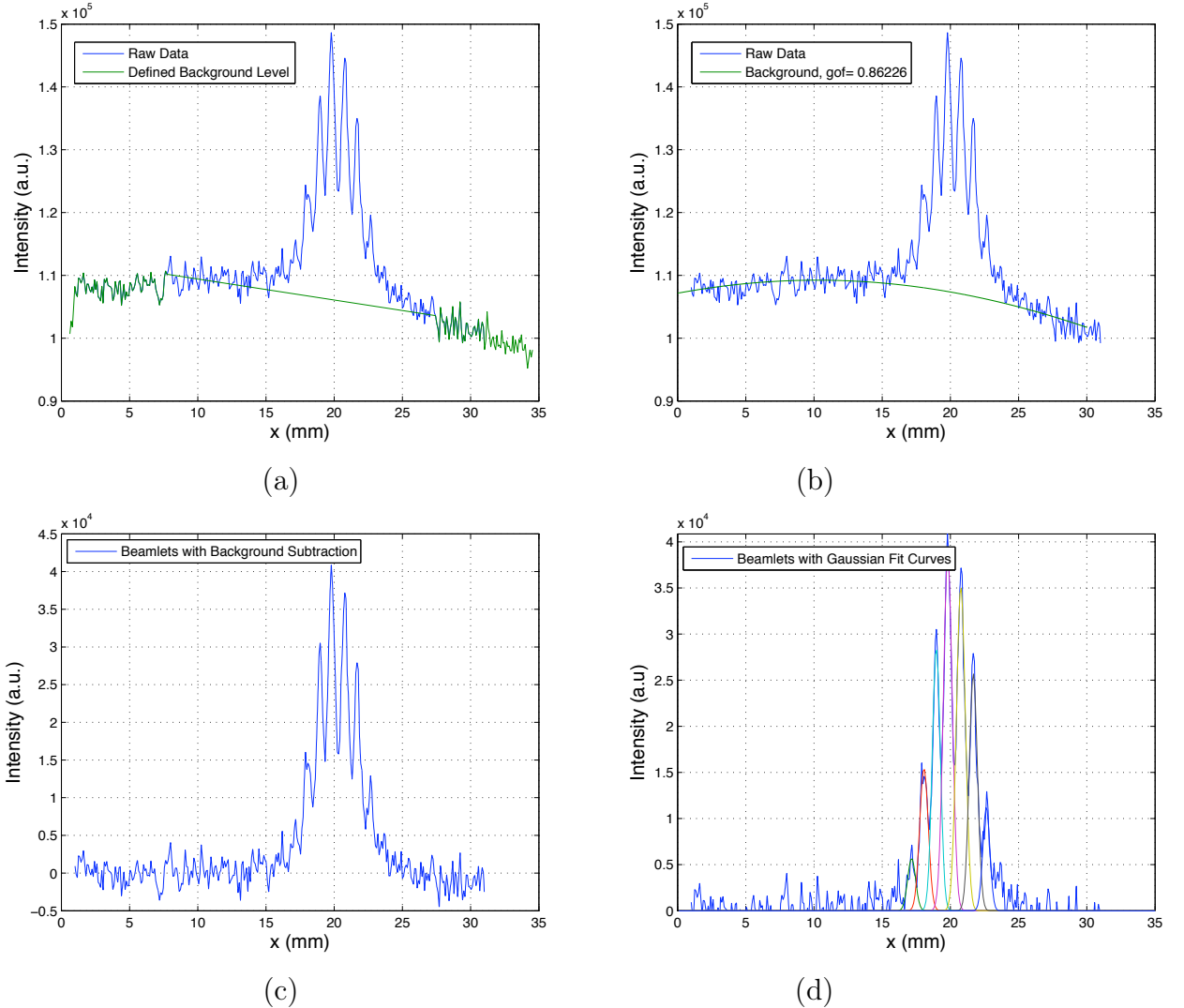


Figure 63: a) The typical beam profile after the multi-slit mask and the region of interest for the background fit. b) Gaussian background on the original profile. c) The beam profile after the Gaussian background subtraction. d) Individual beamlets with the Gaussian fit curves.

The typical beam profile after the multi-slit mask has been shown in Fig. 63. In the beginning of the analysis, the software expects the user to determine a region of interest, for the background, over the raw profile. The selected region is marked in green in Fig. 63-a. The background is determined by fitting the data inside the defined region at the tails of the profile (Fig. 63-b). The initial fit parameters for the 1σ width, the mean and the maximum intensity of the background Gaussian are specified during the fit. Moreover, one can set the initial fit parameter for the maximum intensity as variable in the analysis program. This variable is defined as *the background subtraction level*. A number of fits can be obtained by varying the background subtraction level and a criteria can be defined to select the best defined background. The following selection criteria is used: it has been assumed that, after the background subtraction, the envelope covering the whole beamlets should be a Gaussian curve provided that the profile of incoming beam to the

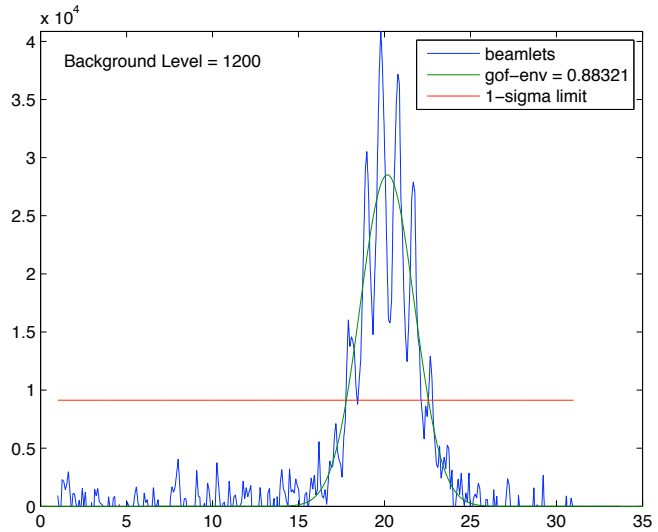
multi-slit mask is Gaussian. The quality of fit for the envelope curve could be a measure for the selection of the background subtraction level and the corresponding best defined background.

During the analysis, the background subtraction level is changed systematically by the program within a user-defined range. The profile after the background subtraction can be seen in Fig.63-c for a particular subtraction level. For this example the background level has been changed in a range of ± 1200 around the initial value with the steps of 200, in arbitrary units of intensity. The first and second moments of each beamlet have been determined for the emittance calculation (Fig.63-d). The *rms* normalized transverse emittance is calculated after the subtraction of each background having different levels. The result of such an investigation is shown in Figure 64. The best fit is determined as the quality of fit (χ^2) value approaches to 1. The subtraction resulting with the best fit of beamlets profile and the envelope has been chosen as the best defined background.

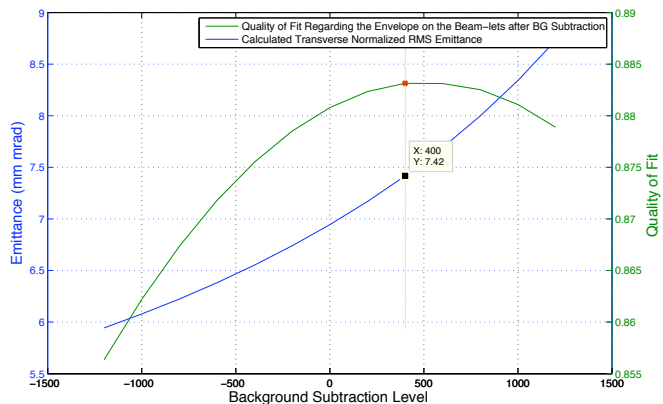
The result of the emittance calculation after the subtraction of the best defined background is 7.4 mm mrad. The steps of the analysis are shown in Fig. 65. The first step is the acquisition of the OTR image of the beam after the multi-slit mask (Fig. 65-a). The second step is the determination of the first and the second moments of the individual beamlets (Fig. 65-b ad c) by using the background determination algorithm and performing Gaussian fit on each beamlet. The third step is the calculation of the emittance using this information in addition with the weighted intensities of each beamlet and finally reconstruction of the transverse phase space (Fig. 65-d).

The emittance for this particular case has been calculated as 7.9 mm mrad without implementing the background subtraction algorithm described above. The background determination algorithm makes 7% difference on the result for this example.

A comparison of the simulated and measured phase space is presented in Fig.66. The 1σ ellipse is denoted for both cases. The simulation and the measurement agree and the system is capable of imaging the transverse phase space of the beam in with a single-shot measurement. However, the reconstruction method is not sensitive to resolve the tails of the distribution in the phase space.



(a)



(b)

Figure 64: The searches for the correct background model for the beam profile. a) The profile with the Gaussian envelope. b) Resulting emittance with respect to different background subtraction levels.

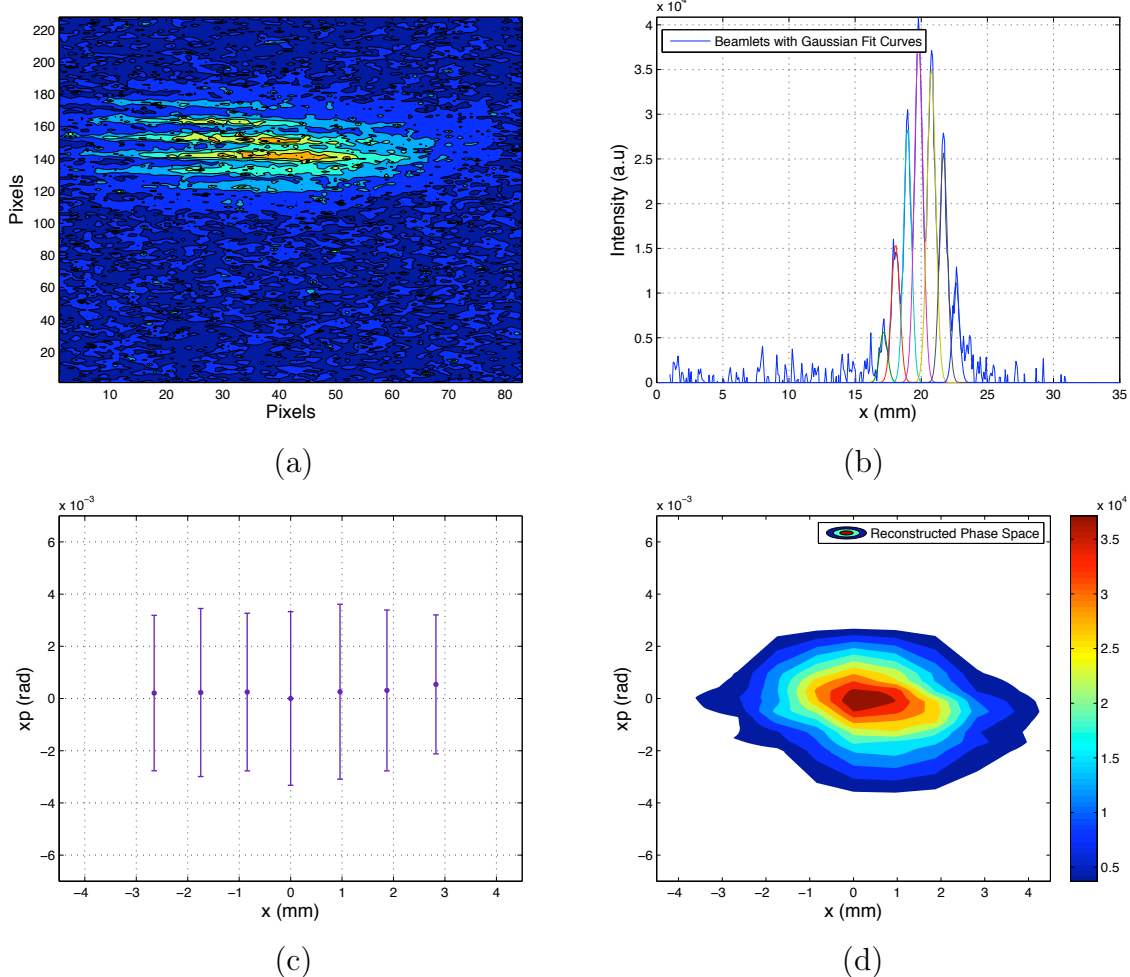


Figure 65: The steps of the emittance analysis. a) The image which is observed after the multi-slit mask. b) Beam profile with Gaussian fit curves for individual beamlets. c) The summary of the mean position and the divergence of each beamlet determined from Gaussian fit curves. d) Reconstructed phase space. The transverse r_{ms} normalized emittance has been measured as 7.4 mm mrad with a single shot measurement.

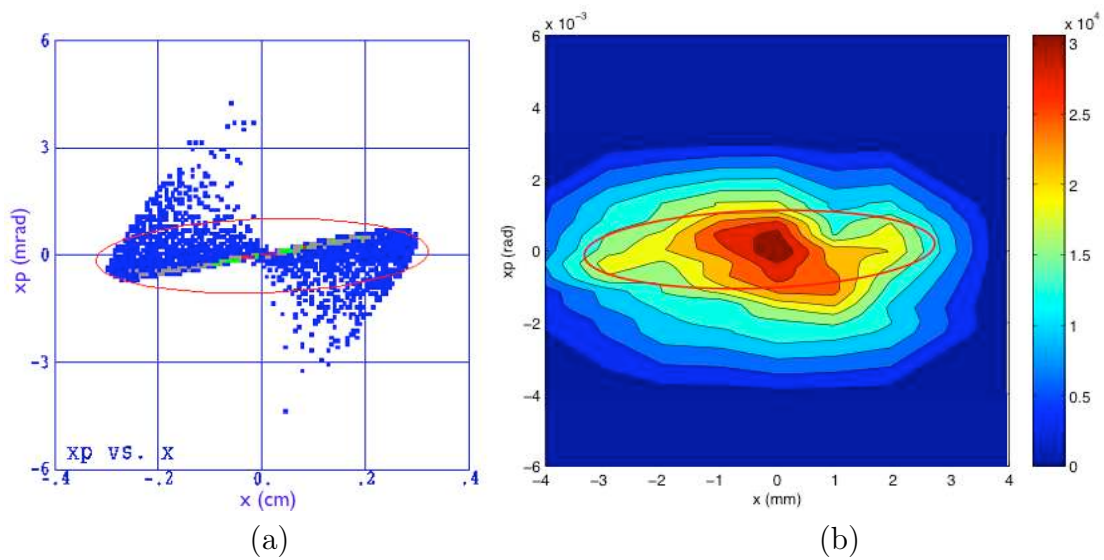


Figure 66: The phase space, simulated (left) and reconstructed from the measurement (right). The emittance was measured as 10.7 mm mrad for 1.28 nC beam at the energy of 5.5 MeV. The measurement was performed with the laser spot size of 4 mm.

5.3.3 Systematic Error Calculation for the Emittance Measurement

For the multi-slit measurement method, the transverse geometric emittance, ϵ , can be calculated by using the formula given in Eq. (67),

$$\epsilon = \sqrt{\frac{(\sum_{i=1}^N \rho_i x_i^2)(\sum_{j=1}^N \rho_j x_j'^2) - (\sum_{i=1}^N \rho_i x_i x_i')^2}{(\sum_{i=1}^N \rho_i)^2}} \quad (67)$$

where, x_i is the position of i th beamlet and x_i' is the divergence of the i th beamlet. The intensity of each beamlet is denoted by ρ_i . An expression has been derived for the systematic error calculations of the transverse emittance measurement. The derivation of the formula and results of the error calculations are presented in this section.

The systematic error on a function $f(x, y, z)$ is derived by using the general expression which is given in Eq. (68). The errors on the function arguments, (x, y, z) , are given as $(\sigma_x, \sigma_y, \sigma_z)$.

$$\sigma_{f(x,y,z)}^2 = \left(\frac{\partial f(x, y, z)}{\partial x} \right)^2 \sigma_x^2 + \left(\frac{\partial f(x, y, z)}{\partial y} \right)^2 \sigma_y^2 + \left(\frac{\partial f(x, y, z)}{\partial z} \right)^2 \sigma_z^2 \quad (68)$$

The error propagation of the observables have been done for the systematic error analysis of the PHIN emittance measurement set-up. The distance between the slits, the distance between the multi-slit mask and the observation screen have been considered in order to determine the errors on the beamlet positions and divergences. Additionally the shot-to-shot intensity stability of the beam has been considered for the calculations. Further systematic error may originate due to the background subtraction method, non-Gaussian intensity distribution of the beamlets close to the emittance minimum and underestimation of the beamsize due to the beamlets at the tails of the profile with low signal to noise ratios. However, the contributions from those sources have not been included in the following calculations.

In order to determine the systematic error on the geometric emittance, the terms in the Eq. (67) have been studied separately. The calculation steps are presented in Eq. (69-74).

$$\sigma_{\sum \rho x^2}^2 = \sum_{i=1}^N x_i^4 \sigma_{\rho_i}^2 + 4x_i^2 \rho_i^2 \sigma_{x_i}^2 \quad (69)$$

$$\sigma_{\sum \rho x'^2}^2 = \sum_{j=1}^N x_j'^4 \sigma_{\rho_j}^2 + 4x_j'^2 \rho_j^2 \sigma_{x_j'}^2 \quad (70)$$

$$\sigma_{\sum \rho x x'}^2 = \sum_{i=1}^N \rho_i^2 x_i'^2 \sigma_{x_i}^2 + \rho_i^2 x_i^2 \sigma_{x_i'}^2 + x_i^2 x_i'^2 \sigma_{\rho_i}^2 \quad (71)$$

$$\sigma_{(\sum \rho x x')^2} = 4 \left(\sum_{i=1}^N \rho_i^2 x_i'^2 \sigma_{x_i}^2 + \rho_i^2 x_i^2 \sigma_{x_i'}^2 + x_i^2 x_i'^2 \sigma_{\rho_i}^2 \right) \left(\sum_{i=1}^N \rho_i x_i x_i' \right)^2 \quad (72)$$

$$\sigma_{(\sum \rho)^2}^2 = 4 \left(\sum_{i=1}^N \sigma_{\rho_i}^2 \right) \left(\sum_{j=1}^N \rho_j \right)^2 \quad (73)$$

$$\begin{aligned} \sigma_{[(\sum \rho x^2)(\sum \rho x'^2) - (\sum \rho x x')^2]}^2 &= (\rho_j^2 x_j'^2)^2 (4\rho_i^2 x_i^2 \sigma_{x_i}^2 + x_i^4 \sigma_{\rho_i}^2) \\ &\quad + (\rho_j^2 x_j^2)^2 (4\rho_i^2 x_i'^2 \sigma_{x_i'}^2 + x_i'^4 \sigma_{\rho_i}^2) \\ &\quad + 4(\rho_i^2 x_i'^2 \sigma_{x_i}^2 + \rho_i^2 x_i^2 \sigma_{x_i'}^2 + x_i^2 x_i'^2 \sigma_{\rho_i}^2) (\rho_i x_i x_i')^2 \end{aligned} \quad (74)$$

Finally the propagation of the errors have been performed for the division by total intensity $\sum \rho$ and the square root to finally derive a formula for the complete emittance equation. These calculations can be followed in Eq. (75-76).

$$\begin{aligned} \sigma_{[(\sum \rho x^2)(\sum \rho x'^2) - (\sum \rho x x')^2]/(\sum \rho)}^2 &= \frac{\left[\sum_{i=1}^N \rho_i x_i^2 \right] (\sum_{j=1}^N \rho_j x_j'^2) - (\sum_{i=1}^N \rho_i x_i x_i')^2}{(\sum_{i=1}^N \rho_i)^8} 4 \left(\sum_{i=1}^N \sigma_{\rho_i}^2 \right) \left(\sum_{j=1}^N \rho_j \right)^2 \\ &\quad + \frac{(\rho_j x_j'^2)^2 (\sum_{i=1}^N 4\rho_i^2 x_i^2 \sigma_{x_i}^2 + x_i^4 \sigma_{\rho_i}^2)}{(\sum_{i=1}^N \rho_i)^4} \\ &\quad + \frac{(\rho_j x_j^2)^2 (\sum_{i=1}^N 4\rho_i^2 x_i'^2 \sigma_{x_i'}^2 + x_i'^4 \sigma_{\rho_i}^2)}{(\sum_{i=1}^N \rho_i)^4} \\ &\quad + \frac{4(\rho_i^2 x_i'^2 \sigma_{x_i}^2 + \rho_i^2 x_i^2 \sigma_{x_i'}^2 + x_i^2 x_i'^2 \sigma_{\rho_i}^2) (\rho_i x_i x_i')^2}{(\sum_{i=1}^N \rho_i)^4} \quad (75) \\ \sigma_{\epsilon}^2 &= \frac{(\rho_j x_j'^2)^2 (4\rho_i^2 x_i^2 \sigma_{x_i}^2 + x_i^4 \sigma_{\rho_i}^2)}{4\epsilon^2 (\sum_{i=1}^N \rho_i)^4} \\ &\quad + \frac{(\rho_j x_j^2)^2 (4\rho_i^2 x_i'^2 \sigma_{x_i'}^2 + x_i'^4 \sigma_{\rho_i}^2)}{4\epsilon^2 (\sum_{i=1}^N \rho_i)^4} \\ &\quad + \frac{(\rho_i^2 x_i'^2 \sigma_{x_i}^2 + \rho_i^2 x_i^2 \sigma_{x_i'}^2 + x_i^2 x_i'^2 \sigma_{\rho_i}^2) (\rho_i x_i x_i')^2}{\epsilon^2 (\sum_{i=1}^N \rho_i)^4} \end{aligned}$$

$$\begin{aligned}
& - \frac{2(\sum_{i=1}^N \rho_i x_i^2)(\sum_{j=1}^N \rho_j x_j'^2)(\sum_{i=1}^N \rho_i x_i x_i')^2 (\sum_{i=1}^N \sigma_{\rho_i}^2)}{\epsilon^2 (\sum_{i=1}^N \rho_i)^6} \\
& + \frac{\epsilon^2 (\sum_{i=1}^N \sigma_{\rho_i}^2)}{(\sum_{i=1}^N \rho_i)^6}
\end{aligned} \tag{76}$$

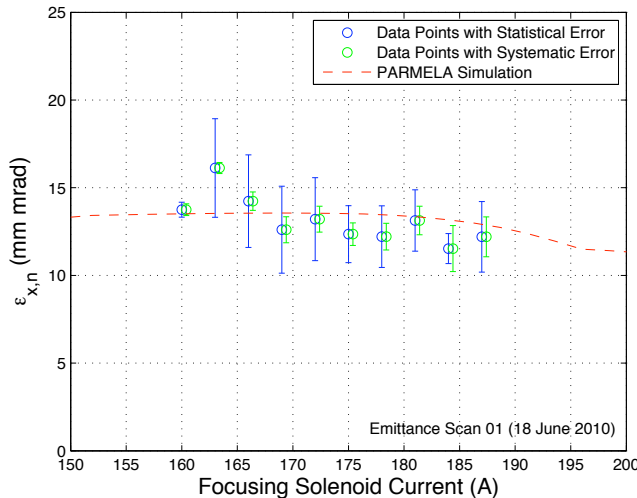


Figure 67: The comparison of the statistical and the systematic errors on the multi-slit method for the emittance measurement.

The systematic error on the geometric transverse emittance can be calculated by using the formula in Eq. (76) in terms of the first moment, second moment and the intensities of the beamlets as well as the individual errors on these observables. The errors on the observables are given in Table 28 as they are used in the calculations. The emittance measurement as a function of the focusing solenoid current is shown in Fig. 67. The figure shows a comparison between the statistical and the systematic error on each measurement point. Each data point represents an average of five subsequent measurements. The statistical error on each point has been calculated as the statistical deviation of the subsequent measurements. The systematic error of each data point has been found by propagation of the systematic errors of each subsequent measurement.

The figure indicates that the systematic and the statistical errors for the measurement system is comparable. Nevertheless, the systematic error for the measurement is less than the statistical deviations, for this particular example. The shot-to-shot stability is an important aspect of the photoinjector systems. Therefore, the multi-slit emittance measurement method is rather suitable for these systems for its single-shot acquisition property. Indeed, the statistical errors on the data points are the indication of the shot-to-shot stability of the beam.

As a matter of fact that the intensities of the individual beamlets are taken into account, one can call the formula in Eq. 76 as the “semi-systematic error formula”. The intensity stability of the electron beam is inherent from the laser beam intensity stability and the

Table 28: The errors on the position and the divergence of the beamlets have been calculated in terms of the slit width and the mask-screen distance. The error on the beamlet intensities have been calculated as the product of measured individual beamlet intensities and the 4% electron beam intensity stability.

Parameter	Value
Error on the mean position, σ_x [mm]	0.01
Error on the beam divergence, $\sigma_{x'}$ [mrad]	0.4
Error on the beamlet intensities, σ_ρ [a.u.]	$0.04 \times \rho_i$

RF pulse shape. Therefore, the systematic errors in the example can be improved by optimizing these systems.

5.3.4 Emittance Measurement Results

In this section, the systematic study of the transverse normalized emittance of the beam will be presented with respect to the laser spot size, phase and gradient of the RF field as well as the length of the pulse train. The analysis methods that are described, previously, have been used for the measurement results.

In Chapter 3, the transverse normalized emittance was shown to be scaled proportional to the laser spot size by using simulation results. This has been also demonstrated by the measurements during the PHIN commissioning. In Fig. 68, the transverse normalized emittance has been measured as a function of the focusing solenoid current for the laser spot sizes of 2 mm and 4 mm as the knife edge values. The measurement agrees with the PARMELA simulation within the measured statistical error ranges. The measurement has been carried out with an electron pulse train of 200 ns . The charge per pulse and the energy of the beam have been maintained as close as possible for each case, though the two measurement were performed in different days. It has been experimentally shown that the emittance scales with the laser spot size.

The dynamics of the electron beam in an RF gun depends on the phase of the RF field, significantly. Therefore it is interesting to measure the emittance with respect to the RF phase. The behavior of the transverse normalized emittance in a range of the focusing solenoid current for different RF phase values is shown in Fig. 69-a. According to the measurements in the figure, the emittance changes with the RF phase. The relation between the transverse normalized emittance and the RF phase is presented more directly in Fig. 69-b in comparison with the PARMELA simulation. For the measurement the $\Delta\Phi = 0^\circ$ denotes the optimum phase for the operation. And the emittance values are given relative to the emittance value measured at this optimum phase. The solenoid current has been adjusted for each phase setting in order to properly focus the beam. A trend, that reveals a minimum around the optimum phase, can be distinguished slightly within the error bars. Nonetheless, there is a certain agreement with the simulated points showing the existence of a nominal phase for the minimum emittance. Therefore, it is important to operate the injector with the correct phase in order to optimize the transverse emittance.

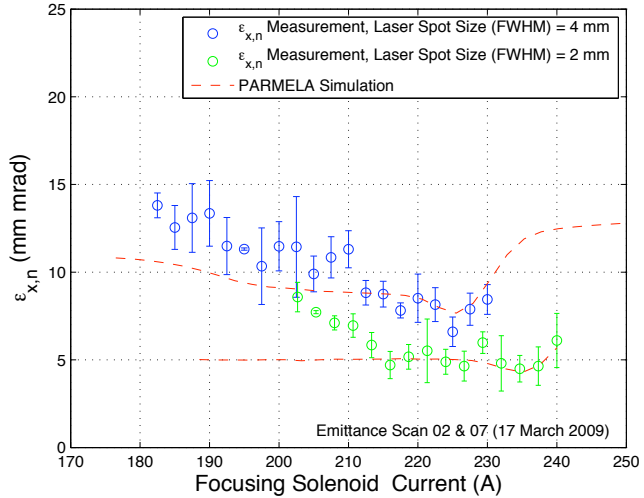


Figure 68: Emittance measurement with respect to the laser spot size. (Blue) $\sigma_{Knife Edge} = 4 \text{ mm}$, $Q=1.28$, $E=5.512 \text{ MeV}$, Train Length = 200ns. (Green) $\sigma_{Knife Edge} = 2 \text{ mm}$, $Q=1.1$, $E=5.67 \text{ MeV}$, Train Length = 200ns.

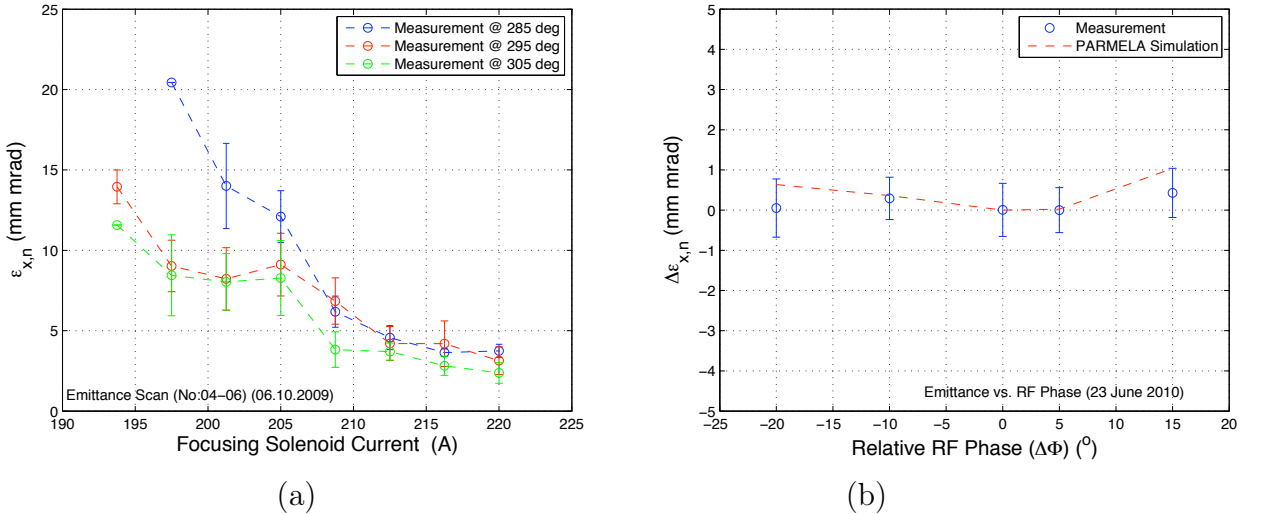


Figure 69: a) Emittance scan with respect to the focusing magnet current at different RF phase values for a bunch train of 500 ns with the 1.6 nC/bunch. b) The emittance measurement with respect to the RF phase for a bunch train of 1300 ns with the 0.4 nC/bunch. The emittance values in (b) are given with respect to the value at $\Delta\Phi = 0^\circ$.

In a laser driven RF gun the pulse train properties of the electron beam can be manipulated by coding the laser temporal structure. This process is called the “phase coding”. During the PHIN commissioning operations, the inner structure of the laser beam maintained at 1.5 GHz, however the length of the laser pulse train has been varied from 200 ns up to the nominal PHIN specification of 1300 ns for different measurements. In Fig. 70, the two emittance scans at different pulse train lengths are compared. The measurements have been performed on the electron pulses with the charge of 1.7 nC and the energy of

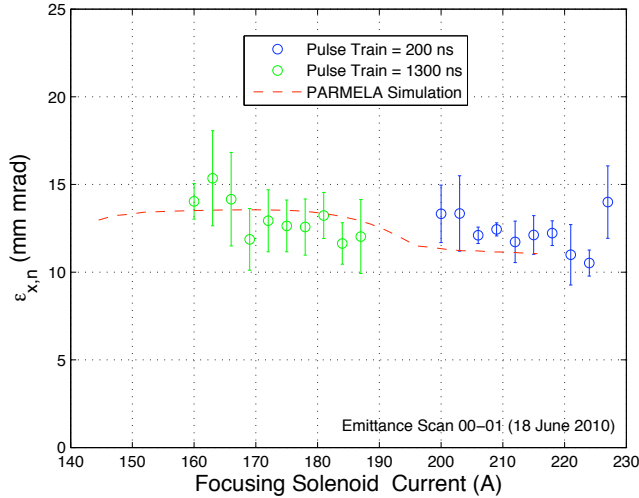


Figure 70: Emittance measurement for different train lengths. 200 ns, 1.7 nC, 5.616 MeV.
1300 ns, 1.7 nC, 5.616 MeV.

5.6 MeV. Though, the emittance scan for the 200 ns train have been performed in a different focusing region. The stronger focusing region has been preferred for the bunch train of 200 ns since a shorter train produces lower OTR intensity and it is more convenient to focus the beam on to the slit mask in order to get an intense enough OTR image for the analysis. The measurement with the shorter bunch train results with the lower emittance values since this measurement has been performed in the emittance compensation region of the focusing current range. This also can be seen from the behavior of the simulation. The decrease of the emittance is not related with the bunch train length. The most significant difference between two measurements appear in the statistical fluctuations on the data points. Even though the both measurements have been analyzed in the same way and the measurements include the same amount of statistics, the emittance fluctuation on the $1.3\ \mu s$ long beam is larger than the 200 ns long beam. This is a result of the fact that the emittance of the pulse train is a projection of the emittances of the individual pulses. This observed phenomenon might reflect the intensity or energy fluctuations which cause the emittance variation along the pulse train. The longitudinal variation of the emittance would result a larger projected emittance for a longer pulse train. The fluctuations in the beam properties can be considered in conjunction with the stability of the laser and the RF field. In the ideal case, the projected emittance of the whole train would be expected to get closer to the emittance of a single pulse, as the stability along the train increases.

Further than the example above, demonstration of the stability along the pulse train is an important prospect for the PHIN photoinjector. This aims to strengthen the proposal of using a photoinjector as the source of the existing CTF3 and as the source of the future CLIC drive beam. Therefore the characterization of the beam properties along the pulse train constitutes a key argument for the PHIN commissioning. Consequently, many measurements have been performed along the bunch train and called the “time resolved” measurements. The time resolved measurements for the transverse and the longitudinal beam parameters for PHIN are given in the following sections.

5.4 Time-Resolved Transverse Characterization of the Beam

The beam properties can be studied as a function of the longitudinal position along the pulse train by using an intensified-gated camera. The measurements are performed by capturing the beam profile images with a constant camera gate along the bunch train. A camera with an adjustable gate duration from 100 ns to several milliseconds has been used for the measurements. The camera is triggered by an external signal which is synchronized to the laser timing. In order to perform the time-resolved measurements, the timing for the camera gate can be delayed according to the beam as illustrated in the Fig. 71. For each shot, the camera gate delay is increased in order to snapshot a different longitudinal position along the pulse train. During the commissioning of the long electron pulse train, a beam of $1.2\text{ }\mu\text{s}$ or $1.3\text{ }\mu\text{s}$ has been provided for the measurements with respect to the PHIN specifications.

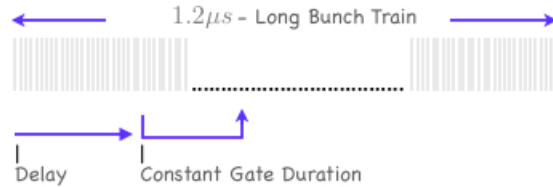


Figure 71: The illustration of the time-resolved OTR profiling of the electron beam. The scheme as shown in the figure would allow a measurement over a region from 400 ns to 600 ns along the bunch train.

As a general notice on the plots of the time-resolved measurements, the horizontal error bars indicate the constant gate duration while the vertical error bars indicate the statistical fluctuations on that particular data point.

5.4.1 Beam size along the Pulse Train of $1.2\text{ }\mu\text{s}$

During the October 2009 run, a bunch train at 4.8 MeV that consisted of 1908 bunches with the charge of 1.4 nC has been provided. In Fig. 72, a time-resolved beam size measurement is presented as a function of the longitudinal location along the bunch train. A magnetic focusing by the solenoid current of 200 A has been applied during this measurement. In the first part of the measurement the gate duration has been set to 100 ns and the beam size has been measured by OTR monitoring for each 100 ns step of the $1.2\text{ }\mu\text{s}$ beam. Regarding the second part of the measurement, the green point in the plot denotes the beam size value, measured in a way to capture the image of the full pulse train. For this measurement the camera gate duration has been set to $1.2\text{ }\mu\text{s}$. The horizontal error bars in the plots, indicate the statistical fluctuations of each point and calculated over 10 subsequent measurements. The mean value of the beam size and the statistical fluctuation along the pulse train are denoted on the plots. The stability along the bunch train has been measured as 21% for the time resolved measurement with the 100 ns resolution. Whereas the statistical deviation of the beam size over several subsequent measurements has been measured as 4% in the case of the measurement with the full train.

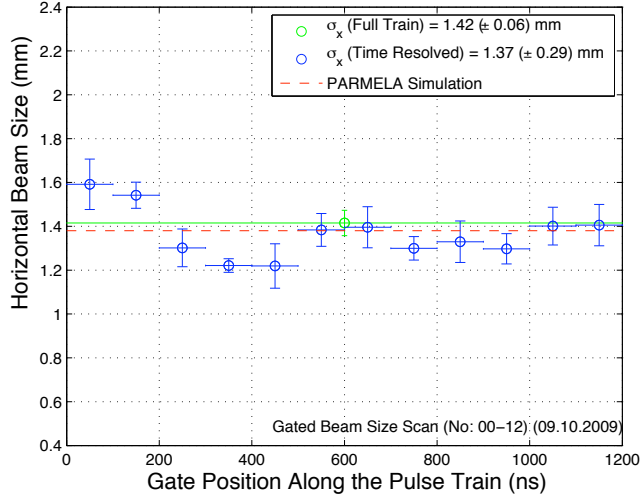


Figure 72: Beam size measurement along the pulse train in comparison with the measurement with the full train. 1.4 nC , 4.8 MeV

A similar measurement has been repeated during the March 2010 run. This measurement includes several solenoid scans depending on the single shot profiles at different longitudinal positions along the pulse train. The Fig. 73-a and b shows the time-resolved solenoid scans to measure both the horizontal and vertical beam sizes. The data points with different colors, at a particular focusing solenoid setting, represent the time-resolved measurements for this setting. A stable beam with a charge per bunch of 1.4 nC at an energy of 4.9 MeV has been provided for this time-resolved solenoid scans. The measurement agrees very well with the PARMELA simulation within the measured statistical error ranges. Although Fig. 73 is a nice visualization of the measurement, it is useful to investigate the results in one particular magnet setting. For this reason a point around the focus region of the solenoid scan has been chosen and presented in Fig. 73-c. The figure represents the time-resolved beam size measurement as a function of the longitudinal position along the train in the units of ns . For this measurement, the variation of the beam size along the train is 0.48 mm and 0.69 mm for the horizontal and the vertical axis, respectively, with the resolution of 200 ns .

5.4.2 Emittance along the Pulse Train of $1.2 \mu\text{s}$

The time-resolved emittance measurements have been also performed similarly to the time-resolved beam size measurements. The emittance has been measured in the steps of 400 ns , 200 ns and 100 ns in different times of the commissioning. An oscillation-like behavior becomes more distinguishable in the measurements that are performed in the smaller gate durations which provides higher resolution along the train.

The difficulty of the time-resolved emittance measurements is to obtain the high enough OTR light intensity in order to observe the individual beamlets. The introduction of the multi-slit mask, when it is within the vacuum chamber, stops a $\sim 80\%$ of the electrons. The ones reaching to the screen emit the OTR radiation with a relatively low intensity compared to the entire beam. A shorter camera gate duration increases the measurement

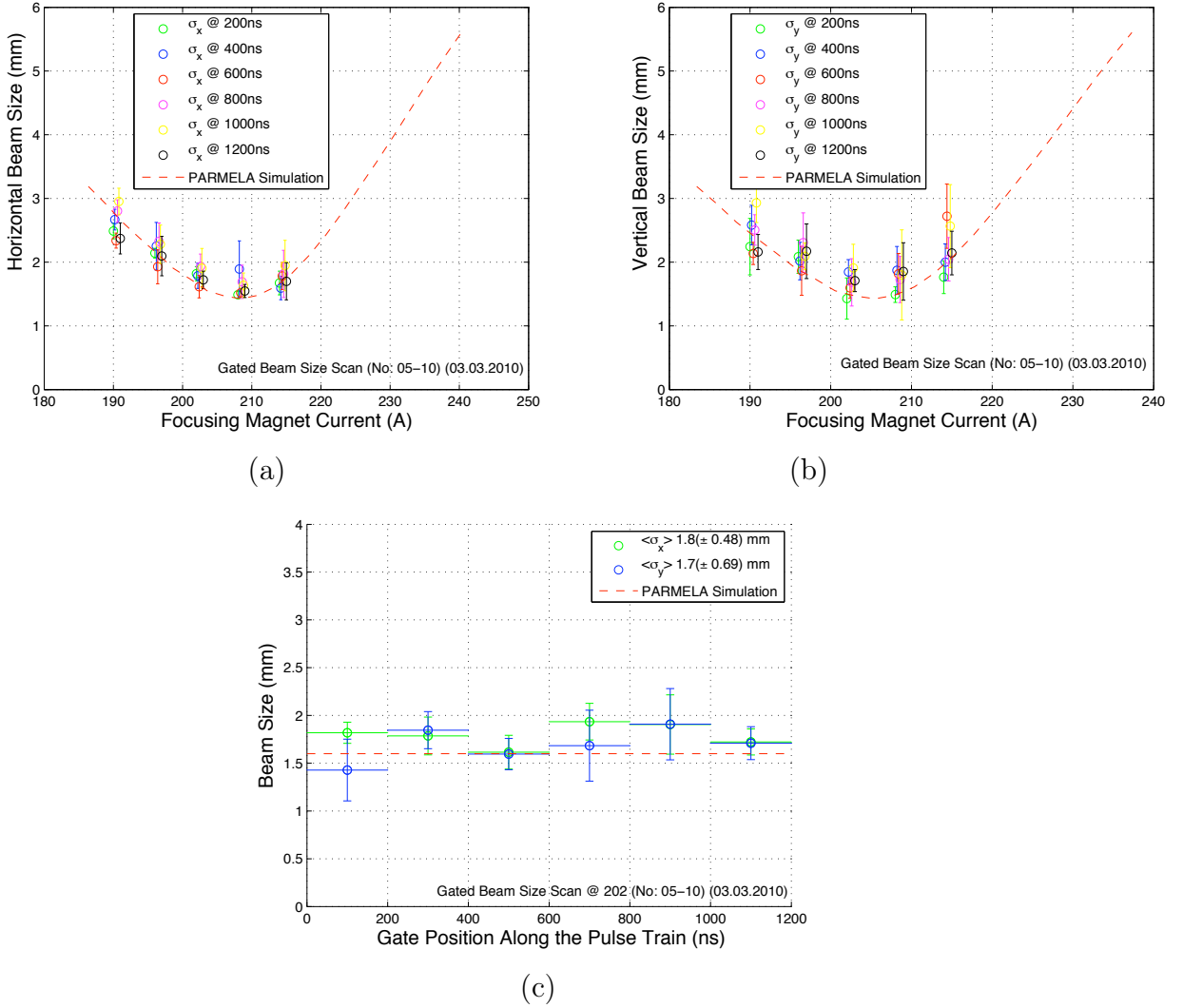


Figure 73: Beam size scan along the pulse train for a beam of 1.4 nC, 4.9 MeV. a) Horizontal beam size. b) Vertical beam size. c) Representation of the measurement under a focusing current of 202 A at different gate positions.

resolution along the pulse train, however in the same time it causes a decrease in the intensity of the OTR light which is detected by the CCD camera. Hence this increases the measurement errors due to the low signal/noise ratio. This issue leads to a compromise between the camera gate duration and camera gain for the measurements. The camera gain can be increased so that the low intensity can be compensated provided that no CCD saturation occurs due to the high camera gain. In addition, implementation of a more sensitive screen can be another solution for the low intensity measurements. Aluminium, ceramic and silicon screens have been used alternatively depending on the experimental conditions for the PHIN measurements. The aluminium and the silicon screens have the similar sensitivity levels while the ceramic screen is more sensitive to the electrons. The camera has to be chosen properly according to its sensitivity for the desired spectral range. And it has to be shielded carefully in order to prevent the x-ray shower on the camera. This would not only produce a background for the OTR measurement but also damages

the CCD camera and shortens its life.

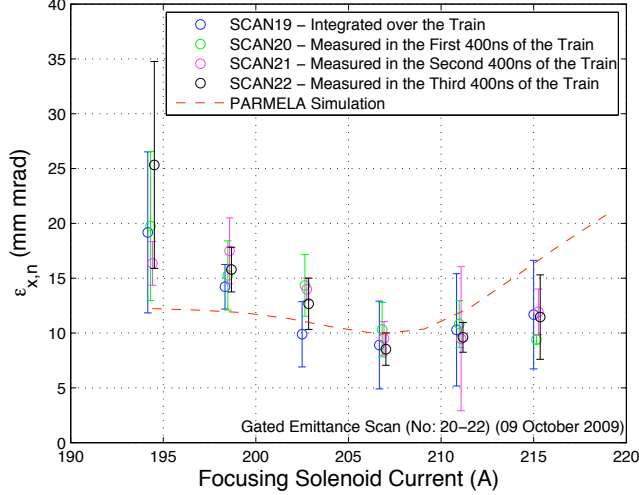


Figure 74: Emittance scan, with a beam of 1.6 nC, 4.8 MeV, along the pulse train with the steps of 400 ns.

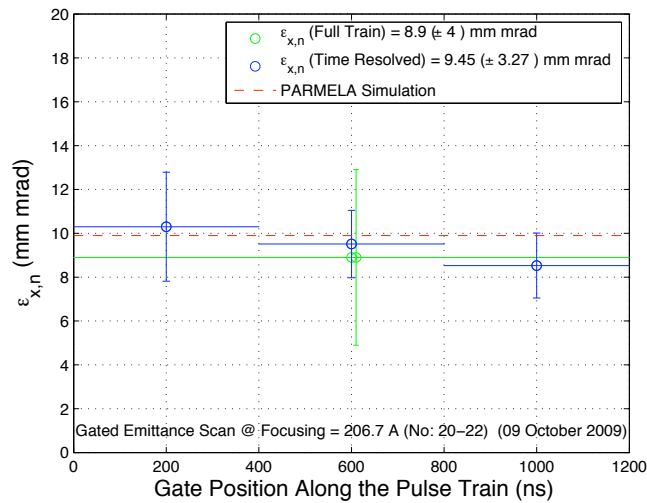
Fig. 74 presents the results of a measurement with a beam of 1.6 nC per pulse at 4.8 MeV. The emittance has been measured in the beginning, in the middle and in the end of the pulse train. The focusing solenoid current has been changed systematically during the measurement. According to the measurement the emittance compensation can be achieved by a focusing that is provided by a solenoid current of 206.7 A. The time-resolved emittance measurement where this minimum occurs is shown in detail in Fig. 75-a. For this particular measurement, the average transverse normalized emittance is 9.45 mm mrad with a fluctuation of 9.4% along the pulse train.

More results from the time-resolved emittance measurements are presented in Fig. 75-b and Fig. 75-c with increasing resolution along the pulse train. The beam parameters and the results of the emittance measurements with different resolutions are summarized in Table 29. In the table, the emittance values are given as the average of the measurements along the bunch train. The $\Delta\epsilon/\epsilon$, represent the emittance fluctuations along the bunch train. For three of the measurements, the $\Delta\epsilon/\epsilon$ values are obtained by the error propagation of the each data point measured along the bunch train.

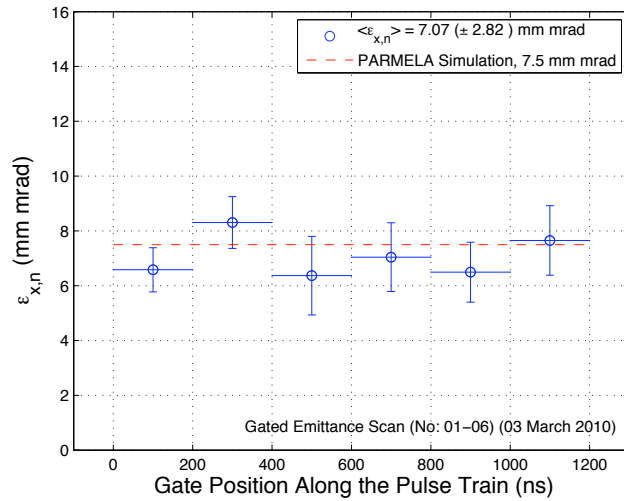
Time-resolved emittance measurements reveal an oscillation-like behavior that is refining with the increasing resolution. The variations in the RF field and the laser are the most probable sources of fluctuation. Therefore, the inheritance of the instabilities from these sources should be studied. Consequently, further investigations have been done in pursuit of a correlation between the RF field and the beam parameters. Fig. 76 shows the fluctuation of the emittance along the bunch train in comparison with the RF pulse shape. The emittance behavior follows the RF power fluctuations. This is a systematic behavior of the RF pulse shape which originates from the high voltage of the klystron. In this sense it can represents the shot-to-shot stability. The emittance stability along the bunch train can be improved by optimizing the modulator that results with a more stable RF pulse shape. The phase and amplitude stability values for the klystron in the system are 0.24° and 1%, respectively.

Table 29: The summary of the results from the time-resolved transverse normalized emittance measurements with different resolutions.

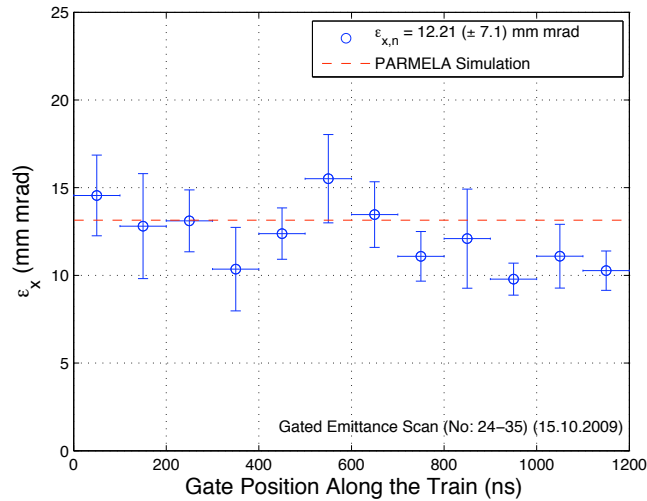
Energy (MeV)	Charge (nC)	Train Length (ns)	$\epsilon_{x,n}$ (mm mrad)	$\Delta\epsilon/\epsilon$ (%)
4.8	1.6	400	9.45	9.4
4.9	1.4	200	7.07	10.8
5	1	100	12.21	14.6



(a)



(b)



(c)

Figure 75: Emittance measurement along the pulse train with the steps of a) 400 ns (1.6 nC, 4.8 MeV), b) 200 ns (1.4 nC, 4.9 MeV), c) 100 ns (1 nC, 5 MeV).

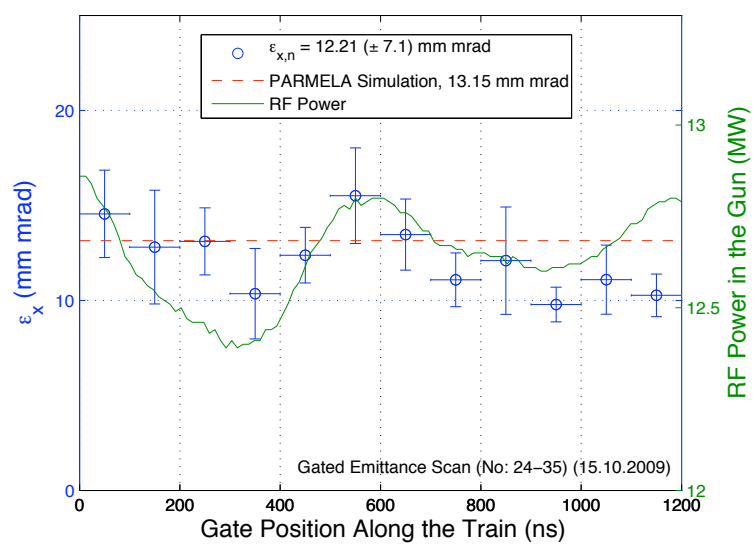


Figure 76: The emittance fluctuations along the pulse train in comparison with the RF pulse shape.

5.5 Longitudinal Phase Space

A magnetic spectrometer has been utilized for the energy and the energy spread measurements during the PHIN commissioning. The spectrometer is equipped with an OTR beam profile monitor and a segmented dump.

An example profile of a typical PHIN beam in the dispersive section is presented in the Fig. 77. The mean energy has been measured as the 5.43 MeV with a spread of 50 keV.

The practical formulas for the magnetic spectrometer has been introduced in Chapter 4. Nevertheless, it is useful to repeat them in this section. The mean energy of the beam has been determined by monitoring the dipole current in the spectrometer. The relation is given in Eq. 77. I_{Dipole} is the spectrometer current that is needed in order to focus the beam in the longitudinal axis, e.i., in the middle of the OTR screen. The OTR profile is analyzed and the energy corresponding to the peak of the profile is determined. The energy spread is retrieved from the profile as the 1σ width of the distribution. The calibration relations are given in the Eq. 78 for the energy at the peak of the profile and in the Eq. 79 for the energy spread.

$$E_0[\text{MeV}] = 0.52 \times I_{Dipole}[\text{A}] \quad (77)$$

$$E_{peak}[\text{MeV}] = E_0[\text{MeV}] + \frac{\mu_x[\text{mm}]}{8.4 \times 100} E_0[\text{MeV}] \quad (78)$$

$$\Delta E[\text{keV}] = 10 \times E_{peak}[\text{MeV}] \times \frac{\sigma_x[\text{mm}]}{8.4} \quad (79)$$

In Fig. 78, a systematic measurements of the energy and the energy spread of the beam are presented in comparison with the PARMELA simulations. The change in these observables are given in the relative units around their mean values. It has been shown that, the deviation in the energy spread reaches a minimum around the on-crest phase which provides the maximum energy.

There is no direct bunch length diagnostics which is implemented in the PHIN beamline. Nonetheless, the bunch length of the electron beam is inherit from the length of the laser pulse. Therefore, the laser pulse length measurement is important in order to determine one of the initial conditions of the electron beam. This measurement has been carried out by using a streak camera for the PHIN laser beam. One of the typical laser beam longitudinal profiles is shown in Fig. 79. The subsequent measurements of the laser pulse lengths resulted with an average 1σ value of 2.8 ps. The statistical deviation has been found as ± 0.2 ps. However, the streak camera, that is used for the measurement, has a resolution of ~ 0.7 ps. Consequently, the pulse length stability can not be determined from this measurement.

The future-implementation of the phase coding system will bring a need for longitudinal profile measurement in the PHIN studies. The measurement of the electron longitudinal profile that is produced by a phase coded laser beam is within the short term plans of the PHIN photoinjector within 2011.

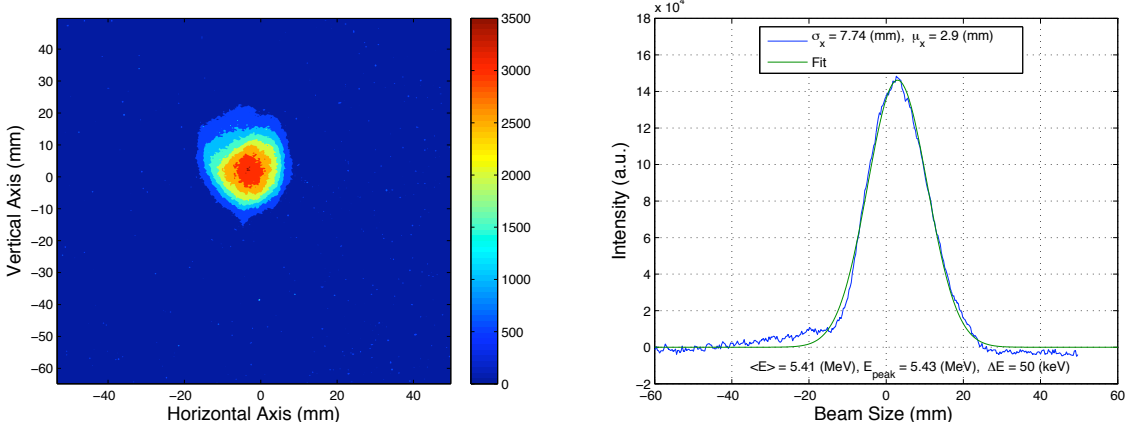


Figure 77: An example from the energy measurement in the spectrometer by OTR monitoring. a) The image that is captured by the CCD camera. b) The horizontal profile of the image.

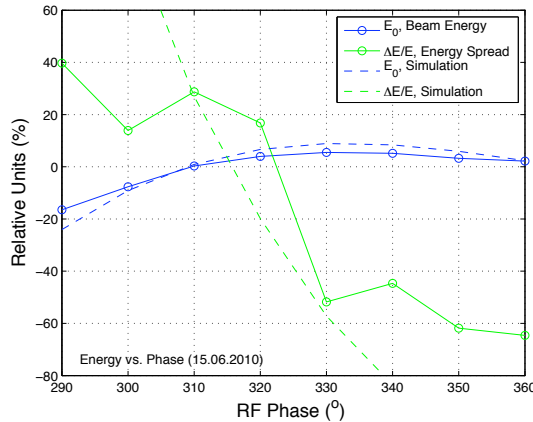


Figure 78: Energy and energy spread measurement with respect to the RF phase.

5.6 Time-Resolved Longitudinal Characterization of the Beam

The time-resolved measurements for the energy and the energy spread are possible by using a segmented dump. A segmented-dump designed and implemented in the end of the spectrometer line within the PHIN research program [88]. During the measurements, the pulse train is dumped on the segments and the signals from the individual segments are acquired enabling a time-resolved monitoring of the beam distribution through the segments [97].

The Fig. 80-a shows the time-resolved contour plot that belongs to a bunch train of 1300 ns . For this measurement the beam energy is 5.97 MeV and the energy spread is 0.73% along the bunch train which is well within the specification of $< 1\%$. The fluctuations in the energy along the bunch train have been shown to be correlated with the RF power fluctuations. The comparison of energy fluctuations and the RF power fluctuations in time, is presented in Fig. 80-b.

Another measurement is presented in Fig. 81. For this measurement, the energy spread

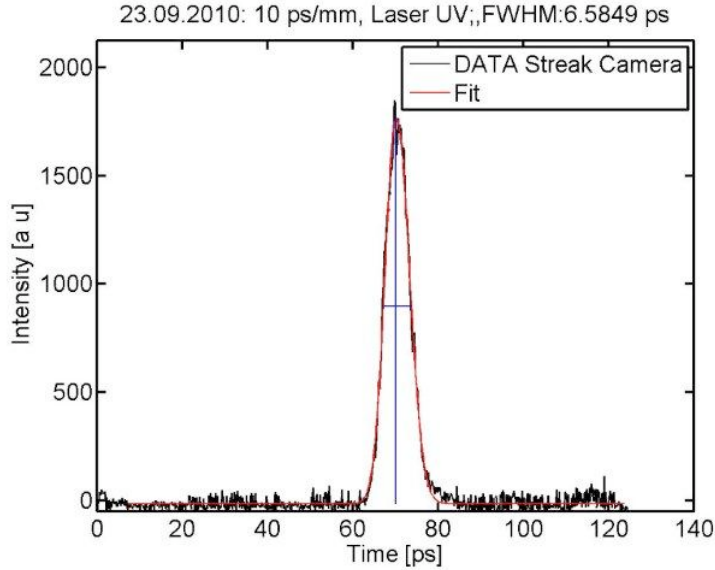


Figure 79: An example from the laser pulse train length measurement with the streak camera. The average of several subsequent measurements resulted with a 1σ of $2.8 (\pm 0.2) \text{ ps}$. This indicates a 7% shot to shot stability for the laser micropulse length.

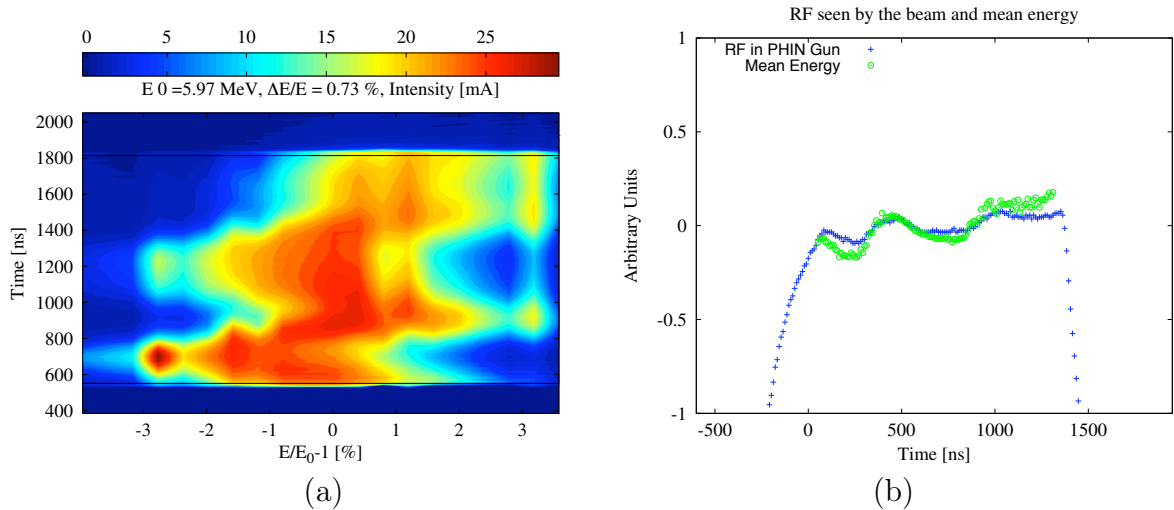


Figure 80: The time-resolved energy and energy spread measurement by the segmented dump. a) The contour plot of the energy change during the 1300 ns electron beam hitting the segmented dump. b) Deviation of the mean energy in correlation with the RF pulse shape.

is 0.6%. The fluctuation of the energy spread along the bunch train is down to 2%. The energy spread is found to be fairly constant along the bunch train.

The energy spread can also be measured by using the OTR monitoring in the dispersive section. A measurement has been presented in Fig. 82 as a function of the longitudinal position along the bunch train. This measurement shows that the results from the segmented dump and the OTR profile monitor are comparable. This reveals the reliability

of the OTR monitor as a time-resolved measurement tool. Besides, the statistical error bars on the OTR profiling results can be considered as the indications of the shot-to-shot energy spread stability.

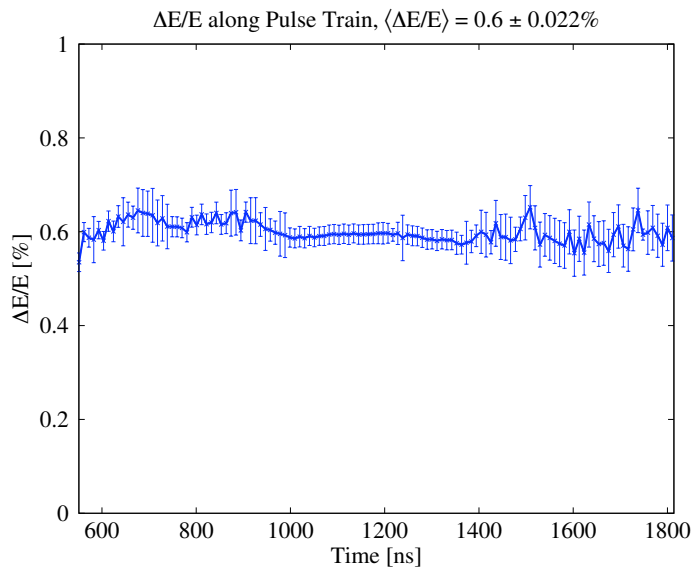


Figure 81: The time-resolved energy spread measurement.

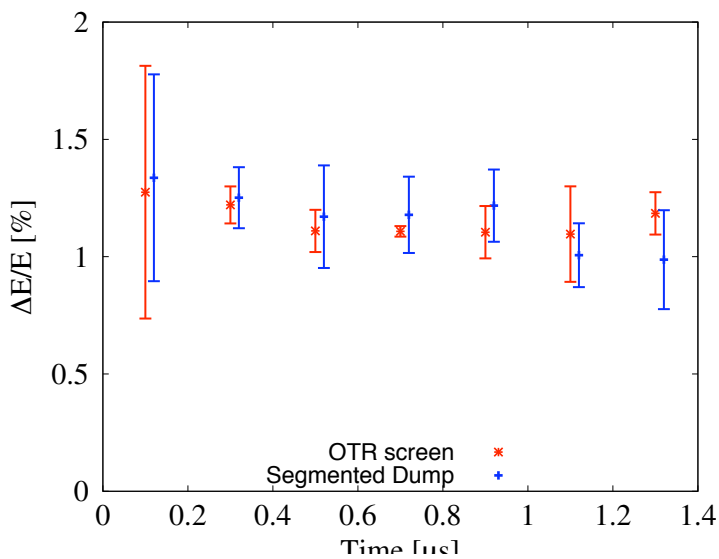


Figure 82: The comparison of the energy spread measurement with the segmented dump and the OTR profiling. The measurement has been performed as a function of the longitudinal position along the bunch train.

5.7 Correlation Between the PHIN Laser Beam and the Electron Beam

The position and the intensity stability of the laser and the electron beam of the PHIN photoinjector have been studied in order to demonstrate the correlation between the laser and the electron beams. The position and the intensity of both beams have been measured in the same time for several hours. The position and the intensity stability of electron beam has been measured using the BPR. The laser beam has been measured by using a virtual cathode and a camera within the laser table placed next to the beam line.

The point stability of both the laser and the electron beams have been measured. The statistical treatment of the data has been presented in Fig. 83 for the horizontal laser and electron beam sizes. The laser spot has been measured to be stable within $\pm 0.15\text{ mm}$ on the virtual cathode. Whereas the BPR readings has shown an electron beam position stability of $\pm 0.32\text{ mm}$. The position of the electron and the laser beams on the observation screens have been shown to be correlated. The correlation plots can be seen in Fig. 84.

The intensity stability of the laser and electron beams have been found as 3% and 4%, respectively. The corresponding histograms are presented in Fig. 85. An example of how the electron beam intensity follows the laser beam intensity is given in Fig. 86-a. During the operations a fairly constant laser beam intensity profile has been provided as in the example given by Fig. 86-b. .

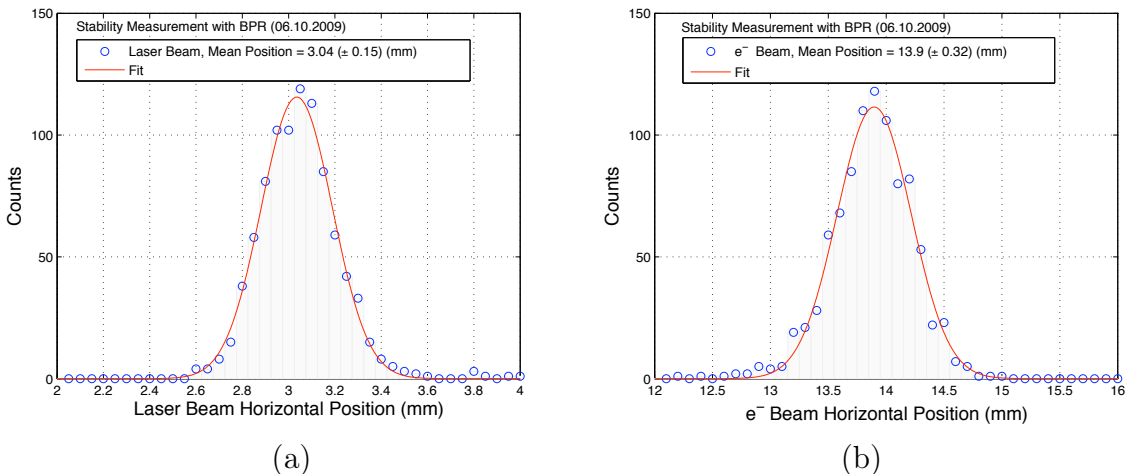


Figure 83: Horizontal position stability for a) laser beam and b) electron beam.

As a conclusion, the position and the intensity stability of the electron beam is mainly determined by the laser. The fluctuations on the RF pulse and quantum efficiency of the cathode also contribute to the beam instabilities, however they have no dominion. Therefore to better stabilize the electron beam, the laser beam has to be optimized.

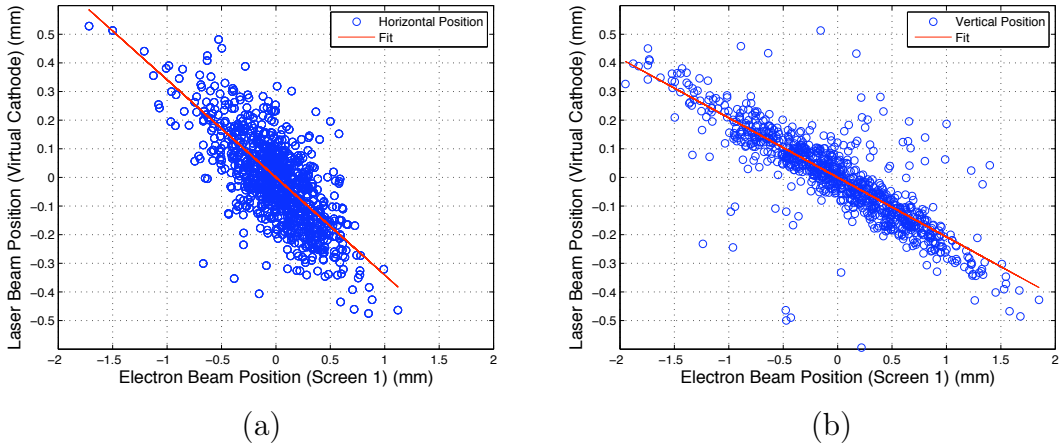


Figure 84: The correlation of the position stability between the laser and the electron beam for a) horizontal and b) vertical beam positions.

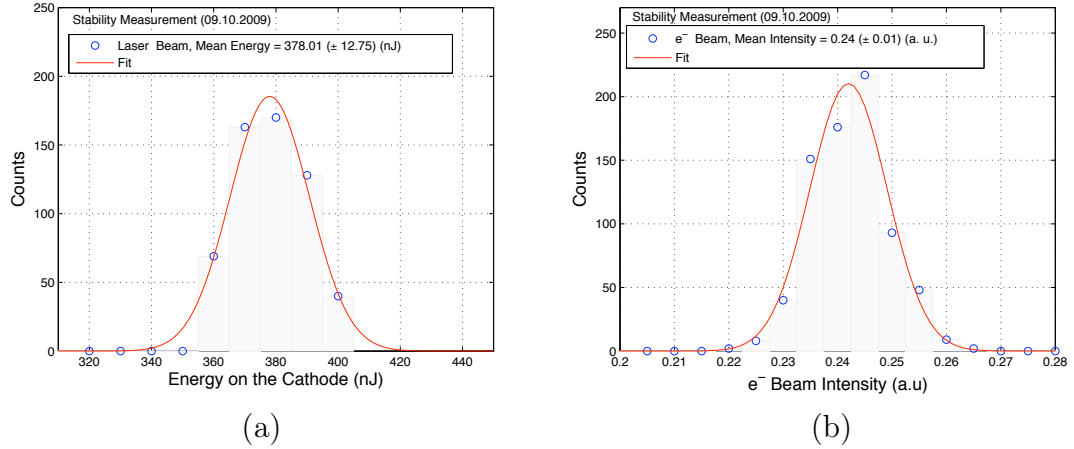


Figure 85: Intensity stability for a) laser beam and b) electron beam.

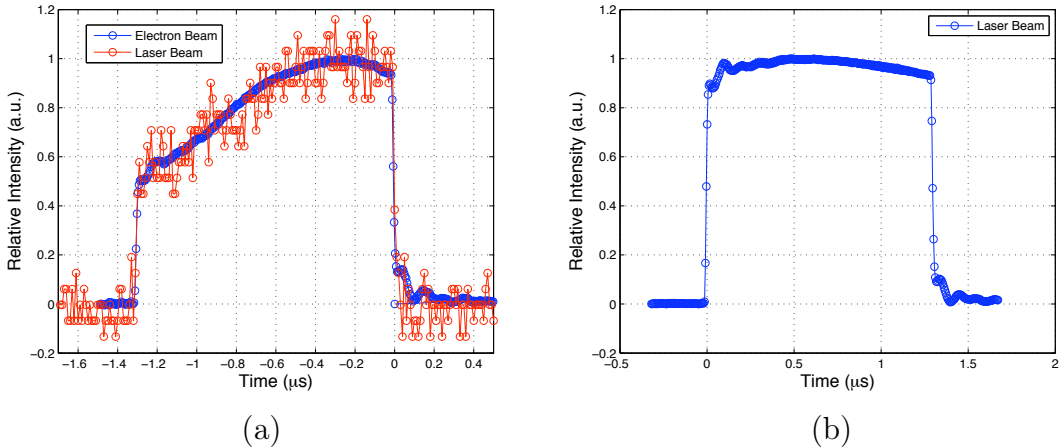


Figure 86: a) An example to demonstrate the intensity of the electron beam follows the laser intensity profile. b) An example of the flat laser intensity profile.

5.8 Conclusions and The Post-Commissioning Activities for PHIN

During the PHIN commissioning, the systematic measurements and the simulations have been done in order to characterize the transverse and longitudinal beam parameters. The stability and the tolerances of the injector have been studied. The results are summarized in Table 30 in comparison with design specifications. As seen in the table, all the design specifications have been satisfied except the charge stability. However, this should be improved by the implementation of a laser feedback stabilization system in 2011.

Table 30: The specifications in comparison with the achieved values for the PHIN photoinjector.

Parameter	Specification	Achieved
<i>Laser</i>		
UV Laser Pulse Energy (nJ)	370	400
Micropulse Repetition Rate (GHz)	1.5	1.5
Macropulse Repetition Rate	1 – 5	1
Train Length (ns)	1273	1300
<i>Electron Beam</i>		
Charge per Bunch (nC)	2.33	4.4
Charge per Train (nC)	4446	5800
Current (A)	3.5	6.6
Transverse Normalized Emittance (mm mrad)	< 25	14
Energy Spread (%)	< 1	0.7
Energy (MeV)	5.5	5.5
Charge Stability (%), rms	< 0.25	0.8
<i>RF Gun</i>		
RF Gradient (MV/m)	85	85
Quantum Efficiency (%)	3	3 – 18

The amplitude instability in a laser system can have different sources. For the PHIN laser system these possible sources have been defined as electrical noise, noise from the pumping diodes, noise from the oscillator and preamplifier, pointing instabilities, thermal drifts and mechanical vibration. The pointing instabilities, which are related to the instabilities on the mean position of the laser on the cathode, can be caused by the water cooling system, temperature variations due to the quality of the air conditioning, vibrations, airflow in the beam transport up to the cathode. A laser feedback system to improve the amplitude and the pointing stability for PHIN laser system is under development. The implementation of this system is within the short term plans. It has been measured that the position stability of the laser beam on the laser table is factor of 2 better than the

position stability of the electron beam after a $\sim 1.5\text{ m}$ of transport in between. Therefore, the transfer medium could be improved for a better transmission of the laser beam. In addition to the inherent laser instability, the electron beam instability can also be a combination of the alignment of the laser on the cathode and the RF instability.

The following aspects could be considered as the possible future improvements of the diagnostics system for the PHIN photoinjector.

The transverse emittance studies have been performed with the multi-slit method. The method was sufficient in terms of the precision of the results and its applicability to the space charge dominated low-energy beams. Though, there could be certain advantages in implementing different emittance diagnostics. The pepperpot method might be proposed as one of the candidates. The method enables to reach the information on both the horizontal and the vertical transverse normalized emittance while the measurement of only one of the axis is possible with the multi-slit method. Additionally the moving-slit method could be considered for its higher sensitivity to the tails of the phase space provided that a good position and intensity stability for the beam is maintained. However the latter would not provide a single shot measurement unlike the pepperpot or multi-slit methods.

Regardless of the method that is used, the emittance measurement on different longitudinal positions of the beamline would certainly reveal important information. Monitoring the emittance until a certain distance from the focusing solenoid magnet would be another satisfactory way of demonstrating the emittance compensation. For this application, installation of the few OTR monitors would be needed on the beamline.

6 The Conceptual Study of a New RF Gun for the CLIC Drive Beam Photoinjector

Contents

6.1 The Requirements and the Stability Challenges of the CLIC Drive Beam Photoinjector	123
6.2 The design of an 1 GHz RF Gun for the CLIC Drive Beam Photoinjector	125
6.3 The Beam Dynamics Aspects	128

The PHIN photoinjector has been designed with respect to the current CTF3 injector requirements. The design has been installed and commissioned in order to demonstrate the feasibility of the implementation as the CTF3 injector and also to motivate a photoinjector system for the CLIC drive beam. In conjunction with these feasibility studies, the aim of the research program is to compile the learned lessons in order to be considered during the future CLIC drive beam injector studies.

The research results, which reflects the current status of the photoinjector R&D within the CLIC study, have been presented and discussed throughout the previous chapters. This chapter is devoted to a conceptual study, regarding the design of an RF gun in order to constitute a preliminary step towards the CLIC drive beam photoinjector. The design steps of the 1 GHz RF gun and the beam dynamics simulations are presented following the introduction to the injector requirements for CLIC drive beam.

6.1 The Requirements and the Stability Challenges of the CLIC Drive Beam Photoinjector

The charge stability of PHIN photoinjector has been considered as a feasibility item which indicates that a photoinjector is, in fact, a suitable candidate to be a drive beam source. The deliverable stability by the PHIN photoinjector meets the drive beam tolerances in the same order of magnitude.

The comparison between the measured stability of PHIN parameters and the simulated drive beam tolerances is presented in Table 31, in terms of the RF and the electron beam stability. In the table, the RF phase stability has been given as 0.24% according

to the current measurements from the CTF3 klystrons. However, the RF stability is a requirement of the CLIC injector and it is independent of the photoinjector option. This issue has been studied within the CLIC feasibility program.

A 0.8% charge stability has been achieved during PHIN commissioning. In addition to the current achievements, several improvements are planned and included within the short term plans of the upcoming PHIN operation schedule. Within this context, a feedback system will be installed to improve the laser intensity stability and the mirror that is used in the vacuum for laser optics will be renewed in 2011. These improvements will provide a better intensity stability of the laser beam on the cathode and should compensate for the factor of five more stability. Consequently, a higher charge stability will have been fulfilled.

The improvement of stability for the high power RF pulse shape might result with a more stable energy and emittance along the pulse train.

Table 31: The measured PHIN stability in comparison with the simulated CLIC Drive Beam (DB) tolerances at the end of the injector.

Parameter	PHIN	CLIC DB
RF Stability		
Phase ($^{\circ}$)	0.24	0.05
RF Amplitude (%)	1	1
Electron Beam		
Beam Current (%)	0.8	0.2
Laser Pulse Length* (%)	7	1

*Laser pulse length stability has been considered as the initial bunch length stability.

A new RF gun design has been initiated, as an additional item of the PHIN photoinjector research. This extensional effort aims to investigate the beam dynamics in an RF gun with the CLIC drive beam specifications. Therefore, the PHIN specifications for the RF gun frequency and the charge per bunch value have been modified according to the CLIC drive beam requirements. Some of the design parameters for the CLIC drive beam linac at the end of the injector is summarised in Table 32. In the table, an RF frequency of 1 GHz is given. The frequency choice is a matter of fact that the bunch spacing for the CLIC drive beam is 500 MHz before the recombination with a factor of 24 in order to produce the 12 GHz bunch repetition frequency.

The frequency choice for the drive beam injector had lead to the study of a new RF gun which is modified from the existing 3 GHz system. Whereas the current baseline design for the drive beam injector is a thermionic gun with the continuing conceptual design efforts as given in reference [98]. Throughout the text, the comparison of the both options will be done according to some beam dynamics aspects of the CLIC drive beam injector.

Table 32: Some the design parameters for the CLIC Drive Beam Linac at the end of the injector with the energy of 50 MeV .

Parameters	Value
RF Frequency (GHz)	1
Charge/Bunch (nC)	8.4
RMS Bunch Length (ps)	10
Transverse Normalized Emittance (mm mrad)	≤ 100
Energy Spread (%)	≤ 1

6.2 The design of an 1 GHz RF Gun for the CLIC Drive Beam Photoinjector

A $2 + 1/2$ cell RF cavity with the resonance frequency of 3 GHz has been used for the current photoinjector studies. Therefore, in order to extend the studies towards the future CLIC drive beam photoinjector, an RF gun design with the resonance frequency of 1 GHz has been obtained by rescaling the current PHIN cavity. The rescaled geometry is presented in Fig. 87 with the accompanying field lines corresponding the π resonance mode. The figure is the solution of an RF design simulation program, SUPERFISH [72]. This rescaled model has been used for the initial investigation of the beam dynamics. A more detailed feasibility study should be conducted.

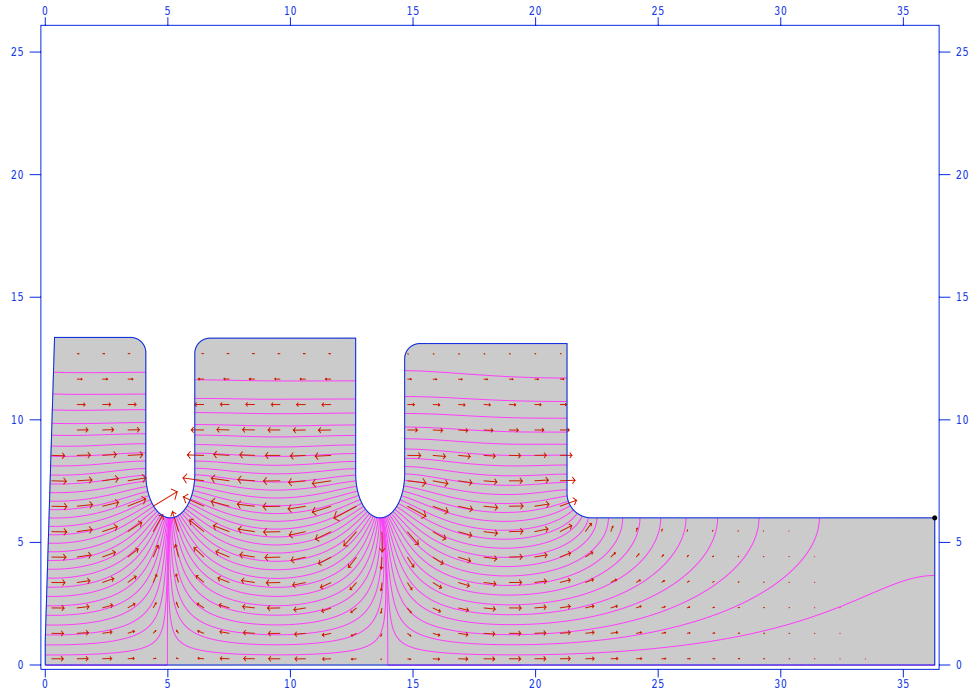


Figure 87: The SUPERFISH solution for the 1 GHz RF gun that is excited in π -mode.

An example SUPERFISH input file can be found in Fig. 88. Once defining the geometry

```

1 GHz RF Gun Design
&reg kprob=1, ; Superfish problem
dx=0.09,
freq=1003.811 , ; Starting frequency in MHz
dslope=-1, ; Allow convergence on first iteration
xdri=2.245,ydri=13.36 ; Drive point location&

&po x=0.0,y=0.0 &
&po x=0.0,y=1.0 &
&po x=0.39,y=13.36&
&po x=3.48,y=13.36&
&po nt=2,x0=3.48,y0=12.74,x=0.62,y=0.0&
&po x=4.1,y=7.79 &
&po nt=2,x0=5.1,y0=7.79,A=1.0,B=1.79,x=1.0,y=0.0 &
&po x=6.1,y=12.72&
&po nt=2,x0=6.72,y0=12.72,x=0.0,y=0.62&
&po x=12.660,y=13.34 &
&po x=12.66,y=7.79&
&po nt=2,x0=13.66,y0=7.79,A=1.0,B=1.79,x=1.0,y=0.0 &
&po x=14.66,y=12.49 &
&po nt=2,x0=15.28,y0=12.49,x=0.0,y=0.62 &
&po x=21.28,y=13.11 &
&po x=21.28,y=7 &
&po nt=2,x0=22.28,y0=7,x=0.0,y=-1.0 &
&po x=36.28,y=6 &
&po x=36.28,y=0.0 &
&po x=0.0,y=0.0 &
```

Figure 88: An example SUPERFISH input file for the 1 GHz RF gun which is designed for the CLIC drive beam photo injector.

of the cavity, a frequency scan have been done in order to determine the modes that can be excited in this cavity. The mode frequencies have been determined for the rescaled cavity. Technically, the result is produced as a plot that shows the behaviour of the Dirichlet function with respect to the frequency². The mode frequencies are determined as the solutions providing a $D = 0$ at the negative slopes of the curve. The result of the frequency scan is shown in Fig. 89. As confirmed with the plot, the given design has been tuned in order to excite the resonance frequencies of 920.5 MHz ($0 - \text{mode}$), 968.5 MHz ($\pi/2 - \text{mode}$) and 1000.5 MHz ($\pi - \text{mode}$). The π -mode is used for the acceleration in the cavity. In Table 33, the RF properties are summarized for the acceleration mode.

The cavity design has been optimized in order to minimize the transverse normalized beam emittance and the energy spread as well as to provide the maximum particle transition. Within this optimization strategy, the angle of the first half-cell wall has been

²For the resonance frequency determination in SUPERFISH the so called Dirichlet function, $D(k^2)$, which is independent of the magnetic field strength or the current in the region of calculations, is defined [72].

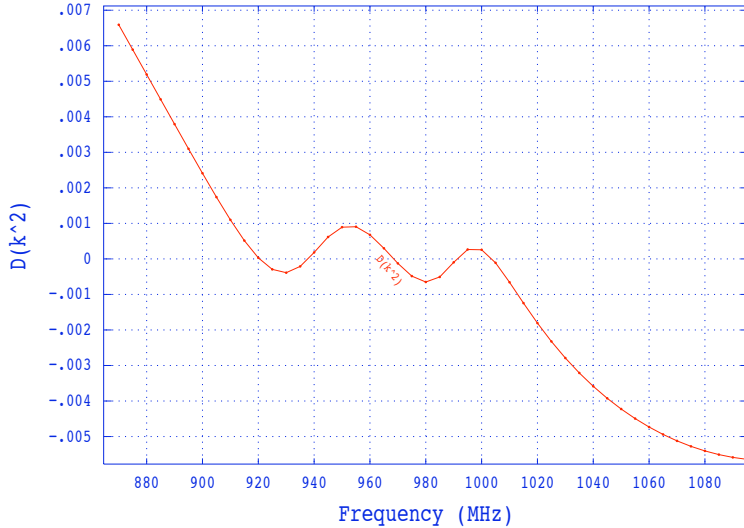


Figure 89: The result of the SUPERFISH frequency scan which shows the resonance frequencies for different modes. The resonance frequency of 1 GHz has been used for the conceptual study of RF gun for the CLIC Drive Beam photoinjector.

Table 33: The RF parameters that are given by the SUPERFISH simulations for the π -mode.

Parameter	Value
Frequency (GHz)	1
Operating Temperature ($^{\circ}\text{C}$)	20
Quality Factor, Q	18657.2
Shunt Impedance ($M\Omega$)	5.7
Peak Power Dissipation ($k\text{W}$)	63.6
RF Power (MW) @ 40 MV/m	67

altered. For different wall angles, the cavity geometry has been adjusted in order to obtain the 1 GHz resonance frequency in π -mode and the corresponding field maps have been produced. These maps have been introduced into PARMELA simulations and the emittance values have been recorded. An angle of 1.6° has been chosen for the final design which provides the minimum transverse normalized emittance.

The flat on-axis electrical field across the cells must be produced in order to control the energy spread. This has been achieved by adjusting the heights of individual cells. However, these adjustments caused the deviation from the design resonance frequency of 999.5 MHz and resulted with a resonance frequency of 1003.811 MHz . The latter value has been used for the beam dynamics simulations which is close to the design frequency.

Several beam dynamics simulations have been performed in order to characterize the beam properties when it is accelerated by the 1 GHz RF gun. The results are presented in the following section.

6.3 The Beam Dynamics Aspects

The main specifications of the RF gun has been investigated under the guidelines of the model which has been described in Chapter 2 and also by performing several beam dynamics simulations.

The beam dynamics simulations have been performed by using the PARMELA program for the cavity which is under investigation. The RF cavity and the essential focusing units have been defined in the PARMELA input file. Several drift sections have been introduced after the cavity in order to study the evolution of the beam parameters. A PARMELA input file for the 1 GHz RF gun is shown in Fig. 90.

```
TITLE CLIC DB RF GUN Test

RUN /n0=1 /ip=999 /freq=1003.8111 /z0=-0.001 /W0=1.0e-6 /itype=1
OUTPUT 5
INPUT 9 /np=5999 /sigr=0.1274 /rmax=1.0 /sigt=6.0 /tmax=25
DRIFT 0 2 1

CELL /l=36.28 /aper=2.0 /iout=1 /phi0=150 /E0=40 /nc=1 /dwtmax=5.0 /sym=-1
CFIELD 1
flatfield06.T7

COIL 0 20 -0.1715e5 0 250
COIL 16.58 20 0.3830e5 0 250
COIL 51.83 20 -0.3017e4 0 250

DRIFT /l=3.72 /aper=6.0 /iout=1
DRIFT /l=10 /aper=6.0 /iout=1
DRIFT /l=50 /aper=6.0 /iout=1
DRIFT /l=50 /aper=6.0 /iout=1
DRIFT /l=50 /aper=6.0 /iout=1
DRIFT /l=50 /aper=6.0 /iout=1

ZOUT 600 0 0 250 0 0
SCHEFF /beam1=8.4 0.5 5 10 20 300 0
START /wt=0 /dwt=1 /nsteps=30000 /nsc=1 /nout=10
end
```

Figure 90: An example PARMELA input file for the 1 GHz RF gun which is designed for the CLIC drive beam photo injector.

The SUPERFISH program can produce an output for on-axis electrical field of the cavity that can be used as an input to the beam dynamics simulation program, PARMELA. The on-axis electrical field that is generated by the designed cavity has been extracted for this purpose and it is presented in Fig. 91.

Regarding the maximum achievable gradient in a cavity, one can recall the Travier's criterion. The formula that has been introduced in Chapter 2, is repeated in Eq. (80) as a reminder. According to the criterion, a maximum gradient of $\sim 60 \text{ MV/m}$ is possible to achieve for the resonance frequency of 1 GHz. A moderate gradient of 40 MV/m has

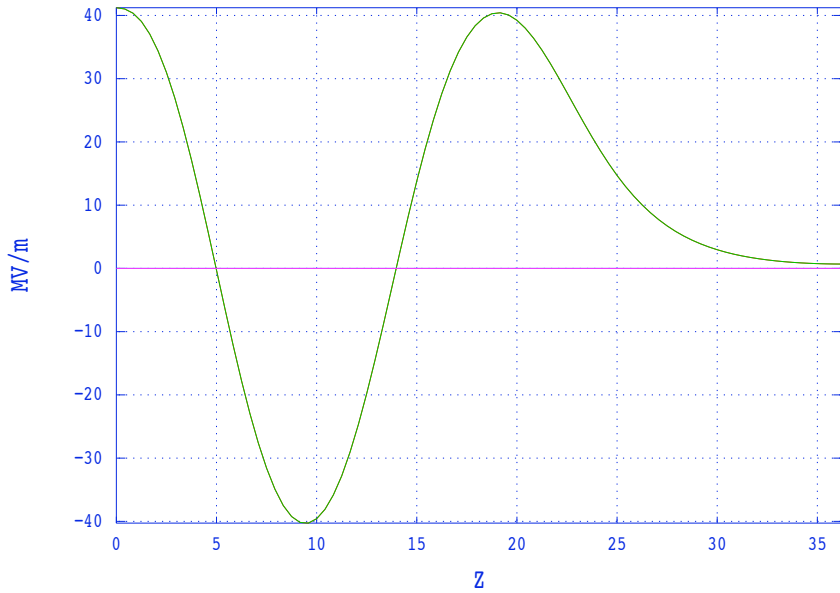


Figure 91: The on-axis electric field of 40 MV/m is excited in the cavity.

been chosen within this range by considering the existing S-band cavities as introduced in Chapter 2. Nevertheless, this value might be higher for the normal conducting technology.

$$E_{0,max}[\text{MV/m}] = 8.47 + 1.57\sqrt{f[\text{MHz}]} \quad (80)$$

The gradient value is given for a particular phase difference between the RF and the beam that is chosen in the PARMELA simulations. The emission phase of the particles with respect to the RF (master clock in PARMELA) is determined according to the result of the simulated phase scan at a given gradient, as discussed in Chapter 3. This emission phase should be chosen which provides the maximum energy gain from the RF field. Additionally, a constant bunch length along the beamline implies a proper bunching. The changes in the bunch length cause a change in the energy spread. Therefore, the evolution of the bunch length along the beamline is another important criteria for the phase choice. According to the model, an upper limit has been set for the initial bunch length as shown in Eq. (81). This upper limit is calculated as 50 ps for a cavity with the resonance frequency of 1 GHz . Therefore, the initial value for the bunch length in the PARMELA input file has been confirmed to fulfill the design guideline. This value has been chosen as 6 ps (1σ), a factor of two larger than the PHIN input bunch length, in order to decrease the space charge effect due to the higher charge.

$$\sigma_b[\text{ps}] \leq \frac{5 \times 10^4}{f[\text{MHz}]} \quad (81)$$

Fig. 92 presents a phase scan that has been done for the current design. The variations of the transverse normalized emittance and the beam energy are shown in comparison, in the figure. According to these results the maximum energy gain occurs at 160° while the minimum emittance is obtained, at the exit of the gun, with an emission phase of 120° . The maximum energy gain and the minimum emittance are not produced at the

same emission phase. As a design strategy, the nominal phase value has been defined as the phase which provides the best trade-off between the energy spread and the bunch length. However, one can still optimize the transverse emittance by employing one of the compensation schemes after the determination of the nominal phase.

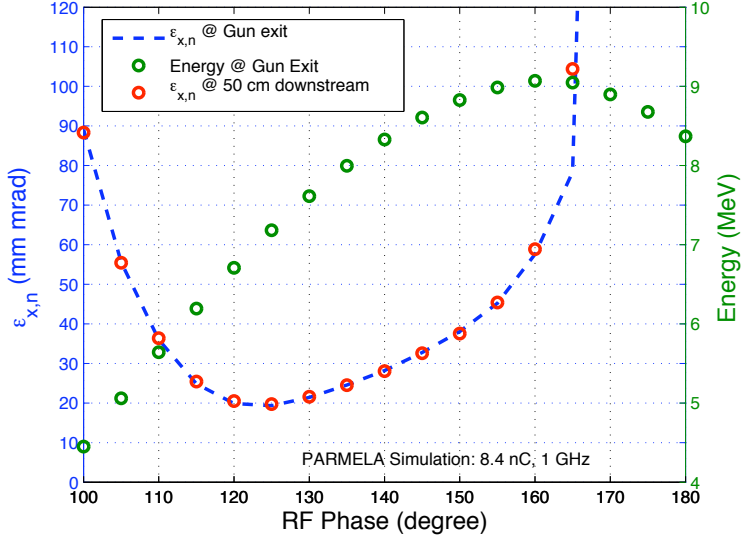


Figure 92: The variation of the beam energy and the transverse normalized emittance as a function of the emission phase.

The evolution of the bunch length, the energy spread and the longitudinal normalized emittance have been simulated for several different phase values. The results of the simulations are presented in Fig. 93. A minimum for the energy spread and the longitudinal emittance has been obtained at the emission phases of 160° and 150° , respectively. Nevertheless, an emission phase of 150° has been chosen which provides the minimum longitudinal normalized emittance, namely, the best compromise between the energy spread and the bunch length. The 160° , that provides the maximum energy, has not been chosen due to the distortion in the bunch length in that phase as seen in the figure. Additionally, the related energy ramp is presented in Fig. 94-a which is increasing as a step function across each cell at different phases.

The parameters have been investigated at the nominal phase of 150° . First of all, a proper bunching has been ensured by maintaining a constant bunch length of 18 ps , along the beamline. Regarding phase choice, the compromise between the energy spread and bunch length results a longitudinal emittance of $75\text{ }\mu\text{m}$. The energy remains constant after the RF gun at the value of 8.8 MeV for the gradient of 40 MV/m . The corresponding energy spread can be rephrased as 3.4% at this beam energy. Additionally, the variation of the transverse normalized emittance is presented in Fig. 94-b, the emittance varies between $36 - 38\text{ mm mrad}$ at different longitudinal positions of the beamline. The further optimization of the transverse normalized emittance has been performed by using a external focusing field. This field has been provided by defining three “COIL” elements in PARMELA simulations. The result of the compensation study will be presented.

The maximum achievable charge per bunch value can be estimated by the laser spot size and the accelerating gradient as given in Eq. (82). In this example, the gradient

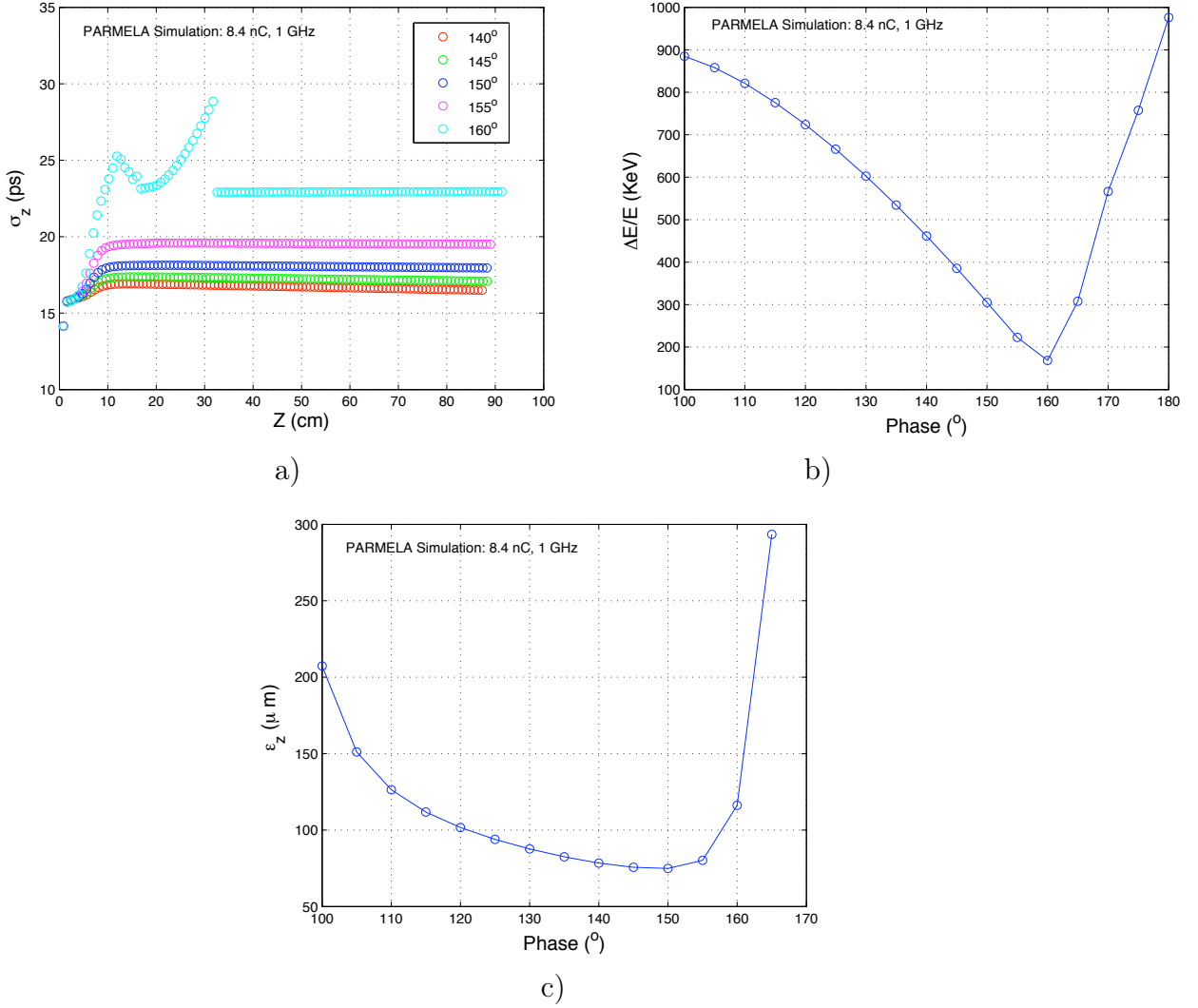


Figure 93: a) The bunch length along the beamline. In PARMELA simulations, a constant the bunch of 19.5 ps has been achieved at the particular emission phase of 155° . b) The variation of the energy spread with respect to the emission phase. The minimum energy spread of 168.6 KeV can be obtained at the emission phase of 160° . c) The variation of the longitudinal emittance as a function of the emission phase. The minimum longitudinal emittance of $75\text{ }\mu\text{m}$ occurs at the phase of 150° .

value is fixed at 40 MV/m and the laser spot size can be considered as the free parameter to increase the charge. The CLIC drive beam specification for the charge per bunch value is 8.4 nC as given in the previous section. Therefore a 1σ laser spot size of $\sim 2\text{ mm}$ is found to be sufficient to produce the required charge of 8.4 nC per bunch regarding the accelerating gradient of 40 MV/m .

$$Q_{max}[\text{nC}] = \frac{E_{acc}[\text{MV/m}]\sigma_L^2}{18} \quad (82)$$

As a matter of fact, the preliminary design is sufficient under the consideration of the

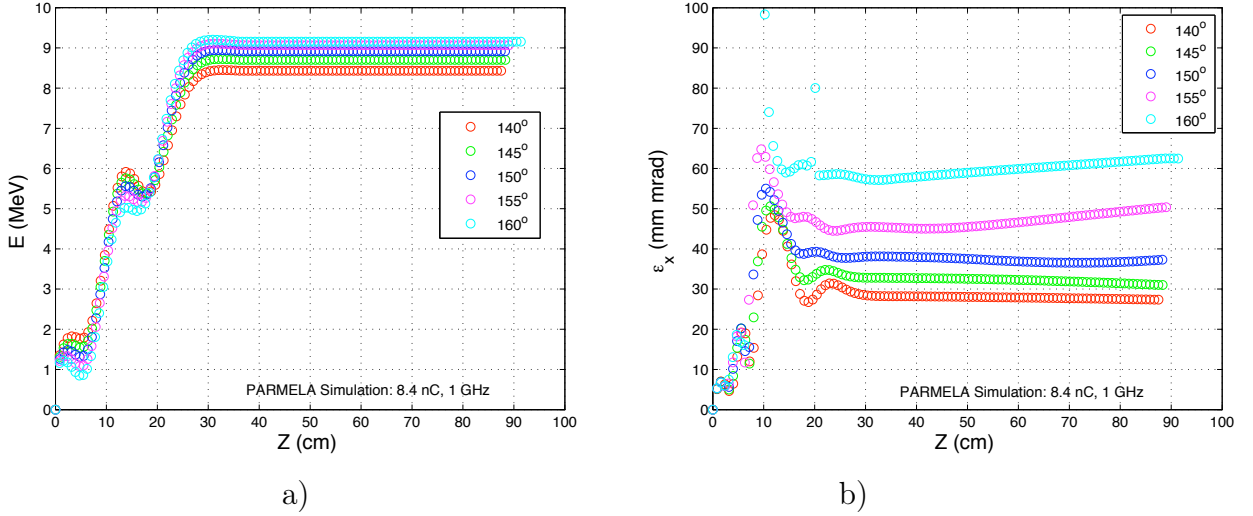


Figure 94: a) The energy ramp up through the cells of the $2+1/2$ cell cavity and throughout the beamline for different emission phases. b) The evolution of the transverse normalized emittance for various emission phases.

main design criteria of the model.

Similar to the PHIN set-up a pair of coils should be placed before and after the RF gun, standing for the so called “bucking” and the “focusing” solenoids. The effect has been simulated by defining three “COIL” elements in PARMELA. The program generates a background magnetic field by taking into account the combined effect of these coils. The placement and the current value of the first coil has been optimized so that the magnetic field on the cathode maintained to be zero. The second and the third coils have been optimized by rescaling from the existing PHIN configuration with respect to the ratio of the cavity lengths. This background field is scaled in order to simulate the different magnetic focusing levels. The behavior of the beam under different magnetic focusing conditions have been investigated. These investigations are necessary in order to study the emittance compensation. The theory of the emittance compensation and the implementation for the PHIN photoinjector have been discussed in detail in the previous chapters.

The evolution of the beam size and the transverse normalized emittance are presented in Fig. 95-a and b. According to the simulations, the emittance compensation occurs at a particular distance from the cathode under the nominal focusing. A transverse normalized emittance of 34.7 mm mrad at the exit of the gun is reduced to 27.1 mm mrad at a distance of 250 cm from the cathode under the magnetic focusing of 965.5 Gauss . This particular longitudinal position can be considered as the location of the next accelerating structure in order to conserve the optimized beam properties.

Consequently, the particular magnetic field of 965.5 Gauss has been determined to produce the nominal focusing and provide the emittance compensation. The calibration of the coils in terms of the PARMELA units is given in Table 34 for this nominal magnetic settings. The resulting magnetic field distribution is presented in Fig. 98.

The behavior of the emittance under different focusing conditions is simulated and a summary is given in Fig. 96. In the figure, the variation of the emittance is shown for

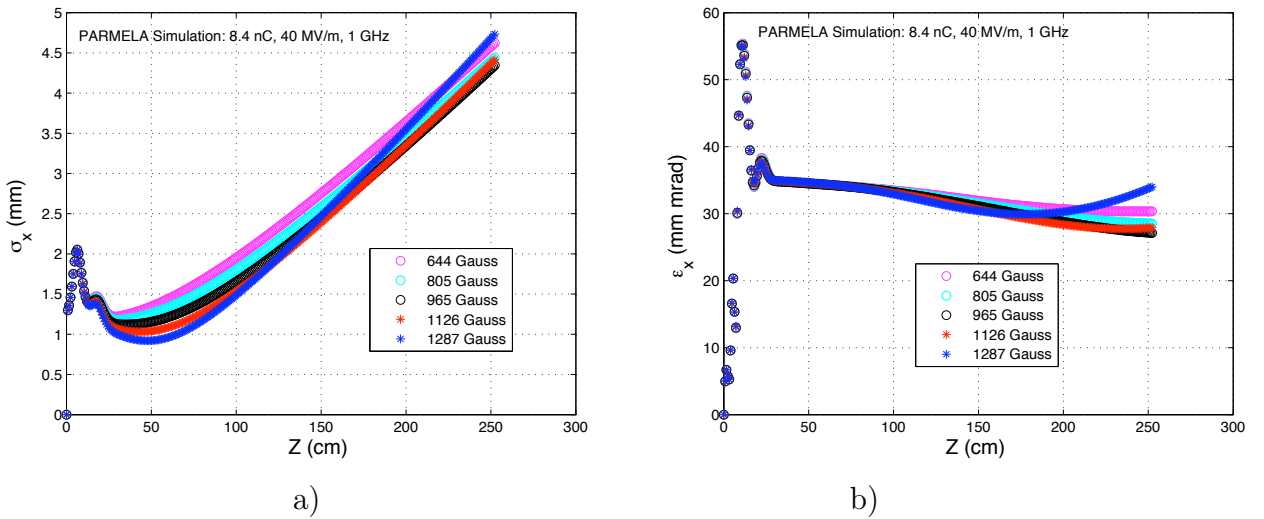


Figure 95: The evolution of a) the transverse beam size and b) the normalized emittance along the beamline. The emittance compensation occurs at a distance of 250 cm away from the cathode.

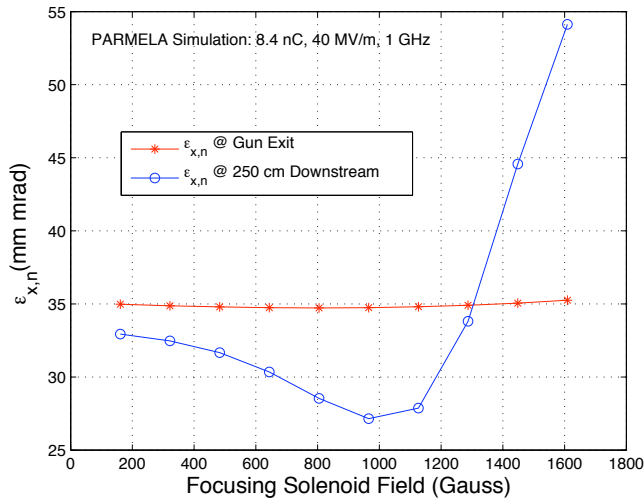


Figure 96: The evolution of the transverse normalized beam emittance with respect to the focusing magnet field at a downstream point, 250 cm away from the cathode. The emittance compensation occurs under the focusing of a magnetic field of 965.5 Gauss.

Table 34: The reference calibration for the nominal settings of the solenoids.

PARMELA Settings ($\times 10^5$)			Peak Magnetic Field (Gauss)
COIL 1	COIL 2	COIL 3	
-0.1715	0.3830	-0.03017	965.5

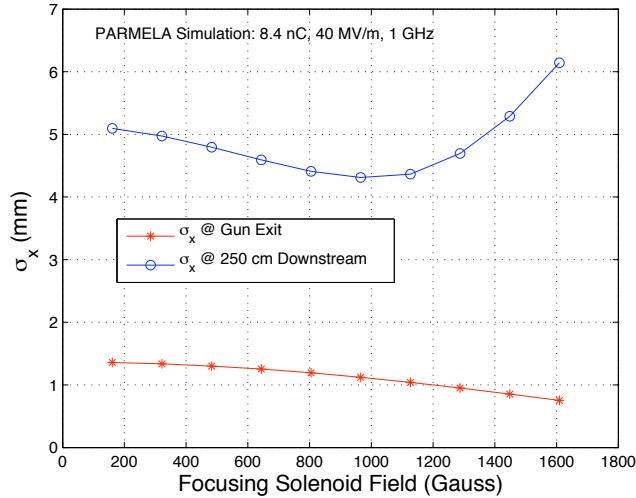


Figure 97: The evolution of the beam size with respect to the focusing magnet field at a downstream point, 250 cm away from the cathode.

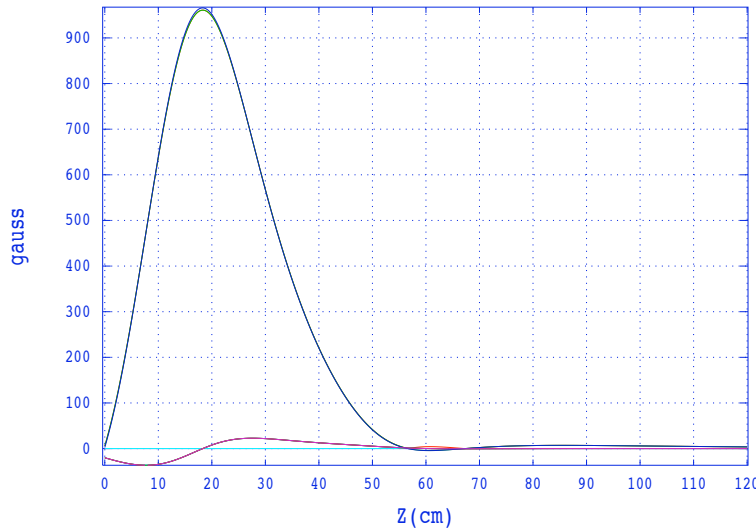


Figure 98: The background magnetic field that is created by PARMELA program as a result of the defined coil positions and currents.

both at the exit of the gun and at the downstream position of 250 cm where the emittance compensation occurs. The evolution of the beam size as a function of the focusing magnet field has been also simulated and is presented in Fig. 97.

The transverse and longitudinal beam parameters have been retrieved for the optimized magnet settings and the RF phase. The design specification and these resulting beam properties are summarized in Table 35 in comparison with the baseline thermionic option. The study indicates that the specifications for the drive beam can be achieved also by a photoinjector without producing unwanted parasitic charge. This parasitic charge between the bunches is a by-product of the bunching system which is used in the case of the thermionic gun. The current preliminary design for the 1 GHz RF gun already provides

the required transverse beam emittance as denoted within the drive beam specifications. The bunch length and the energy spread are slightly exceeding their design values. However, these values can be optimized by the extension of the preliminary design which is presented in this chapter. As an example, the bunch length can be reduced by compression after the gun. Whereas, the energy spread which is given for the RF gun is at the energy of 8.8 MeV and can be reduced by further acceleration after the injector.

Table 35: The design specifications and the resulting beam dynamics parameters for the 1 GHz RF gun in comparison with the thermionic gun.

Parameter	RF Gun	Thermionic Gun	CLIC Drive Beam
RF Frequency (GHz)	1	1	1
Gradient (MV/m)	40	-	-
Charge / Bunch (nC)	8.4	8.16	8.4
Beam Size (1σ), σ_x (mm)	4.3	-	-
Laser Spot Size (1σ), σ_L (mm)	2	-	-
Normalized Emittance, $\epsilon_{x,n}$ (mm mrad)	27.1	32.9	< 100
Beam Energy (MeV)	8.8	53.2	2730
Bunch Length, σ_z (ps)	18	9.43	$10 - 3.33$
<i>RMS</i> Energy Spread, ΔE (KeV) / (%)	297 / 3.37 (8.8 MeV)	450 / 0.84 (50 MeV)	$\leq 1\%$ (50 MeV)
Satellite Bunches (%)	0	4.9	as less as possible

The transverse and the longitudinal phase space distribution of different injector options for CLIC drive beam have been presented in Fig. 99 and Fig. 100. The values for the thermal injector belong to the end of the injector where the beam energy is 50 MeV . For the case of the RF gun, the given values are from a downstream point of 250 cm where the emittance compensation occurs at the current settings. The comparison between the longitudinal phase space distributions from different injector options reveals that a photoinjector is clear from the entailment parasitic charge.

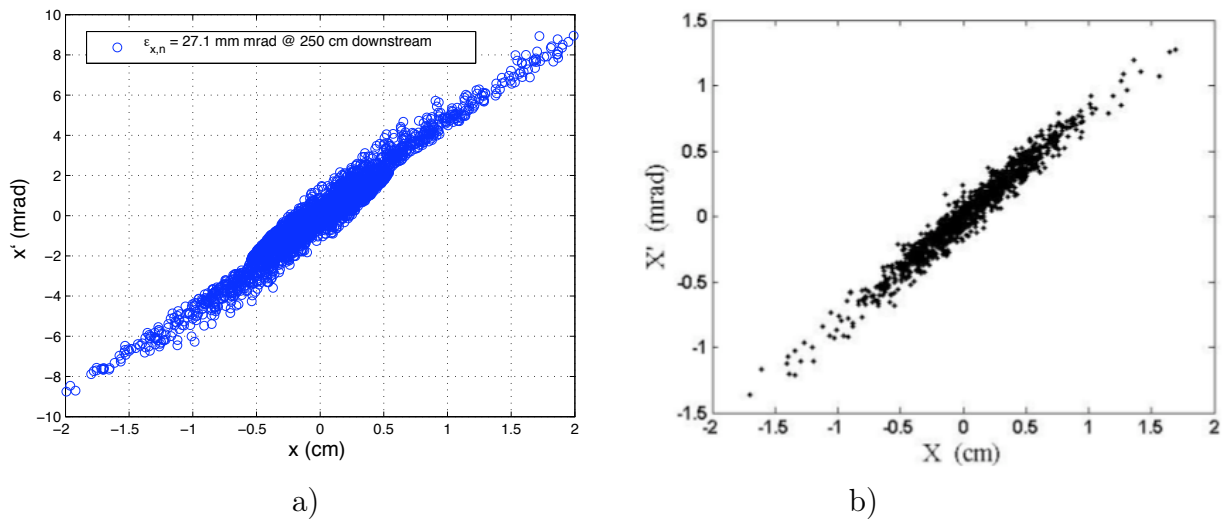


Figure 99: The transverse phase space for the 1 GHz RF gun, at the magnet settings for the emittance compensation a) for the RF gun at a downstream location where the emittance compensation occurs (27.1 mm mrad @ 8.8 MeV), b) for the thermionic gun at the end of the injector (32.9 mm mrad @ 50 MeV).

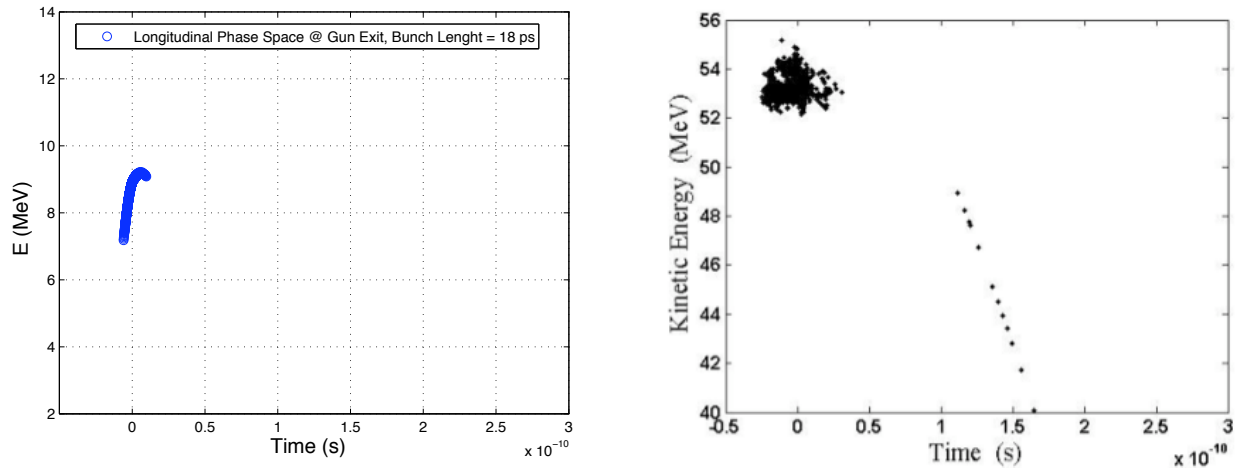


Figure 100: The longitudinal phase space for a) the 1 GHz RF gun and b) the thermionic gun at the end of the injector.

Conclusions

The PHIN photoinjector research and development activity has been continuing at CERN within the CARE program. In this thesis, the transverse and longitudinal beam properties of the PHIN photoinjector have been characterized, the feasibility to become a substitute for the CTF3 thermal injector has been investigated with the intentions to study the photoinjector option as the future CLIC drive beam electron source, as well.

The objectives of this thesis are:

- to show that the injector specifications of the CTF3 can be satisfied by a photoinjector without producing the unwanted parasitic charge (satellite bunches) due to the bunching system of the existing thermionic gun. The current parasitic charge level in the CTF3 beam has been given as 7% in the recent experimental studies. Whereas it can be completely avoided by using a photoinjector system that does not require an additional bunching system.
- to demonstrate the reliable and stable production of a $1.3 \mu s$ long bunch train, with $2.33 nC$ charge per bunch and $4.5 \mu C$ of total charge, by the PHIN photoinjector. The stability of the beam has a paramount importance as a drive beam injector candidate. Because, the stability of the power that is generated in the CLIC decelerators are inherit from the drive beam stability. Therefore, it has an direct influence on the effective acceleration of the CLIC main beams.

In the scope of this thesis, the comprehensive simulations have been performed for the PHIN test beamline by using PARMELA. These simulation studies can be divided into two parts as the benchmark simulations and the simulations for the experimental conditions. The benchmark simulations have been done to reveal the beam properties in a wide range of parameters. The laser spot size on the cathode, charge per bunch, RF phase, on-axis electric field of the cavity and magnetic focusing of the solenoid magnet have been determined as the variables of the benchmark study. The emittance compensation for space charge dominated beams has been studied. As the result of these investigations an optimum working point has been defined for the baseline configuration of the PHIN photoinjector and for a variety of energy and bunch charge values. In each case the trade-off between the longitudinal parameters and the transverse parameters have been investigated. The benchmark simulations have provided a reference for different conditions during the PHIN commissioning and for future photoinjector studies.

The experimental program have aimed the full characterization of the PHIN photoinjector for the short and the long bunch trains. In order to conduct these experiments a set of diagnostics tools have been utilized which enables both single shot and time-resolved measurements. Besides the traditional current monitoring and the OTR profile monitoring systems in the set-up, the non-trivial methods have been successfully imple-

mented such as the multi-slit emittance-meter for the space charge dominated beams and the segmented beam dump for the time-resolved energy measurements. The multi-slit emittance-meter has been commissioned within this thesis research. The programs for the analysis of the data for emittance measurement, in the form of the OTR images, have been developed. The necessary data acquisition programs with online and offline analysis components have been prepared. The computer programs that have been used during the PHIN commissioning have been collected within a software package called “PHINEMA”. The single shot measurements have been performed to provide shot to shot information of the beam. Whereas, the time-resolved measurements have supplied the beam status along the bunch train. In the end of the commissioning the PHIN beam have been fully characterized and the design specifications have been satisfied. Exceptionally, the charge stability have been found to be subject to improvement by a factor of three. The improvement will be done by implementing a feedback stabilization system for the laser intensity on the cathode in 2011. All the experimental results have been compared with the simulations.

The PHIN photoinjector has been commissioned with the intermittent runs between 2008 and 2010 with a total beam time of 60 workdays. The studies led to an eventual success by fulfilling the design specification. As a result, the PHIN photoinjector has been shown to be utilized as the CTF3 source.

The results of the experimental and numerical characterization of PHIN photoinjector have been used to initiate a photoinjector design with the CLIC drive beam parameters. For this purpose the PHIN RF gun have been rescaled to provide a 1GHz resonance frequency at the π -mode. The beam dynamics consequences of the new design have been discussed in comparison with another ongoing scenario which uses a thermionic gun. In both cases, the simulation studies fulfils several CLIC drive beam specific parameters, however the 4.9% of parasitic charge remains to be an issue of the thermionic gun. Therefore in this thesis, the PHIN photoinjector performance and stability as well as the further simulation studies for the 1GHz RF gun ensure that: the photoinjector constitutes a compact, high charge, low emittance option as the future CLIC drive beam electron source.

There are numerous items in the context of the future activities for the PHIN photoinjector. The phase coding system for the PHIN laser will be installed and commissioned during the February 2011 PHIN run. The system, that provides the nominal CLIC drive beam time structure, will be an important step towards the further demonstration of the feasibility of a photoinjector as drive beam source. Additionally, exceeding the nominal PHIN charge specification of 2.33nC , the CLIC drive beam specification of 8.4nC will be aimed within the future charge production studies. This has been planned to be achieved by using a larger laser spot size.

Regarding the future simulation studies for the 1GHz rescaled RF gun, it is important to improve the existing preliminary design in terms of the RF parameters such as the power consumption. The deliverable parameters from the RF gun have to be determined in case of an additional accelerating cavity for both 3GHz PHIN case and 1GHz case. The further acceleration has to be implemented in the position where the emittance compensation occurs. Therefore the emittance will be frozen in its minimum value and the energy spread will be lowered by the acceleration.

Acknowledgments



As a reflection of my three years of research, this thesis, would not be possible without the support of many people.

First and foremost, I would like to express my deepest gratitude to my supervisors Prof. Dr. Leonid Rivkin and Dr. Steffen Döbert. I have always received their endless support and invaluable guidance through the scientific effort which resulted with this thesis.

I would like to show my gratitude also to my colleagues with whom we worked together for the PHIN commissioning, Eric Chevallay, Marta Csatari, Dr. Steffen Döbert, Dr. Valentine Fedosseev, Dr. Massimo Petrarca, Dr. Anne Dabrowski, Daniel Egger, Natalie Lebas, Dr. Thibaut Lefèvre and Maja Olvegaard. I consider it an honor to work with them.

It gives me great pleasure in acknowledging the support and help of my colleagues, Dr. Günther Geschonke, Dr. Louis Rinolfi from CLIC/CTF3. The success of my thesis would not be possible without the advices and the experience of my colleagues within the Compact Linear Collider Project and the CLIC Test Facility 3 Collaboration. I offer my sincere thanks also to those who are not named here.

I would like to thank to Dr. Raphael Roux from Laboratoire de l'Accélérateur Linéaire. His previous works have become the very basics of my research.

I would like to thank to Dr. Hans Braun, Dr. Thomas Schietinger and Dr. Frederic Le Pimpec from Paul Sherrer Institute, for very useful discussions and for their hospitality in opening their laboratory, OBLA, to me. Our fruitful collaboration has become a paramount constituent of my development as a scientist. With the same manner, I would like to offer my thanks to Dr. Frank Stephan and the PITZ team, from Deutsches Elektronen-Synchrotron, for their hospitality and for the discussions during my visit.

I would like to thank to the members of the jury, Prof. Olivier Schneider, Dr. Hans Braun, Dr. Frank Stephan and Prof. Dr. Aurelio Bay for their extensively careful evaluation and appreciation of my scientific work.

Next but not least, I wish to thank to my colleague and friend Dr. Gökhan Ünel, who became an outstanding example to me in scientific curiosity, patience and hard-working, and from whom I have assimilated the part of my scientific attitude to be as stubborn as a Klingon when necessary.

I owe my sincere thanks to all of my friends for their support, understanding and discussions during my research. My social abilities would not be as they are now without them.

Finally, I wish to express my love and gratitude to my beloved mother and father, Aynur Alkan and Mehmet Mete, who raised and supported me in respect with my choices during my education and studies. I am deeply grateful to them for introducing science and scientific approach into my life since the very early stages. My love and gratitude also to my sister Özlem Mete and my brother Halil Mete for bringing joy and pure friendship into my life, for supporting and encouraging me during my studies.

Appendix 1 - Thermal Injector of CTF3

A thermionic gun is utilized in the CTF3 injector [99]. After the continues charge production in the gun, a bunching system has to be implemented to produce the desired time structure. The CTF3 bunching system consists of three 1.5 GHz sub-harmonic bunchers (SHB), an S-band pre-buncher (PB), a tapered phase velocity travelling wave buncher. After the bunching process, beam proceeds to two accelerating sections with the lenght of 1 m. The pre-buncher, buncher and accelerating structures operate at 3 GHz.

Due to the usage of the sub-harmonic bunching system, current CTF3 injector generates unwanted satellite bunches. The charge inside the satellite bunches is unusable for the rest of the operation, therefore it reduces the drive beam current. The amount of charge in the unwanted satellite bunches can be estimated from the streak camera images [100]. The charge in the satellite bunches has been measured as 7 – 8%, recently. The image that has been produced by the acquisition of the synchrotron radiation from the beam by a streak camera, is shown in the Fig. 101.

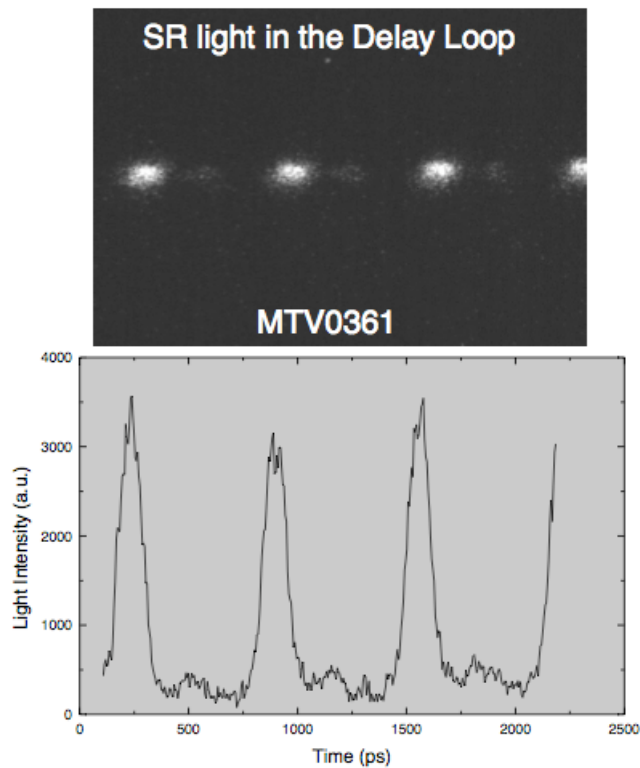


Figure 101: The streak camera image of the bunches in the delay loop and the unwanted satellite bunches.

Appendix 2 - The Beam Dynamics for Different Bunch Charge Values

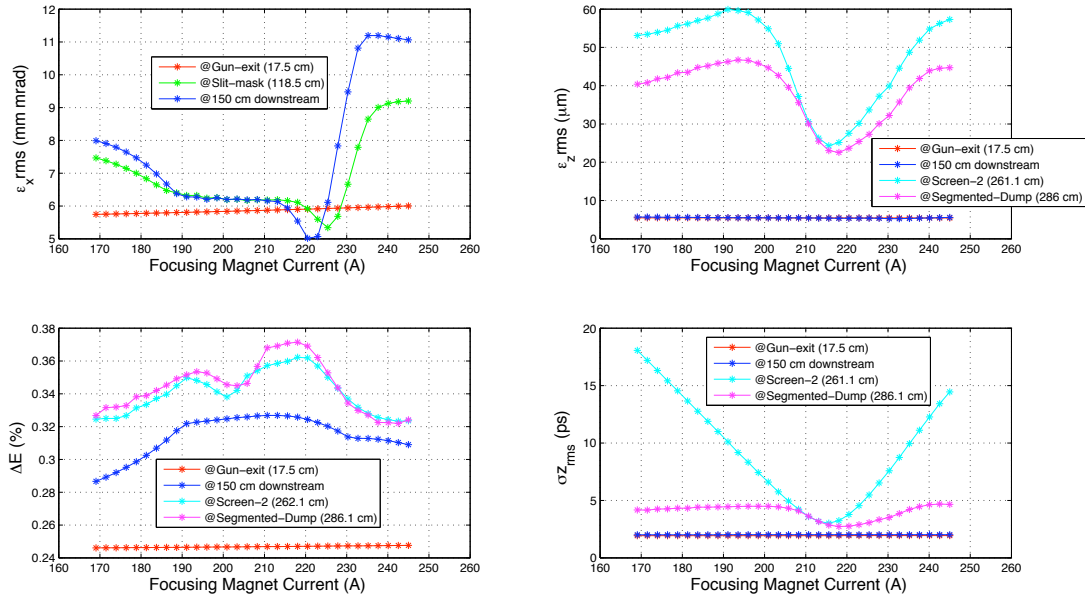


Figure 102: The beam dynamics parameters at the gradient of 85 MV/m for the beam charge of 1 nC.

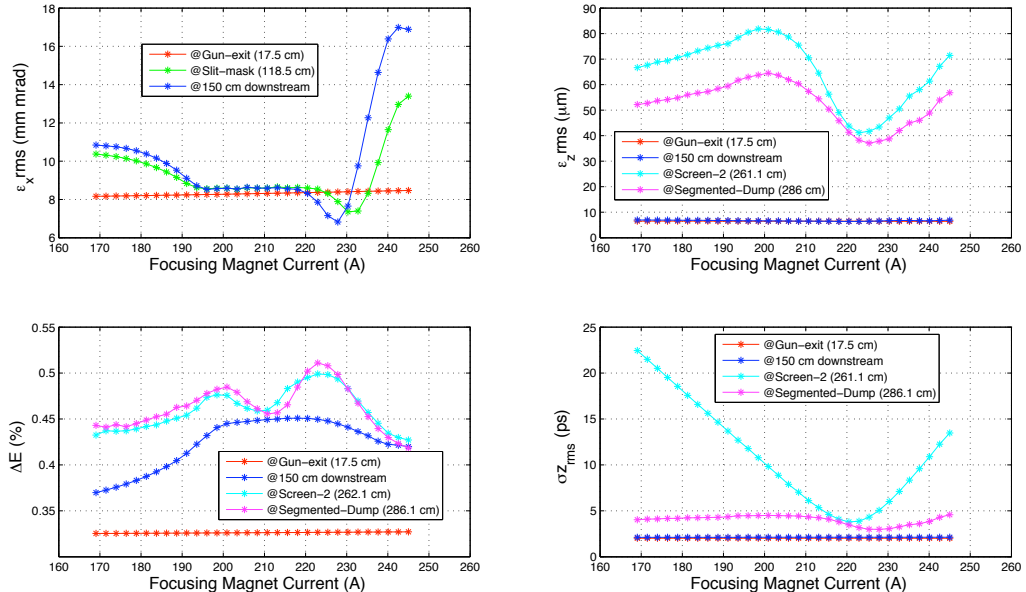


Figure 103: The beam dynamics parameters at the gradient of 85 MV/m for the beam charge of 1.5 nC.

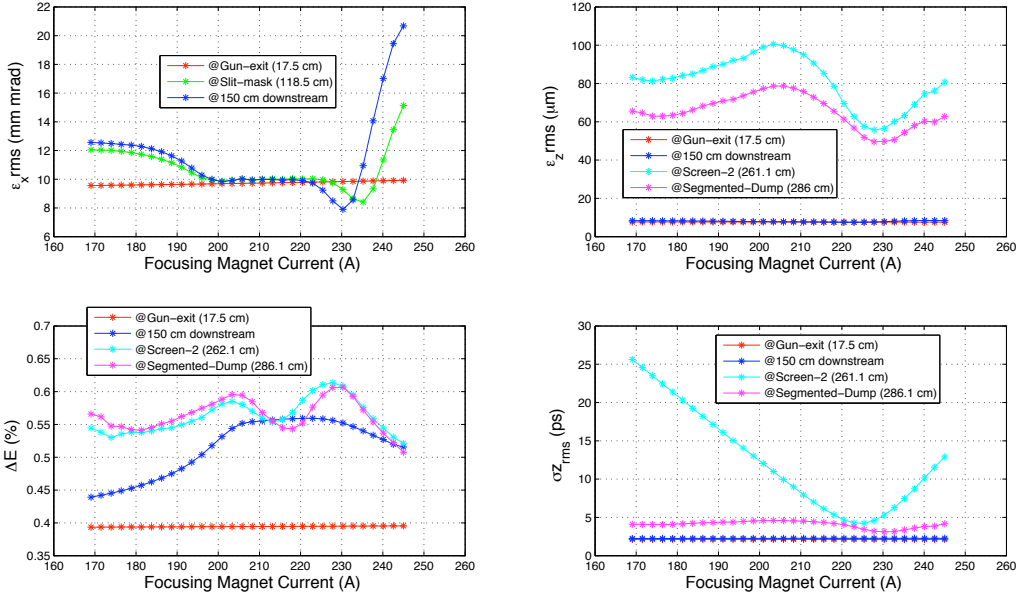


Figure 104: The beam dynamics parameters at the gradient of 85 MV/m for the beam charge of 2 nC.

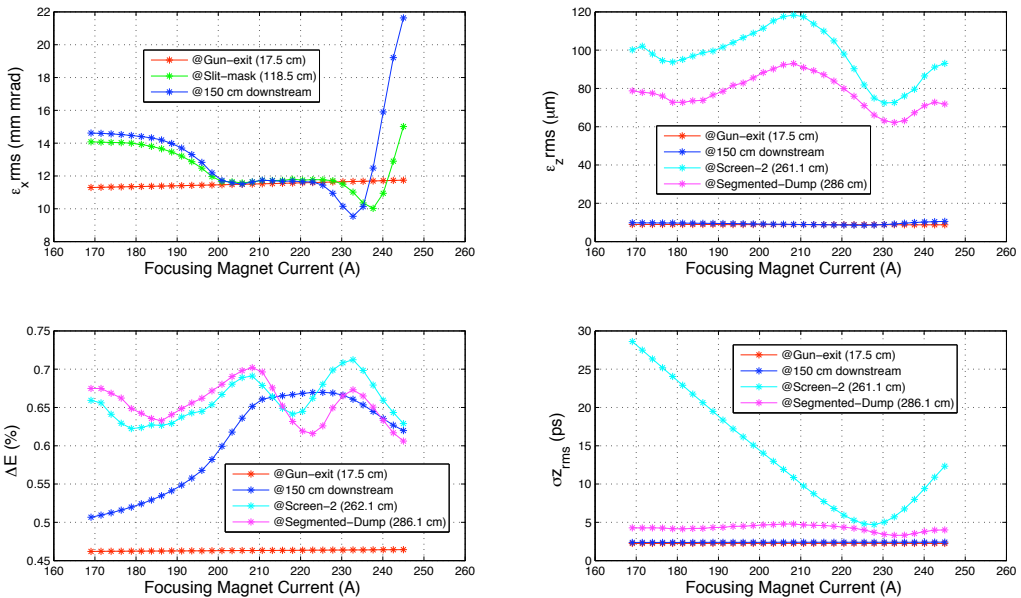


Figure 105: The beam dynamics parameters at the gradient of 85 MV/m for the beam charge of 2.5 nC.

Appendix 3 - Correlation Between the Fluctuations along the Pulse Train and on the RF Field

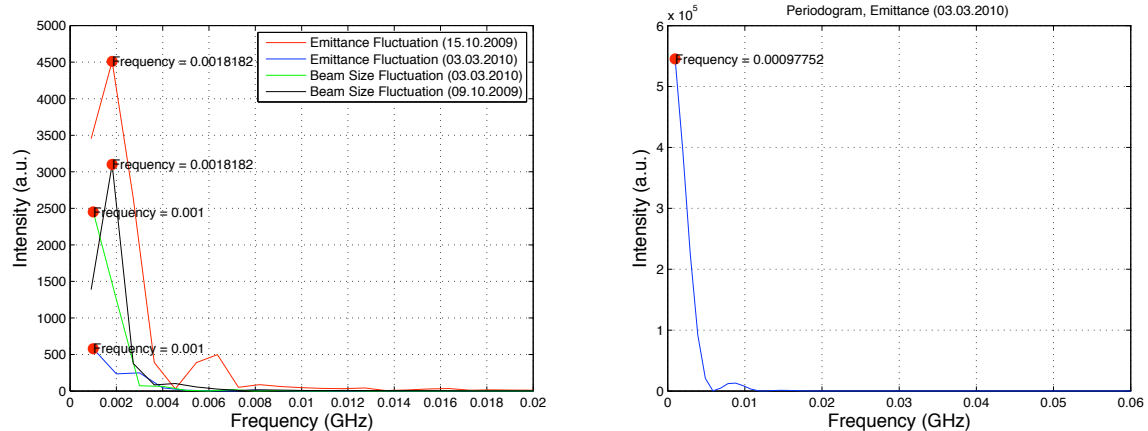


Figure 106: Correlations between the fluctuations along the train.

References

- [1] Frank Zimmermann. Final focus challenges for muon colliders at highest energies. *AIP Conf. Proc.*, 530(CERN-SL-99-077-AP):347–367. 21 p, Jan 2000.
- [2] B J King. High energy muon colliders. 2001.
- [3] B J King. Further studies on the prospects for many-tev muon colliders. (physics/0007064), 2000.
- [4] R. P. Johnson and Y. Derbenev. Technical challenges of moun colliders. *Jefferson National Accelerator Facility*, 2005.
- [5] H. H. Braun, J. P. Delahaye, A. De Roeck, and G. Geschonke. *CLIC Here for the Future*. CERN COURIER, Geneva, September 19, 2008.
- [6] Marco Battaglia, A de Roeck, Jonathan Richard Ellis, and Daniel Schulte. *Physics at the CLIC Multi-TeV Linear Collider : Report of the CLIC Physics Working Group*. CERN, Geneva, 2004.
- [7] S. Doeberl. *Status of Very High-Gradient Cavity Tests*. Proceedings of LINAC 2002, Gyeongju, Korea, 2002.
- [8] S. Doeberl. *RF-Breakdown in High-Frequency Accelerators*. SLAC-PUB-10463, 2004.
- [9] W. D. Kilpatrick. *Criterion for Vacuum Sparking Designed to Include Both RF and DC*. Rev. Sci. Instrum. 28, 824 (1957); doi:10.1063/1.1715731, 1957.
- [10] A. Wolski and W. Decking. Damping Ring Designs and Issues. *Lawrence Berkeley National Laboratory. LBNL Paper LBNL-52580*. Retrieved from: <http://escholarship.org/uc/item/2766w0b8>, 2003.
- [11] Y Papaphilippou and et al. *Design Optimization of the CLIC Damping Rings*. Proceedings of IPAC 2010 Kyoto, Japan, 2006.
- [12] F Antoniou, Y Papaphilippou, and F Zimmermann. Design considerations for the clic pre-damping rings. oai:cds.cern.ch:1212964. Technical Report CERN-ATS-2009-081. CLIC-Note-784, CERN, Oct 2009.
- [13] I. Syratchev, D. Schulte, E. Adli, and M. Taborelli. High rf power production for clic. oai:cds.cern.ch:1055564. 2007.
- [14] H. H. Braun, R. Corsini, S. Doeberl, E. Jensen, F. Tecker, and P. Urschutz. Efficient long-pulse fully-loaded ctf3 linac operation. oai:cds.cern.ch:999488. Technical Report CERN-OPEN-2006-070. CLIC-Note-697, CERN, Geneva, Nov 2006.
- [15] R. Bossart, H. Braun, J. P. Delahaye, K. K. Geissler, J. C. Godot, J. H. B. Madsen, A. J. Riche, L. Rinolfi, S. Schreiber, J. P. H. Sladen, G. Suberlucq, I. H. Wilson, and W. Wuensch. *Performances Obtained with the CERN Linear Collider Test Facility (CTF)*. CLIC Note 231, 1994.

- [16] H.H. for the CTF Team Braun. *Experimental Results and Technical Research and Development at CTF II*. Proceedings of EPAC 2000 Vienna, Austria, 2000.
- [17] H.H. for the CTF Team Braun. *Achievements and Future Plans for CLIC Test Facilities*. Tsukuba, Japan, The 18th International Conference on High Energy Accelerators, HEACC2001, 2001.
- [18] J. Norem, Z. Insepov, and I. Konkashbaev. Triggers for rf breakdown. *Nuclear Instruments and Methods in Physics Research Section A: Accelerators, Spectrometers, Detectors and Associated Equipment*, 537(3):510 – 520, 2005.
- [19] S. Bettoni, E. Adli, R. Corsini, A. Dabrowski, S. Doeberl, D. Manglunki, P. Skowronski, and F. Tecker. Achievements in ctf3 and commissioning status. oai:cds.cern.ch:1212966. Technical Report CERN-ATS-2009-082. CLIC-Note-785, CERN, Geneva, Oct 2009.
- [20] H. H. Braun, S. Doeberl, T. Ekelof, G. Geschonke, M. Johnson, J. Sladen, and V. Ziemann. *The Two-Beam Test-Stand in CTF3*. Proceedings of EPAC 2006 Edinburg, Scotland, 2006.
- [21] P. K. Skowronski, S. Bettoni, A. E. Dabrowski, S. Doeberl, A. Dubrovskiy, and F. Tecker. *Progress Towards the CLIC Feasibility Demonstration in CTF3*. Proceedings of IPAC 2010 Kyoto, Japan, 2006.
- [22] G. Geschonke and A Ghigo. Ctf3 design report, chapter 8. Technical Report CERN-PS-2002-008-RF. CTF-3-NOTE-2002-047. LNF-2002-008-IR, CERN, Geneva, May 2002.
- [23] G. Bienvenu, H. Braun, E. Chevallay, G. Cheymol, M. Divall, S. Doeberl, K. Elsener, V. Fedosseev, A. Ghigo, G. Hirst, M. Jore, N. Lebas, R. Losito, B. Mercier, O. Mete, M. Petrarca, C. Prevost, L. Rinolfi(Editor), R. Roux, A. Variola, and C. Vicario. CTF3 3 GHz RF Gun Test at CERN. *CTF3 Note 093*.
- [24] S. Dobert. Integration of the PHIN RF Gun into the CLIC Test Facility. *Prepared for European Particle Accelerator Conference (EPAC 06), Edinburgh, Scotland, 26-30 Jun 2006*.
- [25] J. S. Fraser and et al. *High Brightness Photoemitter Injector for Electron Accelerators*. IEEE Particle Accelerator Conference, Vancouver, 1985.
- [26] R. L. Sheffield and et al. *High Brightness Electron Injectors: A Review*. IEEE Particle Accelerator Conference, Williamsburg, 1988.
- [27] Kwang-Je Kim. RF and Space-Charge Effects in Laser-Driven RF Electron Guns. *Nuclear Instruments and Methods in Physics Research Section A: Accelerators, Spectrometers, Detectors and Associated Equipment*, 275(2):201 – 218, 1989.
- [28] Christian Travier. An introduction to photo-injector design. *Nuclear Instruments and Methods in Physics Research Section A: Accelerators, Spectrometers, Detectors and Associated Equipment*, 340(1):26 – 39, 1994.

- [29] E. Chevallay, J. Durand, S. Hutchins, G. Suberlucq, and M. Wurgel. Photocathodes tested in the dc gun of the cern photoemission laboratory. *Nuclear Instruments and Methods in Physics Research Section A: Accelerators, Spectrometers, Detectors and Associated Equipment*, 340(1):146 – 156, 1994.
- [30] S.C. Hartman, N. Barov, C. Pellegrini, S. Park, J. Rosenzweig, G. Travish, R. Zhang, C. Clayton, P. Davis, M. Everett, C. Joshi, and G. Hairapetian. Initial measurements of the ucla rf photoinjector. *Nuclear Instruments and Methods in Physics Research Section A: Accelerators, Spectrometers, Detectors and Associated Equipment*, 340(1):219 – 230, 1994.
- [31] B. Leblond. Short pulse photoemission from a dispenser cathode under the 2nd, 3rd and 4th harmonics of a picosecond nd: Yag laser. *Nuclear Instruments and Methods in Physics Research Section A: Accelerators, Spectrometers, Detectors and Associated Equipment*, 317(1-2):365 – 372, 1992.
- [32] T. Srinivasan-Rao and et al. *Photoemission Studies on Metals Using Picosecond Ultraviolet Laser Pulses*. J. Appl. Phys. 69, 3291, 1990.
- [33] Klaus Floettmann. *Note on the Thermal Emittance of Electrons Emitted by Cesium Telluride Photo Cathodes*. TESLA-FEL Report 1997-01, DESY, 1997, 2007.
- [34] S. Lederer and et al. *Investigations on the Thermal Emittance of Cesium Telluride Photocathodes at PITZ*. Proceedings of FEL 2007 Conference, Novosibirsk, Russia, 2007.
- [35] B. E. Carlsten. Space charge induced emittance compensation in high brightness photoinjectors. Technical Report Particle Accelerators, 1995, Vol. 49, pp.27-65, 1995.
- [36] B.E. Carlsten. New Photoelectric Injector Design for the Los Alamos National Laboratory XUV FEL Accelerator. *Nuclear Instruments and Methods in Physics Research Section A: Accelerators, Spectrometers, Detectors and Associated Equipment*, 285(1-2):313 – 319, 1989.
- [37] Michiko G Minty and Frank Zimmermann. *Measurement and Control of Charged Particle Beams*. Particle acceleration and detection. Springer, Berlin, 2003.
- [38] Bruce E. Carlsten and Dennis T. Palmer. Enhanced emittance compensation in a high-frequency rf photoinjector using rf radial focusing. *Nuclear Instruments and Methods in Physics Research Section A: Accelerators, Spectrometers, Detectors and Associated Equipment*, 425(1-2):37 – 50, 1999.
- [39] R. Ganter (Editor). *SwissFEL Conceptual Design Report, PSI Bericht Nr. 10-04*. 2010.
- [40] K. Li and et al. Low Emittance X-FEL Development. *Proceedings of the 27th International Free Electron Laser Conference, California, USA*, 2005.
- [41] H. Tanaka and et al. Low Emittance Injector at SCSS. *Proceedings of FEL 2006,BESSY,Berlin,Germany*, 2006.

- [42] F. Stephan and et al. Recent Results and Perspectives of the Low Emittance Photoinjector at PITZ. *Proceedings of the 2004 FEL Conference*, 347-350, 2004.
- [43] H. Braun. Progress at the XFELs in Europe and Japan. *48th ICFA Advanced Beam Dynamics Workshop on Future Light Sources, California, USA*, 2010.
- [44] J. W. Wang. *RF Properties of Periodic Accelerating Structures for Linear Colliders*. SLAC Report 339, 1989, 1989.
- [45] C. Travier. *High Brightness Photocathode Electron Sources*. arXiv:acc-physics/9411004v1, 1994.
- [46] Mark Curtin, Glenn Bennett, Robert Burke, Anup Bhowmik, Phillip Metty, Stephen Benson, and J. M. J. Madey. First demonstration of a free-electron laser driven by electrons from a laser-irradiated photocathode. *Nuclear Instruments and Methods in Physics Research Section A: Accelerators, Spectrometers, Detectors and Associated Equipment*, 296(1-3):127 – 133, 1990.
- [47] K. Batchelor and et al. *Operational Status of the Brookhaven National Laboratory Accelerator Test Facility*. EPAC'90 p.541, Nice, France, 1990.
- [48] A.H. Lumpkin, R.B. Feldman, B.E. Carlsten, D.W. Feldman, R.L. Sheffield, W.E. Stein, W.J. Johnson, L.E. Thode, S.C. Bender, and G.E. Busch. Initial observations of high-charge, low-emittance electron beams at hibaf. *Nuclear Instruments and Methods in Physics Research Section A: Accelerators, Spectrometers, Detectors and Associated Equipment*, 304(1-3):379 – 385, 1991.
- [49] D. H. Dowell, K. J. Davis, K. D. Friddell, E. L. Tyson, C. A. Lancaster, L. Milliman, R. E. Rodenburg, T. Aas, M. Bemes, S. Z. Bethel, P. E. Johnson, K. Murphy, C. Whelen, G. E. Busch, and D. K. Remelius. First operation of a photocathode radio frequency gun injector at high duty factor. *Applied Physics Letters*, 63(15):2035–2037, 1993.
- [50] A. Michalke and et al. *First Operation of High-Quantum Efficiency Photocathodes Inside Superconducting Cavities*. EPAC'92 p.1014, Berlin, Germany, 1992.
- [51] P. G. O'Shea, S. C. Bender, D. A. Byrd, J. W. Early, D. W. Feldman, C. M. Fortgang, J. C. Goldstein, B. E. Newnam, R. L. Sheffield, R. W. Warren, and T. J. Zaugg. Ultraviolet free-electron laser driven by a high-brightness 45-mev electron beam. *Phys. Rev. Lett.*, 71(22):3661–3664, Nov 1993.
- [52] A. Michalke and et al. *A High-DC-Voltage GaAs Photoemission Gun: Transverse Emittance and Momentum Spread Measurements*. PAC'97 p.2693, Vancouver, Canada, 1997.
- [53] X. Qiu, K. Batchelor, I. Ben-Zvi, and X-J. Wang. Demonstration of emittance compensation through the measurement of the slice emittance of a 10-ps electron bunch. *Phys. Rev. Lett.*, 76(20):3723–3726, May 1996.

- [54] X. J. Wang, X. Qiu, and I. Ben-Zvi. Experimental observation of high-brightness microbunching in a photocathode rf electron gun. *Phys. Rev. E*, 54(4):R3121–R3124, Oct 1996.
- [55] Luca Serafini and James B. Rosenzweig. Envelope analysis of intense relativistic quasilaminar beams in rf photoinjectors:ma theory of emittance compensation. *Phys. Rev. E*, 55(6):7565–7590, Jun 1997.
- [56] G. R. Neil, C. L. Bohn, S. V. Benson, G. Biallas, D. Douglas, H. F. Dylla, R. Evans, J. Fugitt, A. Grippo, J. Gubeli, R. Hill, K. Jordan, R. Li, L. Merminga, P. Piot, J. Preble, M. Shinn, T. Siggins, R. Walker, and B. Yunn. Sustained kilowatt lasing in a free-electron laser with same-cell energy recovery. *Phys. Rev. Lett.*, 84(4):662–665, Jan 2000.
- [57] Jang-Hui Han, Klaus Flöttmann, and Walter Hartung. Single-side electron multipacting at the photocathode in rf guns. *Phys. Rev. ST Accel. Beams*, 11(1):013501, Jan 2008.
- [58] D. J. Gibson, F. V. Hartemann, E. C. Landahl, A. L. Troha, N. C. Luhmann, G. P. Le Sage, and C. H. Ho. Electron beam and rf characterization of a low-emittance x -band photoinjector. *Phys. Rev. ST Accel. Beams*, 4(9):090101, Sep 2001.
- [59] D. Janssen and et al. First operation of a superconducting rf-gun. *Nuclear Instruments and Methods in Physics Research Section A: Accelerators, Spectrometers, Detectors and Associated Equipment*, 507(1-2):314 – 317, 2003. Proceedings of the 24th International Free Electron Laser Conference and the 9th Users Workshop.
- [60] J. W. Lewellen and C. A. Brau. Rf photoelectric injectors using needle cathodes. *Nuclear Instruments and Methods in Physics Research Section A: Accelerators, Spectrometers, Detectors and Associated Equipment*, 507(1-2):323 – 326, 2003. Proceedings of the 24th International Free Electron Laser Conference and the 9th Users Workshop.
- [61] M. Ferrario and et al. Direct Measurement of the Double Emittance Minimum in the Beam Dynamics of the Sparc High-Brightness Photoinjector. *Phys. Rev. Lett.*, 99(23):234801, Dec 2007.
- [62] O. Mete, E Chevallay, A Dabrowski, M Divall, S Doeberl, D Egger, K Elsener, V Fedosseev, T Lefevre, and M Petrarca. The transverse and longitudinal beam characteristics of the phin photo-injector at cern. oai:cds.cern.ch:1262856. Technical Report CERN-OPEN-2010-013. CLIC-Note-809, CERN, Geneva, Mar 2010.
- [63] M. Ferrario and et al. Experimental Demonstration of Emittance Compensation with Velocity Bunching. *Phys. Rev. Lett.*, 104(5):054801, Feb 2010.
- [64] Steven J. Russell. Overview of high-brightness, high-average-current photoinjectors for fels. *Nuclear Instruments and Methods in Physics Research Section A: Accelerators, Spectrometers, Detectors and Associated Equipment*, 507(1-2):304 – 309, 2003. Proceedings of the 24th International Free Electron Laser Conference and the 9th Users Workshop.

- [65] M. Ferrario. *Overview of FEL Injectors*. Proceedings of EPAC 2006, Edinburgh, Scotland, 2006.
- [66] D. H. Dowell and et al. *First Operation of a Photocathode Radio Frequency Gun Injector at High Duty Cycle*. Appl. Phys. Lett. 63, 2035 (1993); doi:10.1063/1.110583, 1993.
- [67] R. Xiang and et al. *Running Experience of the Superconducting RF Photoinjector at FZD*. Proceedings of FEL2009, Liverpool, UK, 2009.
- [68] S. Dobert. Integration of the PHIN RF Gun into the CLIC Test Facility. *Prepared for European Particle Accelerator Conference (EPAC 06), Edinburgh, Scotland, 26-30 Jun 2006*.
- [69] G. Geschonke. Results from the CLIC Test Facility CTF3 and Update on the CLIC Design. *EPAC08 Conference Proceedings*, EPAC'08, Genoa, Italy. June 23-27, THYG02, p.2912 (2008). <http://www.JACoW.org>.
- [70] R. Roux. Conception of Photo-injectors for CTF3 Experiment. *International Journal of Modern Physics A*, Vol.22, No. 22 (2007) 3925-3941.
- [71] L. M. Young and J. Billen. The Particle Tracking Code PARMELA. *Particle Accelerator Conference (PAC 03) 12-16 May 2003, Portland, Oregon*.
- [72] K. Halbach and R. F. Holsinger. Superfish - a computer program for evaluation of rf cavities with cylindrical symmetry. *Part. Accel.*, 7(LBL-5040):213–222. 29 p, Jun 1976.
- [73] R. Roux, G. Bienvenu, and B. Mercier. Design of a RF Photo-Gun. *CARE Note-2004-034-PHIN*.
- [74] Kevin L. Jensen. General formulation of thermal, field, and photoinduced electron emission. *Journal of Applied Physics*, 102(2):024911, 2007.
- [75] Richard G. Forbes. Field emission: New theory for the derivation of emission area from a fowler-nordheim plot. volume 17, pages 526–533. AVS, 1999.
- [76] R. H. Fowler and L. Nordheim. Electron Emission in Intense Electric Fields. *Proceedings of the Royal Society of London. Series A*, 119(781):173–181, 1928.
- [77] W. E. Spicer. Photoemissive, photoconductive, and optical absorption studies of alkali-antimony compounds. *Phys. Rev.*, 112(1):114–122, Oct 1958.
- [78] R. A. Powell, W. E. Spicer, G. B. Fisher, and P. Gregory. Photoemission studies of cesium telluride. *Phys. Rev. B*, 8(8):3987–3995, Oct 1973.
- [79] A. Barbiero, E. Chevallay, K. Elsener, and R. Losito. Cesium-Telluride Photocathode No. 166. *AB-Note-2007-023 ATB, CARE-Report-07-018-PHIN, CTF3-Note-089*, 2007.
- [80] M. Petrarca, V. Fedosseev, and N. Lebas. CTF3 Photo-Injector Laser Amplifier Construction. *CARE-Report-2008-012-PHIN*, CARE-Report-2008-012-PHIN, 2008.

- [81] M. Petrarca and et al. CTF3 Photo-Injector Laser. *CLEO/IQEC Proceedings, 2009, Baltimore, Maryland.*
- [82] M. Petrarca, K. Elsener, V. Fedossev, and N. Lebas. CTF3 Photo-Injector: RF Synchronization of the Laser System. *CARE-Report-2008-030-PHIN*.
- [83] Katja Honkavaara. Optical Transition Radiation in High Energy Electron Beam Diagnostics. *PhD Thesis*, LAL-Orsay, 1999.
- [84] Zhang, Min. Emittance Formula for Slits and Pepperpot Measurement. *FERMILAB-TM-1988*.
- [85] S. G. Anderson and et al. Space-Charge Effects in High Brightness Electron Beam Emittance Measurements. *Phys. Rev. ST Accel. Beams*, 5(1):014201, Jan 2002.
- [86] P Piot, J Song, R Li, G A Krafft, D Kehne, K Jordan, E Feldl, and J C Denard. A multislit transverse-emittance diagnostic for space-charge-dominated electron beams. 1998.
- [87] Luca Serafini and James B. Rosenzweig. Envelope analysis of intense relativistic quasilaminar beams in rf photoinjectors:ma theory of emittance compensation. *Phys. Rev. E*, 55(6):7565–7590, Jun 1997.
- [88] D. Egger, A. Dabrowski, and Lefevre T. The Status of the Design of the PHIN Spectrometer Line Diagnostics for Time Resolved Energy Measurements and First Results from 2009 . *CTF3-Note-099*.
- [89] D. Cornuet and Patron G. Mesure Magnetique du Spectrometre 90 Deg. K. BHZ 240 du C.T.F. *Note Tehcnique*.
- [90] Proxitronic NANOCAM HF4 100N UV Operation Manual. Video Imaging in the Nanosecond Range. <http://www.proxitronic.de/products/nanosecond-camera.html>.
- [91] Performance of the Time Resolved Spectrometer for the 5 MeV Photo-Injector PHIN. Paper in Preparation. . *DIPAC2011*.
- [92] MATLAB. *version 7.6.4 (R2008a)*. The MathWorks Inc., Natick, Massachusetts, 2008.
- [93] R. H. Fowler and L. Nordheim. Electron Emission in Intense Electric Fields. *Proceedings of the Royal Society of London. Series A, Vol. 119, No. 781. 173-181p.* 1928.
- [94] T. P. Wangler. *Principles of the RF Linear Accelerators*. John Wiley & Sons, Inc., New York, 1998.
- [95] A. Ferrari, P. R. Sala, A. Fasso, and J. Ranft. FLUKA: A multi-particle transport code (Program version 2005). *CERN-2005-010*.
- [96] *Private communication with Dr. Anne Evelyn Dabrowski*. CERN Beam Instrumentation Group, Geneva, 2009.

- [97] A. Dabrowski, S. Doeberl, D. Egger, O. Mete, and T. Lefevre. Design and Results of a Time Resolved Spectrometer for the 5 MeV Photo-Injector Phin. Technical Report CERN-BE-2010-018, CERN, Geneva, May 2010.
- [98] CLIC Collaboration. The Conceptual Design Report of the Compact Linear Collider Project (in progress).
- [99] G. Geschonke and A. Ghigo. Ctf3 design report, chapter 7. Technical Report CERN-PS-2002-008-RF. CTF-3-NOTE-2002-047. LNF-2002-008-IR, CERN, Geneva, May 2002. revised version number 1 submitted on 2002-06-19 12:11:29.
- [100] P. Urschutz, H. H. Braun, G. Carron, R. Corsini, S. Doeberl, T. Lefevre, G. McMonagle, J. Mourier, J. P. H. Sladen, F. Tecker, L. Thorndahl, and C. Welsch. Beam dynamics and first operation of the sub-harmonic bunching system in the ctf3 injector. Jul 2006. revised version submitted on 2006-10-03 14:34:35.

Curriculum Vitae

ÖZNUR METE

February 2011

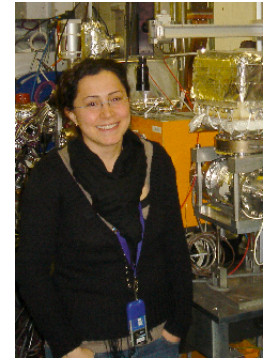
Employee,

CERN, European Organization for Nuclear Research

Beams Department, CLIC Project

PhD Student,

EPFL Doctoral Program in Physics



CERN

CH-1211

Office: 19-03-033

Geneva

Switzerland

Phone : +41 22 767 20 42

Mobile Phone : +41 76 264 88 49

E-mail : oznur.mete@cern.ch

Web: www.cern.ch/omete

Education

EPFL, Ecole Polytechnique Fédéral de Lausanne (01/2008-present)

PhD Student, SB-IPEP-LPAP

Supervisor: Prof. Leonid Rivkin (EPFL)

Thesis: Study and Characterization of a Novel Photo-Injector for CLIC Drive Beam

CERN, CLIC Study (01/2008-present)

CERN Beams Department

Co-Director: Dr. Steffen Doeber (CERN)

Ankara University (08/2004-08/2006)

M.Sc. in Physics Engineering, Accelerator Physics Research Group

Supervisor: Prof. Omer Yavas

Thesis: Accelerator Based Light Sources

Hacettepe University (10/1999-09/2003)

Bachelor of Science in Physics Engineering, Superconductors and Nanotechnology Research Group,

Supervisor: Prof. Tezer Firat

Graduation Project: Superconductor Physics and Applications

Schools and Training

- 2010 International School of Trigger and Data Acquisition, Ankara, Turkey.
- 2009 CERN Accelerator School: ‘Intermediate Accelerator Physics’, Darmstadt, Germany.
- 2008 CERN Accelerator School: ‘Beam Diagnostics’, Dourdan, France.
- 2006 ‘Optimization of a Free Electron Laser (FEL)’, Forschungszentrum Rossendorf, ELBE, Dresden, Germany.
- 2005 ‘Characterization of Magnet Materials by Helmholtz Coils Method’, HASYLAB, DESY Summer School, Hamburg, Germany.
- 2002 ‘Microwave Communication: Transmitter and Receiver Systems’ AES, Anadolu Elektronik Sanayi, Kayseri, Turkey.

Computer Skills

Simulation

- PARMELA - Particle Tracking Code (used professionally)
- Poisson SUPERFISH - Active Components Design (used professionally)
- MADX - Accelerator Design Code (introductory level)
- CompHEP/CalcHEP - Calculations of Elementary Particle Decays and Collision Processes (introductory level)

Development

- MATLAB (used professionally)
- PHINEMA : PHIN photo-injector Emittance Measurement and Analysis software (Readout and Analysis Software, I developed @ CERN).
- MATHEMATICA (Attended to the “Using Mathematica to Analyse and Model Experimental Data” course at EPFL)
- Unix/Basic/Fortran/C/C++

Languages

- Turkish (Native)
- English (Advanced)
- French (Elementary)

Professional Experiences

Project: “**CARE/PHIN, A Joint Research Activity for Photo Injectors**”
CERN - Beams Department, CLIC (Compact Linear Collider) Study, Geneva, Switzerland
Period : 2008 - present
Position: PhD Student
The project is supported by European CARE Program.

Project : “**CLIC Accelerators and Their Applications: CTF3 (CLIC Test Facility 3) Operation** ”
Ankara University - Physics Engineering Department, Ankara, Turkey
Period : 2004-2006
Position: M.Sc. Student / Project Associate
The project is supported by Turkish Atomic Energy Authority.

Project : “CLIC-LHC Based FEL-Nucleus Collider”

Ankara University - Physics Engineering Department, Ankara, Turkey

Period : 2004-2006

Position: M.Sc. Student / Project Associate

The project is supported by State Planning Organization (DPT) and Turkish Atomic Energy Authority.

Project : “Turkish Accelerator Centre Technical Design and Test Laboratory”

Ankara University - Physics Engineering Department, Ankara, Turkey

Period : 2004-2006

Position: M.Sc. Student / Project Associate

The project is supported by State Planning Organization (DPT) .

Project : “Usage of Syncrotron Radiation and Free Electron Lasers”

Ankara University - Physics Engineering Department, Ankara, Turkey

Period: 2003-2006

Position: M.Sc. Student / Project Associate

The project is supported by State Planning Organization (DPT).

Honors and Memberships

- The prize for the best poster was awarded during the CERN Accelerator School - Accelerator Physics, 2009, Darmstadt, Germany
- Official CERN Guide (in the stage of training)
- European Physical Society
- Swiss Physical Society
- A3-EPFL, Association Des Diplômés De L'EPFL
- Middle East Technical University - Astronomy Club (2000-2002)
- Co-convener of CERNTR Physics Forum at CERN (2009-present)
- Member of Organization Committee of Particle Accelerators and Detectors Summer School Program in Turkey (2005, 2006)

Seminars

Conferences / Workshops / Colloquiums

1. **11/2010** The Highlights from the Commissioning of the PHIN Photoinjector, Paul Scherrer Institute, Villigen, Switzerland.
2. **10/2010** The PHIN Photoinjector Commissioning Results, The First International Workshop on Linear Colliders, IWLC2010, Geneva, Switzerland.
3. **09/2010** Commissioning Results of PHIN Photoinjector at CERN, DESY / PITZ, Zeuthen, Germany.
4. **05/2010** PHIN, Experimental Results and Plans for 2010, CLIC-CTF3 Collaboration Meeting 2010, CERN, Geneva, Switzerland.
5. **11/2009** Electron Beam Characterization at an RF Photo-Injector; Measurement Techniques, Results and Simulations, Turkish Atomic Energy Authority (TAEK), Ankara.
6. **10/2009** Photo-Injector - PHIN, Results, CLIC Workshop'09, CERN, Geneva, Switzerland.
7. **07/2009** Status of Beam Measurements @ PHIN Photo Injector, CLIC Meeting, CERN, Geneva, Switzerland.
8. **06/2009** The Measurements of Transverse and Longitudinal Beam Properties of PHIN Photo-Injector @ CERN, Paul Scherrer Institute, Villigen, Switzerland.
9. **05/2009** CERN, Evren'in Sırlarının Peşinde Bir Bilim ve Teknoloji Yolculuğu, Erciyes Üniversitesi, Kayseri, Turkey (Colloquium).
10. **02/2009** The Beam Dynamics Issues for PHIN Photo Injector, CLIC Beam Physics Meeting, CERN, Geneva, Switzerland.
11. **01/2009** PHIN Photo Injector: The First Measurement Results, CTF3 Collaboration Meeting, CERN, Geneva, Switzerland.
12. **08/2008** The Experimental Characterization of PHIN Photo Injector: Initial Simulation Results and the Method for the Emittance Measurement, CLIC Meeting, CERN, Geneva, Switzerland.
13. **11/2006** The Proposal of Accelerator Based Light Sources for TAC Project, Forschungszentrum Rossendorf, ELBE, Dresden, Germany.
14. **11/2006** The Proposal for Accelerator Based Light Sources for the TAC Project, DESY Accelerator Physics Seminar, Hamburg, Germany.
15. **08/2006** The Accelerator Based Light Sources, 4th International Student Conference of Balkan Physical Union (ISCBPU4), Mugla, Turkey.
16. **08/2006** The Parametrization of An IR FEL Oscillator as TAC Test Facility, 4th International Student Conference of Balkan Physical Union (ISCBPU4), Mugla, Turkey.
17. **06/2006** An Optimization Study for an FEL Oscillator at TAC Test Facility, European Particle Accelerator Conference 06 (EPAC06), Edinburgh, Scotland (Poster).
18. **04/2005** Turkish Accelerator Center Test Facility(TAC-TF): Design Predictions and Application Areas, Accelerator Physics Research Group Seminars, Ankara University, Ankara.
19. **11/2004** Wigglers and Undulators as Sources of Radiation, Accelerator Physics Research Group Seminars, Ankara University, Ankara.

Physics Forums / Clubs

1. **04/2010** An Example: MADX Simulations for a Collider Ring in the Light of General Concepts, CERN, Geneva, Switzerland
2. **04/2010** A Review: General Concepts of Accelerator Physics, CERNTR Physics Forum, CERN, Geneva, Switzerland
3. **02/2009** Le Voyage Fantastique: The Dynamics in a Photo-Injector, CERNTR Physics Forum, CERN, Geneva, Switzerland
4. **07/2008** Introduction of CLIC and the Photo-Injector Prototype, CERNTR Physics Forum, CERN, Geneva, Switzerland

Publications

Conference Proceedings

1. The Beam Measurements of PHIN Photo-Injector at CERN, CERN Accelerator School 2009 (CAS09), Darmstadt, Germany (**Best Poster Award**)
2. The Transverse and Longitudinal Characteristics of the PHIN Photo Injector, Diagnostics for Particle Accelerators Conference 2009 (DIPAC09), Dourdan, France
3. First Results from Commissioning of the PHIN Photo Injector, Particle Accelerators Conference 2009 (PAC09), Vancouver, Canada
4. 30 GHz High-Gradient Accelerating Structure Test Results, Particle Accelerator Conference 2007 (PAC07), Albuquerque, New Mexico
5. A High-Gradient Test of a 30 GHz Copper Accelerating Structure, Linear Accelerators Conference 2006 (LINAC06), Knoxville, Tennessee USA, pp 761-763.
6. A High Gradient Test of a 30 GHz Molybdenum-iris Structure, European Particle Accelerators Conference 2006 (EPAC06), Edinburgh, U.K., pp 801-803.
7. An Optimization Study for an FEL Oscillator at Tac Test Facility, European Particle Accelerator Conference 2006 (EPAC06), Edinburgh, U.K., pp 136-138
8. An Infrared FEL as TAC Test Facility, 23rd Turkish Physical Union Conference Proceedings (TFD23), 13-16 Sept. 2005, Mugla University, Mugla, Turkey.
9. CLIC and LHC Based FEL-Nucleus Collider, National Congress of Nuclear Sciences and Technologies IX, 14-15 Sept. 2005, Ege University, Izmir, Turkey.

CLIC (Compact Linear Collider) Internal Notes (Reviewed)

1. The Transverse and Longitudinal Beam Characteristics of PHIN Photo-Injector at CERN, CLIC NOTE-809, 2010
2. The First Results from Commissioning of PHIN Photo-Injector for CTF3, CLIC NOTE-802, 2009
3. CTF3 3 GHZ RF Gun Test at CERN, CTF3 NOTE-093, 2009

In Preparation

1. PHINEMA : PHoto-INjector Emittance Measurement and Analysis software
2. Design of a Photo-Injector for CLIC Drive Beam Based on the PHIN Commissioning Results
3. Beam Dynamics Aspects of the PHIN Photoinjector Commissioning